Metal-Insulator Transition and IR Detection of Thin Films Fabricated by Pulsed Laser Deposition

by

Ryan Thomas McGee

A thesis submitted in partial fulfilment of the requirements for the degree of

Doctor of Philosophy

in

Materials Engineering

Department of Chemical and Materials Engineering

University of Alberta

© Ryan Thomas McGee, 2018

Abstract

Current thin film technologies and devices require high quality deposits in order to fully extract the potential of the material. Pulsed laser deposition (PLD) is one physical vapour deposition method used to synthesize these high quality complex films. PLD offers the distinct advantage of being able to stoichiometrically transfer the target material onto the substrate, enabling the deposition of extremely complicated multi-cation materials. This thesis focuses on the synthesis, characterization, and implementation of PLD deposited films into microelectromechanical systems (MEMS) and photonic applications. Specifically, VO_2 and MoS_2 films will be deposited and subsequently investigated for the above mentioned applications.

The research presented in this thesis targets the synthesis, characterization, device integration, and applications fo thin films deposited by PLD. Characterization by multiple forms of microscopy, X-ray diffraction, spectroscopy, electronic response, and photothermal response provide a multitude of new information integral to successful applications. VO_2 thin film deposition is optimized by implementation of the Taguchi method, where the influence of each variable is elucidated by analysis of variance. The electronic properties of VO_2 are shown to rely heavily on the interfacial structure between the film

and substrate, with increased performance present in epitaxial films. Integration into MEMS devices required the development of a full microfabrication process, accounting for the stability of not only VO_2, but all other materials during the entire process. Once integrated on MEMS devices, the phase transition of VO_2 is manifested as a huge shift in the resonance frequency.

Finally, the mid-IR photothermal response of PLD deposited MoS_2 is investigated. Physical defects imparted by the impactive nature of PLD create trap states in the band structure, leading to improved sensitivity to mid-IR. Additionally, interfacial structure was important in the sensitivity, as a twin interface between MoS_2 and silicon improved the temperature coefficient of resistance, and ultimately the responsivity.

The conclusion presents a variety of potential applications for both VO_2 and MoS_2 thin films that have been, or are currently under investigation. The future applications of these materials seems limitless due to the unique properties of both. This thesis closes with an insight into ongoing research applicable to the work already completed.

Preface

The description of techniques, experimental results and analysis, as well as any conclusions are my original work, as supervised by Dr. Thomas Thundat. The organizational structure of this work is a paper based format, as several chapters have been, or are in preparation for, publication in peer reviewed scientific journals.

Chapter 3 has been published as R. McGee, A. Goswami, B. Khorshidi, K. McGuire, K. Schofield, and T. Thundat, "Effect of process parameters on phase stability and metal-insulator transition of vanadium dioxide (VO_2) thin films by pulsed laser deposition" *Acta Materialia*, **137** 12-21 (2017). I was responsible for the experimental design, conduction of experiments, analysis of results, and preparation of the manuscript. A. Goswami assisted with experimental work and manuscript revisions, B. Khorshidi assisted in the design of experiments and data analysis, K. McGuire and K. Schofield assisted with data collection. T. Thundat was involved with the concept and manuscript revisions.

Chapter 4 has been published as R. McGee, A. Goswami, S. Pal, K. Schofield, S. Bukhari, and T. Thundat "Enhancement of the sharpness and intensity of the metal-insulator transition in ultrathin VO_2 films by interfacial structure manipulation" *Physical Review Materials* **2**, 034605 (2018). I was

responsible for the conception of the experiment, data collection and analysis, and preparation of the manuscript. A. Goswami assisted in planning and conducting experiments, as well as in the preparation of the manuscript. S. Pal conducted the TEM and assisted in the analysis of the data. K. Schofield and S. Bukhari assisted with experimental work and manuscript revisions. T. Thundat was the supervising author and was involved with shaping the research goals and manuscript preparation.

Chapter 5 has been published as R. McGee, A. Goswami, R. Abraham, S. Bukhari, T. Thundat "Phase transformation induced modulation of the resonance frequency of VO_2/TiO_2 coated microcantilevers" *MRS Advances* **3** (6-7), 359-364 (2018). I was responsible for conceiving the idea, performing experiments, data analysis, and manuscript preparation. A. Goswami assisted in data analysis and manuscript preparation. R. Abraham and S. Bukhari helped with data collection. T. Thundat helped form the idea and prepare the manuscript.

Chapter 6 contains work by R. McGee, A. Goswami, S. Bukhari, L. Zhou, and T. Thundat that is undergoing preparation for submission to Journal of Micro/Nanolithography, MEMS, and MOEMS. In this work I was responsible for developing the process, conducting the fabrication, running the experiments, analyzing the data, and preparing the manuscript. A. Goswami, S. Bukhari, and L. Zhou helped with experimental and analysis steps as well as manuscript preparation. T. Thundat helped conceive the idea and prepare

the manuscript.

Chapter 7 has been published as A. Goswami, P. Dhandaria, S. Pal, R. McGee, F. Khan, Ž. Antić, R. Gaikwad, K. Prashanthi, and T. Thundat "Effect of interface on mid-infrared photothermal response of MoS_2 thin film grown by pulsed laser deposition " *Nano Research*, **10**(10), 3571-3584 (2017). My role in this research was integral in device fabrication, data collection and analysis, and significant contributions to the composition of the manuscript.

"The important thing in science is not so much to obtain new facts as to discover new ways of thinking about them."

Sir William Henry Bragg
Nobel Prize in Physics (1915)

Acknowledgements

This thesis is a culmination of years of hard work that would have been impossible to accomplish alone. I received the support from several people, including family, friends, mentors, and colleagues. I would first like to thank my Mom and Dad for not only their support during this work, but for their unwavering love and support since the day I was born. To my Grandmother Theresa, you were always there for me when I needed someone, and for that I am forever grateful. To my sister Megan and brother Reid, you guys have always had my back as kids, and now as adults and your support is always appreciated. To my brilliant girlfriend Sumalee, who inspires me to be better everyday, I would like to thank you for taking care of me, putting up with my nonsense, and being there for me whenever I just needed someone.

My sincerest thank you to my thesis advisor, Dr. Thomas Thundat, who always encouraged me to push my boundaries and strive for more. You taught us all to forever remain curious, and never settle for less than the best. To Dr. Stojan Djokić, you have given me unconditional support from the first time we met, and your confidence in me provided all I ever needed to forge my own path.

Throughout the years of my thesis, I had the wonderful privilege of meeting some amazing people, who all had a part in shaping both me and my work. I would first like to recognize Dr. Ankur Goswami who took me under his wing and together we pushed each other to achieve more. Lab members Syed Bukhari, Dr. Priyesh Dhandharia, Dr. Naresh Miriyala, John Hawk, Jun Liu, and Dr. Behnam Khorshidi were always up for stimulating discussion and providing their expertise to the research at hand. Kalvin Schofield, Kristi McGuire, and Liang (John) Zhou, although your time with us was much shorter than the rest, the help and support from all of you far

exceeded expectations. Jacob Kennedy and Josh Cunningham, who had to suffer with me in the early years through all the coursework, it was nice to sit back and relax sometimes.

The staff in the nanofab at the University of Alberta provided countless hours of assistance and training, making my fabrication and characterization needs much easier. Such a state-of-the-art facility is an enormous advantage to have, and their push for continuous expansion in obtaining the state of the art equipment made life much easier. I would like to acknowledge Josie Nebo who has to put up with the collective needs of our entire group. Without her, our lab would not be where it is today. To everyone, words cannot express how truly appreciative I am of all the support I have received.

Contents

List of Tables **xv**

List of Figures **xviii**

1 Introduction **1**

1.1 Motivation 1

1.2 Thesis structure and content 3

1.3 Related publications 7

1.4 Pulsed laser deposition 10

1.5 Nucleation and grain growth in thin films 13

1.6 Vanadium dioxide (VO_2) 16

1.7 Molybdenum disulfide (MoS_2) 18

2 Characterization and fabrication techniques **20**

2.1 Pulsed laser deposition 20

2.2 X-ray diffraction 21

2.3 Scanning electron microscopy 25

2.4 Additional characterization techniques 30

2.4.1 Transmission electron microscopy 30

2.4.2 Helium ion microscopy 30

2.4.3 Atomic force microscopy 31

3 Effect of process parameters on phase stability and metal-insulator

transition of vanadium dioxide (VO_2) thin films by pulsed laser deposition **33**

3.1 Abstract . . . 33

3.2 Introduction . . . 34

3.3 Experimental . . . 37

3.3.1 Materials synthesis . . . 37

3.3.2 Taguchi method-design of experiment . . . 38

3.3.3 Plasma plume dynamics . . . 38

3.3.4 Characterization . . . 41

3.4 Results and discussion . . . 42

3.4.1 X-ray diffraction analysis . . . 43

3.4.2 Microstructure analysis . . . 45

3.4.3 Surface roughness analysis by AFM . . . 48

3.4.4 Electrical Characterization . . . 49

3.4.5 Taguchi analysis of process variables . . . 51

3.4.6 Confirmation of Taguchi method . . . 54

3.5 Conclusion . . . 55

3.6 Supplementary data . . . 57

4 Enhancement of the sharpness and intensity of the metal-insulator transition in ultrathin VO_2 films by interfacial structure manipulation **64**

4.1 Abstract . . . 64

4.2 Introduction . . . 65

4.3 Experimental . . . 68

4.3.1 Materials synthesis . . . 68

4.3.2 Characterization . . . 70

4.4 Results and discussion . . . 71

4.4.1 X-ray diffraction phase analysis . . . 71

4.4.2 Cross sectional TEM analysis 76
4.4.3 AFM surface characterization 78
4.4.4 Metal-insulator transition 80
4.5 Conclusion 86
4.6 Supplementary data 88
4.6.1 Additional AFM Images 88
4.6.2 Resistivity of VO_2 Films 89

5 Phase transformation induced modulation of the resonance frequency of VO_2/TiO_2 coated microcantilevers 90
5.1 Abstract 90
5.2 Introduction 91
5.3 Experimental methods 92
5.4 Results and discussion 93
5.4.1 VO_2 film characterization 93
5.4.2 Electrical characterization of VO_2 94
5.4.3 Mechanical resonance of VO_2 microcantilevers by LDV 95
5.5 Conclusion 98

6 Fabrication of phase change microstring resonators via top down lithographic techniques: Incorporation of VO_2 into conventional processes 100
6.1 Abstract 100
6.2 Introduction 101
6.3 Experimental process 103
6.3.1 PLD of VO_2 thin films 105
6.3.2 Lithographic pattering of electrical contacts and the strings 105
6.3.3 Removal of VO_2 and TiO_2 layers 109
6.3.4 SiN etching and microstring release 109

6.3.5 Stripping and stability of protective metal layer 110
6.3.6 Frequency measurement technique 111
6.4 Results and discussion 112
6.4.1 Etchability of the VO_2 and TiO_2 layers 112
6.4.2 Suitability of the hard mask material 114
6.4.3 Etching summary and optimized process flow 117
6.4.4 Resonant frequency shift caused by heating 120
6.5 Conclusion 123

7 Effect of interface on mid-infrared photothermal response of MoS_2 thin film grown by pulsed laser deposition 124
7.1 Abstract 124
7.2 Introduction 125
7.3 Experimental 128
7.3.1 Material synthesis and deposition 128
7.3.2 Characterization 129
7.3.3 Mid-IR photothermal response and electrical characterization 130
7.4 Results and discussion 131
7.5 Conclusions 148
7.6 Electronic Supplementary Material 149
7.6.1 Structural Characterization of MoS_2 deposited at 700 °C 149
7.6.2 Calculation of Reflective Power 161
7.6.3 MoS_2 flakes transfer by scotch tape exfoliation and metal contact 163
7.6.4 Responsivity calculation 167

8 Conclusions 169
8.1 Summary of completed work 169
8.2 Recommendation for future work 170

8.2.1 E-MIT of VO_2 thin films 170
8.2.2 Reduced thermal mass mid-IR detectors based on MoS_2 MEMS devices 171
8.2.3 Future work considerations 171

9 Bibliography 173

List of Tables

3.1 Depostion parameters and their levels. 39

3.2 Experimental Layout for VO_2 based on L9 (4-factors and 3-levels) orthogonal array. Response is calculated for each sample and repetition as described in the text. Signal to noise (S/N) ratio was determined using a larger-is-better method. 43

3.3 ANOVA results based on the results tabulated from XRD, SEM, and AFM analysis. 54

3.4 Confirmation experiments of the Taguchi analysis. One factor in each experiment has been varied from the optimized condition to confirm the response predicted by the analysis. . 55

3.5 Surface roughness (nm) measured over a 1 μm^2 area, film thickness (nm) measured at a step edge in the film, grain size (nm) measured by ImageJ image analysis, and resistivity ($\Omega \cdot cm$) as measured by collinear four point probe technique. 61

3.6 Individual response ranking for all nine films for both sets of deposited films. 61

4.1 Deposition conditions for each deposited film. The gas pressure (50 mTorr), target-substrate distance (31 mm), and laser fluence (2.6 J/cm^2) were consistent for all experiments 70

4.2 Surface roughness for VO_2 thin films grown on Si and sapphire. 79

4.3 Magnitude (Ω), hysteresis width (Δ°C), and position (°C) of the metal-insulator transition for VO_2 grown on c-sapphire (0001). 81
4.4 Magnitude (Ω), hysteresis width (Δ°C), and position (°C) of the metal-insulator transition VO_2 grown on p-Si ⟨100⟩. 82
4.5 Lattice parameters (Å) for VO_2, sapphire, and silicon. 84
4.6 Experimental and theoretical d-spacing (Å) for the observed lattice planes. 84
4.7 Resistivity (Ω· cm) of VO_2 films, above and below the T_c deposited on c-sapphire (0001). 89
4.8 Resistivity (Ω· cm) of VO_2 films, above and below the T_c deposited on p-type Si ⟨100⟩. 89

6.1 Etching process parameters for removal of Cr, Al, and W hard mask materials. All 3 metals were removed in the PlasmaPro 100 Cobra Etch system. 111
6.2 VO_2 etching in the PlasmaPro 100 Cobra Etch system 117
6.3 Etching characteristics of the materials and processes used in VO_2 string fabrication. Values in brackets indicate the observed etch rate in $^{nm}/_{min}$. 118

7.1 Estimated mid-IR response characteristics of the MoS_2 film by PLD and exfoliated MoS_2 flakes mechanically transferred onto different substrates at 1300 cm^{-1} (7.7 μm) and at the highest average power of 25 mW of the QCL. The IR exposure area (A) is 5 mm^2. A Johnson noise is reported per unit bandwidth (i.e. Δf Hz) 144
7.2 Sample codes for MoS_2 on various substrates at different deposition conditions. 149

7.3 The E^1_{2g} and A_{1g} Raman peaks of as-deposited MoS_2 films on different substrates at various deposition time, temperature and laser energies. 152
7.4 162

List of Figures

1.1 Graphical representation of the PLD deposition system. The laser enters the vacuum chamber through a glass window and hits the rotating target. The plasma plume is ejected normal to the surface of the target and is directed towards the heated substrate stage. 11

1.2 The crystal structure of the rutile (left) and monoclinic (right) phases of VO_2 are shown. The two are represented with the same spatial configuration, where the vertical axis changes from the c-axis (left) to the a-axis (right), with the vanadium atom restructuring occuring along this axis. The interatomic spacings of the vanadium atoms can be seen to vary pair-to-pair in the monoclinic phase, while the spacings are uniform in the rutile phase. 17

2.1 Schematic representation of Bragg diffraction. Constructive interference occurs if the path length difference between the incoming waves is equal to an integer multiple of their wavelength. 22

2.2 The von Laue condition for diffraction. Here the lattice positions are treated as individual points as opposed to planes demonstrated by the Bragg approach. Constructive interference will occur under the same condition as the Bragg formulation; that is when the path length difference is equal to an integer multiple of the incoming waves wavelength. 23
2.3 Monte Carlo electron trajectory in VO_2 thin films on an arbitrary Si substrate. The accelerating voltage was (a) 1 keV, (b) 5 keV and, (c) 20 keV. 29

3.1 Schematic of PLD experimental setup, including the laser path and the PLD chamber 37
3.2 Theoretical range of the plasma plume as a function of laser energy and gas pressure. It is clear that the plasma travels farther at lower pressures as there is much less aerodynamic drag to compete with. This model served as the basis for determining the different levels of gas pressure, laser energy, and target to substrate distance. 41
3.3 XRD spectra of films grown on SiO_2 substrates. The spectra show the dependence on process parameters, separated into films grown at like gas pressures. a) at 0.1 mTorr, V1 shows no evidence of crystallinity, while V2 and V3 show the appearance of small peaks associated with V_2O_3; b) at 2 mTorr V4 and V5 show more pronounced peaks attributed again to V_2O_3, however, V6 shows the formation of the rarely studied VO_2 triclinic phase; c) V7 shows small peaks characteristic of the VO_2 A-phase, and V8 and V9 both show intense XRD peaks with small FWHM values, indicating that VO_2 M1 has formed. 44

3.4 SEM micrographs of all nine films deposited via PLD. The micrographs are arranged to show constant pressure by row and constant temperature by column (with pressure increasing top to bottom and temperature increasing to the right) and it is apparent that an increase in both temperature and pressure results in much larger grain size. 46
3.5 Temperature dependant resistance measurements for films (a) V6, (b) V7, (c) V8 and (d) V9. Resistance was monitored as a function of temperature and normalized to compare the magnitude of the change in resistance. The sharpest and highest magnitude transition was observed in sample V8, which was determined to be the optimal film. The MIT in sample V6 was of reasonable magnitude with excellent recovery, however the transition was very gradual. Sample V9 showed a small transition, however with poor reversibility. Sample V7 showed no transition as expected. 50
3.6 Mean response and signal-to-noise ratio for each level of the process parameters: (a) gas pressure, (b) temperature, (c) target-substrate distance and (d) laser energy. In the case of both mean response and SNR, a larger value indicates a more desirable result. 52
3.7 Optical images of the plasma plumes at variable deposition parameters. 57
3.8 Mean response and signal to noise ratio of the average grain size to each of the four process parameters: (a) gas pressure, (b) temperature, (c) target-substrate distance and (d) laser energy. A strong dependence on both the gas pressure and temperature is observed. 58

3.9 Mean response and signal to noise ratio of the surface roughness as measured by AFM to each of the four process parameters: (a) gas pressure, (b) temperature, (c) target-substrate distance and (d) laser energy. A strong dependence on both the gas pressure and temperature is observed, with minimal influence from both target-substrate distance and laser energy. 59

3.10 AFM topography of the samples deposited at the nine different conditions. The images are arranged to show constant pressure by row and constant temperature by column (with pressure increasing top to bottom and temperature increasing to the right). From this figure we can see that the roughness is directly proportional to both the temperature and the gas pressure. . . 60

3.11 Mean response and signal to noise ratio of the thickness to each of the four process parameters: (a) gas pressure, (b) temperature, (c) target-substrate distance and (d) laser energy. Here we see a strong dependence on the laser energy as well as target-substrate distance. 62

3.12 XRD spectrum of confirmation experiment C3 to verify the production of VO2 (A) phase. Strong peaks at 2θ values of 14.7 and 29.5 deg, along with smaller peaks at 45.2, 53.8, and 63.1 deg confirm A phase formation. 63

4.1 Schematic of PLD experimental setup, including the laser path and the PLD chamber. 69

4.2 (a) XRD spectra of VO_2 films deposited on a) sapphire (0001) and (b) *p*-type Si $\langle 100 \rangle$ substrates. The films grown on sapphire showed a highly oriented structure with only the (020) and (004) peaks present, while on silicon a much more polycrystalline structure was observed. 72

4.3 Schematic of the proposed DME of VO_2 (red) on sapphire (blue) at (a) deposition temperature where VO_2 is present as its tetragonal form and (b) room temperature where the monoclinic phase is present and the *c*- and *a*-axes have flipped . . . 73
4.4 Off axis scanning of V-SAP-550 of the ($\bar{2}11$) reflection at 2θ = 36.972 ° with ψ angle of 57.635 ° between ($\bar{2}11$) and (020) reflection. Inset shows the absence of the ($\bar{2}11$) reflection at 2θ = 36.972 ° and ψ of 90.297 °, the angle between the ($\bar{2}11$) and (002) planes. 74
4.5 (a) High resolution TEM image of the VO_2/sapphire cross section V-SAP-600 film. Inset on the left corner down shows the diffraction pattern of sapphire. The top right corner shows the diffraction pattern of the VO_2 film (b) FFT of the VO_2/sapphire interface. The diffraction spots in (b) correspond to the [$\bar{1}100$] and [001] zones of sapphire and VO_2, respectively. 77
4.6 (a) High resolution TEM image of the VO_2/silicon interface taken from V-Si-600 and (b) the corresponding FFT pattern of the entire image. 78
4.7 AFM images showing the surface profile of (a) VO_2 on sapphire (V-SAP-600) and (b) silicon (V-Si-600). The RMS roughness values in Table 4.2 were computed from these images. 80
4.8 Resistance as a function of temperature for VO_2 thin films grown on (a) sapphire and (b) silicon substrates. Common to both is no transition present for the films grown at 500 °C, and a sharp transition for films grown at 550 and 600 °C. On Si, VO_2 did not deposit at 400 °C and therefore no measurement was taken. 81

4.9 Roughness of (a) sapphire substrate with no film and VO2 grown at (b) 400 °C (c) 500 °C and (d) 550 °C as measured by AFM. 88
4.10 Roughness of (a) Si substrate with no film and VO2 grown at (b) 400 °C (c) 500 °C and (d) 550 °C as measured by AFM. . . . 88

5.1 (a) XRD spectrum and (b) SEM image of the VO_2 film. Monoclinic (011) reflection was dominant as shown by XRD. Inset (b) shows the geometry of each cantilever, VMC-100 on the left and VMC-200 on the right. Scale bar in (b) is 400 nm. 94
5.2 Resonance frequency of VMC-200 before and after the deposition of VO_2 as measured by LDV. Resonance frequency was shown to increase significantly upon deposition of the VO_2 layer. 95
5.3 Metal-insulator transition for VO_2 cantilevers measured (a) electrically and (b) mechanically. The transition was sharper in mechanical detection, and more pronounced in VMC-200, likely due to lower stiffness of the cantilever. 97

6.1 A generalized outline of the process flow used to fabricate the VO_2 microstring devices shown from the side profile. (a) starting substrate, (b) patterning of contact pads, (c) defining the string geometry and depositing metal mask and photoresist removal, (d) etching the VO_2 and TiO_2 layer, (e) etching SiN, (f) releasing the string (SiO_2 etching), and metal mask stripping. Each of the steps shown in this schematic will be discussed in detail, exploring the possibilities considered for each step and determining the most suitable process for each. 104
6.2 (a) XRD spectrum showing the improved crystallinity of the VO_2/TiO_2 layered structure and (b) AFM topographic scan of VO_2/TiO_2 deposited on $Si_3N_4/SiO_2/Si$ substrate. 106

6.3 General representation of the image reversal process shown step-by-step from the top view (left) and side view (right). (a) Resist is spun onto substrate to a 1.45 µm thickness with a 90 °C soft bake. (b) pattern transfer where the lighter area shows the exposed sections (in reality the photomask is in hard contact with the substrate to reduce diffraction but is shown like so to portray the photomask). (c) second bake step forms insoluble film in exposed areas. (d) flood exposure and (e) development yields the negative of the original exposure. Color legend: grey-substrate, dark red-virgin resist, light red-exposed resist, blue-insoluble resist, black-photomask, purple-light source. . 108

6.4 Optimized process flow formulated by this work to fabricate VO_2 microstring resonatore. (a) Starting substrate with HPR 504 photoresist spun on at a 1.3 µm thickness, (b) lithographic patterning of contact pads and Cr/Au deposition by sputtering, (c) defining the string geometry and depositing Cr mask and photoresist removal by sonication in acetone, (d) etching the VO_2, TiO_2, and SiN via CHF_3, CF_4, and O_2 based plasma in RIE, and (e) releasing the string (SiO_2 VHF etching), and Cr mask stripping by ICP. 119

6.5 SEM micrographs depicting the (a) final VO_2 string (length= 400 µm of the string presented here) and (b) side profile of the same string showing the released nature. 120

6.6 Metal-insulator transition as observed for VO_2/TiO_2 coated cantilevers as showing a significant increase in the resonant frequency across the MIT, determined by LDV. Inset: Resonant frequency peaks showing the Δf of $\sim$43 kHz due to the MIT. . 122

7.1 (a) XRD of MoS_2 grown on different substrates at 800 °C and 35 mJ energy. Raman spectra of MoS_2 grown on different substrates at 800 °C at (b) 35 and (c) 50 mJ laser energy for different deposition times. (d) Photograph of the MoS_2 film grown on sapphire at 800 °C at different times and laser energies. The word MoS_2 was printed on the substrate background. 132

7.2 AFM images of MoS_2 grown at 800 °C on (a) sapphire (SAP8-20) at 35 mJ for 20 s and (b) thermally grown oxide (SO8-5) at 50 mJ for 5 s. The uncovered area of the thermally grown oxide in (b) is caused by the hard mask kept on the substrate while depositing MoS_2. 133

7.3 (a) Cross-sectional TEM image of the MoS2 film grown on sapphire (0001) at 800 °C 20 s deposition time showing stacking of MoS_2 with a (0002) orientation. The inset shows the inverse FFT image of the red marked area of the image showing misfit dislocations. (b) FFT pattern of the corresponding red marked zone of (a). The orientation relationship of the yellow mark area of the FFT pattern is depicted in Figure 7.17 (in the ESM). (c) Cross-sectional TEM image of MoS2 grown on silicon ⟨100⟩. The inset shows the FFT image showing no orientation relationship. (d) Twin formation of the silicon-MoS_2 interface enlarged from (c). 135

7.4 (a) Schematic and (b) photograph of the experimental set up of the mid-IR response of MoS_2 on different substrates. (c) Variation of the resistance under the mid-IR illumination of MoS_2 on the sapphire substrate (SAP8-300) at different wave numbers. The data are plotted using a 2D waterfall mode at 10 % offset to accommodate all the data set. (d) Photothermal response time of MoS_2 on sapphire (SAP8-300). 138

7.5 (a) Sensitivity of the photothermal response of MoS_2 grown on different substrates. The power spectrum of the QCL is shown in the same graph. (b) Relative resistance change and (c) TCR of MoS_2 on different substrates with a function of the temperature using the external heating source from the bottom of the substrate. The data are normalized with the resistance at T = 23 °C (296 K). 139

7.6 (a) UPS spectra of MoS_2 on different substrates and (b) zoomed portion of (a) showing the work function of MoS_2 on different substrates. The band diagram of the PLD-grown MoS_2 on (c) silicon and (d) other three substrates (i.e., Si/SiO_2, sapphire, and Si/SiN) shows how the band structure changes because of the interface. The ionization potential (IP $\sim$ -5.47 eV) and the electron affinity ($\chi \sim$ -4.07 eV) for bulk MoS_2 are obtained from Refs. [181,204] 143

7.7 SEM micrographs showing the MoS_2 nanostring from (a) front and (b) side angle. The thickness of these strings is 200 nm silicon nitride and 15 nm MoS_2. The strings measure 8 µm in length and 250 nm in width. 145

7.8 SEM micrographs showing (a) the diaphragms IR absorbing pad and (b) side profile showing the cross section of the absorbing pad. Inset: top view of the entire device showing the absorber, isolation arms, and the gold contact pads. Holes were included as a means to imporve the lateral etchability of the device. 146

7.9 Mid-IR photothermal response of the MoS_2 nanostring resonators. Rise and fall times are determined to be 250 and 110 ms, respectively. 147

7.10 (a) XRD of MoS_2 grown on different substrates at 700 °C and at 35 mJ laser energy. Raman spectra of MoS_2 (b) bulk, and (c) grown on different substrates at 700 °C and at 35 mJ laser energy. (d) Photograph of the MoS_2 film grown on sapphire at 700 °C different time and laser energy. 150
7.11 AFM images of MoS_2 grown at 700 °C on different substrates and 35 mJ laser energy for 20 s deposition times grown on: (a) silicon (S7-20) (b) sapphire (SAP 7-20) (c) thermally grown oxide SO7-20 (d) LPCVD grown SiN (SN7-20). 153
7.12 AFM images of MoS_2 grown at 800 °C and 35 mJ laser energy for 20 s deposition times on: (a) silicon (S8-20) (b) thermally grown oxide (SO8-20) (c) LPCVD grown SiN (SN8-20) and (d) MoS_2 grown at same temperature and energy for 300 s deposition time on sapphire (SAP8-300). Multiple layers have been grown with increasing the time. 154
7.13 SEM topography of MoS_2 deposited at 800 °C for 300 s on (a) sapphire (SAP8-300) and (b) thermal oxide (SO8-300). (c) Cross sectional SEM of MoS_2 on Si for thickness measurement (S8-300). Inset shows the back scattered image to distinguish the compositional contrast between silicon and MoS_2. All the other 300 s deposited films are of same thickness. 155
7.14 XPS survey spectrum of MoS_2 on (a) sapphire (SAP8-20) (b) silicon (S8-20). 156
7.15 XPS spectra of MoS_2 on Si, SiO_2, SiN showing (a), (c), (e) Mo 3d, and (b), (d), (f) S 2s and S 2p core level peak regions respectively.157
7.16 Optical and photoluminescence spectra of MoS_2 grown on sapphire at 800 °C at 35 mJ energy for different times. 158

7.17 (a) and (b) Orientation relationship of MoS_2 on sapphire from the FFT pattern from a TEM cross-sectional image. In Fig 8 (a) blue and red dots represent the FFT of the sapphire substrate and MoS_2 respectively. In Fig 8(b) no MoS_2 spots are seen since the film was not in edge-on condition. 158
7.18 Variation of resistance and the response time of MoS_2 on different substrates under IR illumination. 159
7.19 FTIR spectra of bulk MoS_2 in order to show the broadband IR absorption from 600 to 2000 cm^{-1} wave number. 160
7.20 (a) SEM image of MoS_2 flakes on silicon with metal contact pad (Ti/Au ~5/50 nm) separated by 10 μm made by EBL and sputtering. Inset shows the image of the whole contact pad. (b) AFM image of the same flake showing the layer thickness. 163
7.21 Sensitivity of the photothermal response of mechanically peeled MoS_2 on two different substrates (a) silicon and (b) thermal oxide (Si/SiO_2) using mid IR QCL. 164
7.22 (a) Relative resistance with temperature and (b) TCR of mechanically peeled MoS_2 flakes transferred on two different substrates i.e. silicon and thermal oxide (Si/SiO_2). 165
7.23 I-V Characteristics of PLD grown MoS_2 different substrates on (a) silicon, (b) sapphire, (c) thermal oxide (Si/SiO_2) and (d) silicon nitride (Si/SiN) and exfoliated MoS_2 transferred on (e) silicon and (f) thermal oxide (Si/SiO_2). 166
7.24 Equivalent circuit to calculate responsivity of MoS_2 thin film. . 168

List of Abbreviations

AFM	Atomic force microscopy
ALD	Atomic layer deposition
BOE	Buffered oxide etch
CPD	Critical point drying
CVD	Chemical vapour deposition
DOE	Design of experiments
EBL	Electron beam lithography
EDX	Energy dispersive X-ray spectroscopy
fcc	Face centered cubic
FFT	Fast Fourier transform
GLAD	Glancing angle deposition
hcp	Hexagonal close packed
HIM	Helium ion microscopy
HSQ	Hydrogen silsesquioxane
ICP	Inductively coupled plasma
IR	Infrared
LPCVD	Low pressured chemical vapour deposition
MBE	Molecular beam epitaxy
MEMS	Micro-Electro-Mechanical Systems
MIT	Metal-insulator Transition
MOEMS	Micro-Opto-Electro-Mechanical Systems
NEP	Noise equivalent power
PECVD	Plasma enhanced chemical vapour deposition
PL	Photoluminescence
PLD	Pulsed laser deposition
PVD	Physical vapour deposition

PMMA	Poly (methyl methacrylate)
QCL	Quantum cascade laser
RF	Radio frequency
RIE	Reactive ion etching
SEM	Scanning electron microscopy
TCR	Temperature coefficient of resistance
TEM	Transmission electron microscopy
TMDC	Transition metal dichalcogenides
UPS	Ultraviolet photoelectron spectroscopy
UV	Ultraviolet
VHF	Vapour hydrofluoric acid
XPS	X-ray photoelectron spectroscopy
XRD	X-ray diffraction

List of Symbols

α	angle between b and c axes (Ch. 1, 4)
α	Optical absorption coefficient
β	angle between a and c axes (Ch. 1, 4)
γ	angle between a and b axes (Ch. 1, 4)
γ	Interfacial free energy (Ch. 1)
γ	Ratio of the specific heats of plasma species (Ch. 3)
θ	diffraction angle (Ch. 2)
θ	Plasma azimuthal angle (Ch. 3)
λ	Wavelength (Ch. 2)
ν_0	Plasma velocity (Ch. 3)
ρ	density (Ch. 2, 5)
τ	Laser pulse width (Ch. 3)
τ_{rise}, τ_{fall}	Rise and fall times of the IR-photoresponse (Ch. 7)
ϕ	XRD sample stage angle (Ch. 2)
ϕ	Plasma altitude angle (Ch. 3)
ψ	XRD detector angle (Ch. 2)
A	Atomic mass (Ch. 2)
A	Plasma plume shape factor (Ch. 3)
A	resonator cross sectional area (Ch. 5)
a_f, a_s	Film, substrate lattice constants (Ch. 4)
$\mathbf{d}$	Scatterer separation vector (Ch. 2)
d, d_0	final and initial grain size (Ch. 1,3)
d	Interplanar spacing (Ch. 2)
E	Young's modulus (Ch. 5)
E	Laser energy (Ch. 3)
E_0	Accelerating voltage (Ch. 2)

f_i	Resonance frequency (Ch. 5)
f_m	Lattice misfit parameter (Ch. 4)
h	Film thickness (Ch. 1)
h, k, l	Miller indices (Ch. 4)
I	Area moment of inertia (Ch. 5)
$\mathbf{k}$, $\mathbf{k}'$	Initial and final wavevector (Ch. 2)
k_b	Boltzmann constant
l	Resonator length (Ch. 6)
l_a	Laser spot size (Ch. 3)
M	Grain boundary mobility (Ch. 1)
$\hat{\mathbf{n}}$, $\hat{\mathbf{n}}'$	Initial and final x-ray direction (Ch. 2)
P_0	Background gas pressure (Ch. 3)
Q	Activation energy (Ch. 1,3)
$\mathbf{R}$	Bravais lattice vector
R	Plasma range (Ch. 3)
R_{KO}	Electron penetration depth (Ch. 2)
r, r^*	Grain and critical grain size (Ch. 1)
S	Tensile force (Ch. 5)
T_c	Critical temperature
t	Resonator thickness (Ch. 6)
V_i	Initial volume of the ablated species (Ch. 3)
Z	Atomic number (Ch. 2)

Chapter 1

Introduction

1.1 Motivation

Government funded nanotechnology research has seen a significant rise over the past decade, both nationally and globally [1]. As society pushes for smaller, faster, and more reliable products, the field of nanotechnology will continue to rapidly expand, with projections of worldwide spending reaching over USD 3 Trillion [2]. This continual increase in funding provides ample resources for research interest in a wide range of nanoscale applications. One of the most important areas in technology development is the ability to deposit thin films in a precise and controlled manner. Thin films are found in virtually every technology sector, with applications in, but not limited to, microelectronic devices, protective coatings, photonics, energy harvesting, and optics.

Perhaps the most crucial part of the aforementioned industries is the deposition of thin films themselves. Unsurprisingly, there are a multitude of thin film deposition methodologies, which are categorized as either chemical vapour deposition (CVD) or physical vapour deposition (PVD). CVD methods generally involve the reaction, on the substrate, of gaseous precursors injected into a deposition chamber which decompose into the desired film.

Often this is done at high temperatures (> 1000 °C), typical of low pressure CVD (LPCVD), or with the assistance of plasma, seen in plasma enhanced CVD (PECVD). PECVD enables the reaction to take place at higher pressures and lower temperatures than its LPCVD counterpart, making it an attractive choice when the high temperatures may be detrimental to the substrate material. Atomic layer deposition (ALD) is another CVD technique that slowly deposits thin films layer by layer in a highly uniform manner by introducing precursor gases one at a time in a self limiting manner. PVD methods involve the physical removal of target material in a vacuum, often distinguished by the mechanism by which the target is vapourized. Sputtering, one of the oldest techniques in use, utilizes an ionized inert gas (typically Ar^{+}) to bombard a negatively biased target surface, ejecting target species out of the surface. Thermal evaporation simply heats the target material until the vapour pressure is high enough for appreciable deposition. Electron-beam evaporation operates under similar principles as thermal evaporation, though in this case an electron beam is rastered across the target in order to achieve uniform heating.

The main benefit of PVD techniques is that the material is physically removed by and external source, and therefore deposition of exotic materials is possible. PVD does, however, rely on line of sight between the target and substrate, limiting the throughput and coverage uniformity. CVD methods allow for a larger batch size due to their reliance on chemical reactions to form highly uniform, conformal films onto many substrates (in some cases with high aspect ratios). While the film quality and uniformity is usually superior in CVD techniques there are, of course, several drawbacks. As mentioned above, CVD relies on gas phase reactions, which are often accompanied by enormous safety precautions, which increases the cost associated with the process. Additionally, these processes are limited to the available reactions, and not all materials can be deposited by CVD. No matter the material being

deposited, it is crucial to have an in depth understanding of the processing parameters of each deposition technique in order to successfully manipulate the properties of the film.

Thin films are particularly useful in the area of optoelectronics, defined as the study of electronic devices that emit, detect, and control light [3]. Generally, to be useful in optoelectronic applications, thin films should possess highly uniform properties throughout the entirety of the film. Porosity, voids, cracks, and any other detrimental flaw should be avoided during deposition, and proper adhesion is also of utmost importance. Electronic and optical interactions are extremely sensitive to discontinuities, and therefore deposition must be done in a manner that produces a dense, uniform, and homogeneous layer to maximize the capabilities of the material under investigation. Laser fluence, substrate temperature, laser pulse frequency, gas pressure, target-substrate distance, deposition environment, and time are all variables in which the properties of the deposited film can be manipulated during PLD. These variables enable the fine tuning of the material transfer process, which can provide huge improvements in the quality of the films.

In this thesis I will present on work conducted by myself, along with collaborative work with other lab members, pertaining to the synthesis, characterization, and application of VO_2 and MoS_2 as fabricated by PLD. A detailed outline of the content of this thesis will be introduced in the following sections, which will also introduce the specific properties of VO_2 and MoS_2 that attracted our attention in the first place.

1.2 Thesis structure and content

This thesis is organized in such a way that first introduces the concept of pulsed laser deposition (PLD), focussing on the advantages it possesses over conventional deposition techniques. Chapter 1 and Chapter 2 will introduce

important aspects pertaining to the thesis as a whole, including motivation towards the research. Subsequent chapters will follow the experimental work in a chronological fashion, with processes and techniques in later chapters often building on, or incorporating results found in preceding chapters.

The content of each experimental chapter is in the format of a journal article, as all of the work has been accepted by or submitted to a peer reviewed journal. Each chapter will start with an introduction to the work to be presented which will outline the significance of the particular research in the chapter. Following the introduction, the experimental outline, highlighting the procedures used as well as any important theory will follow. An in depth analysis of the results, including a discussion on the ramifications of the results, as well as any potential impact they may pose towards technological advancement. A conclusion will tie each chapter together, including any acknowledgements that are deemed necessary. References for all chapters will be presented at the conclusion of the entire thesis.

Chapter 1 provides an introduction to the concept of pulsed laser deposition, and the motivation behind the work. Publications included within this thesis will be described, outlining the contributions from each author. The chapter will conclude with an description of the two main materials used in this thesis, VO_2 and MoS_2. In those sections, the crystal structure, properties, history, and relevant applications will be discussed. In Chapter 2 any relevant characterization or fabrication techniques employed during the work will be described. The techniques described in Chapter 2 will consist of the more important, and more often used ones, rather than every single method. Common techniques such as scanning electron microscopy and X-ray diffraction will be discussed in more detail than the lesser used techniques.

The first experimental chapter of this thesis (Chapter 3) presents an optimization of PLD of VO_2 thin films through the application of a robust design of experiment (DOE), also known as Taguchi design. In this chapter, the PLD

process will be analysed in depth, and the individual contribution from four major PLD process parameters will be explored. An L9 orthogonal array was employed to investigate four independent process parameters with three different levels each. The Taguchi design reduces the overall number of experiments required to fully investigate the influence of each parameter by utilizing statistical analysis techniques.

The Taguchi method, developed by Genichi Taguchi of Japan, is a technique originally developed to increase the quality of manufactured goods, but has since found its way into a multitude of applications in the engineering discipline. He developed a three-stage process, of which the stages include *system design*, *parameter design*, and *tolerance design* [4]. In the technique employed in this chapter, we have chosen 4 process parameters each with 3 different levels. By employing the L9 orthogonal array, the total number of experiments to fully elucidate the effects of processing was reduced from 81 down to 9. Analysis of variance (ANOVA) was then used to extract the influence of each parameter from the codependent results obtained.

Continued in Chapter 4 is a thorough investigation regarding the modulation of the metal-insulator transition in VO_2 thin films by interfacial engineering. In this section we investigate the role interfacial strain has on the manifestation of the MIT for VO_2 grown on sapphire and silicon substrates, as a result of growth temperature and lattice mismatch. In this section we discuss how different substrates influence both the film growth mechanism and shape of the MIT curve. Epitaxial growth on sapphire substrates results in a lower hysteresis, larger magnitude, and sharper transition as compared to polycrystalline VO_2 films grown on silicon. HRTEM and SAED analysis reveals the epitaxial orientation relationship between VO_2 and sapphire, while no such relationship was discovered between VO_2 and silicon. We postulate that the differences in the MIT curves arises from the presence of additional nucleation sites in the form of defects such as grain boundaries.

We demonstrate, previously shown by Park et al. [5], that the position of the MIT can be modulated by stresses in the film which arise from lattice mismatch. However, inconsistencies present in the data indicate that there are competing factors such as grain growth that may also influence the transition.

Once a thorough understanding pertaining to the growth and stability of VO_2 films on amorphous (SiO_2 in Chapter 3) and crystalline (Si and α-Al_2O_3 in Chapter 4) substrates, we moved into the application side of experiments by depositing VO_2 onto v-shaped cantilevers and investigated both the electrical and mechanical response of the MIT (Chapter 5). Additionally, in this chapter we introduce an intermediate TiO_2 layer which has nearly identical lattice constants as VO_2 and is the same space group as the high temperature phase. The TiO_2 layer has been shown to alleviate lattice mismatch and lower stress in the film by bridging the misfit between layers [6]. In both Chapters 5 and 6 we show that the TiO_2 layer successfully increases the crystallinity as well as reduces the film stress, as evidenced by the peak position and intensities present in the XRD spectra.

By depositing an ultrathin layer of VO_2 onto the cantilever the resonance frequency was shown to increase, which is counterintuitive given increased mass generally reduces the resonance frequency. The increase was substantial (up to $\sim$40 %) and was attributed to a high tensile stress in the film imparted during the deposition process. The electrical and mechanical signals were monitored as a function of temperature and both signals displayed a transition at nearly identical temperatures. The mechanical signal was realized much faster over a smaller temperature range.

The success of the resonator device in Chapter 5 spurred interest in fabricating a MEMS device which could improve upon the response of the as-bought cantilever. What we discovered was a significant lack of fabrication procedures for VO_2 devices and set forth to develop a process of our own. A series of processes and materials were investigated as potential candidates

for a VO_2 microstring fabrication process. A microstring (doubly clamped cantilever) was chosen as a model platform as the resonance frequency of such a device is much higher than a single clamped beam, and therefore we believe a more sensitive device could be realized. Using a starting substrate of Si/SiO_2 (1.5 μm)/Si_3N_4 (200 nm) a fabrication process consisting of photolithography, sputtering, RIE, VHF, and ICP-RIE was developed. The resulting string showed a resonance frequency increase of over 5 % across the phase transition.

Chapter 7 introduced MoS_2 thin films used in photodetector applications. While MoS_2 use in visible and near-IR detectors is readily available [7, 8], the use as a mid-IR detector is a novel application. Rather than relying upon photoexcitation of charge carriers across the band gap, the temperature coefficient of resistance (TCR) is exploited to detect low energy photons in the mid-IR. Additionally, PLD introduces a large number of defects at the interface, which may create trap states between the band gap near the band edge that can be excited by the low energy photons incident on the substrate. We show the significance of the interface by comparing exfoliated MoS_2 flakes to those grown by PLD.

The work presented in this thesis provides significant advancement in the sysnthesis, characterization, and application of 2D materials fabricated by PLD. The majority of the contributions in this thesis have been published in peer reviewed journals, or have been submitted to and are under consideration for publication in peer reviewed journals. The specific publications are highlighted in following section.

1.3 Related publications

Many of the chapters in this thesis present work that has been published, under review for publication, or in preparation for submission to scientific

journals. For many of the chapters, the data presented herein can be found in these publications. The following is a list of publications that have been incorporated into this thesis, with the location within and description of the contributions of each author outlined as well.

Effect of process parameters on phase stability and metal-insulator transition of vanadium dioxide (VO_2) thin films by pulsed laser deposition Ryan McGee[a], Ankur Goswami[a,*], Behnam Khorshidi[b], Kristi McGuire[a], Kalvin Schofield[a], and Thomas Thundat[a,*] *Acta Materialia*, **137** 12-21 (2017). This publication is present in the thesis as Chapter 3, where the PLD process for depositng VO_2 thin films was optimized by employing the Taguchi design of experiments. In this publication, the experimental design was a collaboration between RM, AG, and BK. PLD was done by RM and AG, SEM was done by RM, AFM was done by AG, and electrical characterization was done by KM and KS. Statistical analysis of the results was performed by RM, AG, and BK.

[*]*denotes corresponding author*

[a]*Department of Chemical and Materials Engineering, University of Alberta, Edmonton, Canada*

[b]*Department of Mechanical Engineering, University of Alberta, Edmonton, Canada*

Enhancement of the sharpness and intensity of the metal-insulator transition in ultrathin VO_2 films by interfacial structure manipulation Ryan McGee[a], Ankur Goswami[a,*], Soupitak Pal[b], Kalvin Schofield[a], Syed Asad Manzoor Bukhari[a], and Thomas Thundat[a,*] *Physical Review Materials* **2**, 034605 (2018). This paper is included as Chapter 4 in this thesis, in which we further elucidate the correlation between the phase transformation in VO_2 and the substrate. RM and AG performed the PLD, XRD, and AFM. SP performed the HRTEM. RM, AG, and SP all analyzed the SAED patterns and determined the orientation relationship. KS performed the electrical characterization of the films.

[*]*denotes corresponding author*

[a]*Department of Chemical and Materials Engineering, University of Alberta, Edmonton, Canada*
[b]*Department of Chemical Engineering, University of California, Santa Barbara, USA*

Phase transformation induced modulation of the resonance frequency of VO_2/TiO_2 coated microcantilevers Ryan McGee[1], Ankur Goswami[1], Rosmi Abraham[1], Syed Bukhari[1], Thomas Thundat[1,2] *MRS Advances* **3** (6-7), 359-364 (2018). Here, the mechanical resonance of VO_2 coated V-shaped cantilevers is investigated by heating the devices through the MIT, and monitoring the resonance frequency by LDV, incorporated as Chapter 5 in this thesis. Mechanical detection is compared to the electrical response with excellent agreement. Both techniques show indisputable evidence of the MIT at nearly identical positions. RM and AG conducted the PLD, RM performed the SEM and XRD. SB and RA assisted in the set-up and collection of the data from the LDV.

[1]*Department of Chemical and Materials Engineering, University of Alberta, Edmonton, Canada*
[2]*Department of Chemical and Biological Engineering, University at Buffalo, The State University of New York, Buffalo, New York*

Fabrication of phase change microstring resonators via top down lithographic techniques: Incorporation of VO_2 into conventional processes Ryan McGee[a,*], Ankur Goswami[a], Syed Asad Manzoor Bukhari[a], Liang Zhou[a], and Thomas Thundat[a,b,*] *manuscript under preparation for submission to The Journal of Micro/Nanolithography, MEMS, and MOEMS*. Building off the success of VO_2 coated cantilevers presented in Chapter 5, we develop a fabrication process to produce resonators with a much smaller mass in order to increase the sensitivity of the phase transition. Included as Chapter 6 in this thesis, we present several considerations taken regarding the integration of VO_2 into conventional fabrication processes, and outline an optimized approach for device production. RM developed and designed the process flow and

photomasks, and performed the etching steps. AG performed the majority of the optical lithography. SB and LZ assisted with the testing of the finalized devices.

denoted corresponding author

[a]*Department of Chemical and Materials Engineering, University of Alberta, Edmonton, Canada*

[b]*Department of Chemical and Biological Engineering, University at Buffalo, The State University of New York, Buffalo, New York*

Effect of interface on mid-infrared photothermal response of MoS_2 thin film grown by pulsed laser deposition Ankur Goswami[1], Priyesh Dhandaria[1], Soupitak Pal[2], Ryan McGee[1], Faheem Khan[1], Željka Antić[1], Ravi Gaikwad[1], Kovur Prashanthi[1], and Thomas Thundat[1,*] *Nano Research*, **10**(10), 3571-3584 (2017). The mid-IR response of PLD grown MoS_2 thin films was explored by monitoring resistance upon irradiation by QCL. We show enhancement of the TCR of MoS_2 grown on Si as a result of twin boundary formation. The contribution from RM to this work was synthesis of the MoS_2 films, fabrication of the exfoliated devices, some of the IR measurements, analysis of the data, and significant contributions to the writing of the manuscript.

denotes corresponding author

[1]*Department of Chemical and Materials Engineering, University of Alberta, Edmonton, Canada*

[2]*Department of Chemical Engineering, University of California, Santa Barbara, USA*

1.4 Pulsed laser deposition

Pulsed laser deposition (PLD) is a highly versatile PVD technique, capable of depositing high quality thin films of virtually any material. As suggested by the name, PLD employs a pulsed laser as a means to ablate target material.

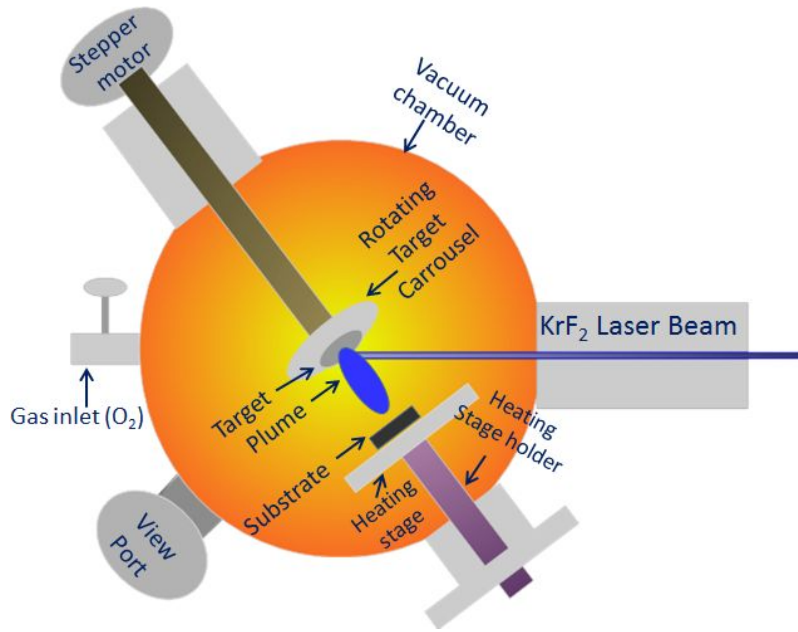

Figure 1.1: Graphical representation of the PLD deposition system. The laser enters the vacuum chamber through a glass window and hits the rotating target. The plasma plume is ejected normal to the surface of the target and is directed towards the heated substrate stage.

The laser incident on the target penetrates the surface (depth dependant upon properties of target material and laser wavelength), and with each pulse a small amount of material is vapourized and forms a plasma. The plasma is ejected from the surface, normal to the target due to strong repulsion, and directed towards a substrate mounted facing the target. The propagation of the plasma is highly non-equilibrium, and has significant dependencies on not only the vacuum level, but the species of gas present in the chamber as well. The substrate is often held on a heatable stage, enabling the control of deposition temperature, further expanding the capabilities of PLD. Once the target material has reached the substrate, film growth is dictated by not only the ablation parameters, but additionally by the properties of the substrate, the process parameters, and the interaction between the deposited material and substrate. A schematic of the process is shown below in Figure 1.1

Even though PLD had been explored as a possible avenue for evaporative

thin film deposition since the 1960's, it wasn't until the late 1980's when Dijkkamp et al. demonstrated direct deposition of superconducting YBCO thin films onto $SrTiO_3$ and Al_2O_3 substrates [9]. This remarkable achievement gained PLD widespread notoriety as a technique which can stoichiometrically transfer complex oxides directly from target to substrate, without sacrificing any of the target materials properties. One of the most significant capabilities of PLD is the ability to transfer complex oxides directly from target to substrate without compromising the integrity of the material. This is often done using a nanosecond pulsed ultraviolet (UV) laser, focused on a small spot to increase energy density and absorption in the target [10]. In conjunction with a high intensity laser pulse, the target material must possess a high optical absorption coefficient, at the laser wavelength. Without high absorption, the laser pulse will penetrate further into the solid target, disabling any chance of vapourization, rendering the process impossible. If the conditions for ablation are met, the resultant plasma is directed towards the substrate where it condenses and forms as solid film.

Excimer laser are the most popular laser for PLD systems. The name excimer is a portmanteau of the words "excited" and "dimer", referring to the operating principle of the laser itself. Although technically incorrect terminology for a *noble gas-halide* laser, the nomenclature originates from homonuclear diatomic gases and the name excimer has been universally accepted. These "dimers" are in a dissociative ground state, and only when ionized into an excited state do they form any bonds. Application of a high voltage across two electrodes, which generates a high energy laser pulse, excites the constituent gases enabling an associative excited state. The lifetime of the bound excited state is typically on the order of a few nanoseconds. Upon relaxation to the ground state, the associative nature reverts back to dissociative and the dimer breaks apart, releasing a photon and re-entering the pumping process.

1.5 Nucleation and grain growth in thin films

Growth of thin films, during the PLD process, is initiated once the ablation products start to condense on the substrate surface. Thin film growth is a highly complex mechanism, which may be influenced by the deposition technique chosen; process parameters such as temperature, gas pressure, and atmosphere; as well as the substrate and target materials. There are two major mechanisms that must be investigated in order to understand and control the properties of thin films, and these are; film growth mode and grain growth. In general, thin film growth may belong to one of three characteristic mechanisms; layer-by-layer, also known as Frank-van der Merwe (FM), island type, known as Volmer-Weber (VW), and a hybrid method of the two, layer-plus-island, known as Stranksi-Krastanov growth (SK) [11]. Depending on the relative bond strength between the adatoms and the substrate, different growth modes will occur. VW growth occurs when the adatoms are more strongly bound to one another than they are to the substrate. Conversely, FM growth occurs when the adatoms are more strongly bound to the substrate, preferring to form a monolayer on the substrate before forming a second layer. Perhaps the most complex method is SK growth, where initially the growth resembles FM type, but after one or few monolayers it switches to VW growth.

Interfacial free energy, denoted as γ, often provides a lot of insight into the determination of thin film growth. When an adatom is deposited on the surface, in order to determine the preferred growth mode, the substrate-vapour (γ_{SV}), film-substrate (γ_{FS}), and film-vapour (γ_{FV}) interfacial energies must be considered. There is two general cases that will be observed regarding the surface energies,

$$\gamma_{SV} < \gamma_{FV} + \gamma_{FS} \tag{1.1}$$

If equation 1.1 holds true, VW growth will occur as surface energy is min-

imized by maintaining as little contact between the substrate and film as possible. If the inequality is flipped, as is the case in equation 1.2, FM growth is preferred as the adlayer has a lower surface energy than the exposed substrate

$$\gamma_{SV} \geq \gamma_{FV} + \gamma_{FS}. \tag{1.2}$$

Growth mode can have significant ramifications on the electronic, optical, and physical properties of thin films, which will be discussed in more detail in later chapters.

Grain growth is another phenomenon which must be considered when depositing thin films. A grain boundary is a two-dimensional defect in the crystal which separates two or more grains within the film. There are many types of grain boundaries, including, but not limited to; twin, twist, and tilt (symmetric or asymmetric). The type of grain boundary is defined by the orientation between the adjacent grains. Such defects can impact the properties of the film as is seen in grain boundary strengthening in the Hall-Petch relationship [12], where grain boundaries prevent the motion of dislocations, or an increase in resistance due to electron scattering, predicted by Fuchs size-effect theory [13]. Reduced electron density in the vicinity of the grain boundary has been shown to affect the reflective properties of polycrystalline films, as well as the photoluminescent properties of thin films [14–16].

Grain growth is driven by an overall system desire to reduce energy. Since interfaces are a major source of system energy, and grain boundaries provide additional interfaces thereby increasing the overall system energy. Grain growth may be broken down into two different regimes, *normal* or *continuous* and *abnormal* or *discontinuous* [17]. In the former, grains tend to grow in a uniform size distribution, while in the latter growth of different grains occurs at different rates, leading to a non-uniform distribution during growth. However, once all other grains have beeen consumed, the resultant

size distribution may be uniform once again [17, 18]. Normal grain growth is governed by an Arrhenius-type equation, of the form [19]

$$d^2 - {d_0}^2 = k_0 t e^{-\frac{Q}{RT}} \tag{1.3}$$

where t is time, d and d_0 are the final and intial grain size, Q is an activation energy, T is temperature, and k_0 is a material constant. From equation 1.3 grain growth is expected to increase with temperature and time, which are both critical parameters in the deposition of thin films. The growth rate for normal grain growth can be approximated as [17],

$$\frac{dr}{dt} = \frac{M\bar{\gamma}_{gb}}{2}\left(\frac{1}{r^*} - \frac{1}{r}\right) \tag{1.4}$$

where $\frac{dr}{dt}$ is the growth rate, r is the grain size, r^* is the critical grain size, $\bar{\gamma}_{gb}$ is the average grain boundary energy, and M is the mobility of grain boundaries, weakly dependent on temperature in an Arrhenius formulation. The situation for abnormal grain growth in thin films becomes much more complicated as now we have variable growth rates for different grains, as shown by Thompson [18]

$$\frac{dr_s}{dt} = M\left[\frac{2({\gamma_s}^* - \gamma_s)}{h} + \bar{\gamma}_{gb}\left(\frac{1}{\bar{r}} - \frac{1}{r}\right)\right] \tag{1.5}$$

where r_s is the radius of the larger, abnormal grain, h is film thickness, $\bar{r}$ is the average grain size, r is the size of the normal grain, and γ_s is the surface energy of the grain under consideration, and ${\gamma_s}^*$ is an average surface energy related to the distribution of grains. Normal or abnormal, grain growth is driven by energy minimization, as well as a dependence on temperature.

In future chapters we will see the influence of grain growth on the properties of several thin film systems. We will elucidate the effect grain growth and growth mode has on the electrical and optical properties of several different

thin film-substrate systems, and how the entirety of the process, from deposition parameters to material selection, influences the resultant properties of the films. As it has already been made obvious when looking at grain boundaries and growth mode, the choice of substrate will have enormous influence on not only the growth mechanisms observed, but ultimately will dictate the quality and properties of the deposited film.

1.6 Vanadium dioxide (VO_2)

Vanadium dioxide is a highly correlated transition metal oxide which has been shown to display a first order phase transformation at a critical temperature of $\sim$340 K [20]. Above the transition temperature, VO_2 is present as a conducting, rutile phase (space group $P4_2/mnm$) structure with lattice constants of a= b= 4.56 Å and c= 2.86 Å, and $\alpha = \beta = \gamma = 90\,^\circ$ [21]. Below the transition, VO_2 exists as an insulating, monoclinic (space group $P2_1/c$) structure which is double the unit cell of the high temperature phase, with lattice constants a= 5.75 Å, b= 4.54 Å, and c= 5.38 Å and $\alpha = \gamma = 90\,^\circ$ and $\beta =$ 122.6 ° [22]. The monoclinic phase is realized by flipping the c- and a-axes of the rutile phase and a dimerization and tilting of alternating vanadium atom pairs along the new monoclinic a-axis. Both of the crystal structures are shown in Figure 1.2 [23], where the changes in the interatomic distances can be visualized.

The nature of the phase transition observed is still under debate, with mechanisms proposed by both Mott (electron-electron interactions) [24, 25] and Peierls (electron-phonon interactions) [26]. The Mott transition takes into account the so called electron-electron interaction e^2/r_{12} which suggests a so called crystallization of the electron gas into a non-conducting state [25]. The Peierls transition is perhaps more intuitive in the sense that it describes a phase transformation as a result of lattice distortion, reducing the overall

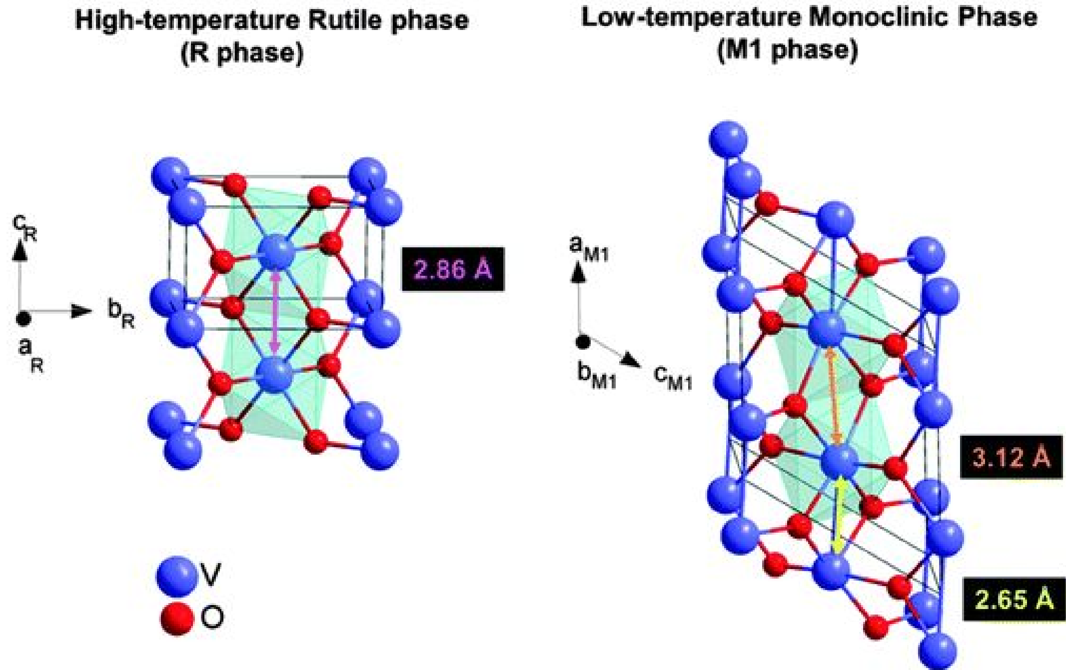

Figure 1.2: The crystal structure of the rutile (left) and monoclinic (right) phases of VO_2 are shown. The two are represented with the same spatial configuration, where the vertical axis changes from the c-axis (left) to the a-axis (right), with the vanadium atom restructuring occuring along this axis. The interatomic spacings of the vanadium atoms can be seen to vary pair-to-pair in the monoclinic phase, while the spacings are uniform in the rutile phase.

symmetry forming an insulating gap at Brillouin zone boundaries, which we most definitely observe in the case of VO_2. The band gap in the insulating phase of VO_2 is $\sim$0.6 eV [27]. However, the exact nature of the transition is still debated to this date, and while fundamentally it would be great to see a solution, we are still able to exploit this property without fully understanding its origin.

VO_2 has a wide variety of applications due to its unique thermochromic, electrochromic, and photochromic properties. The metal-insulator transition has been shown to be modulated by a variety of methods including doping [28] and strain engineering [5]. The ability to tune the phase transition temperature has attracted interest in a variety of applications such as; smart

windows [29, 30], optical switching [31–33], memristors [34], etc. With a societal push to be more eco-friendly and conservative, smart windows provide an excellent avenue to cut down on resource consumption by enabling automated temperature control through window coatings. In addition to the phase transformation, vanadium dioxide possesses a very high temperature coefficient of resistance (TCR) which can be used in infrared radiation (IR) detection [35].

We have chosen to work with VO_2 because there are a lot of unexplored avenues to which this material can be used, in micro-electromechanical systems (MEMS) for example, as well as the fundamental questions pertaining to synthesis and phase stability. Like many transition metals, vanadium has multiple valence states, thereby it may be present in a variety of oxides such as VO_2, V_2O_3, V_2O_5, the Magnéli phases V_nO_{2n-1}, and V_nO_{2n+1} [36]. In addition to these stable oxide compounds, VO_2 itself is known to exist in a number of stable and metastable polymorphs which, in addition to the monoclinic (M1) and rutile (R) phases, include a triclinic (T) phase, another monoclinic (M2) phase, and two metastable phases, denominated as the (A) and (B) phases. Such a wide range of phases introduces an issue with both phase formation and phase stability when synthesizing, and subsequently testing the VO_2 films. Therefore, for successful application of VO_2 into any device, a thorough understanding on the formation and stability of the film is required.

1.7 Molybdenum disulfide (MoS_2)

Molybdenum disulfide, or MoS_2, is one of the so-called transition metal dichalcogenides (TMDC) which is a sheet like structure similar to that of graphene. They have a general formula of MX_2, where M is a transition metal (Mo, W, V, Nb, etc.) and X is a chalcogen atom (S, Se, Te) [37]. MoS_2 is a

layered structure, present in two different predominant phases; 2H-MoS_2 and 3R-MoS_2, indicating hexagonal and rhombohedral symmetry, respectively [38]. Unlike graphene however, MoS_2 is a semiconductor with an electronic band gap of $\sim$1.9 eV as a monolayer, which converts to an indirect band gap of 1.29 eV when the thickness is increased past the monolayer [39]. This newer class of materials offers many potential applications due to their many interesting properties. Traditionally used as a solid state lubricant due to the relatively weak van der Waals forces holding the layers together, or as a catalyst in many petrochemical processes, MoS_2 has recently found its way into state-of-the-art electronic devices [40–44].

Target applications for MoS_2 include optoelectronics [7, 44], photonic structures [45], nanoelectronics [46, 47], valleytronics [41], and spintronics [48] due to remarkable electronic properties. In addition to the direct-indirect band gap present in monolayer and multilayers, MoS_2 has a very high on/off ratio ($> 10^8$) [46] and carrier mobilities (500 $cm^2 \cdot V^{-1} \cdot s^{-1}$) [49], as well as very good electrical conductivity (0.03 $\Omega^{-1} \cdot cm^{-1}$). Such properties are attractive for integration into transistor like devices where on/off ratio, mobility, and conductivity are important factors.

Since it is also a semiconductor, in both the bulk and monolayer forms, MoS_2 has potential in energy applications. Seeing as the band gap of MoS_2 falls in the visible-near IR range, such a material can be used in both detecting and converting light by charge generation. MoS_2 has been shown capable of integrating with Si in a heterostructure for generation of energy via photoexcitation [50] as well as detecting light in the visible [7] and the near-IR [8]. However, it is the lack of work done in the mid-IR range that attracted us to MoS_2 with an intent to uncover a new range of applications for such a material.

Chapter 2

Characterization and fabrication techniques

Several different techniques were used in the fabrication and characterization of the thin film devices set forth in the following chapters. Thin films were deposited via PLD and were subsequently characterized by several spectroscopic and microscopic techniques. Such a wide variety of techniques were required to adequately characterize the structure and composition of the films, which also provides insight into the physical ramifications each process variable has on the resultant film. A brief overview of each of these techniques will be presented herewith.

2.1 Pulsed laser deposition

Although an overview of this specific technique was given in chapter 1.2, that dealt with the process in broad terms and not the system particular to all experiments conducted and present in this thesis. Our PLD system consisted of a KrF (λ=248 nm) excimer laser (Coherent, GmbH), which is capable of supplying laser pulses (pulse width of 20 ns) up to a maximum energy and repetition rate of 700 mJ and 50 Hz, respectively. The PLD deposition chamber

(Excel I=instruments, Mumbai, India) is capable of holding up to six different targets, and heating the substrate up to 850 °C. The chamber is outfitted with a gas inlet and flow controller to precisely control gas flow, and two pressure gauges; a low vacuum Pirani gauge used for deposition, and a cold cathode gauge for high vacuum.

2.2 X-ray diffraction

Perhaps the most critical and most often used technique throughout the course of this work was X-ray diffraction (XRD). XRD is a technique used to determine the atomic (or molecular) structure of a crystalline material by measuring the intensity of diffracted X-rays. Properties such as crystallinity, interplanar spacing, stress/strain, and crystallographic orientation all can be determined by this technique. A specimen is placed onto the sample stage where it is bombarded with X-rays of a specific wavelength (dependant on the source of X-rays), which then interact with the sample material and the outgoing X-rays are collected by a detector. X-rays are capable of scattering from crystalline materials due to the close proximity between the X-rays wavelength and the atomic spacing. The X-ray-sample interaction is where all valuable information resides, and has been explained by both Bragg and von Laue with two equally correct, but fundamentally different methodologies.

The Bragg formulation, depicted below in Figure 2.1, depicts the beam-specimen interaction as a specular reflection from the atoms of a crystal lattice. X-rays will constructively interfere with one another given that the path length difference between the two waves is equal to an integer multiple of the X-ray wavelength. The Bragg equation, shown in eq. 2.1, gives the condition for constructive interference as described above.

$$n\lambda = 2d\sin(\theta) \tag{2.1}$$

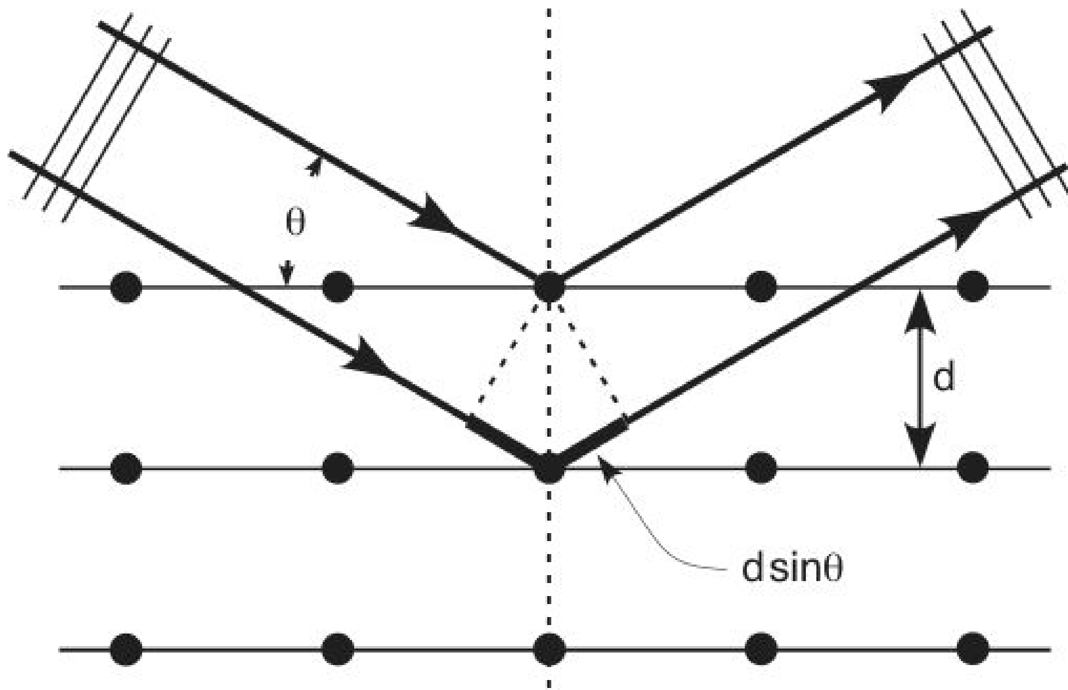

Figure 2.1: Schematic representation of Bragg diffraction. Constructive interference occurs if the path length difference between the incoming waves is equal to an integer multiple of their wavelength.

Here, n is an integer, λ in the X-ray wavelength (Å), d is the spacing between lattice planes (Å), and θ is the angle which results in maximum intensity of the diffracted beam.

The approach taken by von Laue was far more vigorous than Bragg, and treated the atoms of a crystal as centers capable of scattering the incoming radiation in all directions. When radiation from each lattice point interfere constructively, sharp peaks will appear in the XRD spectrum. The von Laue condition in Figure 2.2 [51] shows a simple two scatterer schematic of how he treated X-ray diffraction.

Two scatterers, separated by $\mathbf{d}$, are irradiated along direction $\hat{\mathbf{n}}$, by wavevector $\mathbf{k}= 2\pi\hat{\mathbf{n}}/\lambda$. The vector is now scattered along a new direction, $\hat{\mathbf{n}}'$, with a new wavevector, $\mathbf{k}'= 2\pi\hat{\mathbf{n}}'/\lambda$ given that the path length difference is an integer multiple of the incoming wavelength. Mathematically, this can be

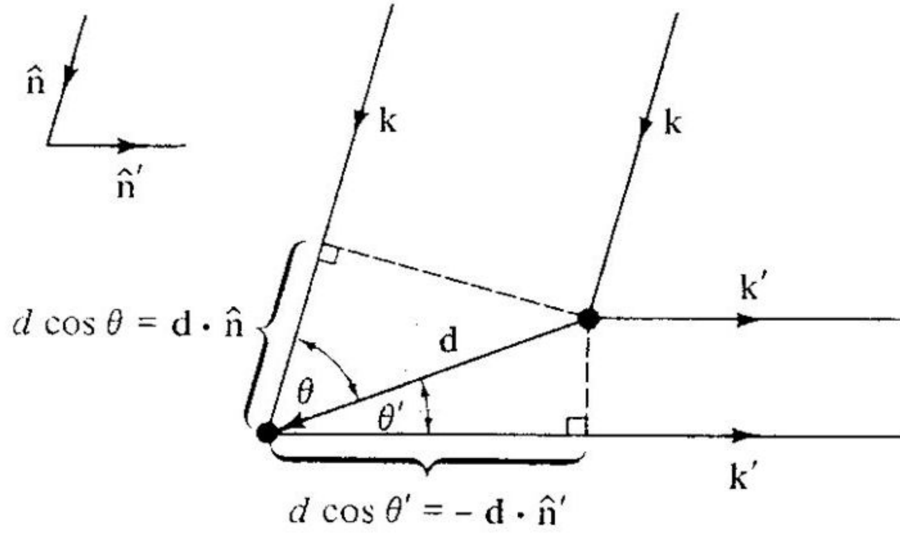

Figure 2.2: The von Laue condition for diffraction. Here the lattice positions are treated as individual points as opposed to planes demonstrated by the Bragg approach. Constructive interference will occur under the same condition as the Bragg formulation; that is when the path length difference is equal to an integer multiple of the incoming waves wavelength.

equated as [51]

$$\mathbf{d} \cdot (\hat{\mathbf{n}} - \hat{\mathbf{n}}') = m\lambda. \tag{2.2}$$

To see the effect on the scattered wave, multiplying both sides by $2\pi/\lambda$ yields

$$\mathbf{d} \cdot (\mathbf{k} - \mathbf{k}') = 2\pi m. \tag{2.3}$$

for any integral m. For a real system with infinite lattice points, the diffraction condition must hold for all values of **d** which are lattice vectors. Bravais lattice vectors, denoted as **R** must meet the diffraction condition set forth in eq. 2.3, and must satisfy the following

$$e^{i(\mathbf{k}'-\mathbf{k})\cdot\mathbf{R}} = 1. \tag{2.4}$$

The reciprocal lattice may be defined as the set of wavevectors, **K**, which

satisfy the following relation:

$$e^{i(\mathbf{K})\cdot\mathbf{R}} = 1. \tag{2.5}$$

From equation 2.4 and 2.5 we can see that constructive interference occurs only when **K**=k′-**k**, indicating that **k**′-**k** must be a reciprocal lattice vector. If we assume the scattering to be elastic in nature, it would follow that **k** and **k**′ are equal in magnitude.

The resultant mathematical description of diffraction by both Bragg and von Laue are equivalent, though the derivations differ greatly. The von Laue approach can be reduced to the Bragg equation, shown by 2.1, by some simple mathematics. Since **k**′-**k** and **k**-**k**′ are both reciprocal lattice vectors, and both **k** and **k**′ have the same magnitude, we get k= $|\mathbf{k}-\mathbf{K}|$. Squaring both sides and simplifying the equation we end up with the following relation

$$\mathbf{k}\cdot\hat{\mathbf{K}} = \frac{1}{2}K, \tag{2.6}$$

which shows that the component of the incident wave along the reciprocal lattice vector must be half the length of **K**. If θ is the angle between and the incoming wavevector **k** and the direction perpendicular to **K**, then it can be shown that

$$K = 2k\sin\theta \tag{2.7}$$

and since the magnitude of the reciprocal lattice vector **K** is $2\pi/d$, the relation can now be written as

$$2d\sin\theta = n\lambda \tag{2.8}$$

which is identical to equation 2.1 shown earlier.

In this work, XRD was performed using a Rigaku Ultima IV diffractometer using a Cu Kα X-ray source and a scintillation counter detector. In this work we used two different scanning geometries, the conventional Bragg-Brentano

(θ-2θ) and a grazing angle mode. Ultrathin films like the ones studied in most of this thesis benefit from the grazing angle mode of detection as it eliminates the appearance of substrate reflections. In this mode the incident X-rays are fixed at a constant angle (for this work it can be assumed that the grazing angle will be fixed at 0.5° unless otherwise specified) and the detector is scanned to collect the reflected signal. Since the incident beam is nearly parallel with the sample surface, a larger amount of reflection will occur within the film, limiting or excluding any reflection from the substrate. In some cases the conventional Bragg-Brentano configuration was used for thicker films, or when necessitated.

In some cases, simply scanning 2θ was not sufficient, and additional scan configurations were needed. For VO_2, several reflections in the monoclinic phases have multiple planes at the same 2θ value, which need to be distinguished. In this case an off-axis ψ scan is performed, where the detector is fixed at a reference 2θ value and rotated out of plane to a ψ value corresponding to the angle between the plane under question and reference plane and the stage is then rotated the desired amount. If the plane under question is in fact the correct plane, reflections indicative of the symmetry of said plane will appear on the ϕ scan. If it is not the correct plane, no reflections should appear.

2.3 Scanning electron microscopy

Scanning electron microscopy (SEM) was one of the primary techniques used to characterize the topological appearance of the thin films. SEM is a powerful technique with a plethora of customizable parameters enabling a broad spectrum of information to be gathered. Accelerating voltage, aperture size, detector type, working distance, and specimen orientation are all parameters that can be manipulated in order to examine the sample. It is also important

to understand how each of these parameters influence the resultant image. The majority of the imaging done in this work was performed on a field-emission scanning electron microscope (FESEM) from Zeiss. This particular microscope uses a field emission (FE) source as opposed to a thermionic emission (TE) source which allows for a much higher resolution. FE sources rely on a very high localized electric field at the tip of a, typically tungsten, wire. FE sources are superior to TE sources as they offer brightnesses of over 10^3 times larger, a much longer lifetime, a lower energy spread, and perhaps most importantly the diameter of the source is significantly smaller in FE sources (5 nm) compared to TE sources (50 µm) [52].

Imaging with an SEM can be done using secondary electrons (SE) or backscattered electrons (BSE). BSEs are beam electrons that have entered the specimen and, through a series of electron-solid interactions, have found their way back to the surface where they are ejected back into the vacuum. BSEs are generally higher in energy as compared to SEs, although the energy spectrum of BSEs encompasses energies from zero all the way up to incident beam energy. BSE yield is strongly dependant on the atomic number, and therefore forms the foundation for a contrast based imaging technique. BSE imaging is particularly useful for samples with two phases of different atomic number (Z), which will show brighter (higher Z) and darker (lower Z) areas depending on the composition. However, BSE imaging is not very useful for conventional surface analysis which is generally reserved for SE imaging.

SEs are electrons which have been generated as a result of electron-solid interactions and come in many forms. The energy threshold for SEs is generally accepted to be any electron collected with an energy less than 50 eV. The electrons are formed when incoming beam electrons collide with the loosely bound outer-shell electrons of the sample, and are called SE_1. SEs may be formed by BSEs near the surface as well, with the BSE ejecting an outer-shell electron from another atom, and these are termed SE_2. When BSEs are ejcted

from the surface, they are ejected in random directions, only collected if their trajectory is in line with the detector. However, when imaging is SE mode, these electrons can collide with the infrastructure within the SEM chamber, generating additional SEs, called SE_3, which are highly undesirable. Unfortunately, SE_3 constitute a majority of the SE yield, and therefore weaken the image quality [52]. If these collisions occur within a reasonable distance from the surface, these electrons can then be collected by a SE detector [52].

SE detectors used in this work were either an Everhart-Thornley (ET) or through-the-lens (TTL) detector. An ET detector can be used to detect both SEs and BSEs, depending on the operational configuration applied. Technically speaking and ET detector is a scintillator (with a large applied bias of 10-12 kV to give sufficient energy to the electrons) housed inside a Faraday cage, connected to a light guide, which is connected to a photomultiplier. The scintillator converts the incident electrons into a photon, which is then passed through a photocathode, converting the signal back into an electron. This electron is then directed towards the first electrode of a photomultiplier tube, which then is directed through a series of electrodes, resulting in a signal gain on the order of 10^5-10^6. The Faraday cage is responsible for dictating the operational mode of the detector. Faraday cages are typically biased in the range of -50 to +250 V, with the negative bias indicating BSE detection, and the positive bias used in SE mode. The negative bias is large enough to repel low energy electrons such as SEs (and a small portion of BSE), and the positive bias is used to attract the SEs. The unfortunate side effect of such a detector is the unavoidable inclusion of SE_3 type electrons.

To overcome the issues of collection "contamination" is to utilize a TTL detector which efficiently captures SE_1 and SE_2, while avoiding BSE and unwanted SE_3. If the configuration of the SEM allows for it, the detector is placed above the objective lens, where low energy electrons are caught and spiral up the lens because they are trapped in the magnetic field that extends

onto the sample. The working principle of the detector is the same, as it is a scintillator (with a large bias, same as the ET detector) connected to a light guide and photomultiplier tube. Because of the superiority of the TTL detector, almost all SEM imaging in this work was conducted using this type of detector. If an ET detector was used it will be explicitly stated.

The other parameters that are routinely manipulated are the aperture and the accelerating voltage. The aperture controls the percentage of the electron beam that passes through to the sample. By controlling the size of the aperture there is always a balance between the depth of focus and the beam current. By limiting the aperture to a smaller size, the convergence angle of the beam is reduced, allowing for a much greater depth of field. This is particularly useful when imaging rough surfaces. However, the signal generated from the sample is relative to the number of electrons incident on the surface, and therefore highly dependant on the size of the aperture. The beam current is related to the aperture size by r^2, which can significantly diminish the signal detected if the aperture is too small.

Choice of accelerating voltage has direct consequences on the information collected in SEM imaging. In this thesis, the primary objective is often to analyze the surface, and so a low voltage mode is often used (5 keV). The interaction volume in SEM operation is directly proportional to the accelerating voltage, as shown by the following equation, developed by Kanaya and Okayama [53]

$$R_{KO}(\mu m) = \frac{0.0276A}{Z^{0.89}\rho} {E_0}^{1.67} \tag{2.9}$$

where R_{KO} is the electron penetration depth in µm, A is the atomic mass (g/-mole), Z is atomic number, ρ is the density (g/cm^3), and E_0 is the accelerating voltage (keV). Monte Carlo simulations of the electron trajectory through a model sample of VO_2 is shown in Figure 2.3 for various accelerating voltages.

For each simulation presented in Figure 2.3 the VO_2 thickness was set at 25 nm, and the substrate was semi-infinite (thickness much greater than the

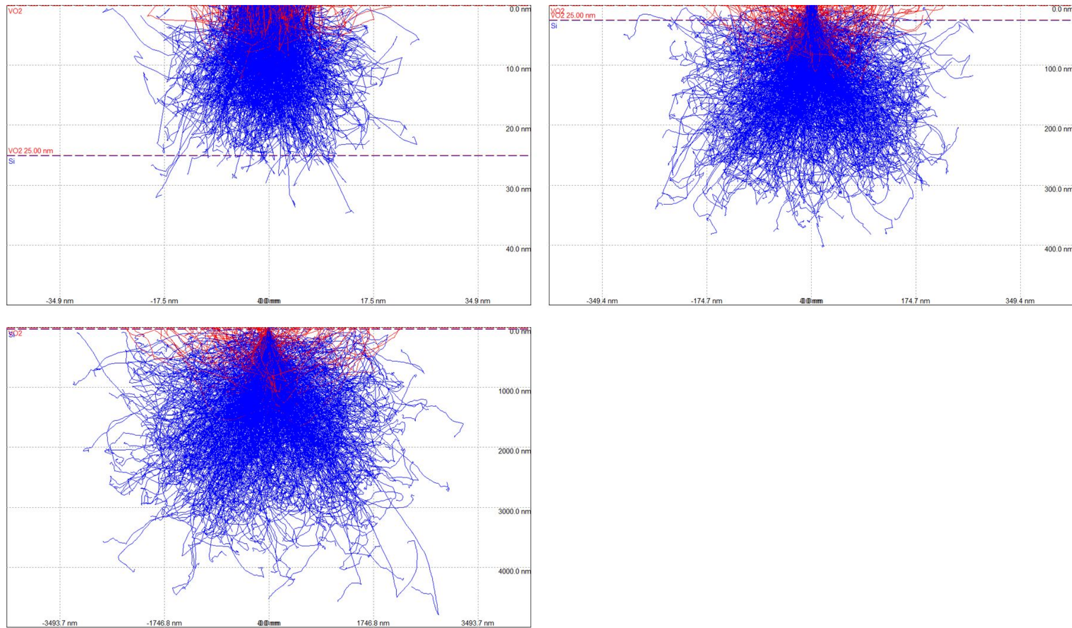

Figure 2.3: Monte Carlo electron trajectory in VO_2 thin films on an arbitrary Si substrate. The accelerating voltage was (a) 1 keV, (b) 5 keV and, (c) 20 keV.

electron penetration depth). The different colours of trajectory (red and blue) shown in Figure 2.3 correspond to the type of electron. Red trajectories are indicative of BSEs that have been ejected from the surface, while the blue trajectories shown electrons that are eventually absorbed into the sample, i.e. they do not participate in the imaging process. The depth of electrons that escape from the sample was approximately 10 nm, 110 nm, and 1200 nm for 1 keV, 5 keV, and 20 keV acclerating voltages, respectively. What is apparent is the higher accelerating voltage penetrates much deeper into the sample, generating backscattered electrons deeper within the sample, which causes a wider spread of electrons. Ideally, imaging would be done with SE_1 type electrons only, so this spreading of the electron source results in degradation of the image. However, too low of an accelerating voltage will ultimately result in a weaker signal so a balance must be achieved.

2.4 Additional characterization techniques

In addition to XRD and SEM, there are a variety of other techniques that are used, albeit less frequently, throughout this work. The following section will briefly introduce each of these techniques, and outline the specific instrumentation and parameters used for data acquisition.

2.4.1 Transmission electron microscopy

A few chapters in this thesis incorporate transmission electron microscopy (TEM), used as a means to analyze the nature of the substrate-film interface. Similar to SEM, TEM uses electrons as an means of imaging a specimen. In TEM, the sample is thin enough to allow for the electron beam to penetrate through to the other side where the beam is collected by an electron detector, commonly a charge-coupled device (CCD) camera. In this thesis, high resolution transmission electron microscopy (HRTEM) as well as selected area electron diffraction (SAED) were used to collect information regarding the crystallographic orientation relationships between film and substrate. HRTEM and SAED provide intricate details about the periodic potential in the sample, and ultimately the crystal structure and atomic positions. In this thesis, HRTEM and SAED were used to analyze the atomic structure of VO_2 and MoS_2 thin films grown on different substrates in an attempt to understand the nature of the growth process.

2.4.2 Helium ion microscopy

Helium ion microscopy (HIM) was used when the specimen was insulating and a conductive coating was not feasible. The operational principle of HIM is very similar to that of SEM, but uses He^+ ions rather than electrons in the beam. There are two very distinct advantages to using HIM over SEM; i) it is possible to image insulating samples without depositing a conductive coating,

and ii) an extremely high depth of field is attainable due to the relatively large mass of a He^+ ion. The large mass of the He^+ ion makes it hard for the electromagnetic coils to deflect them, leading to a small divergent angle. In order to image an insulating surface, the use of an electron flood gun is employed to remove the buildup of positive charges on the surface from the He^+ ions. By using this techniques it is possible to image an insulating sample without the need of disrupting the virgin surface.

2.4.3 Atomic force microscopy

Atomic force microscopy (AFM) is a common technique used to analyze a very wide range of properties of a material. In the simplest operation, the topography of the sample is analyzed by scanning a probe tip across the surface. There are three main modes of AFM operation; contact mode, non-contact mode, and tapping mode. During contact mode operation, the AFM tip is placed into hard contact with the surface and is dragged across measuring the topographic features by monitoring the deflection of the tip, or the force applied to the cantilever. Non-contact mode AFM operation the cantilever is oscillated just above the surface of the sample, and does not come into contact with the sample at any time. Here, rather than rely on the deflection of the tip due to physical contact with features on the sample, the tip is affected by van der Waals forces between the surface and tip.

Tapping mode is perhaps the most significant advancement in AFM technology since its inception. In this mode, the cantilever is brought into contact with the surface, then lifted away by a specified distance (this distance may vary but is usually $\sim$50 nm), where the cantilever is then excited near resonance. Once the cantilever is oscillating, it is moved towards the surface until it starts to tap on the substrate (hence the name, tapping mode). This contact results in an energy loss in the cantilever which is then used to determine the surface structure. Tapping mode offers the advantages of both contact and

non-contact mode as it produces a high resolution image while imparting minimal damage to the substrate. Tapping mode AFM was used throughout this thesis to collect topographical profiles of the deposited VO_2 and MoS_2 films.

Chapter 3

Effect of process parameters on phase stability and metal-insulator transition of vanadium dioxide (VO_2) thin films by pulsed laser deposition

3.1 Abstract

Owing to remarkable thermochromic, electrochromic, and photochromic properties which arise from a first-order phase transition from insulator to metal at 68 °C, vanadium dioxide (VO_2) has an enormous range of potential applications. However, due to such narrow thermodynamic stability, there is a major challenge surrounding selective phase deposition of vanadium dioxide thin films. Here, we present a report that establishes precise conditions for the deposition of three major polymorphs of VO_2 by pulsed laser deposition. By a systematic study of the synergistic effects of the deposition

conditions using a robust design of experiment (Taguchi design), we are able to deposit the VO_2 (M1), VO_2 (T), and VO_2 (A) phases onto SiO_2 substrates with remarkable precision. By electrically probing the temperature induced phase transformation from insulator to metal of each of these polymorphs, we find not only a strong dependence on the phase, but that the nature of the deposition conditions influences the magnitude and hysteresis width of the temperature cycle.

3.2 Introduction

Several transition metal oxides display a so called metal-to-insulator transition (MIT), induced by external factors such as temperature [20, 54], pressure [55], electric field [56, 57], magnetic field [58, 59], etc. This transition is often accompanied by drastic changes in the magnetic, optical, and electrical properties of the material. Vanadium dioxide (VO_2) is of particular interest due to the low temperature (68 °C in bulk) at which this transition is observed. At the critical temperature (T_c= 68 °C) VO_2 undergoes a first order structural phase transition from the high temperature tetragonal (space group $P4_2/mnm$) lattice to a room temperature monoclinic (space group $P2_1/c$) lattice, which is manifested as drastic changes to the electrical and optical properties of the film [6, 20, 60, 61]. This relatively low temperature MIT offers promising applications in technologies such as non-volatile memory [62], microbolometers, [35, 63–65], gas and strain sensing [66, 67], Mott transistors [68], smart window coatings [30, 69], ultrafast optical switches [33, 70, 71], metamaterials [72], and memristors [34, 73]. The critical parameter that allows the exploitation of the MIT is hysteresis width, which is highly dependent upon the properties of the film. For applications like non-volatile memory a large hysteresis width is required, whereas the opposite is true for microbolometers. A common feature of transition metals is their abundance

of valence states, of which vanadium is no different. There is a plethora of stable and metastable oxides of vanadium, including VO, VO_2, V_2O_3, V_2O_5, V_6O_{11}, and V_6O_{13}, which complicates the specific production of the VO_2 phase [74–76]. In addition, VO_2 has several stable polymorphs, each with a unique crystal structure and properties. The most common phase studied is the monoclinic VO_2 (M1), which is one of several VO_2 polymorphs undergo an MIT into the rutile VO_2(R) phase. Additional phases include triclinic VO_2 (T), strained monoclinic VO_2 (M2), and metastable tetragonal VO_2 (A) and monoclinic VO_2 (B) phases [5, 77–79].

Pulsed laser deposition (PLD) offers a unique approach to the fabrication of a wide variety of materials, including VO_2. PLD is categorized as a physical vapor deposition (PVD) technique, taking place in a vacuum chamber under high vacuum or in the presence of a process gas. Laser pulses are focussed onto a target and, given sufficient energy, results in the ablation of the target material creating a highly directional plasma plume. The plume is directed towards the substrate (which is often heated), resulting in deposition of the target material. In many cases, the process gases contained in the chamber undergo reactions in the plasma, altering the stoichiometry of the deposited film as a function of the pressure. PLD gained prominence in 1987 for the stoichiometric deposition of $YBa_2Cu_3O_7YBa_2Cu_3O_7$ superconductor by Dijkkamp et al. [9], and has since gained traction in epitaxial thin film growth [77, 80, 81], superlattice formation [82, 83], superconducting electronic devices, and the deposition of other complex materials [84]. VO_2 thin films have long been produced using PLD, using a variety of target materials, oxygen gas pressures, laser energies, and other process parameters. Perhaps the most intriguing variable is the target material itself, which is commonly V_2O_5 but may also be pure vanadium metal as well as other oxides such as VO_2 and V_2O_3 [85–88]. By using metallic vanadium as a target, oxidation is the only process required to deposit films, while for a V_2O_5 target, in order to produce

VO_2 one must instead reduce the V_2O_5 target to produce said film. There are a few recent reports available on VO_2 film deposition using PLD starting from a vanadium metal target. However, those films were formed by post annealing at high temperature of as deposited films [71, 89]. Recently, Forbes et al, showed synthesis of phase pure VO_2 using vanadium metal target without post annealing and studied the influence of laser energy on the growth of phase pure VO_2 [90]. While the effect of oxygen gas pressure on VO_2 formation has been studied extensively [91, 92], a systematic study on the influence of gas pressure (O2), substrate temperature, target substrate-distance, and laser energy on phase pure VO_2 synthesis is still lacking.

Here we present a detailed optimization of the deposition of VO_2 films onto amorphous thermally grown silicon dioxide (Si/SiO_2) substrates using PLD. SiO_2 was selected as a substrate for two major reasons; by using an amorphous substrate we are not restricting the film to any preferential growth orientation or texture that would be seen on a crystalline substrate [93], and for future applications, with micro- and nanofabrication in mind, thermal oxide is a common material often used as a sacrificial layer [94]. By employing a robust design of experiment (DOE) approach, also referred to as Taguchi design, we were able to optimize the deposition process by adjusting the laser energy, substrate temperature, target-to-substrate distance, and oxygen pressure. The target of the experimental design was to determine which deposition parameters had the greatest influence on the quality of the VO_2 film deposited. The films were characterized by X-ray diffraction (XRD) to determine the phase; atomic force microscopy (AFM) to determine the surface roughness and film thickness; scanning electron microscopy (SEM) to determine grain structure; electrical resistance measurements to determine the magnitude and hysteresis of the heat-cool cycle; and current-voltage characteristics to determine the resistivity of each film. Here we were able to determine the optimal deposition conditions for the production of the M1, A,

and T phases of VO_2. By studying the heat-cool resistance curves we were also able to determine the effect of deposition parameters on the hysteresis width, as well as the response of each unique VO_2 phase.

3.3 Experimental

3.3.1 Materials synthesis

Pulsed laser deposition (PLD) of VO_2 was carried out by ablating vanadium metal target using high energy laser pulse in an oxygen atmosphere at high temperature in a PLD chamber (Excel instruments, Mumbai, India). Krypton fluoride (KrF, λ= 248 nm) excimer laser (Coherent, GmbH) was used with a 20 ns pulse width with a repetition rate of 10 Hz. A vanadium metal (99.9% purity, American Elements) circular disc with a diameter of 0.5 inch and thickness of 0.125 inch was used as a PLD target. Thermally grown silicon dioxide (Si/SiO_2 ~500 nm) substrates were used for the deposition. A schematic of the experimental setup is shown in Figure 3.1. Prior to deposition, the substrates were cleaned in a piranha solution followed by ethanol, IPA, and water. The background pressure of the PLD chamber was maintained below

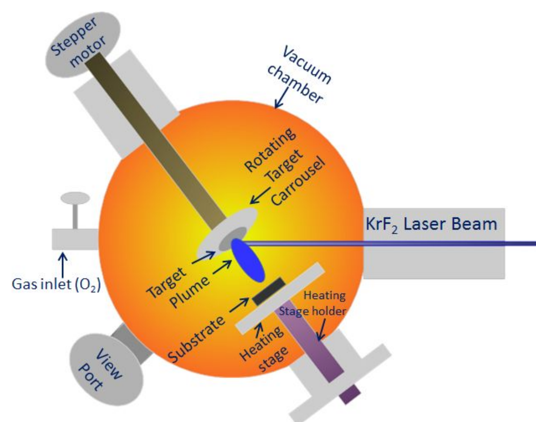

Figure 3.1: Schematic of PLD experimental setup, including the laser path and the PLD chamber

1×10^-5 torr before purging with oxygen. The spot size of the laser was 3 mm $\times$ 1 mm at the target. Oxygen gas pressure, target-substrate distance, laser energy, and temperature were varied simultaneously to perform the Taguchi analysis. The time of deposition was kept constant for 15 min.

3.3.2 Taguchi method-design of experiment

A standard L9 orthogonal array was chosen to study the effects of 4 independent parameters at 3 different levels. The orthogonality here means that the levels of the control factors in the experimental design are balanced and equally weighted. This unique feature allows an independent assessment of the influence of each control factor on the response while changing the levels of the other factors [95]. The Taguchi method allows for the total number of experiments to be significantly reduced while maintaining the amount of information received, and has been successfully implemented for thin film deposition [4, 96]. Table 3.1 presents the four parameters studied in this work, (i) gas pressure (O_2), (ii) substrate temperature, (iii) target-substrate distance, and (iv) laser energy. The three levels for substrate temperature were chosen based on values reported in literature [80, 86, 90], while the remaining three parameters were determined *a priori*. During PLD, a plasma is generated inside the chamber and is directed towards the substrate. For consistent deposition, it is imperative that the plasma plume reach as far as the substrate to avoid diffusion controlled deposition [97]. By theoretically modelling the dynamics of the plasma plume, the remaining three parameters (pressure, target-substrate distance, and laser energy) can be determined.

3.3.3 Plasma plume dynamics

There are several factors that influence the generation and propagation of a plasma when it is generated in a background gas. The species and pressure of

Table 3.1: Depostion parameters and their levels.

Label	Factors	Levels		
		1	2	3
A	O_2 gas pressure (torr)	1×10^{-4}	2×10^{-3}	5×10^{-2}
B	Substrate temperature (°C)	500	600	700
C	Target-substrate distance (mm)	31	38	45
D	Laser fluence (J/cm^2)	1.8	2.2	2.6

the gas and the laser energy play a major role in the dynamics of the plasma. It has been shown that when ablation occurs in a gaseous environment the plasma can be modelled as an ideal blast wave with a spherical shockwave boundary varying with time as [98, 99]:

$$R = \epsilon_0 \left(\frac{E}{P_0} \right)^{1/5} t^{2/5} \tag{3.1}$$

where R is the range of the plasma, ϵ_0 is a constant, E is the energy of the laser, P_0 is the background pressure of the gas, and t is time. However, eq 3.1 holds valid for very short times as the plasma will experience drag and will transition from shockwave to a diffusion controlled motion at some point in time. It has been shown that the range of a plasma, assuming adiabatic expansion and an elliptical plasma front, can be expressed by [97]:

$$L_p = A[(\gamma - 1)E]^{1/3\gamma} P_0^{1/3\gamma} V_i^{(\gamma - 1)/3\gamma} \tag{3.2}$$

Here, γ is the ratio of the specific heats of the plasma species (i.e. oxygen), A is a geometrical shape factor regarding the head of the plasma plume and V_i is the initial volume of the ablation products, expressed as [97]:

$$V_i = \nu_0 \tau l_a \tag{3.3}$$

with v_0 being the initial velocity of the plasma species (1-2 $\times$ 10^4 ms^{-1}) , τ the pulse width of the laser, and l_a the spot size of the laser. The parameter A is given by [98];

$$A = \left(1 + \frac{1}{\tan\theta}\right)\left(\frac{3\tan^2\theta}{\pi\tan\phi + 2\pi\tan\theta\tan\phi}\right) \quad (3.4)$$

where θ and ϕ are the angles of the azimuth and the altitude of the projected plasma, respectively. From here we were able to determine the optimal deposition parameters for the production of VO_2 (M1) phase thin films by generating a 3D surface map of the plume range as a function of laser energy and oxygen pressure. Plasma expansion range is affected by a number of variables (see eqs 1 and 2), several of which are hard to control. However, laser energy and oxygen gas pressure were chosen as model parameters considering they both are critical to the process and easily manipulated. Using the values A= 0.85, γ= 1.4, V_i= 7.5×10^{-10} m^3 (from τ= 25 ns, l_a= 3 mm^2, and ν_0= 10^4 ms^{-1}), the plume range can be seen in Figure 3.2. Due to the capabilities of our system, the minimum target-substrate value possible was 25 mm, therefore the deposition parameters were chosen such that the plume range was larger than 25 mm. From Figure 3.2 it is apparent that the plasma propagates farther at a lower pressure, given that the rest of the parameters remain unchanged. There is the possibility that the shape of the plasma front is variable at different conditions, however it would be impossible to display all possible scenarios here, and so the most probable case is depicted herein, as supported by Doggett and Lunney and their work on the dynamics of plasma expansion [100]. Images taken of the plasma during operation can be seen in the supplementary material (Figure 3.7). The levels chosen for each parameter are summarized in Table 3.1, and the experimental design based on the L9 orthogonal array is summarized in Table 3.2. The full set of deposition conditions, V1-V9, were conducted twice in order to generate

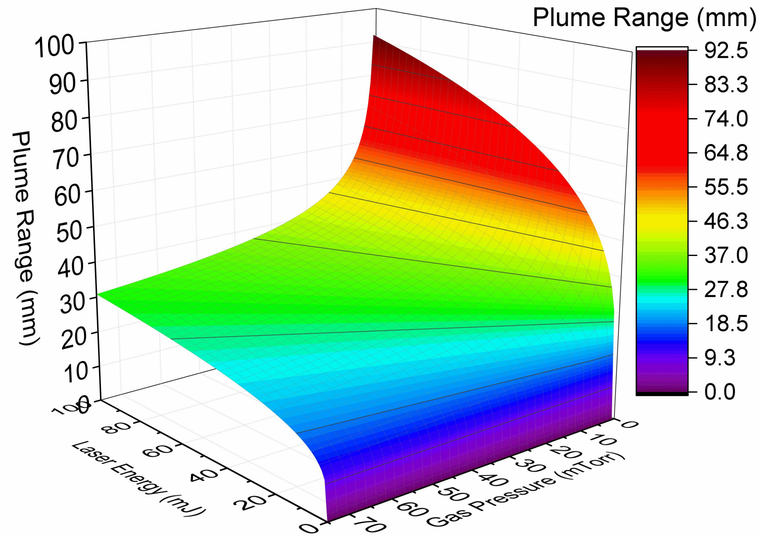

Figure 3.2: Theoretical range of the plasma plume as a function of laser energy and gas pressure. It is clear that the plasma travels farther at lower pressures as there is much less aerodynamic drag to compete with. This model served as the basis for determining the different levels of gas pressure, laser energy, and target to substrate distance.

two separate response values, R1 and R2, and to ensure reproducibility of the deposition parameters.

3.3.4 Characterization

The deposited films were characterized by X-ray diffraction (Cu Kα) using Rigaku XRD Ultima 4 at glancing angle mode with an incident angle of 0.5 °. The surface topography and the thickness of the films were measured by Dimension Fast Scan Atomic Force Microscope (Bruker Nanoscience division, Santa Barbara, CA, USA). Commercially available Pt-Ir coated conductive probes (SCM-PIT) with a spring constant of 2.5 N/m and a resonant frequency of 65 kHz were used for obtaining surface topography. SEM imaging was done using Zeiss Sigma FESEM. Two-probe electrical resistance measurements were taken for each film using a Keithley 194 digital multimeter inter-

faced with LabView. Temperature dependent resistance measurements were carried out using a Signatone probe station 1160 series on a heating/cooling chuck where temperature was varied from 5 to 110 °C at an interval of 2 °C with an equilibration time of 3 min at each interval. Resistivity of each sample was taken using a Keithley 2450 SMU with a linear four probe configuration.

3.4 Results and discussion

Taguchi design employs an orthogonal array to identify the effect of control factors on the target response mean and to estimate the corresponding variation. Here, the films were analyzed using XRD, SEM, AFM, and resistance measurements in order to quantify the results. The response is generated as a product of the experimental outcome for each analysis technique incorporated. The overall response is a culmination of the individual responses, which in the end is displayed as a single numerical value for each film. The deposition factors and the corresponding responses and signal-to-noise ratios (SNR) for each experiment is summarized in Table 3.2. The responses are indicated in Table 3.2 as R1 and R2, with a second set of films deposited and analyzed to produce the second response value. In the case of the present experiments, a higher SNR is desirable, which suggests a higher quality film and less variance, and is calculated using the larger is better method:

$$S/N = -10Log\left(\frac{1}{n}\sum_{i=1}^{n}\frac{1}{{y_i}^2}\right) \tag{3.5}$$

where n is the number of experiments and y_i is the response from each experiment [101]. The responses were determined based on the following analyses, and the methodology used to assign values to each will be discussed in detail in the following sections.

Table 3.2: Experimental Layout for VO_2 based on L9 (4-factors and 3-levels) orthogonal array. Response is calculated for each sample and repetition as described in the text. Signal to noise (S/N) ratio was determined using a larger-is-better method.

Experiment	Deposition Factor				Response		S/N Ratio	Predominant Phase
	A	B	C	D	R1	R2		
V1	1	1	1	1	5	4	12.90	Amorphous
V2	1	2	2	2	6	7	16.18	V_2O_3
V3	1	3	3	3	6	6	15.56	V_2O_3
V4	2	1	2	3	6	7	16.18	V_2O_3
V5	2	2	3	1	8	8	18.06	V_2O_3
V6	2	3	1	2	12	12	21.58	VO_2 T
V7	3	1	3	2	12	12	21.58	VO_2 A
V8	3	2	1	3	17	18	24.85	VO_2 M1
V9	3	3	2	1	12	13	21.92	VO_2 M1

3.4.1 X-ray diffraction analysis

Crystal structure of vanadium oxide films deposited under different conditions were first analyzed by XRD with an incident angle of 0.5 deg. and a scan range of 10-90 deg. XRD scan profiles for all nine samples are shown in Figure 3.3. The deposited films predominantly display one of two phases, VO_2 and V_2O_3, which are strongly dependent upon the deposition parameters. The films tend to become more crystalline as the gas pressure increases, generally exhibiting an amorphous structure at low gas pressures and showing a stronger VO_2 peak as the pressure is increased. From Figure 3.3(a) it is seen that the film deposited at V1 was amorphous, while the films deposited at V2 and V3 result in a weakly crystalline mixed V_2O_3 phase. While the peaks are too hard to resolve in sample V2, the dominant peaks that appear in sample V3 are at 2θ angles of ~ 33.3 and 54.1 deg corresponding to hexagonal V_2O_3 (space group R-3c) and at ~ 55.6 deg which corresponds to monoclinic V_2O_3. Given the low oxygen content present during deposition it is no surprise that

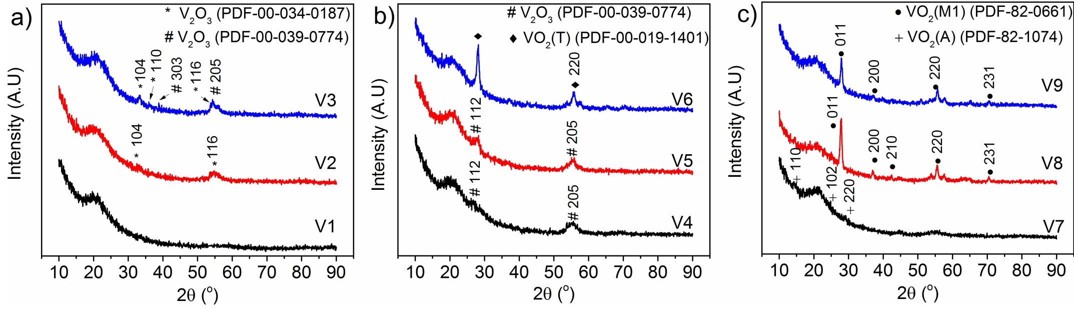

Figure 3.3: XRD spectra of films grown on SiO_2 substrates. The spectra show the dependence on process parameters, separated into films grown at like gas pressures. a) at 0.1 mTorr, V1 shows no evidence of crystallinity, while V2 and V3 show the appearance of small peaks associated with V_2O_3; b) at 2 mTorr V4 and V5 show more pronounced peaks attributed again to V_2O_3, however, V6 shows the formation of the rarely studied VO_2 triclinic phase; c) V7 shows small peaks characteristic of the VO_2 A-phase, and V8 and V9 both show intense XRD peaks with small FWHM values, indicating that VO_2 M1 has formed.

the resultant films deposited at the lowest pressure were deficient in oxygen as well. The absence of VO_2 peaks in all three of V1, V2, and V3 indicate a very strong reliance on the gas pressure for the VO_2 phase formation.

As shown in Figure 3.3(b), by increasing the oxygen pressure within the chamber, more distinct peaks appear in the XRD profiles. V4 and V5 have similar trends to those observed previously in Figure 3.3(a), however, the spectrum for sample V6 indicated the presence of triclinic VO_2. The triclinic phase has not been thoroughly studied due to its narrow stability range [5]; however we were able to reproducibly deposit this phase consistently with the aforementioned conditions. Diffraction peaks in the V6 sample were found at 2θ angles of $\sim$ 28.3, 39.9 and 55.8 deg which differ from the peaks found in the previously discussed samples. Figure 3.3(c) shows the XRD profiles of films deposited at V7, V8, and V9 conditions. Sample V8 shows a very strong VO_2 (M1) peak at a 2θ angle of $\sim$ 27.9 deg, in addition to peaks at $\sim$ 53.2, 55.7, and 57.7 deg, which show excellent correlation to the desired phase. Weaker peaks are present in the expected locations of 2θ angles $\sim$ 37.1,

39.8, and 42.3 deg. Sample V9 showed similar peak location to those that appeared in V8, but with significantly less intensity. Peaks corresponding to the M1 phase of VO_2 appeared in the V9 sample at 2θ angles of ~ 27.9, 55.7, and 57.7 deg, albeit with a shorter and broader appearance. Sample V7 showed peaks that were characteristic to a metastable tetragonal polymorph of VO_2 (A).

XRD analysis confirms the presence of VO_2 in 4 of the 9 samples, however, of these 4 only 2 of them were present with correct crystal structure. Samples V8 and V9 were present as VO_2 (M1) which is well known to undergo a MIT, whereas sample V7 was present in tetragonal form as VO_2 (A), which does not undergo this transition [77]. Sample V6, present as triclinic VO_2, also showed a MIT, however, in this case, the transition was more gradual and of a much lower magnitude when compared with sample V8.

3.4.2 Microstructure analysis

Figure 3.4 shows the SEM micrographs of the samples deposited under different conditions. It is apparent from Figure 3.4 that the microstructure relies heavily on the process parameters as they display a variety of different structures. Upon initial inspection, the films appeared amorphous and lacking in features as shown in V1, but with increasing magnification a very fine microstructure became apparent for all the deposited films. Considering the amorphous nature of the SiO_2 substrate, polycrystalline or amorphous films were expected for all deposition conditions, and the micrographs in Figure 3.4 only confirm the results from XRD. Most notably is the difference in grain size of samples V6 and V9 as compared to the remaining samples. The only commonality between the two deposition conditions was the substrate temperature. Samples V6 and V9 were deposited at the highest temperature, which can account for the grain growth observed. Evidence of grain growth is shown in sample V3, the other sample grown at 700 °C, which was also

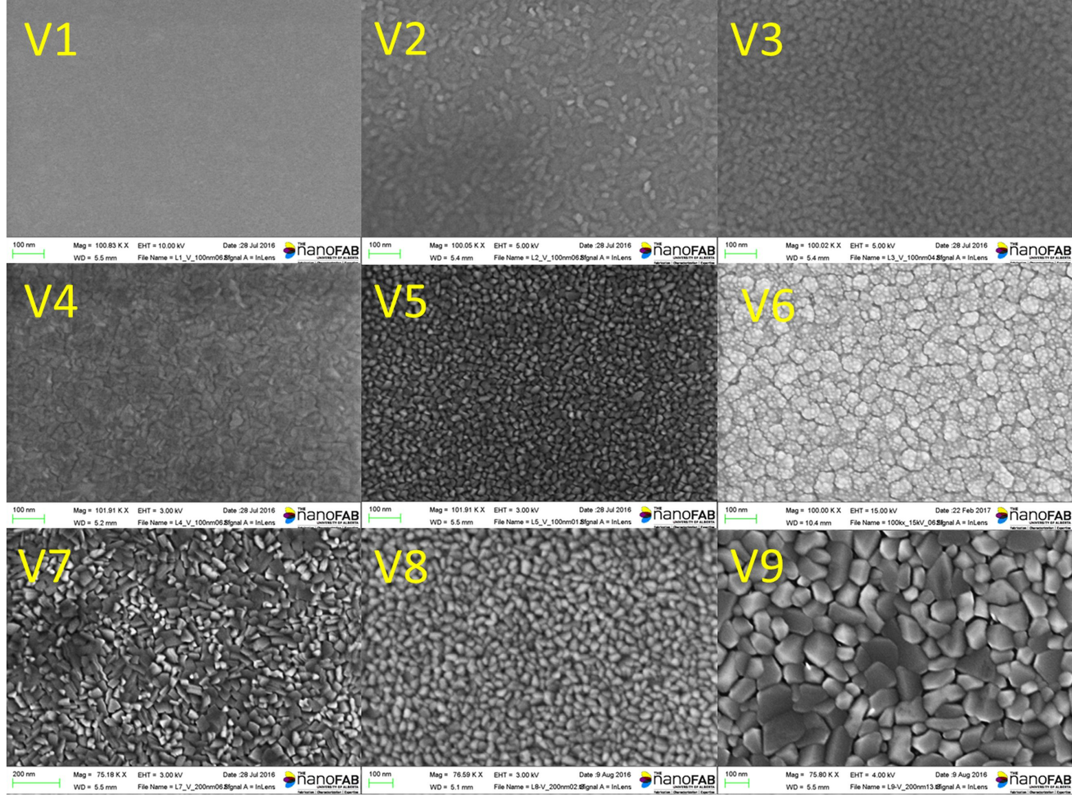

Figure 3.4: SEM micrographs of all nine films deposited via PLD. The micrographs are arranged to show constant pressure by row and constant temperature by column (with pressure increasing top to bottom and temperature increasing to the right) and it is apparent that an increase in both temperature and pressure results in much larger grain size.

shown previously by the decreased full width-half maximum (FWHM) of the corresponding XRD peaks. Compared to V6 and V9, sample V3 appears to have much smaller grains, which are similar in size to V1 and V2, however, when the response is isolated from the other variables, there is a definite trend relating grain growth and temperature (supplementary Figure 3.8). Samples deposited at lower temperatures do not display the same degree of grain growth, which can be attributed to a lack of thermal energy. The driving force behind grain growth is temperature, and is typically governed by an Arrhenius-type equation of the form [19];

$$d^2 - {d_0}^2 = k_0 t e^{-Q/RT} \tag{3.6}$$

where T is the temperature, Q is the activation energy, t is the time, d and d_0 are final and initial grain size respectively, and k_0 is a constant specific to the material. Substrates held at higher temperatures will experience a larger degree of grain growth/coarsening due to a greater amount of surface diffusion of adatoms, of which is also governed by an Arrhenius equation. The micrographs presented in Figure 3.4 and the grain size measurements (Supplementary Table 3.5), along with the Taguchi response (Figure 3.8), confirm this type of behaviour as the grain size increases with temperature in each instance. Additionally, from Supplementary Figure 3.8, oxygen gas pressure was shown to influence grain size in a similar manner as temperature.

There are, however, several other parameters that can influence the resultant microstructure and they are; the laser fluence, the energy of the laser pulse at the target, and the properties of the background gas. Since the gas was oxygen for all depositions, we shall only consider the conditions of the laser energy. Both laser energy and temperature govern the film growth method. Deposition rates can be controlled by the laser energy, the temperature of the substrate, the background gas, the target-substrate distance and the pulse frequency [84], which was maintained at 10 Hz for all experiments presented here. Very large deposition rates are achievable by PLD due to the short pulse duration (tens to hundreds of µs) and the high deposition rate 0.1-1 Å/pulse leading to deposition rates reaching the µm/s range. High deposition rates lead to a high degree of supersaturation on the substrate, which leads to a higher number of nucleation sites on the substrate surface [84]. However, upon examination of the microstructures in Figure 3.4 it is not apparent what, if any, the effect laser fluence has on the resultant film. This ambiguity may be due to the codependence of microstructure on both temperature and laser fluence. While the higher laser fluence will provide more nucleation sites, the higher temperature will drive grain growth in a method that may be described as normal or continuous [17]. Strong evidence

for this is presented between V7 and V8. If temperature was the only factor in determining grain size, V7 should have a smaller grain size than V8 as temperature is lower in the former. However, from Figure 3.4, it is evident that the grains in V7 appear larger, and therefore another factor is influencing the structure. Sample V8 was deposited with the highest laser energy, and therefore a larger supersaturation level than V7, resulting in more nucleation sites and a smaller overall grain size. The significant increase in grain size seen between V8 and V9 may be attributed to both the increase in temperature and the decrease in laser fluence.

3.4.3 Surface roughness analysis by AFM

Surface roughness measurements by AFM provide further insight into how the deposition parameters affect the resultant film. Surface roughness plays a crucial role in both the optical and electrical behaviour of the film, so being able to control this is important [102, 103]. The surface roughness values were found to be directly proportional to both temperature and oxygen pressure values (Supplementary Figure 3.10). By increasing the gas pressure at constant temperature, or increasing both simultaneously, the surface roughness also increases (Supplementary Table 3.5). For the topographical AFM images refer to supplementary material (Figure 3.10). There is no apparent trend observed for the other two parameters studied here, i.e. the laser energy and the target-substrate distance. The surface roughness appears to be related to the degree of grain growth/crystallinity observed in the samples. Samples V1, V2, V4, and V5, which are weakly crystalline/amorphous and possess grains smaller relative to the other samples show the lowest roughness values, while samples with more intense and smaller FWHM XRD peaks and larger grain size, such as samples V6, V8, and V9, show larger roughness values. Samples V3 and V7 produced intermediate roughness values as a direct result of their deposition parameters. Sample V3 was deposited at low pressure,

which favors a smooth film, but at a high temperature, which favors a rough film, while sample V7 was deposited at a high pressure and low temperature, favoring rough and smooth films respectively (Supplementary Figure 3.10). From the SEM images in Figure 3.4 it would appear that normal grain growth is taking place as a uniform size is observed for each individual micrograph. The driving force behind normal grain growth is both time and temperature, and considering each sample was deposited in the same period of time, the only variable able to affect the grain structure is temperature. Grain growth occurs as a means to reduce the total energy of the structure, as grain boundaries are high energy areas [17]. By reducing the total area of grain boundaries, the total energy of the system is also reduced. As previously mentioned, grain growth is controlled by an Arrhenius equation, where the rate is proportional to temperature. As the grains grow on the surface, they form a three-dimensional network of grains in a sort of peak and valley configuration. Given this growth mechanism it is obvious that the samples that experienced a higher degree of grain growth were the same films that demonstrated high surface roughness. Thickness values were also determined via AFM across a step edge in the deposited films, of which the thickness was found via Taguchi analysis to depend strongly on the laser energy (Supplementary Table 3.5 and Figure 3.11).

3.4.4 Electrical Characterization

After the deposition of vanadium oxide, Ti/Au (20 nm/80 nm) contact pads were deposited via magnetron sputtering in order to carry out electrical resistance measurements, to investigate the nature of the metal-insulator transition. The relative resistance change as a function of temperature for samples V6, V7, V8, and V9 are displayed in Figure 3.5 providing further insight to the quality of the films deposited. As expected, three samples showed evidence of a MIT with the lone exception being V7; however, the

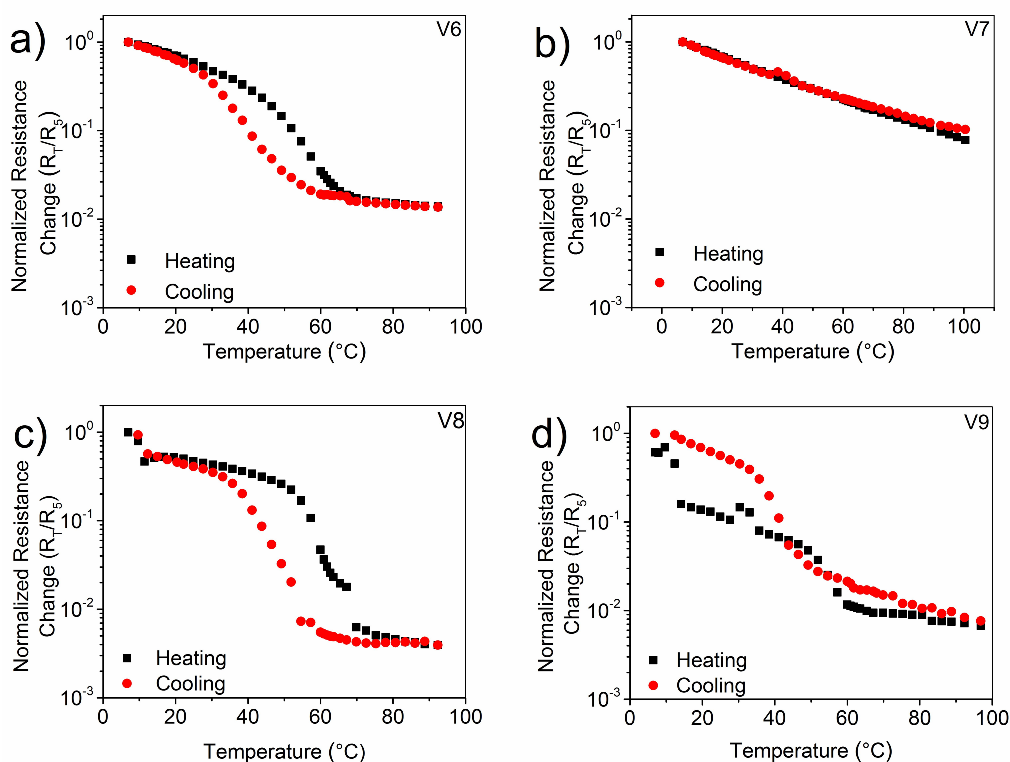

Figure 3.5: Temperature dependant resistance measurements for films (a) V6, (b) V7, (c) V8 and (d) V9. Resistance was monitored as a function of temperature and normalized to compare the magnitude of the change in resistance. The sharpest and highest magnitude transition was observed in sample V8, which was determined to be the optimal film. The MIT in sample V6 was of reasonable magnitude with excellent recovery, however the transition was very gradual. Sample V9 showed a small transition, however with poor reversibility. Sample V7 showed no transition as expected.

magnitude was most pronounced in sample V8. The lack of transition in V7 was predicted considering this particular sample was identified as the A polymorph, which is known not to display an MIT like the other polymorphs, (T) and (M1), produced in this work. Upon the increase in temperature, sample V8 shows a sharp transition from the insulating phase to metallic phase, demonstrated by a resistance drop of nearly three orders of magnitude, however quite a large hysteresis width is observed, as compared to VO_2 grown epitaxially [89]. Hysteresis width is related to the crystalline nature of

the film, with epitaxial single crystal films showing a narrower width, while polycrystalline films such as these display quite a wide hysteresis width [104]. However, we expect to see such character in the MIT of these samples as the films were deposited on an amorphous substrate, SiO_2, which does not translate into an ideal surface for single crystal growth. Resistivity values were calculated from the sheet resistance determined by investigating the I-V characteristics of each film using a collinear four point probe technique (Supplementary Table 3.5). Samples V6, V7, V8, and V9 all experienced a change in resistivity that was similar in magnitude to the change in resistance of the respective film observed during the temperature vs. resistance probing. The importance of these measurements was to confirm, via the presence of the MIT, that proper VO_2 phase growth had occurred and to observe the effect of the process parameters on both the magnitude and hysteresis width of the MIT.

3.4.5 Taguchi analysis of process variables

To deconvolute the results in order to determine the individual effect of each process variable, a numerical value was assigned based upon the desirability of the outcome. The validity of the Taguchi Method hinges upon an accurate portrayal of the results in the analysis step. In some cases, the ranking system is highly subjective and the analysis results can be significantly skewed if proper care is not taken. For the sake of this Taguchi analysis, three so-called responses were analyzed; phase formed, film crystallinity, and surface roughness. The phase of vanadium oxide formed is most important, with the highest value of 10 being assigned to the films that demonstrated VO_2 (M1) phase formation, and 1 point being deducted for each deviation away from the desired result. Purely amorphous films were given the lowest value of 1 considering it was too difficult to accurately determine the phase formed. The samples that lay between the two extremes in phase formation were

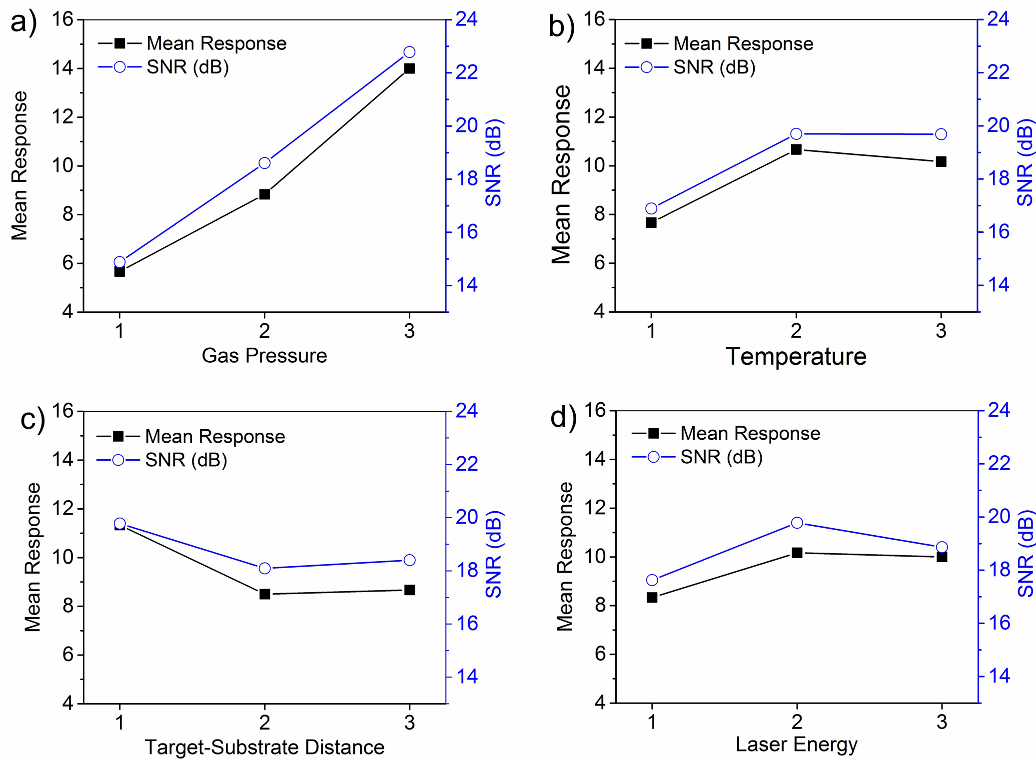

Figure 3.6: Mean response and signal-to-noise ratio for each level of the process parameters: (a) gas pressure, (b) temperature, (c) target-substrate distance and (d) laser energy. In the case of both mean response and SNR, a larger value indicates a more desirable result.

ranked based on the deviation from the target M1 phase. Crystallinity was approached in a similar manner to phase formation, and values were assigned by considering the XRD peak FWHM and the SEM micrographs. Films that had no crystalline appearance were given a 1 and those that displayed a high intensity, small FWHM XRD peaks and visible evidence of grain structure in SEM were assigned a 5. It is the values in between these two that the analysis become significantly more subjective and careful valuation is critical for the success of the design. The final response, surface roughness, was much easier to analyze considering it is a quantitative technique were subjectivity in valuation is drastically reduced. Here there is a 3-point scale used; for roughness values exceeding 5 nm, a 1 is assigned, for values between 1-5 nm,

a 2 is assigned, and for values less than 1 nm, a 3 is assigned. A total response is calculated by the summation of the three responses (i.e. phase, crystallinity, and surface roughness), which is then used in the Taguchi analysis (a detailed breakdown of the response can be found in Supplementary Table 3.6).

The outcome of the Taguchi analysis is shown in Figure 3.6 which shows the mean response of each control variable with respect to its individual levels. In this case, the larger response value indicates a more desirable outcome at that level. Perhaps most apparent from the outcome of the analysis is the strong dependence on gas pressure and minimal to no dependence on the laser energy. The first is intuitive as we observed that M1 VO_2 did not form at low or moderate oxygen pressures, rather it only formed at the highest assigned level. Additionally, VO_2 T phase formed at moderate gas pressure, but only when the combination of the other factors was favorable. The lack of dependence on laser energy was somewhat surprising as laser energy plays a large role in the plasma dynamics as well as the energy of adatoms (and therefore supersaturation), however this effect may be overwhelmed by the effect of substrate temperature [84]. The plateau in the temperature graph indicates minimal temperature dependence past 600 °C. Target distance played an important role in the final response as only one of the three levels produced the desired response of VO_2 (M1). Due to the high number of stable and metastable phases in vanadium oxide, these observations strongly support that the crystallinity of desired VO_2 films depend strongly upon the oxygen pressure to control the stoichiometry of the film, as well as the substrate temperature in order to control the degree of crystallinity.

Analysis of variance (ANOVA) was used to assess the significance and contribution percentage of each control factor on the target response [4]. Table 3.3 shows the ANOVA results for each parameter studied in the growth VO_2 thin films on SiO_2 substrates. The ANOVA indicates that all four parameters are statistically significant within a 95 % confidence interval. However,

Table 3.3: ANOVA results based on the results tabulated from XRD, SEM, and AFM analysis.

Factor	Sum of Squares	Degree of Freedom	Variance	F-Ratio	Percent Contribution
A	280.11	2	106.17	382.20	73.60
B	19.11	2	15.50	55.80	10.75
C	18.11	2	15.17	54.60	10.51
D	5.44	2	6.17	22.20	4.27
Error	3.00	9	0.28	-	-

it is also evident that the contribution from each parameter is not equivalent. Gas pressure contributes the most, at 73.60 %, as expected after analysis of the results, while laser energy contributes the least, at 4.27 %, which was also expected. The remaining two variables, substrate temperature (10.75 %) and the target-substrate distance (10.51 %), provided relatively equal contributions.

3.4.6 Confirmation of Taguchi method

Confirmation of the optimized process parameters was carried out to confirm the dependence (or lack thereof) on certain process parameters. Tests to confirm the strong dependence on the gas pressure and the minimal dependence on laser energy were conducted to validate the design. The parameters for each confirmation experiment are summarized in Table 3.4. Confirmation experiment C1 was used to verify laser energy contributes very minimally to the overall response by using optimal values for parameters A, B, and C, while using the least optimal level of laser energy. Similarly, the enormous dependence on gas pressure was tested in confirmation experiment C2 by maintaining parameters B, C, and D at their optimal values and reducing the pressure to the least optimal value.

Another confirmation test was performed to verify and improve upon the production of the A phase that was apparent in V7. Indicated as C3 in

Table 3.4: Confirmation experiments of the Taguchi analysis. One factor in each experiment has been varied from the optimized condition to confirm the response predicted by the analysis.

Experiment	Deposition Factors				Predicted Response	Actual Response
	A	B	C	D		
C1	3	2	1	1	16.2	16
C2	1	2	1	3	8.2	7
C3	3	1	1	3	15.2	15

Table 3.4, this confirmation manipulated the deposition temperature, while maintaining the remaining factors at the optimized values for VO_2 (M1). The response aligned nicely with the predicted response, as well as confirming a far more crystalline production of A phase VO_2, as shown by the XRD (Figure 3.12).

The response value for both of these experiments, shown in Table 3.4, correspond with the expected values as predicted by the Taguchi analysis. The predicted response values were in excellent agreement with the experimental response values, which were based on the results from XRD, SEM, and AFM measurements.

3.5 Conclusion

The synergistic effect of four process parameters of pulsed laser deposition of vanadium oxide thin films onto amorphous thermally oxidized SiO_2 substrates was systematically investigated using Taguchi robust design of experiment. The target film, VO_2, was successfully grown on three of the substrates, each at 50 mTorr of oxygen. Each film was deposited at the same frequency (10 Hz) and for the same duration (15 minutes). From the Taguchi analysis, the ideal film of VO_2 (M1) was produced using a substrate temperature of 873 K (600 °C), a laser fluence of 2.6 J/cm^2, a target-to-substrate distance of 31 mm, and an oxygen pressure of 50 mTorr. Film V8 showed the greatest

magnitude in the metal-insulator transition, indicating a higher quality film. ANOVA was conducted on the response values, and it was determined that, although all variables were determined to be significant, the oxygen pressure influences the outcome the greatest (> 73 %), and the laser energy the least (< 5 %). This analysis was investigated further to ensure accuracy by running confirmation experiments on the effect of gas pressure and laser energy with excellent agreement in the outcome to the predicted values. This work provides valuable guidelines in optimization of the deposition of VO_2 by PLD. Furthermore, the outcomes of this works present useful information to establish a robust recipe for adjusting the PLD parameters to produce not only the M1 phase of VO_2, but the A and T phases as well.

3.6 Supplementary data

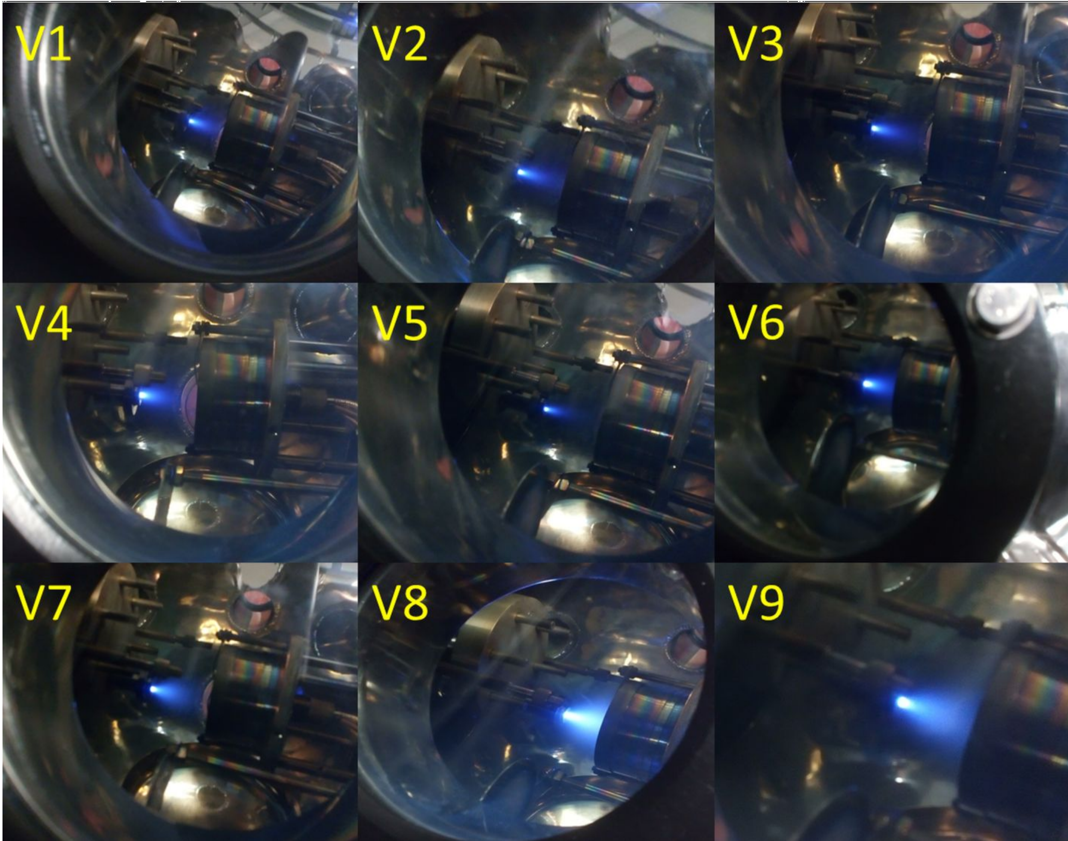

Figure 3.7: Optical images of the plasma plumes at variable deposition parameters.

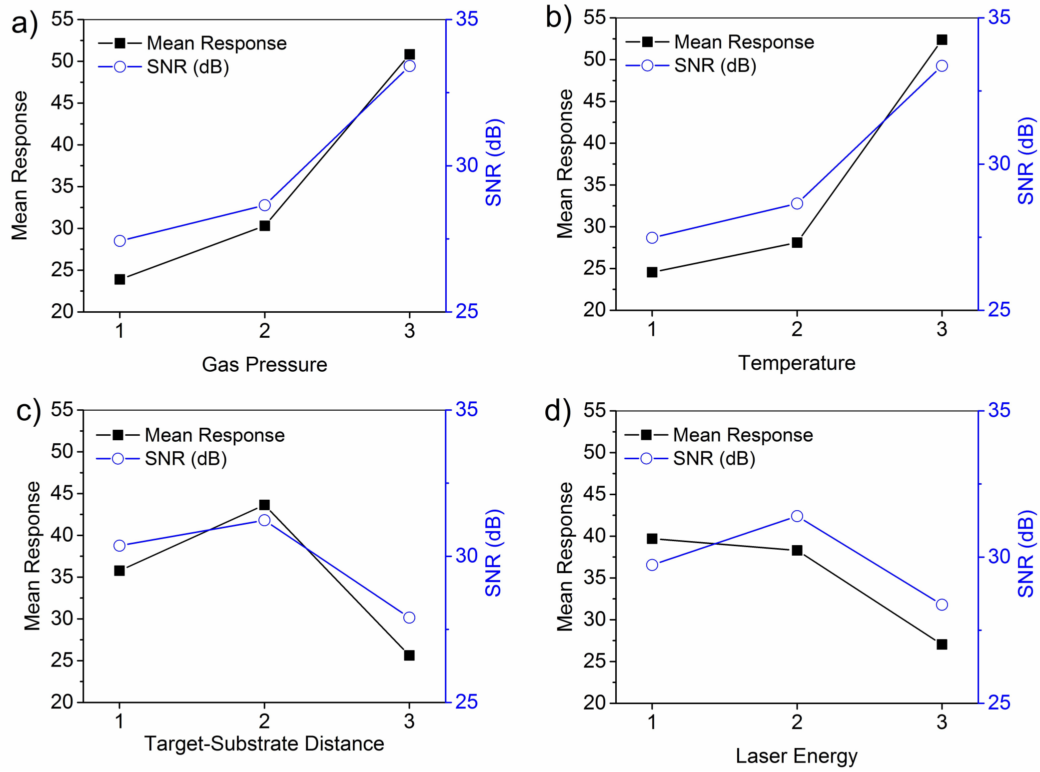

Figure 3.8: Mean response and signal to noise ratio of the average grain size to each of the four process parameters: (a) gas pressure, (b) temperature, (c) target-substrate distance and (d) laser energy. A strong dependence on both the gas pressure and temperature is observed.

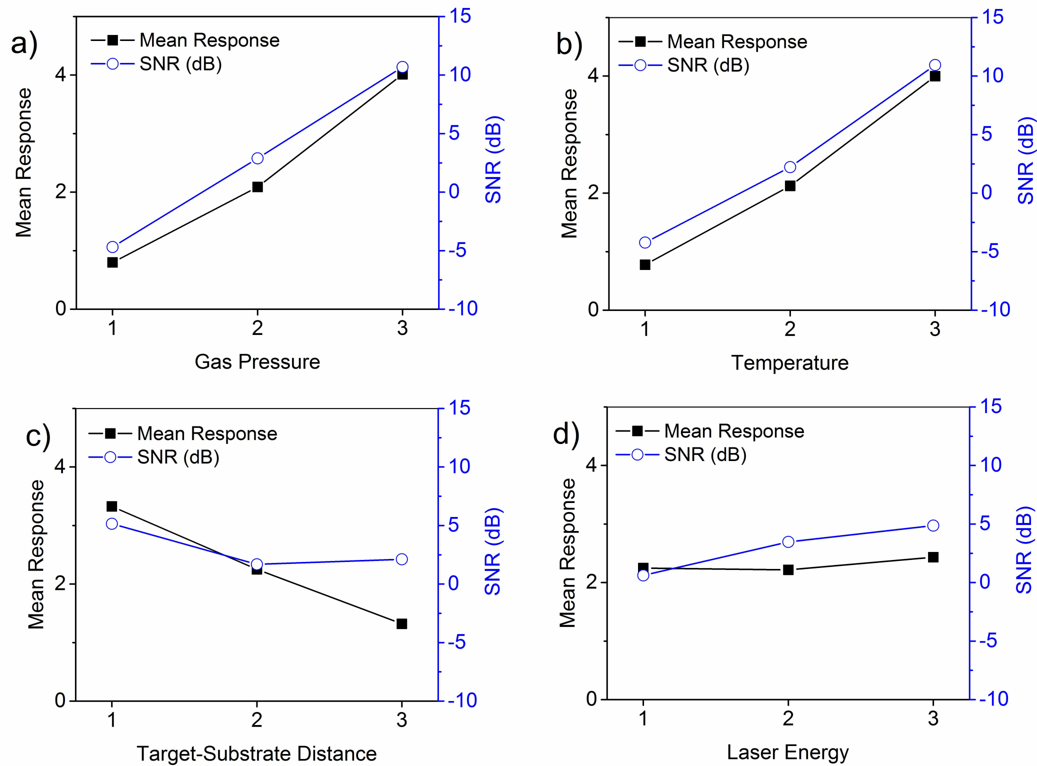

Figure 3.9: Mean response and signal to noise ratio of the surface roughness as measured by AFM to each of the four process parameters: (a) gas pressure, (b) temperature, (c) target-substrate distance and (d) laser energy. A strong dependence on both the gas pressure and temperature is observed, with minimal influence from both target-substrate distance and laser energy.

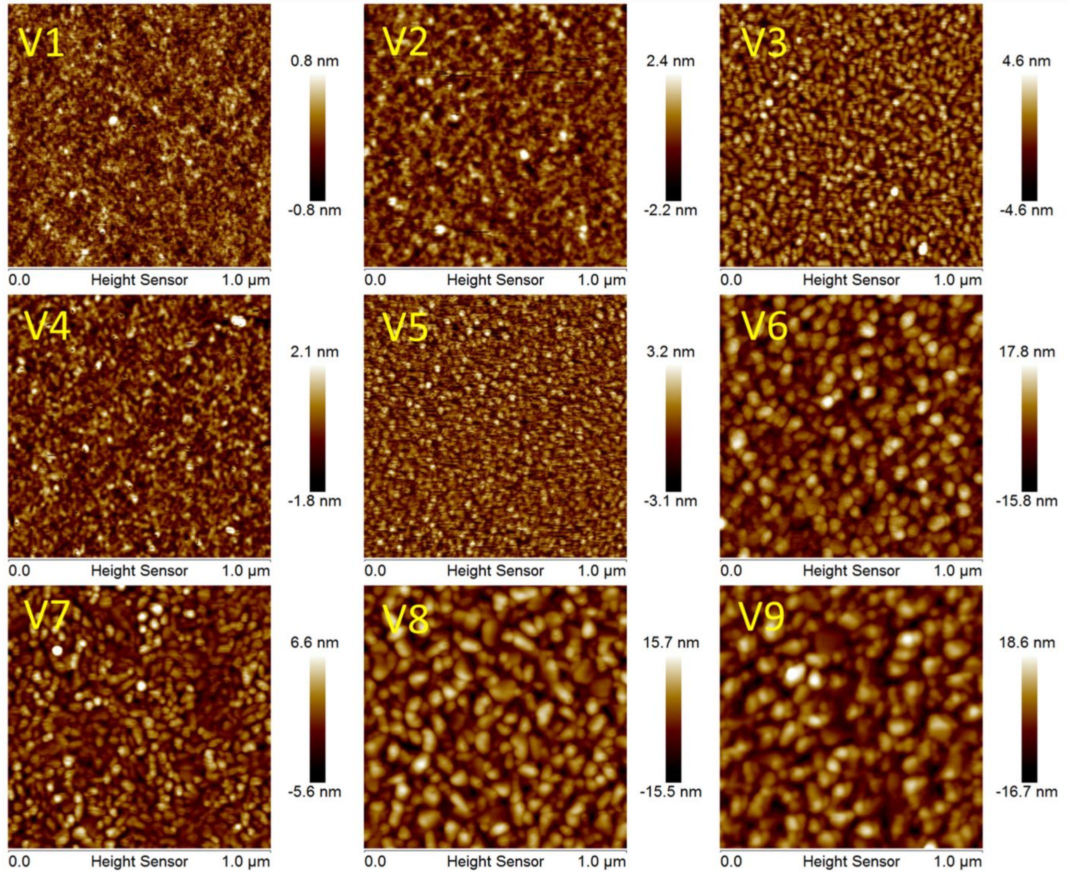

Figure 3.10: AFM topography of the samples deposited at the nine different conditions. The images are arranged to show constant pressure by row and constant temperature by column (with pressure increasing top to bottom and temperature increasing to the right). From this figure we can see that the roughness is directly proportional to both the temperature and the gas pressure.

Table 3.5: Surface roughness (nm) measured over a 1 μm^2 area, film thickness (nm) measured at a step edge in the film, grain size (nm) measured by ImageJ image analysis, and resistivity (Ω·cm) as measured by collinear four point probe technique.

Experiment	Surface roughness	Film thickness	Grain size	Resistivity (20 °C)	Resistivity (100 °C)
V1	0.25	7.83	18.86	6.30×10^{-4}	5.61×10^{-4}
V2	0.49	17.18	28.90	3.38×10^{-3}	2.39×10^{-3}
V3	1.65	13.91	23.91	2.61×10^{-2}	1.13×10^{-2}
V4	0.65	26.51	20.51	9.28×10^{-4}	7.26×10^{-4}
V5	0.88	2.79	18.71	33.9	1.33
V6	4.73	19.50	51.72	2.69×10^{-2}	9.28×10^{-4}
V7	1.43	6.18	34.27	4.62	0.75
V8	5.00	21.91	36.70	1.85	3.05×10^{-3}
V9	5.61	18.61	81.52	2.35	2.37×10^{-2}

Table 3.6: Individual response ranking for all nine films for both sets of deposited films.

Experiment	Deposition Factor				Response					
	A	B	C	D	Phase		Crystallinity		Surface Roughness	
					R1	R2	R1	R2	R1	R2
V1	1	1	1	1	1	1	1	1	3	2
V2	1	2	2	2	2	2	2	2	3	2
V3	1	3	3	3	2	2	2	2	2	2
V4	2	1	2	3	2	2	1	2	3	3
V5	2	2	3	1	2	2	3	3	3	3
V6	2	3	1	2	7	7	4	3	1	2
V7	3	1	3	2	8	8	2	2	2	2
V8	3	2	1	3	10	10	5	5	2	3
V9	3	3	2	1	8	9	3	3	1	1

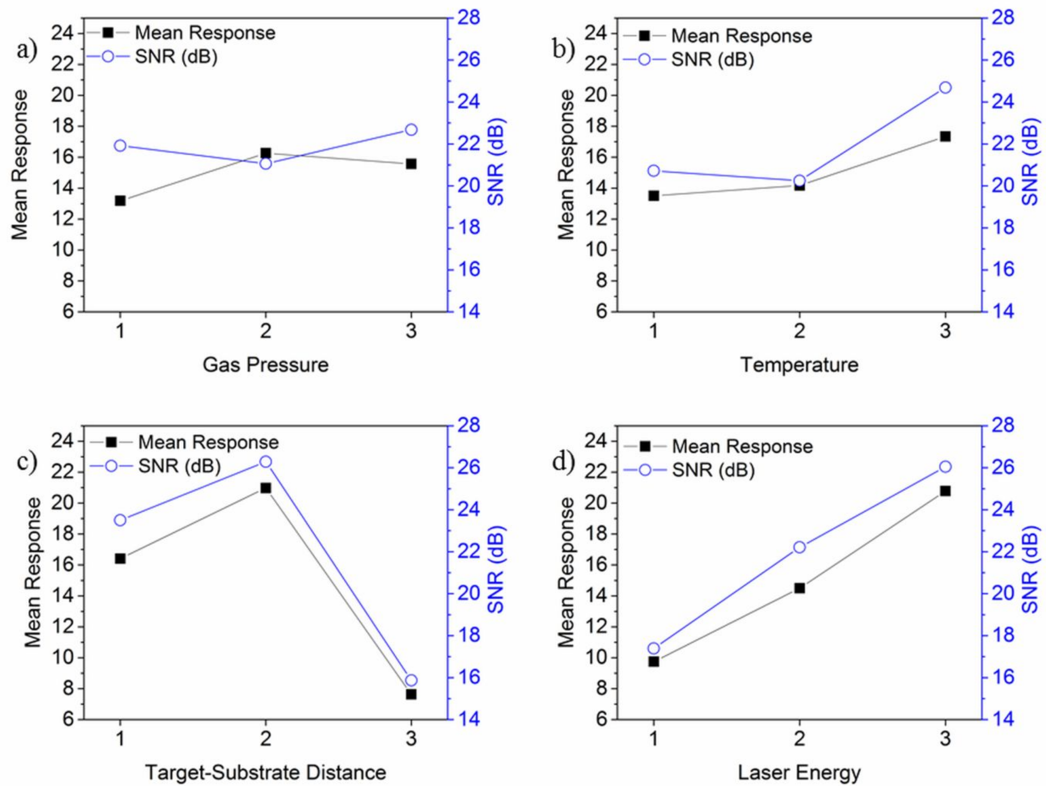

Figure 3.11: Mean response and signal to noise ratio of the thickness to each of the four process parameters: (a) gas pressure, (b) temperature, (c) target-substrate distance and (d) laser energy. Here we see a strong dependence on the laser energy as well as target-substrate distance.

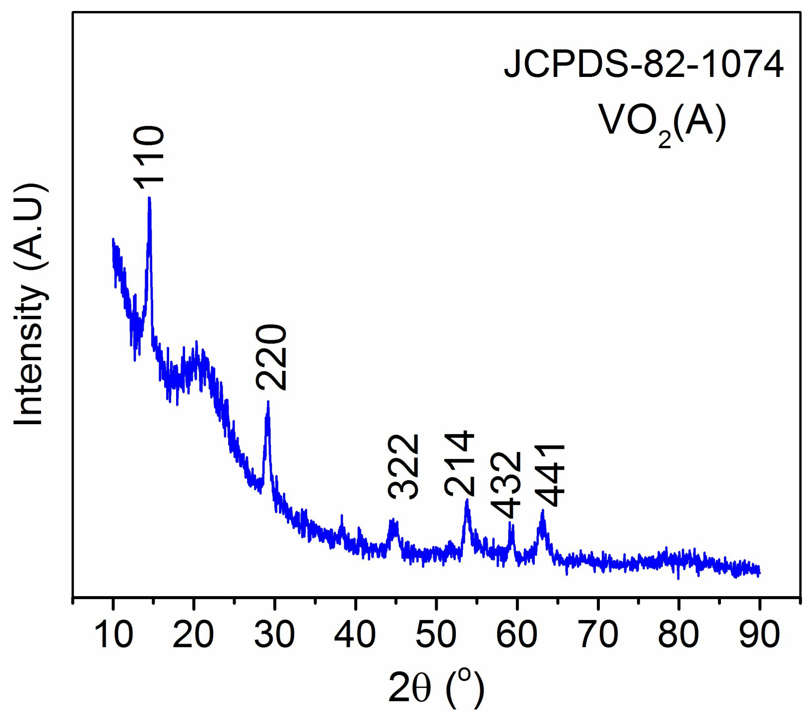

Figure 3.12: XRD spectrum of confirmation experiment C3 to verify the production of VO2 (A) phase. Strong peaks at 2θ values of 14.7 and 29.5 deg, along with smaller peaks at 45.2, 53.8, and 63.1 deg confirm A phase formation.

Chapter 4

Enhancement of the sharpness and intensity of the metal-insulator transition in ultrathin VO_2 films by interfacial structure manipulation

4.1 Abstract

Vanadium dioxide (VO_2) undergoes a structural transformation from monoclinic (insulator) to tetragonal (metallic) upon heating above 340 K, accompanied by abrupt changes to its electronic and optical properties. Not only is this transition scientifically intriguing, but there are numerous applications in sensing, memory, and optoelectronics. Here we investigate the effect different substrates have on the characteristics metal-insulator transition (MIT), and how the properties can be tuned for specific applications. VO_2 thin films were grown on c-plane sapphire (0001) and p-type silicon $\langle 100 \rangle$ by pulsed laser deposition. High resolution X-ray diffraction along with transmission electron microscopy reveals textured epitaxial growth on sapphire, while the presence of a native oxide layer on silicon prevented any preferential

growth resulting in a polycrystalline film. An orientation relationship of $\langle 001\rangle(010)_{VO_2}||\langle 1\bar{1}00\rangle(0001)_{Al_2O_3}$ was established for VO_2 grown on sapphire, while no such relationship was found for VO_2 grown on silicon. Surface energy minimization is the driving force behind grain growth, as the lowest energy VO_2 plane grew on silicon, while on sapphire the desire for epitaxial growth was dominant. Polycrystallinity of films grown on silicon caused a weaker and less prominent MIT than observed on sapphire, whose MIT was higher in magnitude and slope. The position of the MIT was shown to depend on the competing effects of misfit strain and grain growth. Higher deposition temperatures caused an increase in the MIT, while compressive strain resulted in a decreased MIT.

4.2 Introduction

A discussion on the paper "Semi-conductors with partially and with completely filled $_3d$-lattice bands", authored by de Boer and Verwey, sparked significant interest in transition metal oxides [105]. Conventional band theory at the time predicted NiO and other transition metal oxides to behave as conductors; however this is not the case. Proposed by Mott and Peierls in their discussion of de Boer and Verwey's paper, and theoretically described by Hubbard, this behaviour can be attributed to strongly correlated d-orbital electrons [106, 107]. Though described by Ashcroft and Mermin as a "highly oversimplified model" [51], the Hubbard model has been used to understand several anomalous behaviours including the metal-insulator transition, antiferromagnetism, and superconductivity [108]. The metal-insulator transition (MIT) in transition metal oxides is driven by the electron correlation effects previously mentioned and is manifested by an incredible change in resistance, on the order of five to ten orders of magnitude [20, 25]. This transition is observed in vanadium dioxide (VO_2) at a near room temperature of T_c = 340

K for the bulk material.

VO_2 undergoes what is described as a first order phase transition at T_c from a monoclinic (M1) insulating phase (space group $P2_1/c$) below T_c to a rutile (R) metallic phase (space group $P4_2/mnm$) above T_c [20, 61, 109]. The transition causes a dimerization of alternating V atoms resulting in two different V-V bond lengths and tilting of these dimers with respect to the c-axis. The low temperature phase shows an indirect bandgap of 0.6 eV and a large negative temperature coefficient of resistance (TCR) [27, 35]. Upon heating past T_c, there is a remarkable increase in conductivity as the lattice transforms into the metallic phase.

These unique properties have resulted in the application of VO_2 thin films towards uncooled microbolometers [65, 110], non-volatile memory [62, 111], thermal, optical and electronic switching [33, 112, 113], smart windows [29, 30, 114], memristors [34], gas sensors [66], and strain sensors [67]. Although VO_2 has shown promising properties for such a wide range of applications, the deposition of pure phase VO_2 thin films is difficult due to a narrow thermodynamic stability range and a large number of stable and metalstable oxide phases such as VO, V_2O_3, V_2O_5, V_nO_{2n-1}, and V_nO_{2n+1} [36]. The characteristics of the MIT have been shown to depend on grain size, interfacial strain, and film thickness which are strongly influenced by temperature and substrate choice [60, 89, 115–121].

Pulsed laser deposition (PLD) offers an excellent opportunity to study the MIT of VO_2 due to its ability to stoichiometrically transfer target material directly to the substrate. The magnitude of both the hysteresis width and resistance change of the temperature-driven MIT of VO_2 thin films , as well as a shift in the transition temperature, can vary drastically between films deposited on different substrates, or under different conditions [60, 117, 120]. By controlling the microstructural properties of the deposited film, the nature of the MIT can be controllably engineered for the desired application. However,

in order to exploit the remarkable optical and electronic versatility of VO_2, a strong understanding of the film-substrate interface is crucial for a seamless integration into existing micro- and nanofabrication processes. Unfortunately, there has been little work carried out investigating the effect substrate choice and temperature has on the quality of both the crystal structure and MIT of PLD produced VO_2 thin films.

Recently, Marvel et al. have reported VO_2 deposition on Si, sapphire, and glass by PLD, sputtering, and electron beam (e-beam) evaporation, however, the samples did not exhibit any phase transformation without post annealing [60]. However, there was not a significant difference in the MIT temperature or hysteresis characteristics with annealing times less than 90 minutes. Lee et al. have reported on the fabrication of several VO_2 polymorphs on several different perovskite substrates, but with little emphasis on the growth condition [77]. Yang et al. have reported on the growth of textured VO_2 thin films on heavily doped n^+-Ge (100) and n^+-Si (100) using RF sputtering, however, the reported MIT was underwhelming, and little was done to elucidate strain effect on the MIT [56].

Here we present an investigation into how the choice of substrate and deposition temperature affects the growth behaviour and MIT of VO_2 thin films deposited by PLD without post annealing. We have investigated how the choice of substrate impacts the texture of the film, phase stability, and the characteristics of the MIT. Competing effects from growth temperature (resulting in grain coarsening) and lattice mismatch strain are investigated in regards to the influence on the MIT. Substrate choice imparts a significant impact towards the film growth mode, as factors such as crystal structure, wettability, and surface energy vary significantly between substrates [122]. Surface energy minimization is shown to be the major driving force behind film growth, as we investigate how interfacial strain impacts the growth mode. Cubic p-type Si $\langle 100 \rangle$ and trigonal c-plane sapphire (0001) were chosen as

model substrates for deposition of VO_2.

We show that interfacial strain, as a result of the temperature and substrate, significantly impacts the MIT temperature and characteristics. Epitaxial growth of VO_2 on sapphire substrates is achieved through a process called domain matching epitaxy, which is not observed on silicon. Through cross sectional transmission electron microscopy, we show that textured growth is inhibited on silicon due to a thin native oxide layer, which brings a disordered, amorphous barrier between VO_2 and crystalline silicon. This oxide layer has large ramifications on the growth mode, as the surface energy is significantly lower than pristine silicon, thereby enabling an island type growth mode as a means to reduce the overall energy. We have monitored the resistance of VO_2 films as a function of temperature in order to quantify the influence growth parameters have on the MIT. We show that we are able to control the growth of VO_2 thins films by selection of both the substrate and deposition temperatures, and as a result we are able to modulate the behaviour of the MIT.

4.3 Experimental

4.3.1 Materials synthesis

VO_2 films were deposited via PLD in an oxygen atmosphere (99.993% purity, Praxair) using a vanadium metal (99.9% purity, American Elements) circular disc target. A schematic of the setup can be seen in Figure 4.1. The target and the substrate are both contained inside a PLD chamber (Excel Instruments, Mumbai, India), with the substrate temperature maintained at one of four temperatures chosen for deposition. The distance between the target and substrate for all experiments was 31 mm. The oxygen pressure inside the chamber is maintained at 50 mTorr throughout the entire deposition. Laser

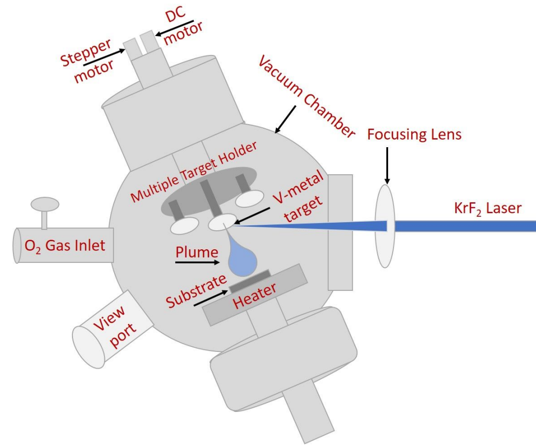

Figure 4.1: Schematic of PLD experimental setup, including the laser path and the PLD chamber.

pulses with a 20 ns pulse width from a krypton fluoride (KrF, λ=248 nm) excimer laser (Coherent, GmbH) were directed at the target with a repetition rate of 10 Hz. The laser has a spot size of 1 mm $\times$ 3 mm at the target and is maintained at a constant energy density of 2.6 J/cm^2. The deposition time was 15 minutes onto p-type silicon $\langle 100 \rangle$ and c-cut sapphire (0001) substrates. Deposition parameters were investigated and optimized in our previous work [117]. Prior to deposition the substrates were cleaned with piranha, followed by sonication in milli-Q water, ethanol rinsing, and drying with nitrogen. The chamber pressure was evacuated below 1×10^{-5} Torr before the introduction of oxygen. A total of eight films were produced (four for each substrate) and the deposition parameters for each are listed in Table 4.1. Our previous work proved temperature had a negligible effect on film thickness, and therefore thickness was considered constant (at 20 nm) for all depositions [117]. Electrical contacts of Ti/Au (20 nm/80 nm) were deposited onto the film via electron beam evaporation.

Table 4.1: Deposition conditions for each deposited film. The gas pressure (50 mTorr), target-substrate distance (31 mm), and laser fluence (2.6 J/cm^2) were consistent for all experiments

Sample ID	Substrate	Temperature (°C)	Phase Formed
V-SAP-400	c-Sapphire (0001)	400	VO_2 (M1)
V-SAP-500	c-Sapphire (0001)	500	VO_2 (A)
V-SAP-550	c-Sapphire (0001)	550	VO_2 (M1)
V-SAP-600	c-Sapphire (0001)	600	VO_2 (M1)
V-Si-400	p-Si ⟨100⟩	400	VO_2 (mixed)
V-Si-500	p-Si ⟨100⟩	500	VO_2 (A)
V-Si-550	p-Si ⟨100⟩	550	VO_2 (M1)
V-Si-600	p-Si ⟨100⟩	600	VO_2 (M1)

4.3.2 Characterization

X-ray Diffraction

Thin film samples were characterized by XRD (Rigaku XRD Ultima IV) operating under glancing angle mode with a 0.5 ° incident angle and conventional Bragg-Brentano geometries. Such a low incident angle was necessary to eliminate any background signal present from the substrate due to the ultra-thin nature of the films. 2θ scanning identified the peak locations, however, due to the close proximity of (020) and (002) peaks, off axis ϕ scanning was required to properly index the peaks.

Surface analysis by AFM

Dimension Fast Scan Atomic Force Microscope (Bruker Nanoscience division, Santa Barbara, CA, USA) was used to measure the surface topography of the films. Commercially available Pt-Ir coated conductive probes (SCM-PIT) with a spring constant of 2.5 N/m and a resonant frequency of 65 kHz were used for obtaining surface topography. The roughness of the samples were determined using nanoscope analysis software from Bruker.

Transmission Electron Microscopy

The film-substrate interface was investigated by transmission electron microscopy (TEM)(Titan, FEI, the Netherlands) operated at 300 kV. TEM foils of less than 100 nm thickness were prepared by Focused Ion Beam (FIB) machining (Hellios 600, FEI, The Netherlands), followed by lift off. Film thickness measurements and diffraction analyses were carried out to determine the crystallinity through selected area diffraction pattern (SAED) and Fast Fourier Transform (FFT) method using Digital Micrograph Software (Gatan Inc.).

Metal-Insulator Transition Measurement

Temperature dependant resistance measurements were performed using a Keithley 2450 source-measure unit (SMU) and the inbuilt Kickstart software in a two probe configuration. A Signatone 1160 series probe station with a heated chuck connected with the multimeter was used to determine the resistance of the deposited films they were heated from 5 to 110 °C with 2 °C steps and a 3 minute equilibration time for each step. Both heating and cooling cycles were monitored with the same intervals to probe the hysteretic properties of the MIT. Using a collinear four-point probe configuration on the 2450 SMU, I-V characteristics of the thin films were collected to determine resistivity.

4.4 Results and discussion

4.4.1 X-ray diffraction phase analysis

XRD of the VO_2 thin films revealed that highly textured growth is possible on sapphire (0001) substrates. Figure 4.2(a-b) illustrate the resultant X-ray spectra from 2θ scanning of VO_2 films grown at different temperatures on sapphire and silicon. VO_2 grown on sapphire (Fig. 2a) presented a unique case where

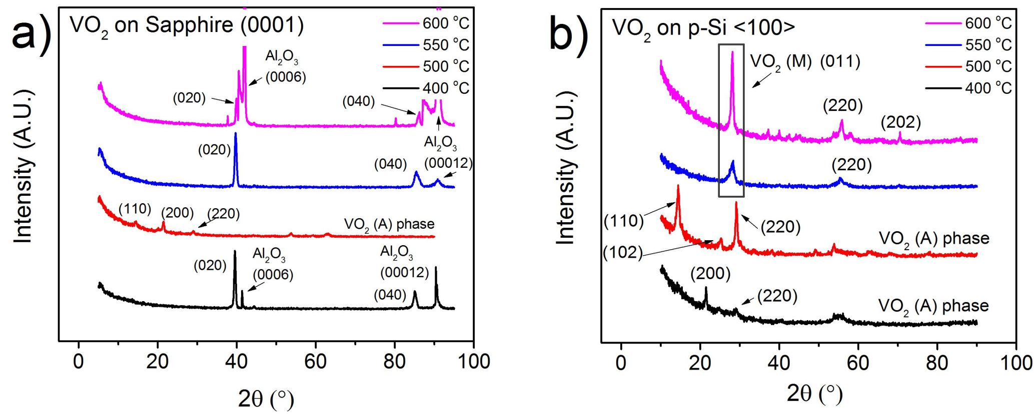

Figure 4.2: (a) XRD spectra of VO_2 films deposited on a) sapphire (0001) and (b) *p*-type Si ⟨100⟩ substrates. The films grown on sapphire showed a highly oriented structure with only the (020) and (004) peaks present, while on silicon a much more polycrystalline structure was observed.

highly textured films were observed for multiple growth temperatures, with one such film grown at 400 °C, which is far below the optimized growth conditions previously observed for VO_2 [117]. There is strong evidence for epitaxial growth of VO_2 films on sapphire at 400, 550, and 600 °C deposition temperatures, as the films show diffraction peaks from the (020) plane at 39.7 and 39.5 °and the (004) planes at 85.1 and 85.4 °, respectively. The peaks that appear at 41.35 and 90.4 ° correspond to the (006) and (0012) planes of the substrate, respectively. VO_2 deposited at 500 °C appeared as the (A) phase (JCPDS #82-1074), which is a metastable polymorph of VO_2.

The appearance of singular peaks for sapphire samples allude to a sort of epitaxial growth behaviour. However, at the deposition temperature, the tetragonal and hexagonal crystal systems do not offer an ideal match. The fourfold symmetry of VO_2 (R) does not align nicely with the sixfold symmetry seen in sapphire. Additionally, the c parameter of VO_2 (R) results in an absurdly high lattice mismatch with the sapphire a parameter. It has been proposed by Narayan that an additional type of epitaxial growth is possible, which is unlike lattice matching epitaxy (LME), and has been termed as do-

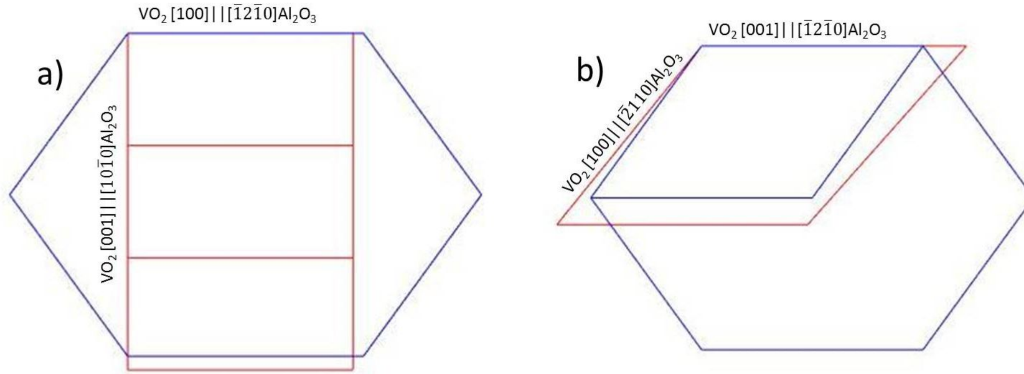

Figure 4.3: Schematic of the proposed DME of VO_2 (red) on sapphire (blue) at (a) deposition temperature where VO_2 is present as its tetragonal form and (b) room temperature where the monoclinic phase is present and the *c*- and *a*-axes have flipped

main matching epitaxy (DME) [123]. DME results when integer multiples of the epilayer matches with integer multiples of the substrate domains, observed in our $(020)_{VO_2}||(0001)_{Al_2O_3}$ system, shown schematically in Figure 4.3. What we have discovered is the (020) VO_2 plane domain matches the (0001) plane of sapphire if VO_2 is present as tetragonal and monoclinic (accounting for the switching of *a* and *c* axes). The difference between the two scenarios is just the ratio of VO_2:α-Al_2O_3 domains. During deposition VO_2 is present as rutile and the (020) plane is rectangular with side lengths of *c*=2.86 Å and *a*=4.55 Å, with the [001] and [100] directions of VO_2 aligned along the [$\bar{1}2\bar{1}0$] and [$10\bar{1}0$] directions of sapphire, respectively. At room temperature upon cooling, the orientation of the (020) plane has been tilted and the *a* and *c* axes have flipped, as per the nature of the transition. The (020) plane is now oriented on the substrate with the [001] and [100] directions of VO_2 aligned with the [$\bar{1}2\bar{1}0$] and [$\bar{2}110$] directions of sapphire, respectively. In the former case, the DME relationship is 3:1 VO_2:sapphire along the *c*-direction of VO_2, and a 1:1 ratio along the VO_2 *a*-direction, resulting is a mismatch of 4.3 % in both cases. For the latter case, for VO_2 to sapphire ratios of 7:8 and 4:5 along the VO_2 *c*- and *a* directions, respectively, lattice mismatch is reduced to

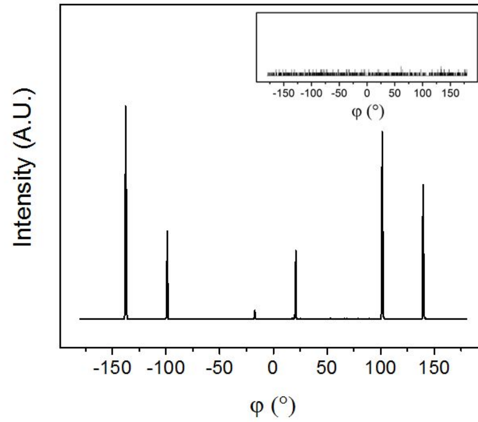

Figure 4.4: Off axis scanning of V-SAP-550 of the ($\bar{2}11$) reflection at 2θ = 36.972 ° with ψ angle of 57.635 ° between ($\bar{2}11$) and (020) reflection. Inset shows the absence of the ($\bar{2}11$) reflection at 2θ = 36.972 ° and ψ of 90.297 °, the angle between the ($\bar{2}11$) and (002) planes.

0.89 % and 3.1 %. Without the possibility of DME growth, epitaxial films in this system would be highly unlikely as the lattice mismatch is too great to overcome. DME enables psuedomorphic growth of high quality films, that would be otherwise impossible, by matching domains rather than individual lattice sites, thereby reducing mismatch [124].

The primary peaks of VO_2 located at 39.55, 39.7, and 39.9 for V-SAP-400, V-SAP-550, and V-SAP-600, respectively, were attributed to the (020) reflection, and not (002) which also appears at the 2θ value. This was solved by performing off axis ϕ scanning of the ($\bar{2}11$) reflection of VO_2 which has ϕ angles of 57.635 °and 90.297 °with the (020) and the (200) reflections, respectively. Figure 4.4 shows the resultant profile of the off axis scans, with the appearance of six peaks between the ($\bar{2}11$) and (020) system, and none between ($\bar{2}11$) and (002) (inset).

XRD spectra for VO_2 films grown on silicon substrates showed a more random orientation than those grown on sapphire, indicated by the presence of multiple diffraction peaks. At 400 °C, there are weak peaks that correspond to VO_2 (A), which is in stark contrast to the film grown on sapphire at 400

°C. Again, at 500 °C the deposition resulted in the (A) phase polymorph, also observed for VO_2 deposited on sapphire. When deposited at 600 °C, the XRD spectrum revealed the presence of a polycrystalline VO_2 thin film with primary 2θ peaks at 28.15, 37.2, and 55.8 deg., which correspond to the (011), (200), and the (220) planes, respectively. However, it is apparent that VO_2 grows with a higher preference as (011) when compared to the intensity of other peaks. A common theme observed for films deposited on both substrates is a deviation from the ideal peak location. Deviations of the diffraction peaks can be affected by many things, among them is lattice mismatch. Lattice mismatch is realized as an in-plane tensile or compressive strain which is capable of impacting the d-spacing, as observed here. The lattice misfit parameter, f_m can be calculated by:

$$f_m = \frac{a_f - a_s}{a_s} \tag{4.1}$$

where a_f and a_s are the film and substrate lattice constants respectively. High sensitivity of XRD enables detection of subtle changes in the lattice plane d-spacing, which was manifested as a shift in 2θ values. This change can be mathematically determined by the Bragg equation, which relates the interplanar spacing to the angle of the diffracted beam as [125]:

$$2dsin\theta = n\lambda \tag{4.2}$$

where d is the spacing between lattice planes, θ is the angle of the diffracted beam, n is a positive integer, and λ is the wavelength of the incoming X-ray beam (here the source is Cu K-α λ=0.15418 nm). Lattice mismatch results in a combination of in-plane strain and the formation of strain relaxing misfit dislocations, both of which have been shown to profoundly impact the characteristics of the MIT [56].

Mentioned briefly above was the deposition of VO_2 (A) phase at 500 °C,

regardless of substrate. The (A) phase differs from the low temperature (M1) phase both structurally and electronically. Debate over the exact structure of the (A) phase persists, though it is accepted to be of the tetragonal crystal system at room temperature, and does not exhibit any phase transition at the T_c observed for VO_2 (M1) films. On sapphire, the VO_2 (A)-phase manifested as the appearance of diffraction peaks at 2θ values of 14.5, 21.5, and 29.0, which correspond to the (110), (200), and the (220) planes respectively. VO_2 grown on Si results in the appearance of diffraction peaks at 2θ values of 14.4, 25.25, and 29.1 deg for the (110), (102), and (220) planes, respectively. Evidence of peaks shifting from their ideal values was present in both film-substrate systems, however, due to the difference in both the lattice constants and crystal structure of Si and sapphire, the peak shifts were not equivalent for the two different films. This further confirms the suspicion that the peak shift was a result of strain imparted by lattice mismatch, as each unique film-substrate interface will result in varying degrees of strain. The appearance of VO_2 (A) at 500 °C is commensurate with our previous parametric study of PLD of VO_2 thin films on SiO_2 substrates which also showed the formation of VO_2 (A) at 500 °C [117]. The consistent formation of VO_2 (A) at 500 °C regardless of substrate indicates the presence of a local minima in the free energy framework of VO_2, which appears independent of substrate-film related phenomena such as interfacial strain and crystallinity.

4.4.2 Cross sectional TEM analysis

The substrate-film interface has been characterized using cross-sectional HRTEM on the V-SAP-600 and V-Si-600 films. Figure 4.5(a) shows the cross-sectional HRTEM of the sapphire/VO_2 interface displaying epitaxial growth of the VO_2 phase on the sapphire substrate. The FFT pattern captured from the film-substrate conjugate is shown in Figure 4.5(b). Orientation of the sapphire substrate parallel to the beam direction is $\langle 1\bar{1}00 \rangle$, whereas the orien-

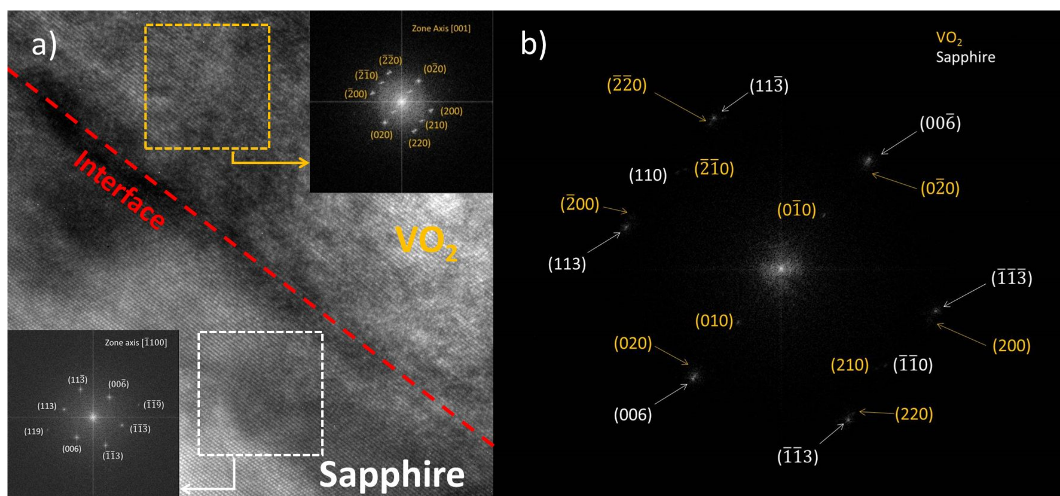

Figure 4.5: (a) High resolution TEM image of the VO_2/sapphire cross section V-SAP-600 film. Inset on the left corner down shows the diffraction pattern of sapphire. The top right corner shows the diffraction pattern of the VO_2 film (b) FFT of the VO_2/sapphire interface. The diffraction spots in (b) correspond to the [$\bar{1}$100] and [001] zones of sapphire and VO_2, respectively.

tation of the film is $\langle 001 \rangle$. The (006) planes of alumina and the (020) planes of VO_2 are parallel to the interface, where the normal directions to those planes, $\langle 0001 \rangle$ and $\langle 010 \rangle$, respectively, are also parallel to each other. HRTEM analysis also supports the observed growth of $\langle 020 \rangle$ texture of VO_2 on sapphire. Comparing the lattice parameter values of monoclinic VO_2, given in Table 4.5, we can further comment that the growth along the $\langle 010 \rangle$ direction of monoclinic VO_2 will be more feasible. Growth of VO_2 on silicon does not select any special orientation relationship but rather it grows in a non-textured manner following the ideal powder diffraction pattern of VO_2, as shown in Figure 4.2(b). The cross-sectional HRTEM image of the V-Si-600 sample and the corresponding FFT pattern show the film, marked in Figure 4.6(a), does not exhibit any orientation relationship with the substrate. Furthermore, a thin native oxide layer of $\sim$ 3 nm is clearly visible at the film-substrate interface.

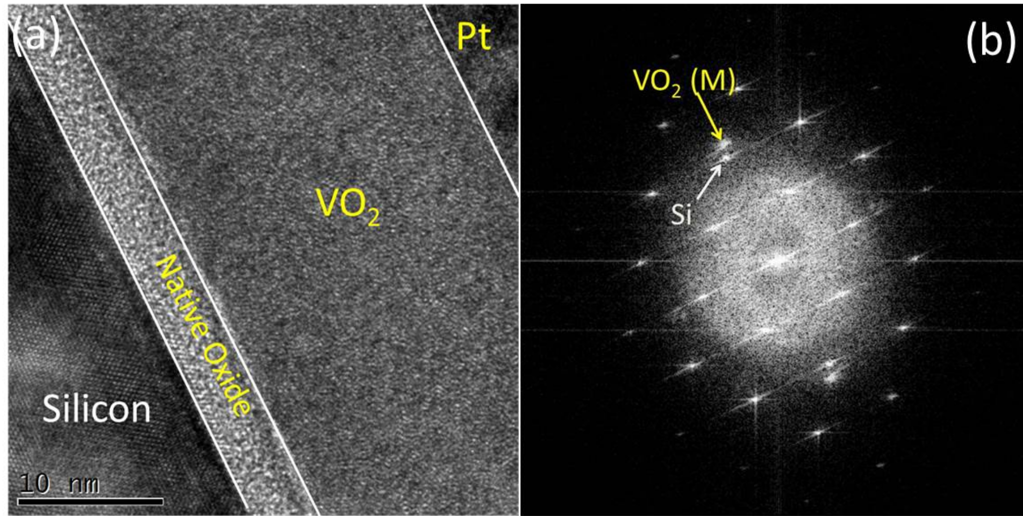

Figure 4.6: (a) High resolution TEM image of the VO_2/silicon interface taken from V-Si-600 and (b) the corresponding FFT pattern of the entire image.

4.4.3 AFM surface characterization

We have used AFM to investigate the physical nature of the deposited VO_2 thin films. Surface roughness was found to depend significantly on the temperature and the substrate, although the trend was not very straightforward. The surface roughness of the virgin substrates and the deposited films are presented in Table 4.2. Immediately it is apparent that VO_2 (A) resulted in the roughest surface, regardless of substrate, and that roughness responded to temperature differently for each substrate. Surface roughness is highly affected by the growth mode, of which there are three main methods; Frank-van der Merwe (FM, layer by layer), Volmer-Weber (VW, island growth), and Stranski-Krastanov (SK, layer plus island) [126]. The determination of growth mode depends upon the surface energies of the film, substrate, and the film-substrate interface (γ_f, γ_s, and γ_i) investigated. The driving force between which growth mode is observed is a minimization of the overall surface energy of the system, which may be affected by surface diffusion. FM growth will occur if $\gamma_f + \gamma_i \leq \gamma_s$ and VW growth will occur if $\gamma_f > \gamma_s$. The surface energy of the (0001) surface ranges between 2.03-12.85 J/m^2, with

Table 4.2: Surface roughness for VO_2 thin films grown on Si and sapphire.

	Surface Roughness (nm)			
Sample ID	400 °C	500 °C	550 °C	600 °C
VO_2/Sapphire[a]	2.83	3.14	0.74	0.51
VO_2/Si[b]	2.0	3.2	1.74	1.9

[a]bare sapphire roughness was 0.14 nm

[b]bare silicon roughness was 0.15 nm

the value for VO_2 being an order of magnitude lower indicating a strong likelihood to see FM growth [127]. On the other hand, the native oxide on Si wafers has a much lower surface energy, ranging from 0.164-0.237 J/m^2 which is of the same magnitude as that of (110) VO_2 [128, 129].

Surface energy minimization is why we see the growth of the (011) plane on the Si substrate, as this is the lowest energy plane for VO_2. Surface roughness does not vary much for the Si/VO_2 (M1) system, likely due to this fact. The slight decrease in the roughness as temperature increases can be attributed to an increase in surface diffusion of adatoms, allowing for greater coverage of the surface. On the other hand, the sapphire/VO_2 (M1) system showed a significant decrease in surface roughness when temperature is increased. AFM micrographs from the two samples grown at 600 °C are shown in Figure 4.7. For the AFM images of the remaining six samples and the bare substrates refer to supplementary data Figures 4.9 and 4.10. From XRD and TEM we showed that VO_2 grows in a textured polycrystalline structure, which means the lowest energy plane (i.e. (011)) did not grow on sapphire. However, the appearance of textured epitaxial growth, as observed for VO_2 on sapphire, indicates a minimization of the interfacial surface energy by growing in preferential orientations. By minimizing the interfacial surface energy, we still satisfy the equation for FM growth mode; $\gamma_f + \gamma_i \leq \gamma_s$. The decrease in roughness as temperature increased can also be attributed to the increase in surface mobility of adatoms, as seen on Si.

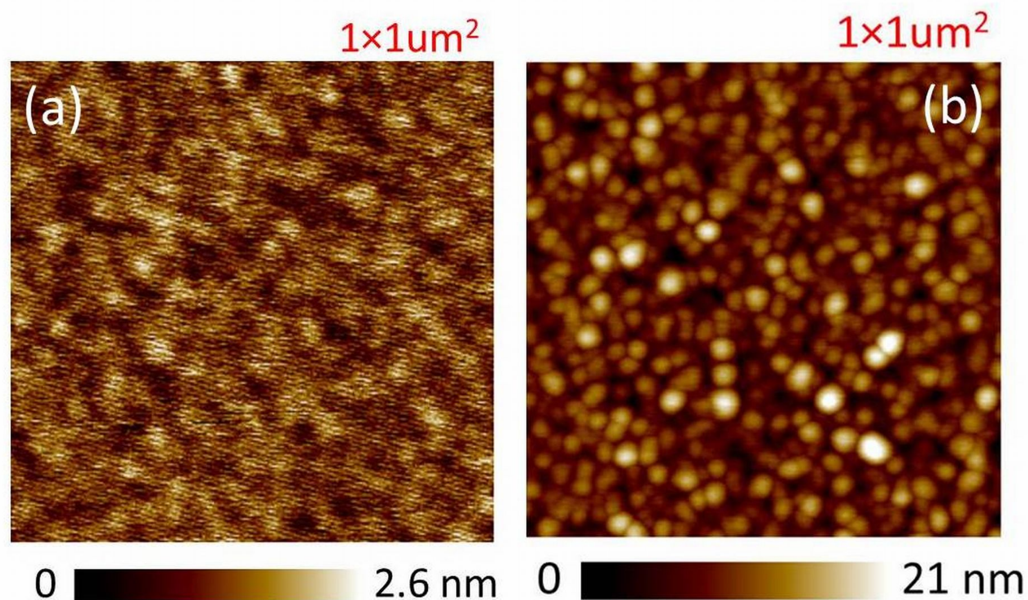

Figure 4.7: AFM images showing the surface profile of (a) VO_2 on sapphire (V-SAP-600) and (b) silicon (V-Si-600). The RMS roughness values in Table 4.2 were computed from these images.

4.4.4 Metal-insulator transition

Temperature vs. resistance measurements

We have investigated the substrate dependant nature of the MIT of VO_2 thin films by monitoring the variation in electrical resistance as a function of substrate temperature. We found that VO_2 grown on sapphire (Figure 4.8(a)) resulted in the sharpest MIT, with the highest magnitude and lowest hysteresis. The films grown on silicon (Figure 4.8) showed a narrow hysteresis as well, but suffered from a low magnitude MIT. Compared to our previous results probing the MIT for VO_2 grown on SiO_2, VO_2 grown on sapphire and silicon had a much narrower hysteresis width, with similar transition magnitudes.

Figure 4.8(a) shows the temperature vs. resistance curves for the heating-cooling cycle of VO_2 on sapphire. Of the four films grown on sapphire, only one (V-SAP-500) did not show any evidence of an MIT, as the VO_2 (A) phase

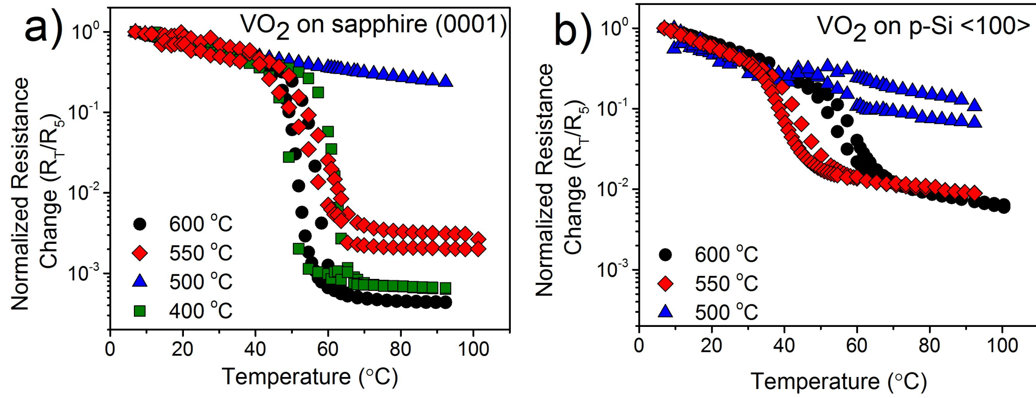

Figure 4.8: Resistance as a function of temperature for VO_2 thin films grown on (a) sapphire and (b) silicon substrates. Common to both is no transition present for the films grown at 500 °C, and a sharp transition for films grown at 550 and 600 °C. On Si, VO_2 did not deposit at 400 °C and therefore no measurement was taken.

does not undergo such a transition in the temperature range studied. The remaining three films all demonstrated evidence of the MIT with varying properties as listed in Table 4.3. V-SAP-400, grown at 400 °C, demonstrated over three orders of magnitude change in resistance, but also the largest hysteresis width. However V-SAP-400, along with V-SAP-600, displayed sharp transitions from both metal-insulator and insulator-metal, with values exceeding 10^4 Ω/°C, which makes for an attractive choice for ultrafast switching applications [112]. Both V-SAP-550 and V-SAP-600 do not show such a large magnitude or transition slope, but they do have minimal hysteresis width throughout the entire heat-cool cycle, which is an attractive property in itself.

Table 4.3: Magnitude (Ω), hysteresis width (Δ°C), and position (°C) of the metal-insulator transition for VO_2 grown on c-sapphire (0001).

Sample ID	Magnitude	Hysteresis width	Position
V-SAP-400	10^3	10.8	51.9
V-SAP-550	10^3	8.1	45.15
V-SAP-600	$>10^3$	3.6	51

Table 4.4: Magnitude (Ω), hysteresis width (Δ°C), and position (°C) of the metal-insulator transition VO_2 grown on p-Si ⟨100⟩.

Sample ID	Magnitude	Hysteresis width	Position
V-Si-550	10^2	4.5	37.05
V-Si-600	10^2	5.4	51.9

As shown previously by XRD, VO_2 grown on silicon substrates produced the (M1) phase for deposition temperatures of 550 and 600 °C, and this is apparent from the temperature vs. resistance measurements shown in Figure 4.8(b). Of the four films, only three formed VO_2, and of those only two (V-Si-550 and V-Si-600) displayed a transition, while the other (V-Si-500) did not. V-Si-500 was present as VO_2 (A) phase, so no transition was expected as reported previously [77, 117]. V-Si-600 showed a very narrow MIT hysteresis width, with a transition magnitude of almost three orders. V-Si-550 showed similar hysteresis and magnitude to that of V-Si-600, but the transition occurred at a much lower temperature. The MIT for both of these films was found to have a much gentler slope as compared to VO_2 grown on sapphire. Summarized in Table 4.4, the MIT properties of VO_2 thin films grown on silicon were found to differ significantly from those grown on sapphire. In addition to a much lower magnitude compared to VO_2 on sapphire, the MIT of the films grown on silicon were not nearly as pronounced, i.e. their slope was much less than on sapphire. Resistivity measurements were conducted at temperatures below (room temp $\sim$ 20 °C) and above (100 °C) to see the effect of substrate and temperature. Presented in supplementary data Tables 4.7 and 4.8, resistivity is shown to decrease as temperature increases, while between substrates, resistivity of VO_2 is shown to vary significantly more for films grown on sapphire. Increased temperature has been shown to result in larger grains, thereby decreasing the grain boundary density, which should (and does) result in a lower resistivity.

Correlation between structure and MIT of VO_2

It has been shown that interfacial strain, that may arise from lattice mismatch, has a profound effect on the MIT. Aetukuri et al. showed the ability to manipulate the MIT in VO_2 by controlling orbital occupancy by means of epitaxial strain modulation [130]. Nagashima et al. have shown that the c-axis length in VO_2 thin films influences the position and slope of the MIT [131, 132]. With deposition occurring at 600 °C, VO_2 was present as the tetragonal phase, which produces a small lattice misfit strain on sapphire (-4.4%) as opposed to a much larger value when the substrate is silicon (-16.2%). However, upon cooling below the transition temperature, the tetragonal phase transforms to the monoclinic phase, defined by a flipping of the a- and c- axes, coupled with dimerization and tilting of alternating vanadium atoms along the monoclinic a-axis (resulting in an elongation along this axis by 1%).

The nature of the strain (compressive or tensile) can be determined for each system by looking at the d-spacing equation for each system. Here, we have deposited both the (A) and (M1) phase, which are tetragonal and monoclinic, respectively. The d-spacing for each crystal system is measured as the reciprocal of length of the reciprocal lattice vector [133]. For the tetragonal system

$$\frac{1}{d_{hkl}^2} = \frac{h^2 + k^2}{a^2} + \frac{l^2}{c^2} \tag{4.3}$$

and for the monoclinic system

$$\frac{1}{d_{hkl}^2} = \frac{h^2}{a^2 \sin^2\beta} + \frac{k^2}{b^2} + \frac{l^2}{c^2 \sin^2\beta} + \frac{2hl\cos\beta}{ac\sin^2\beta} \tag{4.4}$$

where a, b, and c are the lattice parameters, β is the angle between the a and c axes, and h, k, and l are the the Miller indices (hkl). Lattice parameters for the substrates and VO_2 phases can be found in Table 4.5, which have been taken from literature and used to determine theoretical lattice misfit [21, 22, 134–

136].

Table 4.5: Lattice parameters (Å) for VO_2, sapphire, and silicon.

Substrate	System	a	b	c	β	Space Group
c-Sapphire (0001)	rhombohedral	4.76	4.76	12.99		$R\bar{3}c$
p-Si ⟨100⟩	cubic	5.43	5.43	5.43		$Fd\bar{3}m$
VO_2 (R)	tetragonal	4.56	4.56	2.86		$P4_2/mnm$
VO_2 (M1)	monoclinic	5.75	4.54	5.38	122.65	$P2_1/c$
VO_2 (A)	tetragonal	8.48	8.48	7.62		$P4_2/ncm$

Based on the results from XRD and the values in Table 4.5, we were able to determine the nature of the strain (tensile or compressive) due to the apparent change in the d-spacing observed. The change in d-spacing can be used to determine, by using equations 4.3 and 4.4, how the lattice parameters are affected by the mismatch. Summarized in Table 4.6 are the theoretical and experimentally determined d-spacing values for the primary peaks observed in XRD, and the corresponding strain type.

Table 4.6: Experimental and theoretical d-spacing (Å) for the observed lattice planes.

Sample ID	Observed plane	d-spacing (theoretical)	d-spacing (actual)	Strain type
V-SAP-400	(020)	2.2689	2.2768	Tensile
V-SAP-500	(110)	5.9983	6.1039	Tensile
V-SAP-550	(020)	2.2689	2.2691	Compressive
V-SAP-600	(020)	2.2689	2.2576	Compressive
V-Si-500	(110)	5.9983	6.1460	Tensile
V-Si-550	(011)	3.2067	3.1620	Compressive
V-Si-600	(011)	3.2067	3.1675	Compressive

What is apparent from the table is that not only does the substrate affect the observed d-spacing, but also the temperature of deposition. For the sapphire/VO_2 (M1) system, an increase in the temperature resulted in a lower value of d-spacing, with the deviation from the ideal value increasing

as well. For the Si/VO_2 (M1) system, the opposite scenario is true, where the d-spacing increases with temperature, and the d-spacing becomes closer to the theoretical value. In both cases, however, the strain is seen to be of the same type, as all cases involving VO_2 (M1) resulted in a compressed d-spacing, with the exception of V-SAP-400. Park et al. have shown that a compression results in a lower MIT temperature from monoclinic to rutile, which was observed for all cases of VO_2 (M1) studied herein [5]. This is not the only factor which influences the MIT, as in the sapphire/VO_2 (M1) system the transition temperature fluctuates, and does not follow a specific trend. It has been shown that the grain size also influences the MIT temperature, and in our previous work we have shown that deposition temperature has a significant impact on the resultant grain size. Miller and Wang have shown that samples with a higher density of grain boundaries (smaller grain size) offer a greater amount of nucleation sites, resulting in a lower T_c [115]. This is likely the reason we observed the increased transition temperature for sample V-SAP-600, as the competing effects of grain size vs. strain had a larger contribution from grain size. On the other hand, V-SAP-400 has a higher transition temperature with a larger density of grains and a tensile strain in the film, showing the opposite competition between strain and grain size. V-SAP-400 has much smaller grain size, which should reduce the T_c, but the tensile stain causes an increase. Here, since T_c is less than the bulk value a larger effect is seen from the reduced grain size.

The primary difference observed between the Si and sapphire system was the presence of multiple diffraction peaks on Si. Considering both substrates were single crystals, one would assume there to be preferential growth for Si as there was for sapphire. However, the clean silicon surface will undoubtedly form a native oxide layer prior to deposition due to exposure to atmospheric oxygen as well as the oxygen in the PLD chamber as also shown in Figure 4.6(a). In addition to the oxidation, it has been shown by

high energy ion backscattering techniques that the first few Si layers of the Si-SiO_2 interface are non-registered, and are their positions are incommensurate with the bulk Si lattice (shifting of up to 1 Å is observed) [137]. This subsurface reconstruction has ramifications on the nature of the oxide layer as well, resulting in the stoichiometric SiO_2 surface layer displaying amorphous behaviour, similar to that of thermally grown SiO_2 substrates. Ultimately, rather than depositing on virgin Si substrates, the VO_2 is actually deposited on an amorphous oxide layer, similar to that of the thermal oxide. Due to the nature of this surface reconstruction and oxidation it is not surprising that VO_2 grown on these substrates exhibit a slower transition and a greater degree of polycrystallinity.

4.5 Conclusion

In this work we have deposited VO_2 thin films onto c-cut (0001) sapphire and p-type Si $\langle 100 \rangle$ by PLD at multiple temperatures to establish any substrate related influence on the structural and electronic properties of the deposited films. VO_2 on sapphire was shown by TEM and XRD to grow epitaxially, with the (020) plane growing preferentially, whereas on silicon, VO_2 showed a polycrystalline nature, with the appearance of several diffraction peaks. TEM also revealed that a thin ($\sim$ 2 nm) native oxide layer had formed on the surface, preventing any preferential growth. Surface roughness measurements showed VO_2 grown on sapphire had a much stronger roughness vs. temperature dependance, with a significant decrease in roughness as temperature increased. On silicon, the roughness decreased marginally with increasing temperature, indicating two different mechanisms at play. Surface energy minimization dictated the growth mode, and therefore the surface roughness, as VO_2 on sapphire was driven to reduce interfacial surface energy (as evidenced by epitaxial growth), while similar surface energies between

VO_2 and native SiO_2 show more layer-plus-island growth resulting a rougher film. Roughness decrease as a result of increasing temperature is attributed to grain boundary migration due to increased diffusion. Characteristics of the metal-insulator transition depended on the temperature and substrate chosen, as VO_2 on sapphire had a much sharper and larger resistance drop at the transition temperature as compared to VO_2 on silicon, which showed a weaker, more gradual change from insulator to metal. Compressive strain pushes the MIT temperature to a lower value, while competing effects from grain growth prevent a large decrease. VO_2 (M1) on Si grows in a much more polycrystalline nature than on sapphire due to the amorphous characteristics of the native oxide overgrowth.

4.6 Supplementary data

4.6.1 Additional AFM Images

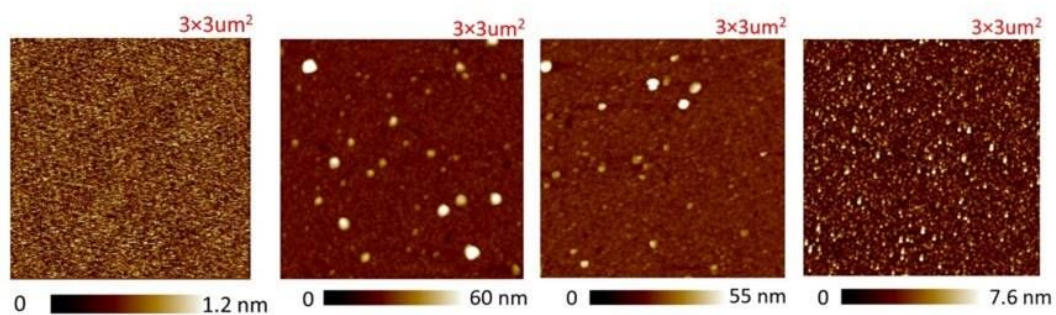

Figure 4.9: Roughness of (a) sapphire substrate with no film and VO2 grown at (b) 400 °C (c) 500 °C and (d) 550 °C as measured by AFM.

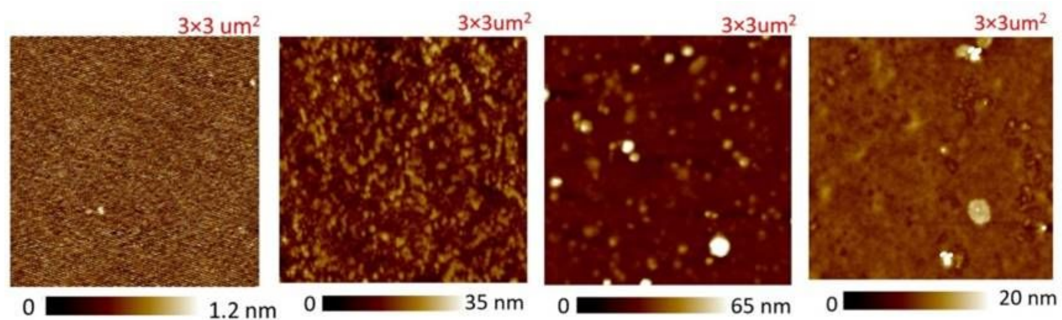

Figure 4.10: Roughness of (a) Si substrate with no film and VO2 grown at (b) 400 °C (c) 500 °C and (d) 550 °C as measured by AFM.

4.6.2 Resistivity of VO_2 Films

Table 4.7: Resistivity ($\Omega\cdot$ cm) of VO_2 films, above and below the T_c deposited on c-sapphire (0001).

Sample ID	Resistivity at 20 °C	Resistivity at 100 °C
V-SAP-400	3.55	9.17×10^{-3}
V-SAP-500	2.87	0.69
V-SAP-550	0.25	2.59×10^{-4}
V-SAP-600	0.355	6.38×10^{-4}

Table 4.8: Resistivity ($\Omega\cdot$ cm) of VO_2 films, above and below the T_c deposited on p-type Si $\langle 100 \rangle$.

Sample ID	Resistivity at 20 °C	Resistivity at 100 °C
V-Si-400	0.055	4.15×10^{-3}
V-Si-500	0.0114	2.46×10^{-3}
V-Si-550	7.54×10^{-3}	6.86×10^{-4}
V-Si-600	4.92×10^{-3}	7.21×10^{-4}

Chapter 5

Phase transformation induced modulation of the resonance frequency of VO_2/TiO_2 coated microcantilevers

5.1 Abstract

Here we present an investigation into the phase change mechanism and detection methods of the metal-insulator transition of vanadium dioxide (VO_2). We are able to detect the onset of the phase transition, and track it to completion using both the mechanical and electrical response by depositing VO_2/TiO_2 layers onto microcantilever devices by pulsed laser deposition. The resonance frequency of v-shaped cantilevers was shown to increase by up to 41 % upon deposition of VO_2 as detected by laser Doppler vibrometry. Such a large increase in resonance frequency is ascribed to high tensile stress imparted onto the cantilever during the deposition process. The insulator-metal transition manifested as a 5 % increase in the resonance frequency as a result of lattice compression, resulting in additional tensile stress in the

more ordered metallic phase. Electrically, the transition was confirmed by over three orders magnitude decrease in resistance upon heating past the transition. The metal-insulator transition was measured with an accuracy of a few °C when comparing the two methods, however, the transition was much sharper in the mechanical response.

5.2 Introduction

Vanadium dioxide (VO_2) undergoes a reversible first-order phase transition from a low temperature insulating (monoclinic, M1) phase, to a high temperature (rutile, R) metallic phase at $T_c \sim 340$ K[20]. The transition is manifested as drastic changes to the electronic, optical, and structural properties of the crystal. When cooling through the T_c the structural change is manifested as a dimerization and tilting of alternating vanadium atoms in the rutile c-axis (which is now the monoclinic a-axis). Consequently, the V^{4+}-V^{4+} pairing results is differential spacing in the V atoms, with 2.65 and 3.12 Å separating the paired and unpaired atoms, respectively[61]. The exact nature if the metal-insulator transition (MIT) is debated between electron-lattice effects (Peierls transition) and electron-electron effects (Mott transition), with a conclusion yet to be decided. Regardless of the origin, a material with a critical temperature near room temperature such as VO_2 is an intriguing material for a variety of applications including smart window coatings[30], microbolometers[64], gas and strain sensors[66, 67], and non-volatile memory[62].

Although a plethora of research exists regarding VO_2, the majority of these works focus on the electronic or optical response to an external stimulus, while little work has been done to manipulate the mechanical properties associated with the phase change. Due to the structural reconfiguration which occurs during the phase transformation the rutile c-axis of VO_2 is compressed by 1 %, which can have a significant impact on the mechanical properties

of the film. Elastic strain, much like doping, has significant impact on the position of the MIT, which, if controllable, would be a suitable material for use in micro-actuators. Here, we investigate the resonant frequency of a VO_2/TiO_2 coated microcantilever as it passes through the MIT temperature. The active VO_2 layer is responsible for changes in the mechanical properties, while the TiO_2 layer provides a buffer layer with superb lattice commensurability with VO_2, which facilitates the growth of VO_2. This work provides excellent progress towards integrating VO_2 thin films into current micro- and nanoelectromechanical systems (MEMS/NEMS).

5.3 Experimental methods

VO_2 and TiO_2 were deposited onto v-shaped cantilevers by pulsed laser deposition (PLD) from V- and Ti- metal targets in an oxygen environment. The cantilevers are commercially available (Nanoworld) 0.5 µm thick tipless scanning probe microscopy silicon nitride (SiN) cantilevers. A KrF (λ= 248 nm) excimer laser (Coherent, GmbH) was directed at the rotating target with a laser fluence of 2.6 J/cm^2 and a repetition rate of 10 Hz. The substrate, maintained at 600 °C for the duration of the deposition, was placed directly opposite the target, 31 mm apart. Oxygen pressure was maintained at 50 mTorr and the deposition lasted 15 minutes. Parameters for the VO_2 deposition have been fully optimized in our previous work[117]. After deposition the phase and crystallinity was determined by X-ray diffraction (XRD) and the surface morphology by scanning electron microscopy (SEM).

Frequency measurements were conducted under high vacuum by laser Doppler vibrometry (LDV). The cantilevers were fixed to a heating element and were stimulated into resonance by an adjacent piezoelectric actuator. The resonance frequency was continuously monitored while temperature was increased from 25-90 °C. The microcantilevers were initially characterized

prior to deposition to establish a baseline response, and again after deposition to elucidate the impact of VO_2. Temperature was applied by a Peltier element being driven by a BK Precision 9183 power supply and temperature was monitored using a Pt-1000 thermocouple connected to a Keithley 197 multimeter interfaced with LabView.

5.4 Results and discussion

5.4.1 VO_2 film characterization

The XRD spectrum of the VO_2 coated cantilevers is presented in Figure 5.1(a). It is obvious from the spectrum that the VO_2 is polycrystalline with a sharp peak at a 2θ value of 27.8 ° indicative of the monoclinic (011) reflection. The amorphous nature of the SiN cantilever precludes the possibility of any textured or epitaxial growth, thereby surface energy minimization will be driven by growing the lowest energy plane, which for VO_2 it has been shown that the rutile (110) plane has the lowest surface energy. Though we present the presence of the monoclinic (011) plane by XRD, PLD was conducted at 600 °C which would result in the deposition of rutile phase VO_2 as the deposition temperature is above the MIT temperature. Upon cooling VO_2 through the MIT temperature, the rutile (110) reflection will appear at room temperature as the monoclinic (011) reflection due to the flipped a- and c-axes. The appearance of TiO_2 rutile peaks was evident in the XRD spectrum, with peaks appearing at almost identical 2θ values as for VO_2. This is to be expected as rutile TiO_2 shares the same space group and similar lattice constants as rutile VO_2.

Polycrystallinity of the VO_2 layer was confirmed by SEM as shown in Figure 5.1(b) (inset shows the geometry of one of the cantilevers). Two different cantilevers were used, labelled as VMC-200 and VMC-100, where

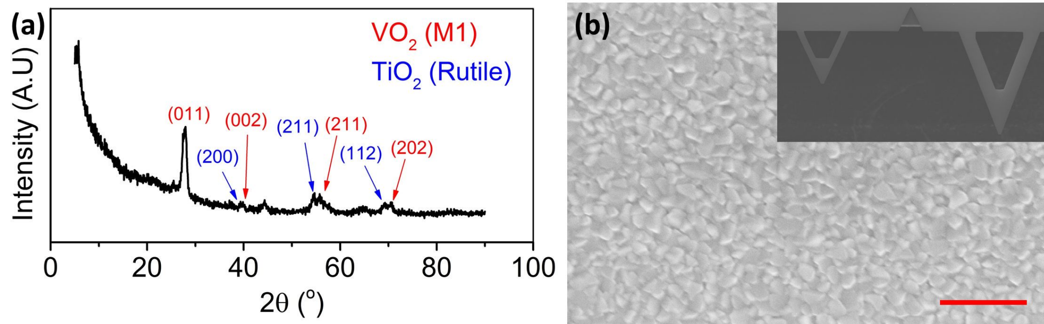

Figure 5.1: (a) XRD spectrum and (b) SEM image of the VO_2 film. Monoclinic (011) reflection was dominant as shown by XRD. Inset (b) shows the geometry of each cantilever, VMC-100 on the left and VMC-200 on the right. Scale bar in (b) is 400 nm.

the numbers indicate the length of each in μm. Each arm on VMC-200 was 28 μm wide, and for VMC-100 the width of each arm was 13.5 μm. Figure 5.1(b) suggests normal grain growth, indicative of an isotropic film, which is desirable for integration into a mechanical actuator. Thickness was determined by atomic force microscopy (AFM) and was determined to be 20-25 nm for each cantilever.

5.4.2 Electrical characterization of VO_2

Two probe resistance measurements were used to determine the position and magnitude of the MIT of VO_2 as the temperature was increased from 5-100 °C. From Figure 5.3(a) it is apparent that the position of the MIT was 45 °C, with a change in resistance over 3 orders of magnitude. Also evident in Figure 5.3(a) is the MIT is reversible with mild hysteresis in the heat-cool cycle. Hysteresis likely arises due to the polycrystalline nature of the film, as grain boundaries and other defects can cause localized transition from metal to insulator and insulator to metal. Even considering that amorphous substrates provide an inferior response, the MIT of VO_2 grown on these substrates is more than enough to incorporate into MEMS/NEMS devices.

5.4.3 Mechanical resonance of VO_2 microcantilevers by LDV

Although they provided a weaker and more prolonged MIT in the electronic response, commercially available SiN cantilevers were used in order to understand the effect VO_2 has on an already existent platform, and to apply these findings towards fabrication and optimization. SiN is integrated with existing microfabrication processes, so future fabrication of devices based on this material will be seamless. For the bare cantilevers the resonant frequency was measured as 16.25 and 47.07 kHz at room temperature (25 °C) for VMC-200 and VMC-100, respectively. This is demonstrated in Figure 5.2 which shows the resonance frequency increase by over 6 kHz for VMC-200. Upon deposition of 20 nm of VO_2 the resonant frequency increased significantly

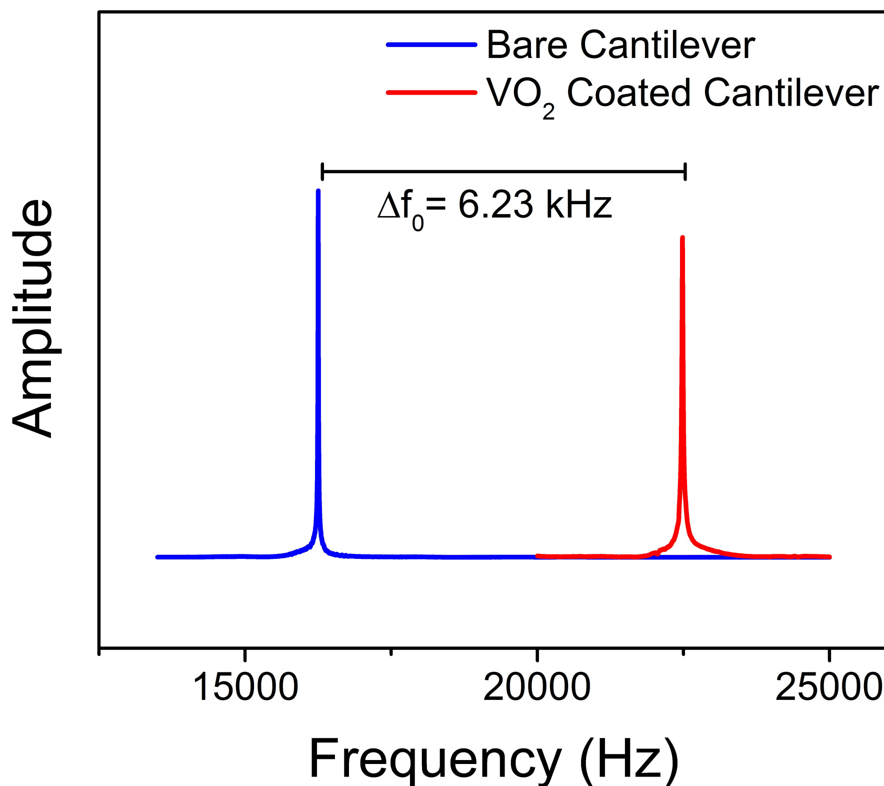

Figure 5.2: Resonance frequency of VMC-200 before and after the deposition of VO_2 as measured by LDV. Resonance frequency was shown to increase significantly upon deposition of the VO_2 layer.

to 22.41 and 66.79 kHz, or 37.9 and 41.9 %, for VMC-200 and VMC-100, respectively. Resonance shift for VMC-200 is shown in the inset of Figure 5.3(b). Such a large increase in resonance frequency is unprecedented for VO_2 based systems, where typically the increase is on the order of 5-10 %[138]. The addition of VO_2 to the cantilever constitutes an increase in mass by only 5 %, which, by conventional wisdom, should result in a decrease of the resonant frequency. Traditional beam theory dictates that the application of a tensile force, S, is capable of increasing the resonance frequency, as given by the following formula[139],

$$f_i = \frac{i^2 \pi}{2l^2} \sqrt{\frac{EI}{\rho A}} \sqrt{1 + \frac{Sl^2}{i^2 EI \pi^2}} \tag{5.1}$$

Where E is Young's modulus, I is the area moment of inertia, ρ is the density of the SiN, A is the cross sectional area, l is the length, and S is the tensile force applied axially along the direction of the cantilever. Equation 5.1 will hold true for v-shaped cantilevers as well, with the addition of some geometric shape factor considerations[140]. For the VO_2/SiN system, the stress, S, arises from both the phase transformation and from thermal mismatch. Thermal mismatch will occur due to differences in thermal expansion coefficients of the substrate and VO_2, which results upon cooling from deposition temperature to room temperature. Thermal expansion mismatch imparts a tensile stress into the film, which may explain the overall increase in resonance frequency. However, as seen in Figure 5.3(b), the resonant frequency of VO_2 coated cantilevers shows a marked increase of 5 % at the same temperature the MIT was observed electrically. Such a response cannot simply be explained by thermal expansion, which should behave linearly, but rather can be explained by additional stress caused by the phase transformation.

In the monoclinic phase, the VO_2 unit cell has expanded, thereby compensating for a small amount of the thermal mismatch stress, reducing the

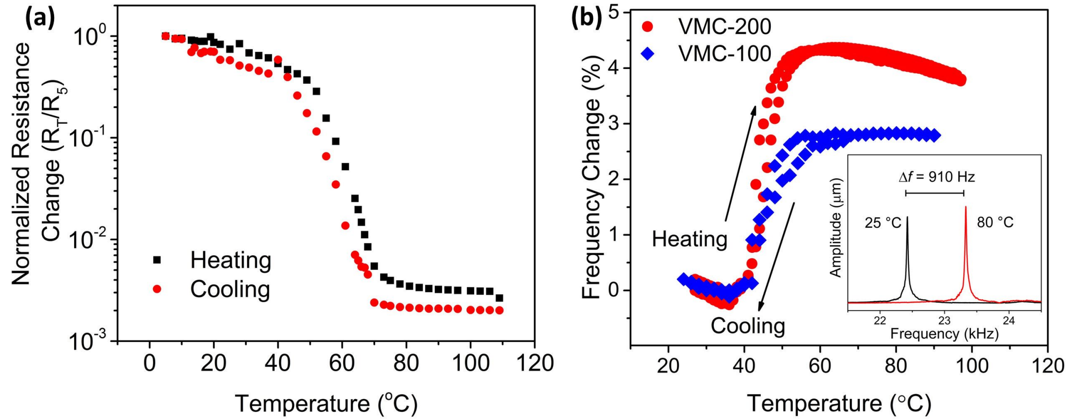

Figure 5.3: Metal-insulator transition for VO_2 cantilevers measured (a) electrically and (b) mechanically. The transition was sharper in mechanical detection, and more pronounced in VMC-200, likely due to lower stiffness of the cantilever.

resonance frequency. By increasing the temperature across the MIT, the VO_2 unit cell contracts due to atomic restructuring, which introduces a tensile stress along the axial direction. Though this has been observed previously, this work would like to highlight the importance of device geometry and film thickness. From this work, we show an ultrathin layer of VO_2 can elicit a comparable response to films an order of magnitude thicker, which indicates frequency shift as a function of film thickness behaves non-linearly with some critical value. In fact, we demonstrate a lower limit for the film thickness as the MIT is not as clearly present when the film thickness is reduced below $\sim$12 nm. While the trend does show an overall increase in frequency, the transition is no longer as pronounced, and the magnitude has diminished to $<$1 %. In addition to thickness, the effect of cantilever geometry was also investigated by using two different sized cantilevers. As shown in Figure 5.3(b), the VO_2 film facilitated a larger frequency change in VMC-200 as compared to VMC-100. The difference can be explained by considering the relative effect that VO_2 imparts onto each device. VMC-100 has a reported force constant of 0.32 N/m, which is four times larger than that of VMC-200. The VO_2 film was identical between the two cantilevers, so any stiffness change would have a

much larger effect on the less rigid device (VMC-200 in this case), which is precisely what was observed. This information provides us with the ability to manipulate stiffness in an effort to control the frequency shift observed.

In addition to the frequency shift, the deflection of the cantilever was also noticed to have changed, although it is yet to be quantified. The observation was made via optical microscopy where the cantilevers moved in and out of focus as a function of temperature. This leads us to believe that in addition to the frequency change, the structural rearrangement of the crystal is capable of deflecting the cantilever to a noticeable amount. Future works are being initiated to further evaluate and quantify the magnitude and applicability of this static deflection.

5.5 Conclusion

Here we have presented an investigation regarding the effect the structural phase transformation inherent to VO_2 has on the mechanical properties of two different microcantilever devices. By depositing TiO_2 first, VO_2 growth is more ordered and interfacial stress is lower, which greatly reduces residual interfacial stress. Films are deposited onto the cantilevers by PLD and by monitoring the resonant frequency; we detect, by LDV, significant changes in the mechanical response. Two major factors, thermal mismatch and atomic rearrangement, are responsible for both the overall increase in resonance frequency, and the sharp transition observed at the MIT temperature. We have investigated the influence of film thickness, and determined that a lower limit exists for detecting the MIT, as thinner films produced a very small (<1 %) change at the MIT. VO_2 films of $\sim$20 nm thickness elicited an increase in resonance frequency by $\sim$40 % (with respect to the bare cantilever) due to large tensile stresses, and the phase transformation produced a sharp increase in resonant frequency of $\sim$5 % at the MIT temperature, likely resulting from

additional tensile stress from lattice compression. Cantilevers with a lower stiffness were shown to be more greatly influenced by the presence of the VO_2 layer. Significant changes in the static deflection was also noticed near the MIT temperature which indicates that resonant frequency is not the only parameter that can be exploited by manipulating device geometry. This work paves the way for future investigations to maximize and integrate the mechanical response by careful design of resonator geometry and structure.

Chapter 6

Fabrication of phase change microstring resonators via top down lithographic techniques: Incorporation of VO_2 into conventional processes

6.1 Abstract

Exploitation of the metal-insulator phase transition of VO_2 has become an important area for MEMS and MOEMS devices. The electronic and optical properties of VO_2 can be significantly altered by external stimuli such as heat, electric field, or mechanical stress. While the properties and potential applications of this material have been widely studied, there is minimal efforts put forth regarding the integration of VO_2 into existing fabrication processes. Here a process for fabricating VO_2 coated microstring resonators is presented, where the stability of VO_2 is monitored throughout the entire process. Reac-

tive ion etching (RIE), vapour HF etching, ablation, and inductively coupled plasma etching were used throughout the process and their effect on the VO_2 film, as well as the structural and masking layers, is reported. VO_2 was shown to etch with excellent selectivity to the metal mask layer by RIE, with a mixture of CHF_3, CF_4, and O_2. Metallic masking, as opposed to photoresist, was necessary due to the use of VHF as the polymers are porous enabling the gas molecules to compromise this layer. Of the metals considered, Cr was the most stable in all processes. The resonant frequency of these devices was monitored by LDV where an increase in the resonance frequency by over 5 % was observed upon heating through the transition. This report provides a foundation for future processing of VO_2 based MEMS/MOEMS devices.

6.2 Introduction

Vanadium dioxide (VO_2) is a strongly correlated transition metal oxide which exhibits a reversible first order phase transformation at a critical temperature (T_c) of 340 K [20]. Above the T_c, VO_2 is present as a tetragonal metallic phase, and upon cooling below the T_c, the structure transforms into an insulating monoclinic phase with a band gap of $\sim$ 0.6 eV [27, 141]. In addition to the structural modification, the optical and electronic properties are significantly altered upon crossing the transition threshold. This phase transition can be readily detected optically, electronically, and mechanically, making it an attractive material for integration into conventional fabrication processes for application in photodetectors [142], uncooled bolometers [35, 143, 144], gas and strain sensing [66, 67], memory devices [62, 111], smart window coatings [29, 30], etc.

There are several processes available for the synthesis of VO_2 thin films, including common techniques such as sputtering and evaporation, and more specialized methods like pulsed laser deposition (PLD) and molecular beam

epitaxy (MBE) [60, 117, 145]. While the former two techniques are well established and easily integrable with existing processes, the latter two techniques provide a more sophisticated growth technique that enables precise control over the stoichiometry and crystallinity of the deposited layer. PLD enables direct stoichiometric transfer of virtually any material in an inert or reactive background gas making it an attractive choice for many complex oxides [9]. Such abilities are extremely valuable in optoelectronics and CMOS device production where precise control on both the band structure and physical properties is necessary for a desirable outcome. The metal-insulator transition (MIT) present in VO_2 is highly dependant upon the interfacial structure, as epitaxial films demonstrate a much larger and sharper transition region, resulting from a lower density of both grain boundaries and dislocations (as shown in Chapter 4 of this thesis). Such crystal defects are known to induce the MIT in VO_2 by providing a heterogeneous nucleation site to initiate the phase transition [146]. Therefore, VO_2 provides a unique challenge from both a synthesis and processing standpoint that must be addressed in order to successfully integrate VO_2 into existing technologies. For successful integration of VO_2 into a fabrication process, knowledge surrounding its stability and compatibility with conventional fabrication techniques is of paramount importance. Traditional top-down fabrication processes involve several lithography, deposition, and etching (wet and dry) steps that must be compatible with VO_2. Hence, an intimate understanding into how VO_2 behaves in a wide variety of solvents, plasma chemistries, and deposition conditions is critical to developing VO_2 based devices.

Here, we present a process for synthesising VO_2 coated microstring resonators with a silicon nitride device layer and buried oxide sacrificial layer, all on a p-type Si $\langle 100 \rangle$ handle wafer. In some instances a buffer layer of TiO_2 was used as an intermediate layer to facilitate textured growth of VO_2 due to the fact that both VO_2 and TiO_2 have similar lattice constants and the

same crystal structure at the deposition temperature. We will discuss the ramifications of the available process choices, as well as the behaviour of VO_2 in each one of these processes. Furthermore, we will present the process used to fabricate VO_2 microstrings in full detail, from the deposition of VO_2 by PLD, patterning and development by lithography, etching (plasma, wet, and vapour processes considered), and finally, release of the strings. This work will set the foundation for device fabrication based on VO_2 thin films, as there is not, to our knowledge, a comprehensive study pertaining to the stability of VO_2 thin films in microfabrication processes.

6.3 Experimental process

All devices fabricated in this paper were done so using the same base substrate, fabricated in house. Boron doped p-type $\langle 100 \rangle$ Si wafers were thermally oxidized via wet oxidation in a tube furnace (Tystar) at 1050 °C until the thickness reached 1.5 µm, after which stoichiometric silicon nitride (SiN) was deposited on top by low pressure chemical vapour deposition (LPCVD) until the film thickness was 200 nm. Film stress was measured by a Flexus 2320 stress measurement tool and was found to be ~ 1.2 GPa. The following sections will discuss the optimized process for device fabrication, as well any alternative methods that were conducted and deemed either unsuitable, or sub-optimal. In Figure 6.1, a general outline of the process flow used to fabricate VO_2 microstrings on Si_3N_4 substrates is given. The steps shown in Figure 6.1 that will be examined will include the lithography, etching of VO_2 and TiO_2, and the metal etching. The removal of the SiN and the sacrificial SiO_2 layers will be briefly mentioned, as even though these processes are thoroughly understood, the ramifications the etching has on the protective materials (Cr, W, or Al hard mask and the photoresist) necessitate some investigation. The reason the hard mask material is important is during this

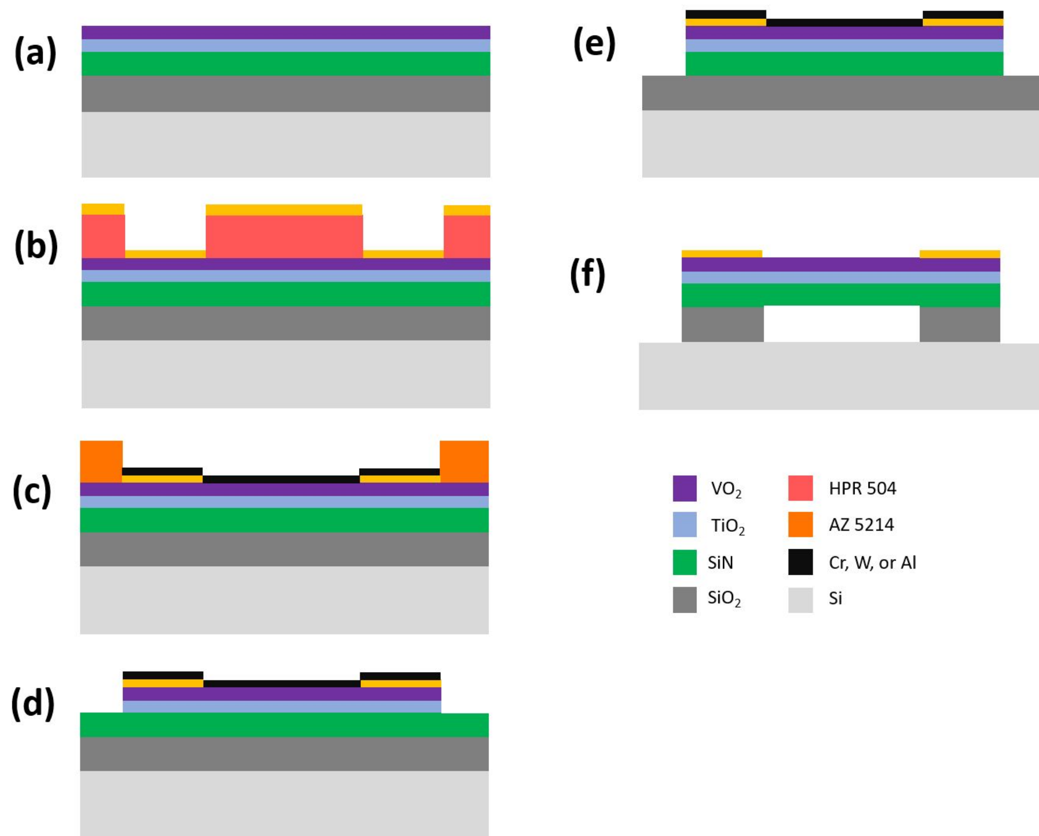

Figure 6.1: A generalized outline of the process flow used to fabricate the VO_2 microstring devices shown from the side profile. (a) starting substrate, (b) patterning of contact pads, (c) defining the string geometry and depositing metal mask and photoresist removal, (d) etching the VO_2 and TiO_2 layer, (e) etching SiN, (f) releasing the string (SiO_2 etching), and metal mask stripping. Each of the steps shown in this schematic will be discussed in detail, exploring the possibilities considered for each step and determining the most suitable process for each.

removal step the underlying active VO_2 layer must remain unaltered by this plasma chemistry as precise control of the etch rate to nanometer precision is just not plausible. Proper removal of the metal layer is critical for the successful application of the device.

6.3.1 PLD of VO_2 thin films

Deposition of VO_2 was carried out via PLD. A pure V metal target (99.9 % purity, American Elements) was ablated by a KrF (248 nm) excimer laser (Coherent, GmbH) with a laser fluence of 2.6 J/m^2 and a repetition rate of 10 Hz. Substrate temperature was maintained at 600 °C, the target was positioned directly across from the substrate with a 31 mm separation, oxygen pressure was set at 50 mTorr, and deposition time was 15 minutes. The VO_2 deposition parameters used for this work have been studied extensively in our previous work [117]. In some cases TiO_2 was deposited onto the substrate prior to VO_2 deposition as a means to increase the crystallinity and decrease the strain in the VO_2 lattice due to the strikingly similar lattice constants and space group ($P4_2/mnm$ above the T_c) [6]. TiO_2 was deposited onto the substrate at the same conditions as the VO_2 layer, with the exception of oxygen gas pressure which was maintained at 10 mTorr. The films grown by PLD in this work are 20-25 nm in thickness, and have a surface roughness less than 4 nm as determined by atomic force microscopy (AFM). X-ray diffraction (XRD) of the deposited VO_2 films reveal a polycrystalline nature with strong reflection from the (011) planes which is further enhanced by the addition of the TiO_2 layer. AFM images and XRD spectra of the deposited films can be found in Figure 6.2.

6.3.2 Lithographic pattering of electrical contacts and the strings

In order to electrically probe the device once it is completed, electrical contacts at either end of the string needed to be deposited prior to defining the string geometry. The contacts are deposited prior to string definition to avoid damage to the working area of the device. Additionally, by defining the contact pads first, alignment of the string layer is simplified. Generally, there are two methods to deposit metal layers: pattern the contact pad area first

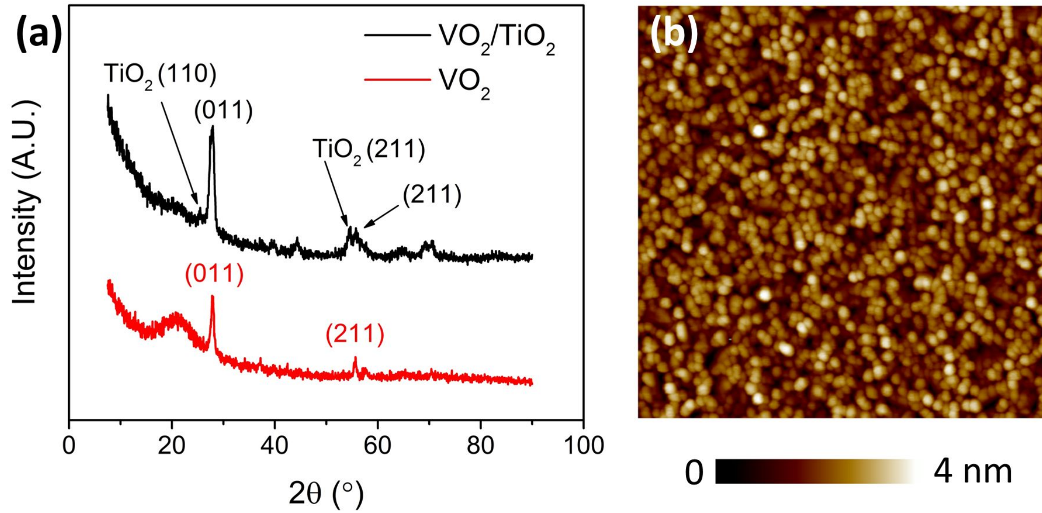

Figure 6.2: (a) XRD spectrum showing the improved crystallinity of the VO_2/TiO_2 layered structure and (b) AFM topographic scan of VO_2/TiO_2 deposited on $Si_3N_4/SiO_2/Si$ substrate.

and deposit metal on top, or deposit metal first and then define the contacts. The former method relies on lift-off to remove unwanted photoresist and metal, while the latter uses wet or dry metal etching (typically wet etching though plasma etching is gaining popularity) to strip off the unwanted metal. There are pros and cons associated with both choices, however, due to uncertainties pertaining to the stability of VO_2 in certain etching processes, the lift-off technique was preferred (less aggressive solvents are used in lift-off as compared to etching).

Metal contact pads were patterned onto the substrate using an HPR 504 positive resist, which was spin coated on and soft baked for 90 seconds at 115 °C. Resist thickness was $\sim$ 1.3 µm as measured by contact profilometer (KLA Tencor), which is more than adequate for metal lift-off. After allowing the resist to rehydrate for 15 minutes following the soft bake, the sample was exposed to UV light (365 nm/405 nm) for 3 s with an incident power density of 55.8 mW/cm^2. Development was in a standard NaOH based developer (354, Dow®), for 20 s (at our discretion for each run as the endpoint is visually discerned). The Cr/Au (20 nm/80 nm) metal contact pads were

then deposited via magnetron sputtering. Following sputter deposition, the samples were sonicated in acetone for 5 min to remove the unwanted metal and remaining photoresist.

Once the contact pads were defined, another lithography step is required to define the string. In this case, a hard mask covering the area of the string needs to be deposited as a means to protect the VO_2 device layer underneath. A hard mask was required over a photoresist mask due to compatibility issues with other process equipment that will be explored in subsequent sections. Here, an image reversal photoresist was used in order to achieve a negatively sloped sidewall profile to improve the metal lift-off process. The concept of an image reversal resist is that a positive tone photoresist can be converted into a negative tone resist with additional baking and exposure steps. The resist, AZ5214, was spin coated onto the substrate to a thickness of 1.45 µm and soft baked for 90 seconds at 90 °C. After a rehydration time of 15 minutes, the pattern was transferred to the substrate by exposing UV light (365 nm and 405 nm) through the mask for 0.5 seconds. A second baking step, 115 °C for 120 seconds, is used in order to initiate the image reversal process. Image reversal results from the presence of a particular crosslinking agent that activates when heated above 110 °C and forms a nearly insoluble (in the developer solution) compound. However, this crosslinking agent is only activated in areas that had been previously exposed to UV light in the previous step. The rest of the device is then exposed in a flood exposure (no photomask) in order to break down the remaining (unexposed) photoresist. The chip is then developed in MF 319 developer (Microchem) for $\sim$40 seconds. A representative diagram showing schematically what happens during this step can be seen in Figure 6.3.

Once the string has been defined by the image reversal process, a hard mask was deposited via magnetron sputtering. Materials considered for the hard mask included Cr, Al, and W, the stability and etching chemistries of

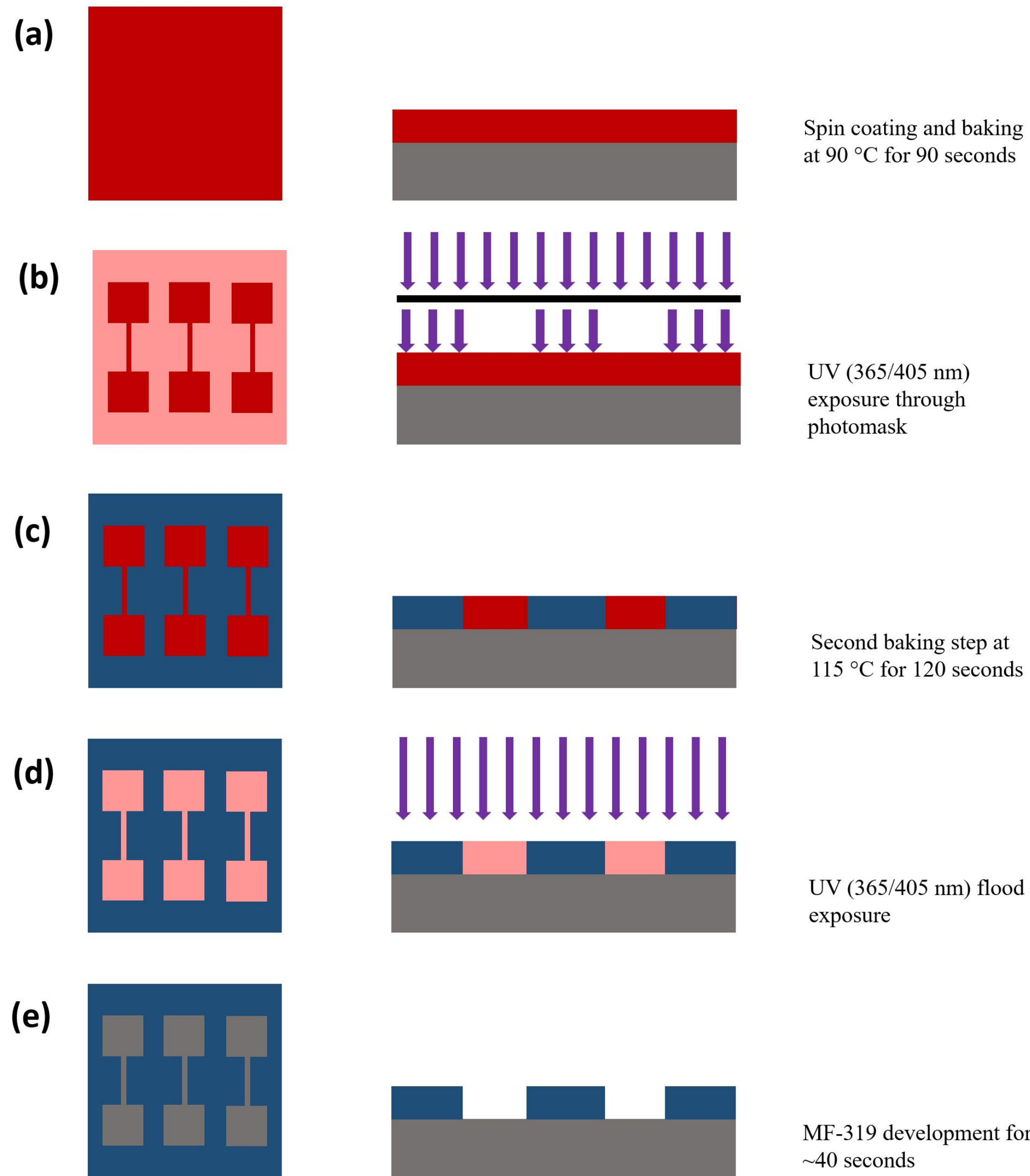

Figure 6.3: General representation of the image reversal process shown step-by-step from the top view (left) and side view (right). (a) Resist is spun onto substrate to a 1.45 µm thickness with a 90 °C soft bake. (b) pattern transfer where the lighter area shows the exposed sections (in reality the photomask is in hard contact with the substrate to reduce diffraction but is shown like so to portray the photomask). (c) second bake step forms insoluble film in exposed areas. (d) flood exposure and (e) development yields the negative of the original exposure. Color legend: grey-substrate, dark red-virgin resist, light red-exposed resist, blue-insoluble resist, black-photomask, purple-light source.

which were tested for compatibility with VO_2.

6.3.3 Removal of VO_2 and TiO_2 layers

Removal of any layer can be done either physically or chemically, depending on properties of the material. To remove VO_2, reactive ion etching (RIE), vapour HF (VHF), and ablation techniques were considered. RIE and ablation were performed using an Oxford NGP80 system, while VHF was done in a memsstar Orbis Alpha system. Considerations for RIE consist of plasma chemistry (compounds and flow rates), substrate temperature, and power. The RIE recipe used consisted of CHF_3, CF_4, and O_2, with flow rates of 25, 40, and 4 sccm, respectively, 200 W RF power, 30 mTorr pressure and 10 °C platen temperature. This recipe was chosen deliberately as the underlying SiN layer etches with this exact chemistry which would allow for a more streamlined process. VHF was selected as a candidate for two reasons: first, it is a well established process of which the majority of materials used within this work are stable, and second, some vanadium oxides have shown limited success in etching with fluoride based chemistries [147, 148]. Ablation was done in an inert argon plasma, using the same equipment used for RIE. An RF power of 300 W, Ar and O_2 flowrates of 50 and 5 sccm, respectively, 30 mTorr gas pressure, and a 10 °C plate temperature were used for ablation.

6.3.4 SiN etching and microstring release

Once the VO_2 and TiO_2 layers have been removed, the device SiN layer must be etched prior to releasing the device. SiN and SiO_2 removal processes are well established, we must still understand their influence on the active materials. The SiN was etched using a standard SiN anisotropic etch on the NGP80 RIE system using the same recipe as listed in the previous section. Standard etch rate for the removal of LPCVD stoichiometric nitride using

this recipe is $\sim 70\ ^{nm}/_{min}$. The sacrificial SiO_2 layer removal was limited to VHF, with the primary goals of avoiding stiction, limiting the number of solvents used, and limiting additional process steps (i.e. critical point drying). Device release was one of the most critical steps in the process for a number of reasons: first, if unsuccessful the device is useless, and second, the etch time for this step is the longest which requires all other exposed materials to have excellent etch resistance. For VHF, a two step process was used, a main etch step and an undercut step, both using a mixture of HF and H_2O and a buffer gas of N_2. The difference between the two step is the relative amounts of each process gas and the pressure (higher pressure is used to force the undercut).

6.3.5 Stripping and stability of protective metal layer

In order to avoid complications arising from stiction, the metal hard mask layer was removed via inductively coupled plasma (ICP) RIE. The system used here was a PlasmaPro 100 Cobra Etch (Oxford Instruments). All three metals (Cr, Al, and W) were stripped using the same system, operated using different chemistries and powers. A summary of the etching process is given in Table 6.1, including gas flow, temperature, power, and pressure. It should be noted that for these processes there is significantly different powers used, which may drastically affect the stability of our materials. This is one of the main benefits of inductively coupled plasma etching where the ion energy and density can be controlled seperately. The very low power ensures that the energetic ions are not ablating the surface but rather are reacting chemically with the surface. The thickness of each metal layer was also different, due to prior knowledge regarding the etch resistance in CHF_3, CF_4, and O_2 plasmas (a necessary step for SiN removal). W is known to etch in some mixtures of these gases so it was the thickest layer deposited at 250 nm [149]. The other two metals, Cr and Al, both showed little to no problems exposed to these

Table 6.1: Etching process parameters for removal of Cr, Al, and W hard mask materials. All 3 metals were removed in the PlasmaPro 100 Cobra Etch system.

Metal	Etch Step	Etch Parameters	Plasma Constituents	Gas Flow (sccm)	Etch Rate
Cr	Cr Etch	2 W HF 1200 W ICP 12 mTorr 20 °C	Cl_2 O_2	42 8	190 $^{nm}/_{min}$
Al	Al_2O_3 breakthrough	110 W HF 1000 W ICP 10 mTorr 50 °C	BCl_3	30	N/A
	Al Etch	65 W HF 1000 W ICP 4 mTorr 50 °C	Cl_2 BCl_3 HBr	10 10 30	220 $^{nm}/_{min}$
W	W etch	20 W HF 1000 W ICP 5 mTorr 20 °C	CHF_3 SF_6	15 15	160 $^{nm}/_{min}$

gases so a thinner 100 nm layer was used for these metals.

6.3.6 Frequency measurement technique

Laser Doppler vibrometry (LDV) was used as a means to monitor the resonance frequency of the fabricated MEMS devices. The samples were loaded into a vacuum chamber placed on top of a Peltier heating element with a mechanical clamp. A piezoelectric actuator was fixed onto the heater beside the chip and was used to drive the strings into resonance. The chamber was pumped down to a vacuum level below 1×10^{-5} Torr for when the measurements were taken. A laser was incident on the string near the longitudinal center, and the frequency was monitored along with amplitude by an external program. The heating element was driven by an external power supply in a stepwise manner from 20-100 °C.

6.4 Results and discussion

In the preceding sections, several processes were discussed and performed towards the goal of fabricating a VO_2 microstring. Here, we will discuss the outcome of each of these steps, and conclude with a detailed, optimized process for the integration of VO_2 into conventional MEMS fabrication processes. In each section, the success or failure of each process will be presented, along with an explanation regarding the best way to proceed.

6.4.1 Etchability of the VO_2 and TiO_2 layers

Three different process were investigated for the removal of the VO_2 and TiO_2 layers; RIE, VHF, and ablation. While it is no surprise that ablation was successful in removing the desired layers, an unwanted consequence of this technique is that it also removes the protective layer, and introduces a rough surface which may be more reactive to future processing. However, it is possible to deposit a thicker protective layer although there is a practical limit to which that is feasible, and therefore this method should only be used if all other methods have failed.

RIE etching of VO_2/TiO_2 proved to be extremely successful using the SiN anisotrpic etch. Successful etching of VO_2 has been shown previously with O_2 and CHF_3 plasma chemistries in CN Patent 104332392 A [150]. The issue with this process proposed is the high pressure, flow rates, and relatively high power (up to 800 W) can cause significant damage to the resist/etch mask materials. Ruzmetov et al. have shown that VO_2 can be etched using a CF_4/Ar gas mixture (10/20 sccm flow rates) at a lower power than the previous CHF_3 based chemistry (90 W forward bias) [151]. With a mixture such as this, it is possible the contribution of the CF_4 can be questioned due to the abundance of Ar gas, which would just physically remove the material via ablation. US Patent 6333270 B1 showed the possibility of etching VO_2 thin

films by a mixture of SF_6 and CO_2, at a high etch rate over 200 $^{nm}/_{min}$, but at a relatively high power and flow rate (500 W and almost 200 sccm) [147].

The proposed etch chemistry used in this work comprised of CHF_3, CF_4, and O_2 in a one step process at a lower power (200 W) and a much lower gas flow rate (<50 sccm). While we suffer from a much slower etch rate, the use of a metallic masking layer allows for the slower removal. The VO_2 and TiO_2 films were deposited to a thickness of $\sim$ 25 nm each, and the etch time for complete removal was approximately 5 minutes. This gives us an average etch rate between the two layers of ~ 10 $^{nm}/_{min}$. We can confirm that the method is chemically etching the film as opposed to ablating it by measuring the thickness of an inert layer, which should remain unchanged if there is no ablation. By inserting a sample of VO_2/TiO_2 with some areas covered in a known thickness of Cr/Au (Au on top) we were able to confirm the absence of ablation by monitoring the metal layer thickness.

VHF etching of the VO_2/TiO_2 films showed minimal success. profilometry along with film thickness measurements (Filmetrics) showed minimal changes in the thickness of the device, even with a prolonged exposure to a higher pressure VHF etch. However, visual appearance indicated some change to the surface, which may provide alternative avenues for VO_2/TiO_2 removal. However, considering RIE proved more successful, and eliminates an extra process step (SiN can be removed in the same procedure by increasing the RIE etch time), there was no purpose to explore this process further.

From the three options investigated, there are two viable methods for etching the VO_2 and TiO_2 layers, both of them in the same NGP80 RIE. The chemical removal of the films is the preferred method as this ensures the stability of the protective layer for subsequent processing steps. Additionally, since this step uses the same process parameters and etch chemistry as the SiN step, it reduces overall processing time by enabling the etching of three

layers consecutively with one process by just increasing the etching time. There is no need to vent the chamber, remove the samples, clean the chamber and re-insert the samples to run another process if the processes are identical.

6.4.2 Suitability of the hard mask material

Perhaps the most critical parameter in this entire process is the selection and performance of the hard mask material. This material needs to be able to withstand the VO_2, TiO_2, SiN, and the SiO_2 removal steps, in addition to being able to remove said material without damaging the underlying films. Three materials were selected as candidates for this step, and to determine the most suitable mask material, each was subjected to all the steps that would be encountered during processing. Cr, W, and Al were all chosen as mask materials as they are easy to deposit and remove, and are commonly used in fabrication as hard mask materials.

VHF and RIE resistance of Cr, W, and Al

The metal mask layer was deposited onto the substrate after the second lithography step had defined the area for the string. All three of the metals showed no stability issues during the resist removal step (with occured in acetone) so the first step was to test how the mask would withhold VHF etching. The VHF etching step was determined to be more critical as there exists some literature on the stability of these metals in RIE (some of our previous experiments also confirmed this) [149, 152]. The metallic films were prepared on the VO_2 coated substrates by magnetron sputtering. Once the metal layer was deposited, the samples were placed into the VHF system simultaneously and subjected to the etch outlined in the string release section (in subsequent tests the etch time was increased to accommodate wider devices and thicker oxide layers).

According to the work done by Williams et al. in 2003, Cr and W both showed excellent resistance to VHF etching, while Al showed a visibly roughened surface [149]. What was observed upon removing the samples from the etching chamber was the following: Cr displayed no visual signs of etching, the Al films were visibly altered but still present, and the W films appeared to be etched away. These findings agree partially with those of Williams, apart from the W etching that was observed in this work. Of course, the differences could arise from different equipment and processing conditions, but it should be noted that the VHF system used in this work did in fact, attack the W film to the point it was deemed unsuitable as an etch mask. From these results it is clear that the best choice of metal would be Cr, however, there is still the etch resistance in RIE and the VO_2 stability in the metal stripping to be considered. This step does not rule out W or Al, as the VHF was shown to not affect the VO_2 significantly, but it would be preferred to limit the exposure of VO_2 to as much processing as possible.

The resistance of each of the metals to RIE was tested in the same way as for VHF etching. Each metal was placed into the NGP80 plasma etching system and subjected to the same etch processes it would incur during the actual process. For Cr and Al, visual inspection indicated no noticeable change, and this was confirmed by profilometry and film thickness monitoring which showed minimal to no etching (measurements before and after etching were all within $\sim$5 nm of one another). For W however, there was appreciable etching, though the rate was low enough to still consider it as an option (i.e. the etch rate was much slower than the time needed to etch the underlying films completely). From these results it is clear that all three of the metals are suitable etch masks to this point.

Stability of VO_2 during metal stripping

Once we have established which of the metals would survive VHF and RIE, the stability of VO_2 during the metal stripping step must also be established. If VO_2 was etched in this step, this would ruin the device as the phase change effect caused by VO_2 would be lost. While each etch recipe has known etch rates, which should theoretically mean we can time the etch to the nanometer, the reality is that there are many variables to consider that can slightly alter the etch rate. Film uniformity from the deposition process will cause thinner and thicker locations on the substrate, position in the plasma chamber can lead to variable etch rates, and in general each etch process may vary in etch rate by a certain degree. Because of these reasons, there is a very high probability that the underlying VO_2 layer will in fact be exposed to the harsh chemicals required to etch the Cr, W, and Al layers, making it a necessity that we understand which metal etch has the lowest effect on the quality of the VO_2 films. To test VO_2 stability, much like the testing of metals to the RIE and VHF, VO_2 was exposed to the etching process required to strip the metals.

VO_2 films were etched with the conditions shown in Table 6.1, and the results will be discussed hereafter. Given the etch rates listed in Table 6.1, and the thicknesses of each metal (W= 250 nm, Cr, Al= 100 nm) the etch times for W, Cr, and Al are approximately 95, 32, and 28 seconds respectively. Given the possible variability in each layers thickness and corresponding etch rates, each etch time was rounded up by 5-10 % to ensure complete removal. This indicates that the underlying VO_2 layer could be exposed for significant time (up to $\sim$ 20 % of the total etch time). Shown in Table 6.2 are the parameters and results of each metal etch on the VO_2 films. The etch time in each case was exaggerated to encompass any extreme cases that may arise.

As shown in Table 6.2, the W etch completely ruined the VO_2 film, while the Cr etch had virtually no effect on the VO_2 layer. This is to be expected once we had established that CHF_3 based plasmas chemically etched VO_2 in

Table 6.2: VO_2 etching in the PlasmaPro 100 Cobra Etch system

Etch Process	Etch time (mm:ss)	VO_2 physical appearance after
Cr	1:15	no visual change to the film
Al	1:00	no visual change to the film
W	1:45	VO_2 was visibly altered/removed

previous sections. Perhaps the more surprising fact of these results is that the chlorine based plasmas used for both Cr and Al etching did not affect the VO_2 film, although previous reports have been published on successful Cl_2/Ar based plasma etching of VO_2 [153, 154]. Though those reports both suggest that the mechanism is dominated by the production of VCl_3 and VCl_2 volatile byproducts, the results presented herein suggest this is not the case. By using such a low forward power, as we have in this work, the etching process is dominated by the chemical processes and not by the physical ablation. Common to the work done by Ham et al. [153] and Efremov et al. [154] is the use of a high percentage of Ar (~ 75 % in both) and high forward power indicating that the etching may occur by ablation instead.

6.4.3 Etching summary and optimized process flow

Several etch processes were attempted on a variety of materials, with varied success. A summary of the etch processes and materials investigated in this work is shown in Table 6.3, where etch rates are included when known, otherwise the result is indicated qualitatively rather than quantitatively.

From the information present in Table 6.3, we can start to assemble the most appropriate fabrication process for the VO_2 strings. This process is summarized by the specific process flow diagram shown in Figure 6.4, which is presented as an updated and more specific version of Figure 6.1. After defining the microstring with the image reversal resist, a Cr hard mask layer was deposited to use as a sacrificial masking layer. From Table 6.3, Cr performed the most admirably throughout the entire spectrum of etch

processes making it the obvious choice over W and Al. W was eliminated right away after determining VO_2 was removed during this etch process and Al, although it would work, was not chosen as it was roughened in the VHF step, while Cr was not.

Three methods were tested to etch the VO_2 and TiO_2 layers, with RIE resulting in the optimal choice. RIE was chosen over ablation as it did not have any affect on the mask material, while sufficiently etching the layers. VHF was eliminated from contention as it did not etch the desired layers in an appropriate amount of time. Another reason for choosing RIE was that the underlying SiN layer was removed with the same etch recipe, thus saving time and limiting the exposure to additional processes.

To release the MEMS devices, typically a buffered oxide etch (BOE) is used, followed by critical point drying (CPD) to prevent stiction. Here, we opted for VHF in order to remove the necessity for CPD as the vapour phase process prevents stiction from occuring. The VHF process etched and undercuts the oxide layer, with little effect on the other materials, besides SiN. When exposed to the VHF process, the SiN layer will form an NH_4F layer on the surface, which results in a roughened layer. This layer can be easily removed in to gas phase NH_3 and HF vapours by heating the sample above 200 °C. As evident by Table 6.3, none of VO_2, TiO_2, or Cr layers are affected by VHF,

Table 6.3: Etching characteristics of the materials and processes used in VO_2 string fabrication. Values in brackets indicate the observed etch rate in $^{nm}/_{min}$.

Etch Process	VO_2	TiO_2	SiN	Cr	Al	W
SiN RIE	E ($\sim$ 10)	E ($\sim$ 10)	E ($\sim$ 70)	N	N	E (rate unknown)
VHF	N,C	N,C	N,R	N	R,C	E,C
Cr etch	N	$^N/_A$	$^N/_A$	E ($\sim$ 190)	$^N/_A$	$^N/_A$
Al etch	N	$^N/_A$	$^N/_A$	$^N/_A$	E ($\sim$ 220)	$^N/_A$
W etch	E ($\sim$ 15)	$^N/_A$	$^N/_A$	$^N/_A$	$^N/_A$	E ($\sim$ 160)

E=Etch works
N=Material unaffected
R=Surface roughened
C=film changed color
$^N/_A$=Etch not applicable

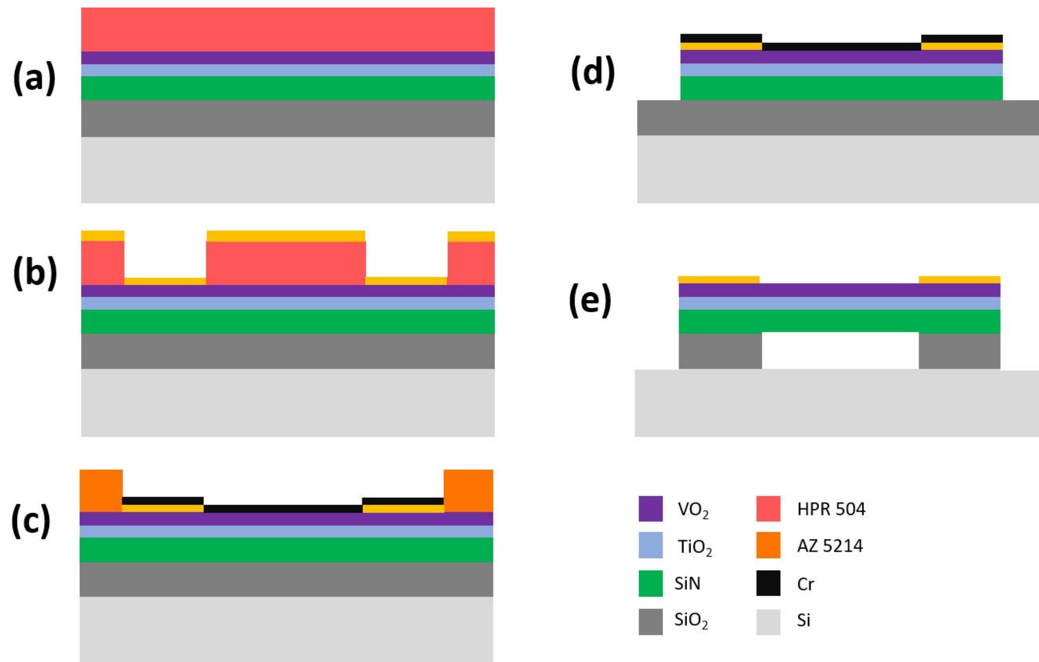

Figure 6.4: Optimized process flow formulated by this work to fabricate VO_2 microstring resonatore. (a) Starting substrate with HPR 504 photoresist spun on at a 1.3 µm thickness, (b) lithographic patterning of contact pads and Cr/Au deposition by sputtering, (c) defining the string geometry and depositing Cr mask and photoresist removal by sonication in acetone, (d) etching the VO_2, TiO_2, and SiN via CHF_3, CF_4, and O_2 based plasma in RIE, and (e) releasing the string (SiO_2 VHF etching), and Cr mask stripping by ICP.

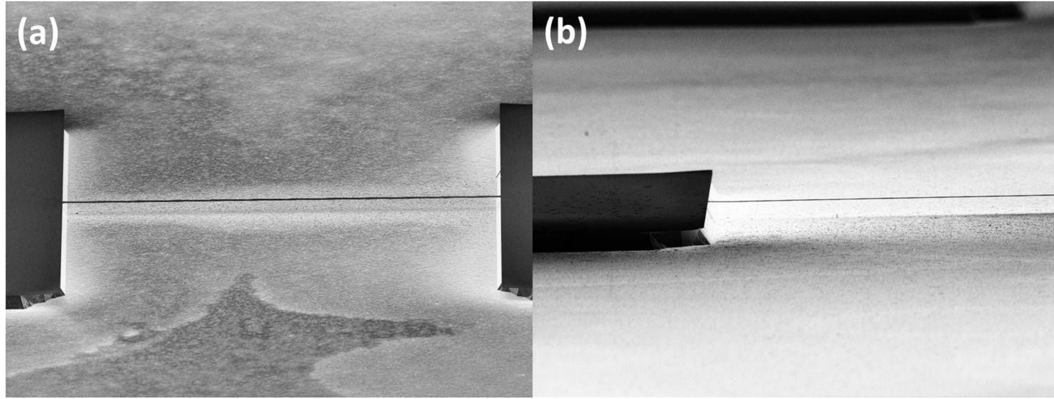

Figure 6.5: SEM micrographs depicting the (a) final VO_2 string (length= 400 µm of the string presented here) and (b) side profile of the same string showing the released nature.

therefore preventing any lateral etching of the device layer. Once the devices had been released, the Cr layer was removed via metal etching with the recipe outlined in Table 6.1. The resulting string, as fabricated by this process, can be seen in Figure 6.5 taken via SEM.

6.4.4 Resonant frequency shift caused by heating

LDV was used to measure the resonant frequency of the microstring under vacuum in order to confirm the string was successfully released. The resonant frequency of a doubly clamped cantilever beam can be calculated by [139],

$$f_0 = \frac{(i + 1/2)^2 \pi}{2l^2} \sqrt{\frac{EI}{\rho A}} \tag{6.1}$$

where f_0 is the resonance frequency, i is the mode of vibration, E is Young's modulus, I is the area moment of inertia, ρ is the density of the beam material, and A is the cross-sectional area of the beam in question. Here we are investigating the first mode of vibration, and the term inside the square

root can be simplified so equation 6.1 can be re-written as,

$$f_0 = 1.03\,\frac{t}{l^2}\sqrt{\frac{E}{\rho}}. \tag{6.2}$$

However, equation 6.2 does not account for the internal stress accumulated by the deposition conditions of the SiN layer. To accurately represent the frequency of the string, the tensile stress in the SiN layer must be accounted for (1.2 GPa in our SiN layer). Shown in equation 6.3 is a representation of the resonant frequency with residual stresses accounted for [139].

$$f_0 = 1.03\,\frac{t}{l^2}\sqrt{\frac{E}{\rho}}\sqrt{1+\frac{Sl^2}{i^2 EI\pi^2}} \tag{6.3}$$

In Equation 6.3, S is actually the tensile force, not stress, and shall be converted accordingly. Additionally, equation 6.3 is valid for a single material beam, but provides an excellent starting point to determine the frequency of the string. Since the majority of the string thickness is the SiN layer, the values of E and ρ were selected to be those of SiN. Using input values of 290 GPa and 2.75 g/cm^3 as E and ρ, respectively, dimensions of 3 µm wide $\times$ 250 nm thick $\times$ 200 and 400 µm long, and a tensile force of 1.5 mN to 150 µN, the expected resonant frequencies range from 1.2-2.4 MHz. Of course the additional VO_2 and TiO_2 layers will affect these values, both by the additional mass and stress added by deposition. The actual resonant frequency of the strings tested in this work, at room temperature, was 365.6 and 739.2 kHz for the 400 and 200 µm strings, respectively. The resonant frequency for each string was monitored as temperature was increased and the resultant Δf is shown in Figure 6.6

As shown in Figure 6.6, both strings showed the same magnitude change relative to the room temperature resonant frequency. This change in magnitude is clearly attributable to the phase transition, as the resonant frequency

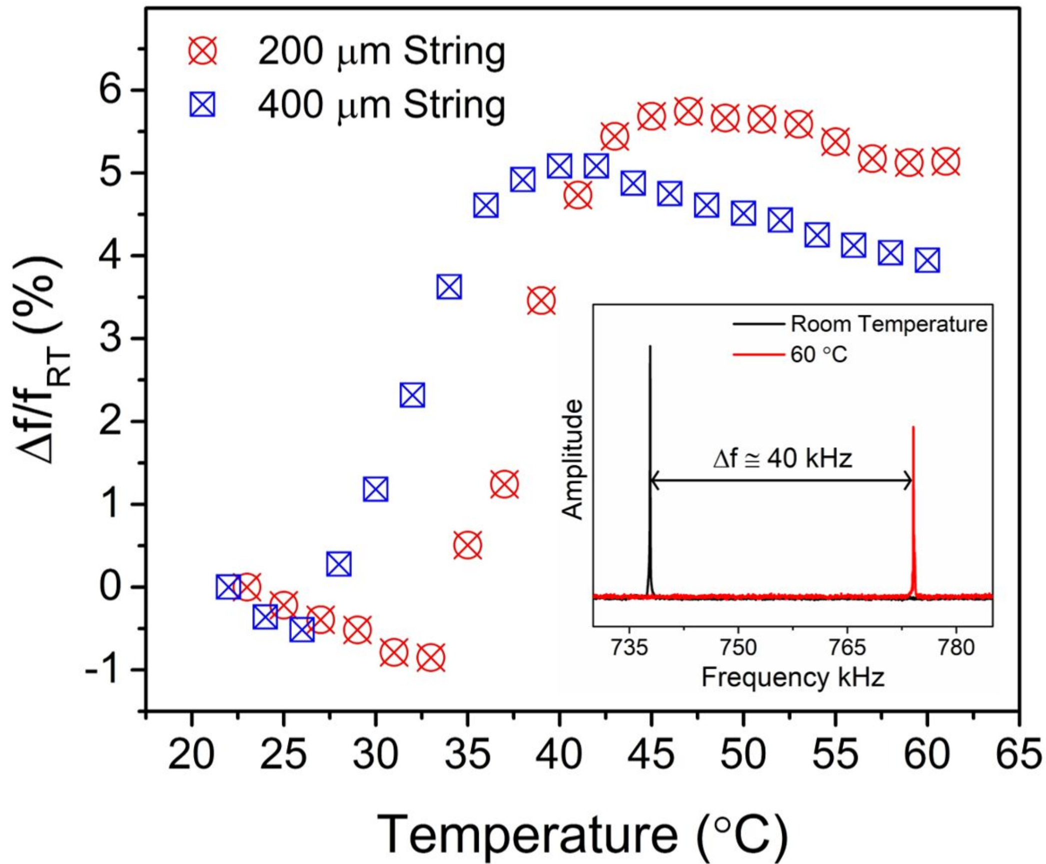

Figure 6.6: Metal-insulator transition as observed for VO_2/TiO_2 coated cantilevers as showing a significant increase in the resonant frequency across the MIT, determined by LDV. Inset: Resonant frequency peaks showing the Δf of ∼43 kHz due to the MIT.

of such a device typically decreases with increasing temperature. The usual decrease is due to a softening of the material leading to a decreased Young's modulus, as shown in equations 6.2 and 6.3 would result in a decrease in the resonance frequency. These experiments provide proof of the two objectives: first, the string was released properly as demonstarted by the fact the string did resonate, and second, that the process put forth did not destroy the VO_2 layer, evident by the MIT observed in Figure 6.6.

6.5 Conclusion

Here we presented a detailed report on the fabrication and process considerations for VO_2 microstrings. Primarily, we investigated the ramifications certain microfabrication processes had on the structure and stability of not only VO_2, but how these methods affect the entire process and all materials involved. Such a thorough, full-scale investigation into VO_2 based device fabrication does not yet exist. RIE, VHF, and metal etching were conducted for cross-compatibility with one another. We established an optimized process for VO_2 based MEMS devices by a full scale investigation into a variety of processes. We determined that the best route for fabrication involved VO_2, TiO_2, and SiN etching by RIE with a Cr hard mask protecting the device. The string was released by VHF instead of BOE to avoid stiction or the use of CPD, and ICP etching was used to remove the Cr layer. The successful fabrication of the strings was confirmed by LDV monitoring of the resonance frequency, and frequency shift induced by external heating. A resonance frequency increase of over 5 %, regardless of the string length, was evidence of the MIT which confirms the process is successful. This investigation will provide invaluable information for future fabrication of VO_2 MEMS structures.

Chapter 7

Effect of interface on mid-infrared photothermal response of MoS_2 thin film grown by pulsed laser deposition

7.1 Abstract

This study reports on the mid-infrared (mid-IR) photothermal response of multilayer MoS_2 thin films grown on crystalline (p-type silicon and c-axis-oriented single crystal sapphire) and amorphous (Si/SiO_2 and Si/SiN) substrates by pulsed laser deposition (PLD). The photothermal response of the MoS_2 films is measured as the changes in the resistance of the MoS_2 films when irradiated with a mid-IR (7 to 8.2 μm) source. We show that enhancing the temperature coefficient of resistance (TCR) of the MoS_2 thin films is possible by controlling the film-substrate interface through a proper choice of substrate and growth conditions. The thin films grown by PLD are characterized using X-ray diffraction, Raman, atomic force microscopy, X-ray photoelectron microscopy, and transmission electron microscopy. The high-

resolution transmission electron microscopy (HRTEM) images show that the MoS_2 films grow on sapphire substrates in a layer-by-layer manner with misfit dislocations. The layer growth morphology is disrupted when the films are grown on substrates with a diamond cubic structure (e.g., silicon) because of twin growth formation. The growth morphology on amorphous substrates, such as Si/SiO_2 or Si/SiN, is very different. The PLD-grown MoS_2 films on silicon show higher TCR (-2.9%$\cdot K^{-1}$ at 296 K), higher mid-IR sensitivity ($\Delta R/R$ = 5.2%), and higher responsivity (8.7 $V \cdot W^{-1}$) compared to both the PLD-grown films on other substrates and the mechanically exfoliated MoS_2 flakes transferred to different substrates.

7.2 Introduction

Ultrathin two-dimensional (2D)-layered transition metal dichalcogenides (TMDCs) with the MX_2 formula, where M = Mo, W, Nb, Ta, Ti, Re and X = S, Se or Te, have attracted significant attention because of their potential applications in nanoelectronics [43, 155], optoelectronics [44, 156] valleytronics [41], and spintronics [48]. Among all the TMDCs, molybdenum disulphide (MoS_2) is a semiconductor ($\geq$1.9 eV) with a direct electronic band gap when formed as a monolayer ($\sim$6.5 Å in thickness). However, MoS_2 behaves like an indirect band gap semiconductor with a band gap of 1.29 eV when the film thickness is more than five layers [157].

Devices based on monolayer MoS_2, specifically transistors, exhibit high current density, excellent electrostatic integrity, large on/off ratio (>108), unpre- cedented carrier mobilities of 200-500 $cm^2 \cdot V^{-1} \cdot s^{-1}$, and good electrical conductivity ($\sim 0.03 \Omega^{-1} \cdot cm^{-1}$) [158, 159]. In addition, single and multilayer (>5 layers) MoS_2 have shown much promise as ultrasensitive visible and ultraviolet (UV) photodetectors [7, 160], field emitters [161], gas sensors [162], and piezoelectric and piezotronic devices [163, 164]. They have also exhibited

potential in photoelectrochemistry applications [165]. The photo- detection mechanism of MoS_2 depends on its high absorption in the UV-visible (Vis) range and the generation of electron-hole pairs under photo-excitation [7]. This allows the device to produce large photocurrents/voltages under the applied bias and reduces its electrical resistance. Aside from the UV-Vis range, some recent literature also showed that MoS_2 hybrid structures can be used as an ultrasensitive near-infrared (IR) photodetector based on the hetero- junction and electrostatic field tuning principle [8, 166]. However, no such reports on the variation of the electrical resistance of MoS_2 irradiated in the mid-IR range, which can be the basis of mid-IR detection devices, exist.

The materials for the mid-IR (7 to 8.5 μm) detection require a smaller band gap of 140 to 170 meV, which is similar to that of the routinely used HgCdTe (MCT) that operates on the typical photoconductive mechanism [167]. Despite its outstanding performance as an IR detector, the MCT suffers from disadvantages, such as weak Hg-Te bond, toxicity caused by heavy metals, and high power consumption [168]. In addition, this device requires cryogenic cooling to increase the high signal-to-noise ratio [169]. Hence, alternative materials, such as vanadium oxide (VO_2) or amorphous silicon, are used as uncooled IR detectors and micro-bolometers working with the use of the resistance change caused by the IR illumination [170–172]. Despite much effort, limited literature is available on mid-IR detection using these materials. Promising reports have recently been presented on the near-IR and mid-IR photothermal responses of 2D materials, such as graphene and graphene oxide (GO) [173–175]. Bae et al. demonstrated the photothermal effect of GO in the mid-IR range (7 to 14 μm) under external heating [173]. Nevertheless, investigation of the room temperature mid-IR photo- thermal response of these materials is still lacking. However, it can show a significantly enhanced photothermal response in the mid-IR range because of the broadband mid-IR absorption of MoS_2 [176]. The resistance of MoS_2 changes

when exposed to mid-IR because of the photothermal effect. The resistance variation of a material caused by heating depends on its temperature coefficient of resistance (TCR). Hence, materials with a high TCR can be used for IR detection using the photothermal effect. The TCR of a thin film is greatly influenced by its microstructure and the substrate-film interface for materials, such as $La_{0.7}Ca_{0.3}MnO_3$ on $LaAlO_3$ and $SrTiO_3$ substrates [177]. However, no systematic study has been conducted on the effect of the film-substrate interface and the film morphology on the TCR of MoS_2, except for a brief report in the early literature [178].

In this work, we systematically investigated the growth condition and behavior of MoS_2 thin films deposited by pulsed laser deposition (PLD) on four different substrates. We also explored the photothermal response of the MoS_2 films in the mid-IR range (7 to 8.2 μm). The PLD technique offers great advantages because it rapidly and directly transfers the phase from the target to the substrate to achieve a uniform deposition. However, PLD also produces defects at the substrate-film interface because of the highly non-equilibrium growth and high ion bombardment from the target to the substrate [179, 180]. These defects can cause remarkable property changes in the film [10]. For instance, in terms of the electrical properties of MoS_2, the defects may introduce additional energy states in the band gap, which can change the n-type MoS_2 thin film to p-type and vice versa [181]. A phonon- assisted phenomenon can also be introduced because of the presence of the defect states in the band gap demonstrated by Raman spectroscopy [182]. Hence, two crystalline substrates of different crystal structures (i.e., p-type silicon and single crystal sapphire) and two amorphous substrates (i.e., Si/SiO_2 and Si/SiN) with no specific orientations were chosen for this study. Although a few reports on the substrate effect on the optical and electrical properties of MoS_2 have been published, they are restricted to the film transfer method only [183, 184]. Therefore, enhancing the TCR of MoS_2 films is possible by choosing the right

substrate for deposition. We employed the simple concept of the theoretical lattice mismatch strain between the highest atomic density plane of MoS_2 (i.e., (0001) plane) and the planes parallel to the substrate surface to optimize the film's structural characteristics. On the one hand, the *hcp* crystal structure of MoS_2 and the (0001) orientation of sapphire allowed a theoretical lattice mismatch strain of $\sim$6%, which results in a semi-coherent interface. On the other hand, the theoretical lattice mismatch strain between the p-type silicon and the highest atomic density plane of MoS_2 is $\sim$40%, which can form an incoherent interface. The films grown on the amorphous substrates with no specific orientation can grow with spatially large structures because no lattice mismatch strain occurs in the film and the substrate. Therefore, tuning the TCR characteristics and the mid-IR response is possible by controlling the lattice mismatch strain between the substrate and the MoS_2 film. We also compared the mid-IR response of mechanically exfoliated MoS_2 flakes with the PLD-grown MoS_2 on different substrates.

7.3 Experimental

7.3.1 Material synthesis and deposition

A two-inch MoS_2 target was prepared by pelletizing MoS_2 powder with a 99% purity (Sigma Aldrich) using a 50 kN force load in a hydraulic press. The pellet was sintered at 800 °C for 12 h in a tubular furnace in a continuously flowing Ar atmosphere. The MoS_2 pellet was then mounted on a target holder inside the PLD chamber (Excel Instruments, Mumbai, India). Four different substrates were used for deposition: p-type silicon $\langle 100 \rangle$ oriented (ρ = 10-20$\Omega \cdot$cm), single crystal sapphire (0001), thermally grown silicon oxide (Si/SiO_2 $\sim$500 nm) on silicon, and low-pressure chemical vapor deposition (LPCVD)-grown low stress silicon nitride (amorphous SiN $\sim$250 nm) on

silicon. The deposition was performed at two different substrate temperatures of 700 to 800 °C to investigate the effect of the deposition temperature on the growth morpho- logy. The distance between the target and the substrate was maintained at 5 cm for all the depositions. A high- base vacuum was achieved (1×10^{-2} to 2×10^{-2} mTorr) in the chamber prior to the deposition. The deposition was done in the presence of argon (Ar) at a chamber pressure of 11 mTorr to prevent oxidation and sulfur evaporation. A krypton fluoride (KrF, λ = 248 nm) excimer laser (Coherent, GmbH) was used with a 20 ns pulse width and a repetition rate of 5 Hz. Two different laser energies (i.e., 35 and 50 mJ) were used for deposition. The effective laser fluence was approximately 1.2 $J \cdot cm^{-2}$ (energy: 35 mJ) and 1.7 $J \cdot cm^{-2}$ (energy: 50 mJ), considering a laser spot size of 3 mm $\times$ 1 mm measured at the target. The deposition time was varied from 5 to 300 s to investigate its effect on the MoS_2 film morphology. The substrates were cooled down to room temperature in the same Ar atmosphere while maintaining a constant chamber pressure of 11 mTorr. Table 7.2 (in the Electronic Supplementary Material (ESM)) shows the different deposition parameters used to grow the MoS_2 thin films on various substrates. In addition to the PLD-grown film, the mechanically exfoliated MoS_2 flakes from molybdenum disulfide single crystal were also transferred on two different substrates (i.e., silicon and Si/SiO_2). The details are mentioned in the ESM.

7.3.2 Characterization

The PLD-deposited MoS_2 samples were characterized by X-ray diffraction (Cu Kα) using Rigaku XRD Ultima 4 in a glancing angle mode with an incident angle of 0.5°. Raman spectroscopy was performed using an Almega XR dispersive Raman microscope (Nicolet, Thermo Scientific) at 5 mW laser power using 50× objectives. An excitation wavelength of 532 nm was used, and a spot size of 1 μm was maintained to avoid the possible heating effects.

The surface topography and film thickness were measured using the Dimension Fast Scan Atomic Force microscope (Bruker Nanoscience Division, Santa Barbara, CA, USA). Commercially available Pt-Ir coated conductive probes (SCM-PIT) with a spring constant of 2.5 $N{\cdot}m^{-1}$ and a resonant frequency of 65 kHz were used to obtain the surface topography. Meanwhile, X-ray photoelectron spectroscopy (XPS) and ultraviolet photoelectron spectroscopy (UPS) were performed at a base vacuum of 1.5×10^{-5} mTorr using a Kratos imaging spectrometer to discern the chemical com- position and the work function of the film. UPS was conducted using a helium source. A UV-Vis spectroscopy of the MoS_2 samples deposited on sapphire was performed using a Perkin Elmer spectrophotometer, while photoluminescence was done using the LabRAM HR system. The film thickness and morphology were characterized using scanning electron microscope (SEM) (Zeiss Sigma) and transmission electron microscope (TEM) (Titan, FEI, The Netherlands operated at 300 kV). TEM foils with less than 100 nm thicknesses were prepared using a focused ion beam machine (Hellios 600, FEI, The Netherlands), followed by a lift-off method. The film thickness measurements and the diffraction analyses were conducted to determine the crystallinity through the fast Fourier transform (FFT) method using digital micrograph software (Gatan Inc.).

7.3.3 Mid-IR photothermal response and electrical characterization

The mid-IR photothermal IR characterization of the deposited MoS_2 films was performed using a quantum cascade laser (QCL) model ÜT8 (Daylight Solutions, USA). The QCL was operated at a 5% duty cycle pulsed at 100 kHz with a peak power of 400 mW in the mid-IR range (1,200 to 1,400 cm^{-1} $\sim$ 8.3 to 7.1 µm) and with a spot size of $\sim$2.5 mm. In these experiments, the average power of the QCL was varied up to 25 mW. The contact pads

of Ti/Au (5/50 nm) of 0.5 mm diameter, which were separated by a 1 mm distance, were deposited by e-beam evaporation using an aluminum hard mask. The films were annealed at 200 °C for 1 h in a vacuum (10 mTorr) oven to reduce the contact resistance. Relatively thicker films (300 s deposited at 800 °C) of MoS_2 deposited on different substrates were used for this study to ensure a measurable resistance within the contact pad distance. The electrical resistance of the films was measured by a two-probe method using a Keithley 194 digital multimeter interfaced with LabView. The resistance changes were monitored by pulsing the laser every 120 s without any external bias. The temperature- dependent resistance measurements were conducted using a Signatone probe station 1160 series on a heating chuck, where the temperature was varied from 23 to 110 °C at 2 °C intervals with an equilibration time of 5 min for each interval. The I-V measurements were performed using Keithley 2450 SMU.

7.4 Results and discussion

MoS_2 was deposited on various substrates at two different temperatures and deposition times as mentioned earlier. The detailed structural and morphological characterizations of the samples deposited at 700 °C are discussed in the ESM. Figure 7.1 shows the XRD and Raman characterizations of the as-deposited MoS_2 thin film grown on various substrates at 800 °C. The thin films of the MoS_2 deposited at 800 °C showed a higher degree of crystallinity of than those deposited at 700 °C. Figure 7.1(a) illustrates that the film crystallinity improves as the deposition time increases to 300 s.

Raman spectroscopy was performed on all the samples to confirm the MoS_2 formation. The Raman spectra evidently showed that the samples deposited at 800 °C exhibited an appreciable crystallinity for 20 s and 300 s deposition times. Figure 7.1(b) demonstrates that the layer thickness of

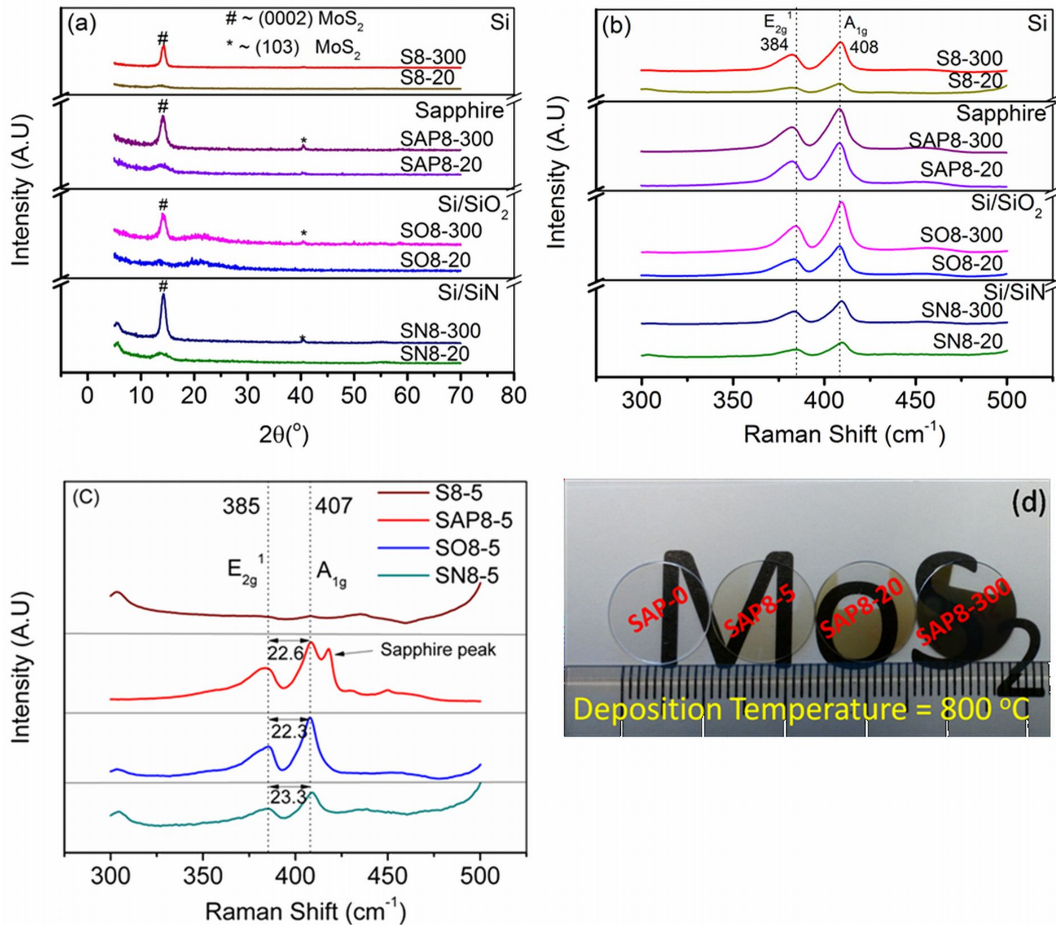

Figure 7.1: (a) XRD of MoS_2 grown on different substrates at 800 °C and 35 mJ energy. Raman spectra of MoS_2 grown on different substrates at 800 °C at (b) 35 and (c) 50 mJ laser energy for different deposition times. (d) Photograph of the MoS_2 film grown on sapphire at 800 °C at different times and laser energies. The word MoS_2 was printed on the substrate background.

the MoS_2 for 20 s deposition time was approximately three to four layers (Table 7.3 in the ESM). Meanwhile, Figure 7.1(c) depicts the formation of the ultrathin MoS_2 observed at a lower deposition time (5 s). Except silicon, all the substrates showed an appreciable growth of three to four layers at the above mentioned deposition condition. Figure 7.1(d) shows a photograph of the MoS_2 grown on the sapphire substrates at 800 °C for two different deposition times and energies. The image indicates a uniform coverage of the film and the changes in the optical transparency of the sapphire with the

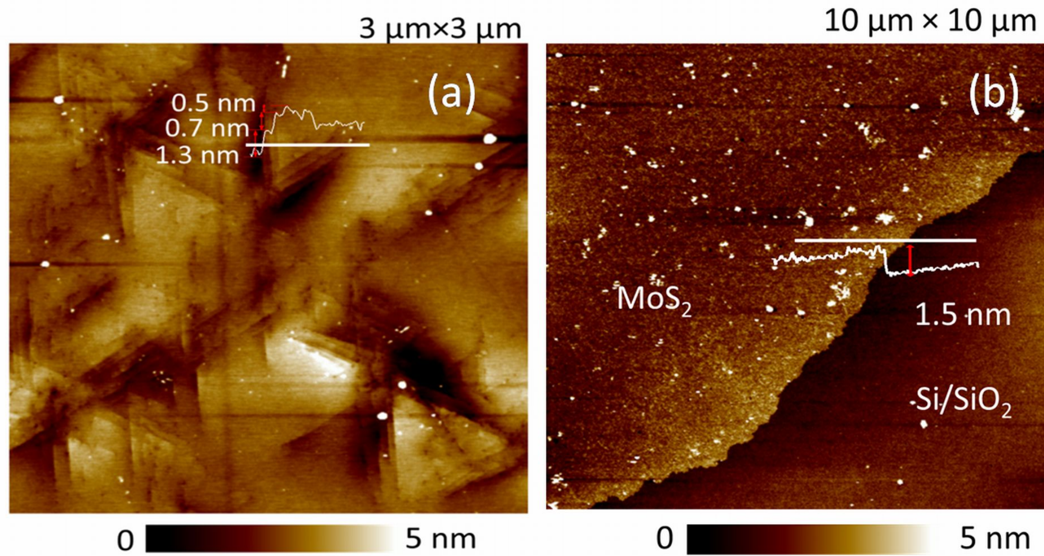

Figure 7.2: AFM images of MoS_2 grown at 800 °C on (a) sapphire (SAP8-20) at 35 mJ for 20 s and (b) thermally grown oxide (SO8-5) at 50 mJ for 5 s. The uncovered area of the thermally grown oxide in (b) is caused by the hard mask kept on the substrate while depositing MoS_2.

increasing MoS_2 layer thickness.

The surface morphologies of the films grown at 800 °C for 20 s and a laser energy of 35 mJ were different for all the substrates, as shown in the atomic force microscope (AFM) image in Figure 7.2(a) and Figure 7.12 in the ESM. The growth of MoS_2 on silicon was disrupted because the (0001) plane of MoS_2 grew on Si (100), which was not the lowest surface energy plane of silicon. Consequently, the adatoms of MoS_2 on the substrate surface were required to overcome the crystalline barrier of the (100) plane of silicon, which created more strain in the film and resulted in hairline streaks on the surface (Figure 7.12(a) in the ESM). However, the MoS_2 grown on sapphire showed a triangular morphology (Figure 7.2(a)), which was possibly caused by the growth of MoS_2 on the basal plane (0001) of the sapphire that is a hexagonal close-packed structure (*hcp*) similar to the 2H-MoS_2 structure. Meanwhile, the morphology of the MoS_2 deposited on the thermally grown oxide (Si/SiO_2) resembled a sheet with 1.5 nm thickness (Figure 7.2(b)). This result indicated

that 2 ML (monolayer) of MoS_2 sheets formed on the Si/SiO_2 substrates. The average surface roughness of the MoS_2 deposited on all the substrates at 800 °C for 20 s was in the 0.3-0.6 nm range. Furthermore, the morphology at 800 °C deposition temperature and 300 s deposition time showed a Stransky-Karstinov type of growth, which resulted in the formation of the dense nanostructures of MoS_2 in all the substrates (SEM in Figures 7.13(a) and 7.13(b) in the ESM) and agreed with the findings of Late et al. [161]. The film thickness (300 s deposited) found from the cross-sectional SEM was 16 to 18 nm (Figure 7.13(c) in the ESM). The samples deposited at 800 °C were structurally optimized. Hence, a further study on the photothermal response was performed on these samples.

X-ray photoelectron spectroscopy was conducted for all the thin films grown at 800 °C and 20 s deposition times (Figures 7.14 and 7.15 in the ESM). Regardless of the substrate they were deposited on, all the films showed a typical binding of Mo-3d and S-2p, which confirmed a typical MoS_2 growth at these conditions. A slight peak of Mo^{6+} indicated the possibility of MoO_2 and MoO_3 existence. However, no amorphous sulfur was found in the peak, indicating that the samples were of highly crystalline quality.

The optical properties of the films were characterized by UV-Vis and photoluminescence (PL) spectroscopy and shown in Figure 7.16 in the ESM. A detailed analysis and the data were also presented in the ESM. The PL spectra (Figure 7.16(b) in the ESM) clearly showed that the SAP8-5 sample exhibited a peak at 653 nm (1.89 eV), which was the direct excitonic transition from the band gap because this contained two to three layers of MoS_2. This result was also confirmed from Raman (Table 7.3 in the ESM) and AFM measurements. The peak showed a red shift as the number of layers increased while the peak intensity reduced. The signal intensity for bulk MoS_2 (SAP8-300) was very small and consistent with the reports in the earlier literature [185]. This finding confirmed that the band gap of MoS_2 changed with number of layers,

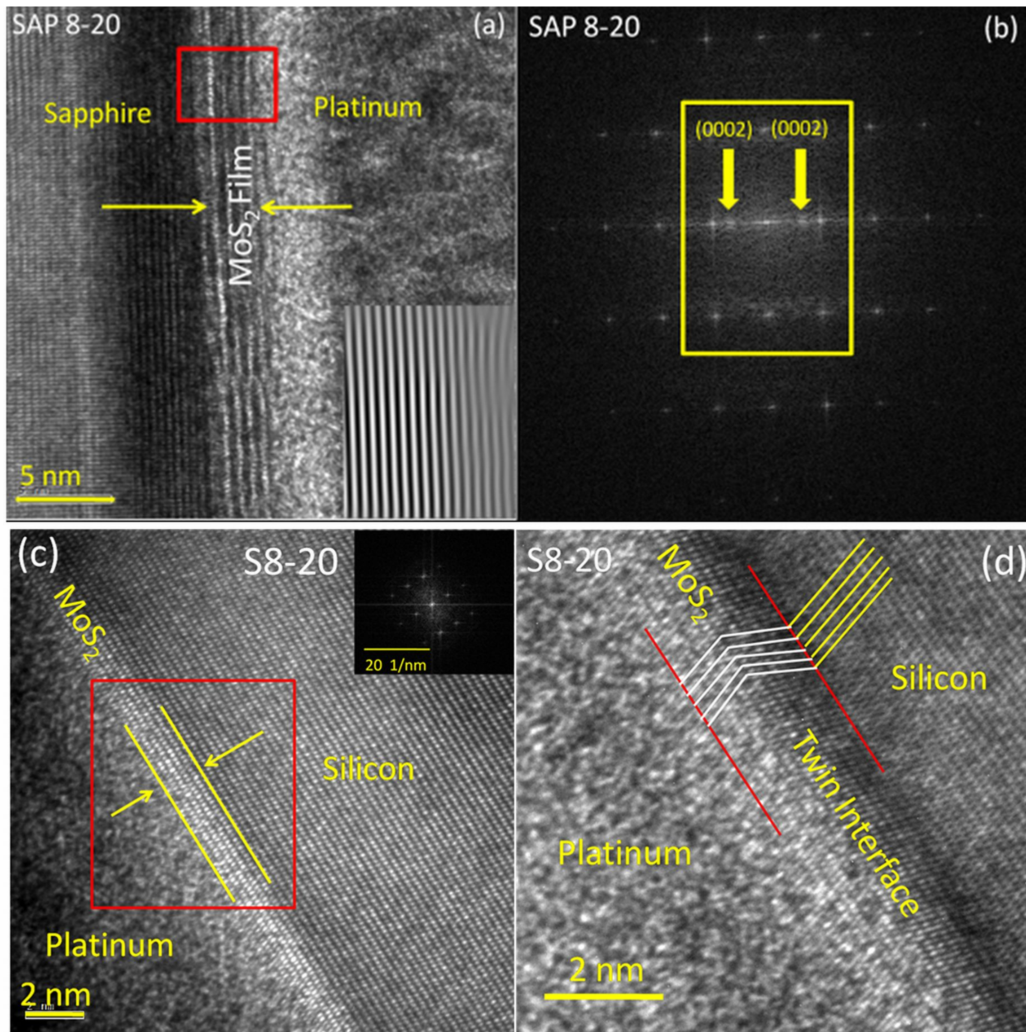

Figure 7.3: (a) Cross-sectional TEM image of the MoS2 film grown on sapphire (0001) at 800 °C 20 s deposition time showing stacking of MoS_2 with a (0002) orientation. The inset shows the inverse FFT image of the red marked area of the image showing misfit dislocations. (b) FFT pattern of the corresponding red marked zone of (a). The orientation relationship of the yellow mark area of the FFT pattern is depicted in Figure 7.17 (in the ESM). (c) Cross-sectional TEM image of MoS2 grown on silicon $\langle 100 \rangle$. The inset shows the FFT image showing no orientation relationship. (d) Twin formation of the silicon-MoS_2 interface enlarged from (c).

and the band gap of the multilayer MoS_2 deposited in all the substrates converged from 1.3 to 1.4 eV as reported in various literatures [39, 186].

The growth morphology and the film-substrate interface were characterized using a transmission electron microscope. The HR TEM image of the

SAP8-20 specimen (Figure 7.3(a)) showed stacking of the MoS_2 layers on the sapphire substrate, whereas the FFT pattern (Figure 7.3(b)) captured from the film substrate conjugate suggested that the foil normal was $\langle 11\bar{2}0 \rangle$. The spots corresponding to the (0002) planes of MoS_2 with a d-spacing of 6.147 Å were identified in the FFT image and marked using yellow arrows. The other spots from the MoS_2 film were not detected in the FFT pattern because of the presence of only a few atomic layers in the film, which reduced the amplitude of the exit wave function. A careful observation of the high-resolution transmission electron microscopy image shown in Figure 7.3(a) depicted that the film formation occurred through a stacking of a few layers (4-5 ML) of MoS_2 forming a semi-coherent relationship with the sapphire substrate. Figure 7.17(a) in the ESM shows a schematic of the observed orientation relation between the sapphire and the MoS_2 film, where the orientation relationship followed $(0003)_{Al_2O_3}||(0002)_{MoS_2}$ and $\langle 0001 \rangle_{Al_2O_3}||\langle 0001 \rangle_{MoS_2}$ Eventually, the $\langle 11\bar{2}0 \rangle$direction of MoS_2 became perpendicular to the $\langle 0001 \rangle$ direction. X-ray diffraction (XRD) showed a strong (0002) peak of MoS_2. These results confirmed that the growth of the MoS_2 film on the sapphire substrate occurred through the formation of a layered structured film. The HRTEM observations also confirmed the number of layers determined from Raman spectra and mentioned in Table 7.3 (in the ESM) and the AFM image shown in Figure 7.2(a).

The interface formation between the silicon and MoS_2 was different from that of the MoS_2-sapphire interface. The HRTEM images of the film-substrate interface of the MoS_2-Si showed that {020} types of planes of silicon were parallel to the interface, whereas the foil normal was a $\langle 103 \rangle$ direction (Figure 7.3(c)). In a similar fashion in the MoS_2-sapphire interface, the (0002) planes of MoS_2 were parallel to the (0003) planes of sapphire. The interface also exhibited a relatively smaller lattice mismatch strain of $\sim$5.6%. As a result, the interface can accommodate the strain by forming a semi-coherent

interface, creating subtle misfit dislocations (Figure 7.3(a), inset). The theoretical lattice mismatch between the Si (020) and MoS_2 (0002) planes for the MoS_2-Si system was approximately 42%. Therefore, the formation of the MoS_2 layer while maintaining this huge strain misfit was not practically realistic. The film grown on the silicon substrate formed an incoherent interface through twin formation (Figure 7.3(d)) to minimize the strain energy. This phenomenon is common in the case of the *hcp* crystal system when growth occurs on a diamond cubic or *fcc* structure through non-equilibrium processes such as the PLD [187]. The twin formation in the non- equilibrium growth of the *hcp* films occurred because of its low stacking fault energy and the limited availability of slip planes [188].

The mid-IR photothermal response of MoS_2 was studied by illuminating the top surface of the MoS_2 films grown on four different substrates using a QCL. In the following text, the samples were named by the sample code mentioned in Table 7.2 (in the ESM): S8-300, SAP8-300, SO8-300, and SN8-300. These samples were relatively higher in thickness (16 to 18 nm) than the 20 s deposited (thickness $\sim$3 to 4 nm) samples. However, the film substrate interface of these samples (300 s deposited) would be similar to the 20 s deposited samples. Hence, the explanation related to the film-substrate interface of 300 s deposited samples was based on the TEM studies of the 20 s deposited one. Figures 7.4(a) and 7.4(b) show the schematic and photograph, respectively, of the experimental set up of the MoS_2 thin film under IR illumination using a QCL. A baseline of the photo-response was taken on the bare substrates that showed no significant change in the resistance upon IR illumination. Most of the substrates (i.e., sapphire, Si/SiO_2, and Si/SiN) used in this study were highly insulating at room temperature (resistivity $\sim$1014$\Omega\cdot$cm) [189–191]. Hence, the bare substrates showed no response to the IR on/off pulses (data not shown). Figure 7.4(c) shows the variation of the resistance of MoS_2 on sapphire as a function of the different wavelengths of the pulsed IR. The

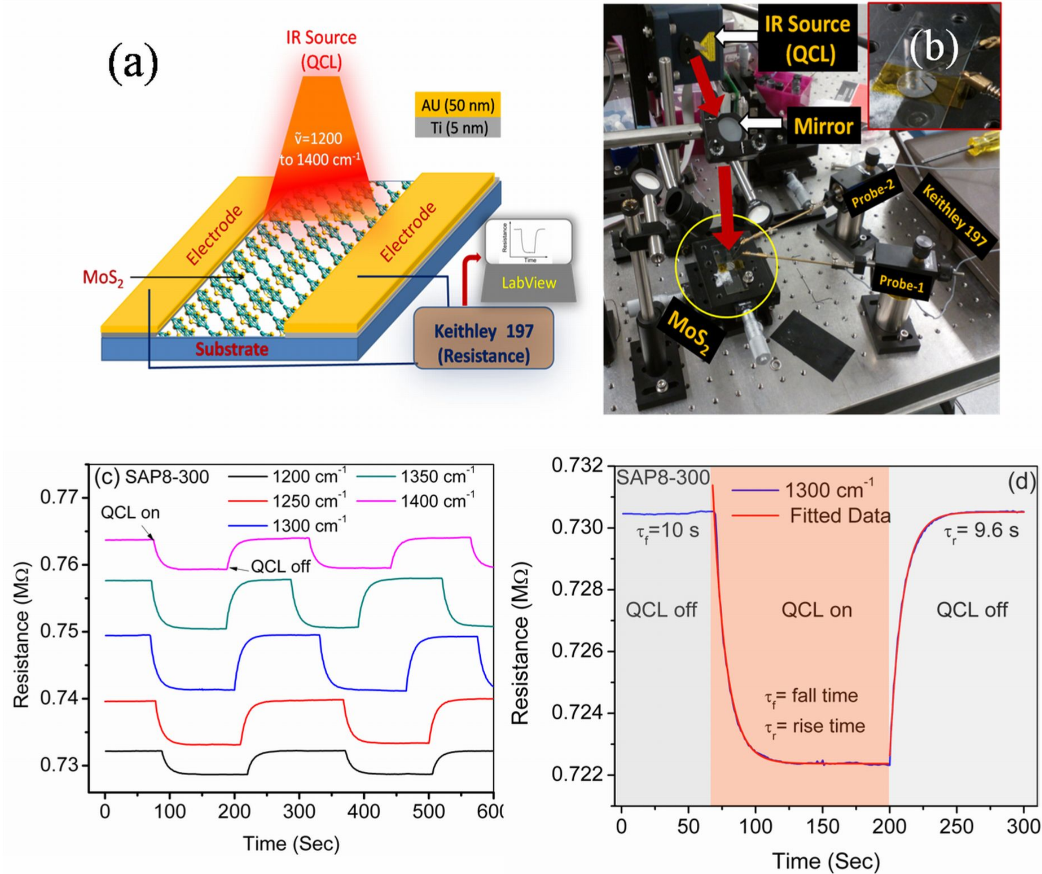

Figure 7.4: (a) Schematic and (b) photograph of the experimental set up of the mid-IR response of MoS_2 on different substrates. (c) Variation of the resistance under the mid-IR illumination of MoS_2 on the sapphire substrate (SAP8-300) at different wave numbers. The data are plotted using a 2D waterfall mode at 10 % offset to accommodate all the data set. (d) Photothermal response time of MoS_2 on sapphire (SAP8-300).

rise (τ_{rise}) and fall (τ_{fall}) times of the device (SAP8-300) to reach 63% of the saturation state was 9 and 10 s, respectively (Figure 7.4(d)). Figure 7.18 in the ESM shows the IR data of the other samples (i.e., S8-300, SO8-300, and SN8-300). The time constant was calculated by fitting an exponential decay/rise function of the measured data.

Figure 7.5(a) presents the inter-comparison of the device sensitivity in terms of the resistance change (i.e., sensitivity= $^{\Delta R}/_{R_0} \times 100\%$, where ΔR = R-R_0; and R_0 and R are the resistance before and after the IR illumination,

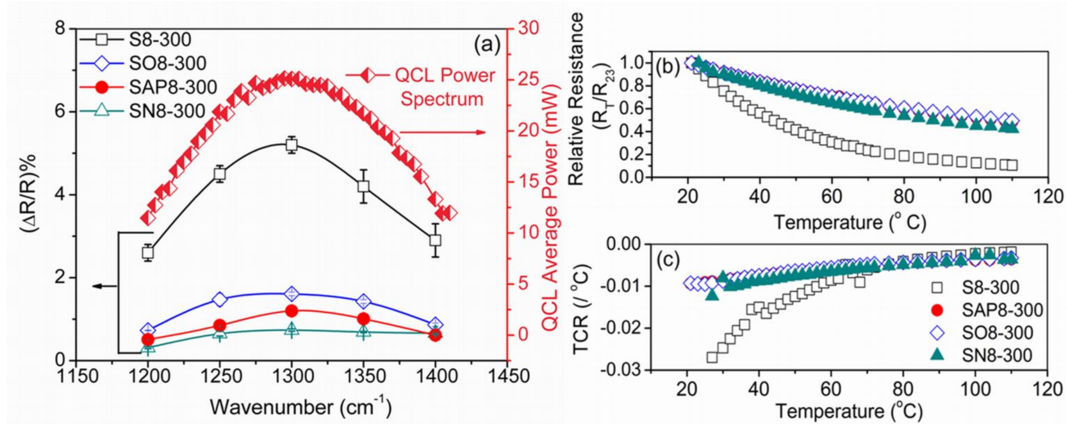

Figure 7.5: (a) Sensitivity of the photothermal response of MoS_2 grown on different substrates. The power spectrum of the QCL is shown in the same graph. (b) Relative resistance change and (c) TCR of MoS_2 on different substrates with a function of the temperature using the external heating source from the bottom of the substrate. The data are normalized with the resistance at T = 23 °C (296 K).

respectively). MoS_2 on silicon (S8-300) showed a significantly higher sensitivity than any of the other devices. The influence of the reflection from the MoS_2 interface was investigated to determine the "real" incident power, which may cause inflated sensitivity values. Using the index of the refraction value of MoS_2 determined by Wieting et al. as 3.9 ± 0.05 [192], the reflectivity in the mid-IR from the different substrate-film interface is Si = 0.43% (S8-300), SiO_2 = 42.98% (SO8-300), sapphire = 24.35% (SAP8-300), and SiN = 9.90% (SN8-300) (see ESM for a detailed derivation) and tabulated in Table 7.4 (in the ESM). The effect of the reflected light would be pronounced only in the SiO_2 and sapphire samples, while there would be a negligible effect present in the other two substrates. In addition, the MoS_2 that was mechanically peeled off from the molybdenum disulfide crystal and transferred onto two different substrates (silicon and Si/SiO_2) showed much lower sensitivity and higher response time compared to the PLD-grown films (Figure 7.21 in the ESM). Therefore, we believe that the remarkably high sensitivity of the PLD-grown MoS_2 on silicon (S8-300) in the mid-IR range was caused by the interface, and

not for the reflected power.

The observation of the mid-IR response of the MoS_2 thin film was quite interesting. The band gap of the MoS_2 used for the mid-IR measurement was 1.3 to 1.4 eV because the films were multilayered and considered to have bulk properties [193]. The energy of photons (140 to 170 meV) in the mid-IR range (7 to 8.2 µm) was much lower than the band gap of bulk MoS_2. We anticipated two mechanisms that can dominate the mid-IR response. The first and the prominent mechanism involved a significantly enhanced IR absorption (from Fourier Transform Infrared Spectroscopy (FTIR) data) of MoS_2 in the wavelength range of 6 to 9 µm, as shown in Figure 7.19 (in the ESM). This observation was similar to the photothermal response of the semiconducting 2D thin films, such as graphene oxide [194], and 1D structures, such as nanowires [195]. As mentioned earlier, the temperature coefficient of resistance, TCR $\left(\alpha = \frac{1}{R_0}\frac{dR}{dT}\right)$ is the most important parameter in estimating the mid-IR response of MoS_2. Figures 7.5(b) and 7.5(c) show the temperature dependence of the relative resistance and the TCR of the MoS_2 film on all the substrates caused by the externally applied heat. On average, the TCR of MoS_2 is found to vary from -0.9%·K^{-1} (296 K) to -0.3%·K^{-1} (383 K) for most of the substrates (sapphire, thermal oxide, and SiN), which was commendable for the 2D material in comparison to graphene and strongly reduced graphene oxide (s-GO) [173]. However, a strong substrate dependence of the TCR of MoS_2 was observed, as seen in case of the film grown on silicon. The TCR was found to vary from -2.9%·K^{-1} (296 K) to -0.3%·K^{-1} (383 K) in the S8-300 sample (Figure 7.5(c)). This finding could be caused by the twin formation between the silicon and MoS_2 interface, as discussed earlier. The twin boundaries play an important role in the electrical and thermal conductivity because they are the weak scattering center of the electrons and the phonons [187, 196, 197]. The increasing temperature increases the mobility of the electrons because of a change in the effective mass resulting

in a higher TCR for MoS_2 on silicon [187, 196]. The similar observations were made by Zande et al., where the in-plane electrical conductivity of MoS_2 increased because of the mirror twin boundaries [198]. Twin boundaries at the interface may also open up an interfacial defect conduction, which increases with temperature and results in a higher TCR. Meanwhile, as discussed earlier, sapphire and MoS_2 had a lattice mismatch of 5.6% and formed a semi-coherent interface with a low elastic strain (Figure 7.3(a)) and subtle misfit dislocations. Similarly, a low strain interface also formed when the film was grown on amorphous substrates, such as thermally grown oxide (Si/SiO_2) or SiN, because of the absence of a long-range lattice ordering in the substrates. Therefore, these films were also prone to form dislocations at the interface. The dislocations were the Coulomb scattering centers for the electron pathways, which significantly reduce the electron mobility in MoS_2 and 2D electron gases [199–201]. Therefore, the MoS_2 grown on all the three substrates (i.e., sapphire, thermally grown oxide, and SiN) showed relatively low TCR values because of an increased number of scattering centers. Their TCR remained in a similar range, as depicted in Figure 7.5(b). The MoS_2 grown on silicon showed a higher photo- thermal sensitivity than that grown on any other substrates because of its high TCR. To confirm that the interface was playing a significant role, MoS_2 was mechanically peeled and transferred to the silicon and thermal oxide substrates displaying a much lower TCR (0.3%-0.5% at 20 to 100 °C regime) compared to the PLD-grown films (Figure 7.22 in the ESM). This ensured that films grown through PLD imparted defects in the substrate-film interface, especially in the silicon-MoS_2 interface, and proved the crucial role of the interface in the TCR and mid-IR sensitivity.

Additional experiments were also performed to elucidate the physics of the charge transfer from silicon to PLD-grown MoS_2. Silicon is not insulating. Hence, is a potential for charge transfer from silicon to MoS_2 exists, as reported in Refs. [202, 203]. Figure 7.23 in the ESM shows the I-V measurements

of both the PLD-grown MoS_2 on all the substrates and the mechanically exfoliated MoS_2 transferred to the silicon and the thermal oxide. The PLD-grown MoS_2 on silicon (S8-300) showed a non-linear I-V curve (Figure 7.23(a) in the ESM) in the presence and absence of a mid-IR illumination. This result was unlike that obtained for the PLD-grown and mechanically exfoliated MoS_2 on the other substrates, which mostly showed an Ohmic behavior. The result depicted an overall charge transfer on the PLD-grown MoS_2 from silicon with and without IR illumination. This happened possibly because of the Fermi energy pinning at the silicon-MoS_2 interface. However, no drastic change was observed in the I-V characteristics with mid-IR illumination in any of the cases, ensuring that charge transfer did not influence the TCR and did not play a critical role in the mid-IR sensitivity.

For further assurance, we conducted a UPS measurement of the PLD-grown MoS_2 on the different substrates used in this study. We observed in Figures 7.6(a) and 7.6(b) that the work function (ϕ) of the MoS_2 grown on silicon (S8-300) was significantly lower (4.56 eV) than that grown on the other substrates (4.85 eV). We proposed a possible band diagram of the PLD-grown MoS_2 on silicon and other substrates (i.e., sapphire, Si/SiO_2 and Si/SiN) from the reported value of the ionization potential (IP) and the electron affinity (χ) of bulk MoS_2 (Figures 7.6(c) and 7.6(d)) [50, 181, 204]. The Fermi energy (EF) of MoS_2 on silicon moved closer to the conduction band edge, allowing an enhanced thermal promotion of the electrons and resulting in an increase in the TCR and the IR sensitivity. We argue that the band structure may be modified because of the twin boundary formation of MoS_2 on silicon, which strongly influences the above-mentioned properties. However, this observation demands a more thorough theoretical understanding of the phonon and electron transport across the MoS_2-substrate interface with the increasing temperature.

Aside from the TCR, another possibility that can contribute slightly to

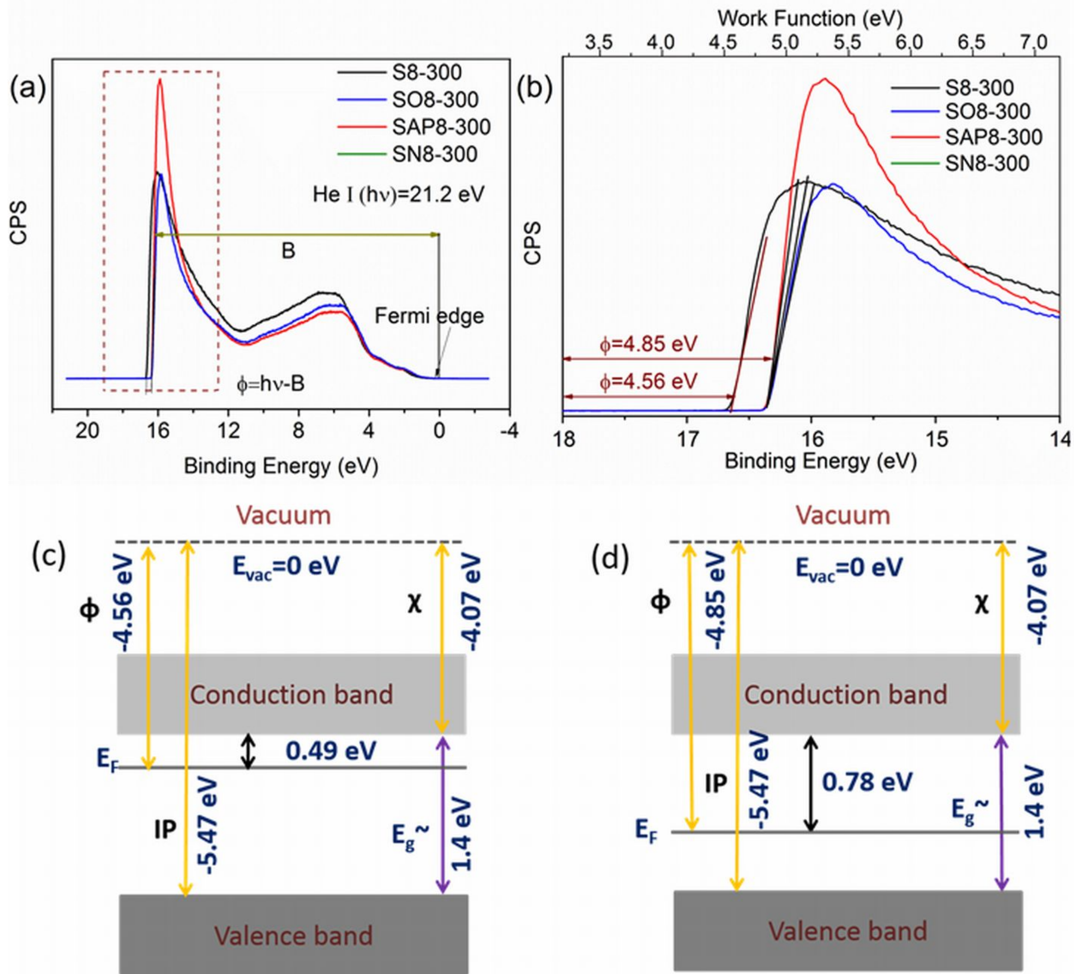

Figure 7.6: (a) UPS spectra of MoS_2 on different substrates and (b) zoomed portion of (a) showing the work function of MoS_2 on different substrates. The band diagram of the PLD-grown MoS_2 on (c) silicon and (d) other three substrates (i.e., Si/SiO_2, sapphire, and Si/SiN) shows how the band structure changes because of the interface. The ionization potential (IP $\sim$ -5.47 eV) and the electron affinity ($\chi \sim$ -4.07 eV) for bulk MoS_2 are obtained from Refs. [181,204]

the mid-IR response also exists. The XPS analyses (Figure 7.15 in the ESM) showed that oxygen molecules adsorbed on the MoS_2 surface after the film deposition, which can cause multiple surface traps at the interface. These surface traps in MoS_2 were generally within the vicinity of $\sim$200 meV of the valence band (VB) and conduction band (CB), as described by Tongay et al. [205]. As a result, a low- energy IR could be enough to excite more elec-

Table 7.1: Estimated mid-IR response characteristics of the MoS_2 film by PLD and exfoliated MoS_2 flakes mechanically transferred onto different substrates at 1300 cm^{-1} (7.7 µm) and at the highest average power of 25 mW of the QCL. The IR exposure area (A) is 5 mm^2. A Johnson noise is reported per unit bandwidth (i.e. Δf Hz)

Sample	Substrate	Thermal diffusivity of the substrates ($cm^2 \cdot s^{-1}$)	Responsivity (R_{resp}) ($V \cdot W^{-1}$)	Johnson noise or thermal noise (V_n)($V \cdot Hz^{-1/2}$)	Noise equivalent power (NEP) ($W \cdot Hz^{-1/2}$	Response time (s) τ_f) & τ_r	Detectivity (D^*) ($cm \cdot Hz^{1/2} \cdot W^{-1}$)
S8-300	Si	800×10^{-3}	8.7	5.9×10^{-7}	6.8×10^{-8}	8.5 & 7.5	2.8×10^{7}
SAP8-300	Sapphire	83×10^{-3}	1.9	1.1×10^{-7}	5.8×10^{-7}	10 & 9.6	7.2×10^{6}
SO8-300	Si/SiO_2	6.4×10^{-3}	2.6	4.7×10^{-7}	1.8×10^{-7}	10.5 & 10.1	3.1×10^{6}
SN8-300	Si/SiN	0.5×10^{-3}	1.3	1.7×10^{-7}	1.3×10^{-7}	10.4 & 8.7	2.1×10^{6}
MoS2 flake (exfoliated)	Si	800×10^{-3}	0.56	5.9×10^{-8}	1.06×10^{-7}	12.5 & 15.2	1.17×10^{4}
MoS2 flake (exfoliated)	Si/SiO_2	6.4×10^{-3}	1.04	1.85×10^{-8}	1.78×10^{-8}	21 & 26.7	1.3×10^{5}

trons to the CB and reduce the overall resistance. Although this phenomenon justifies the overall IR response of MoS_2 on all the substrates, it does not explain the enhanced response of MoS_2 on silicon. A detailed figure of the merit calculation and experimental measurements were performed as tabulated in Table 7.1 to understand the IR response of the film. The infrared responsivity, $\left(R_{RESP} = \frac{V}{W}\right)$, thermal noise (or Johnson noise) $\left(V_n = \sqrt{4k_B T R \Delta f}\right)$ (where k_B is the Boltzmann constant, and Δf is the bandwidth of measurement), noise equivalent power $\left(NEP = \frac{V_n}{R_{resp}}\right)$, and detectivity $\left(D^* = \frac{R_{resp}\sqrt{A}}{NEP}\right)$ (A = 5mm^2) of MoS_2 on different substrates were reported. The definition of all these figures of merit can be found elsewhere [173, 206]. Table 7.1 shows that he MoS_2 grown on silicon (S8-300) exhibited the highest responsivity among all the substrates investigated. However, S8-300 also showed a relatively high thermal noise because of the higher electrical resistance of the film at room temperature. In the case of thermal detectors, the response time was an important parameter that largely depended on thermal characteristics, such as thermal diffusivity. The substrates with high thermal diffusivity exhibited higher response and recovery time than the other substrates. This result was evident for the MoS_2 films deposited on silicon (S8-300) (Table 7.1). However, in all these cases, the MoS_2 films were attached on the substrates, thereby

resulting in higher characteristic times caused by a very large thermal mass of the system. Using suspended MoS_2 structures could reduce the thermal mass that could result in a highly responsive and sensitive bolometer.

Two different designs were explored for improving the response time to mid-IR exposure. One utilized nanostrings that were fabricated using electron beam lithography, and one was a diaphragm fabricated using conventional top down fabrication techniques. Both devices were built on the same wafer system, composed of a p-type Si $\langle 100 \rangle$ handle which was thermally oxidized to a thickness of 1.5 μm with a 200 nm layer of high stress (1.2 GPa) silicon nitride grown on top by LPCVD. For the MoS_2 nanostrings, shown in Figure 7.7, electrical contacts were deposited onto the substrate prior to MoS_2 deposition. The MoS_2 for both the nanostrings and the diaphragm was deposited via PLD to $\sim$ 15 nm thicknessunder the same conditions used for the previously studied films.

The nanostrings were patterned onto the electrical contacts using electron beam lithography (RAITH150 Two) with a negative tone hydrogen silsesquioxane (HSQ) resist. The resist was spun onto the substrate to a thickness of 190 nm in order to properly act as an etch mask for subsequent processing. A conductive coating of aquaSAVE™ (Mitsubishi Chemical) was

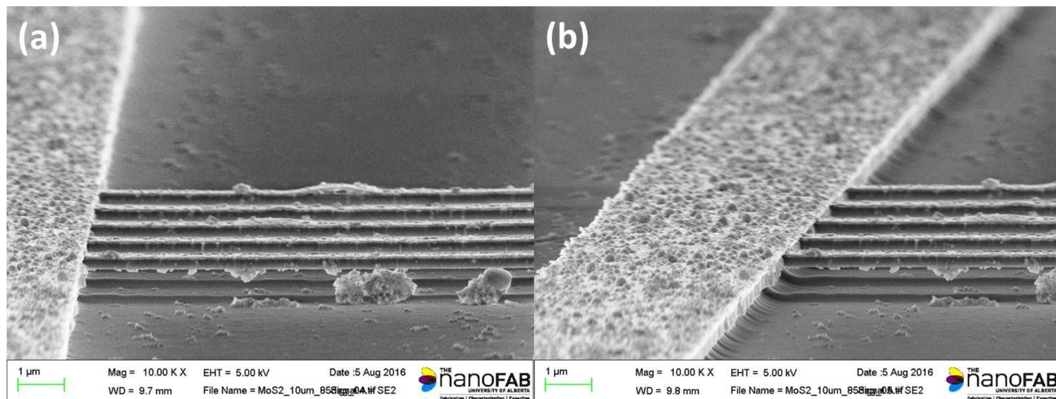

Figure 7.7: SEM micrographs showing the MoS_2 nanostring from (a) front and (b) side angle. The thickness of these strings is 200 nm silicon nitride and 15 nm MoS_2. The strings measure 8 μm in length and 250 nm in width.

spun on to a 75 nm thickness to prevent unwanted charging effects during the lithographic process. Operating conditions for the electron beam pattern transfer were as follows: 10 keV accelerating voltage, 10 µm aperture, 300 $^{\mu C}/_{cm^2}$ electron dose, writefield size of 100 $\times$ 100 µm, and a working distance of 7.7305 mm. The beam current was measured at 19.68 pA, and using 10 nm step size the dwell time and beam speed were 15.24 µs and 0.39356 $^{mm}/_{s}$, respectively. Once exposed the chip was allowed to sit for at least one hour before developing. After this, the aquaSAVE™ was removed with water by rinsing, and the HSQ was developed in 25 % TMAH for 4 minutes, followed by 1 minute in deionized water bath, 30 seconds deionized water rinse, and finally dried with nitrogen.

The MoS_2 diaphragm, shown in Figure 7.8, was constructed using a more conventional microfabrication process. Using the same base substrate as the nanostring, electrical contacts were patterned by photolithography using HPR 504 photoresist and sputtering. Once the contact pads were down, a second mask was used to transfer the diaphragm pattern onto the substrate using a thicker positive tone HPR 506 photoresist. This layer acted as the

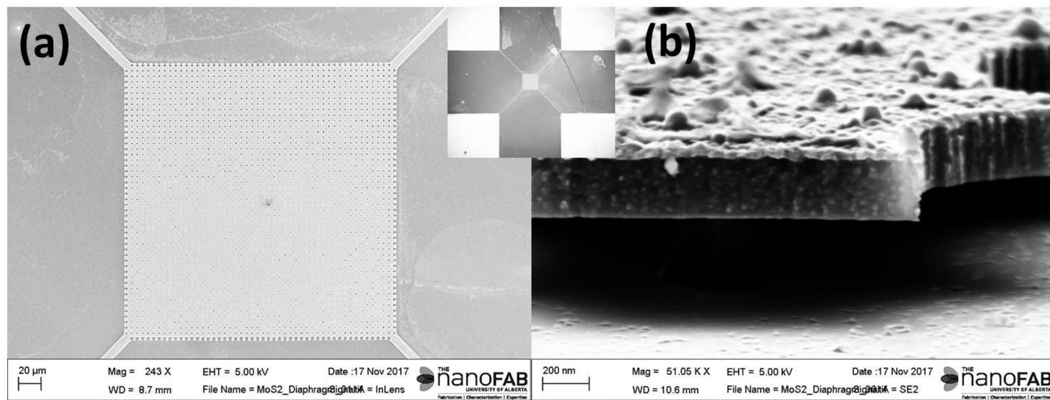

Figure 7.8: SEM micrographs showing (a) the diaphragms IR absorbing pad and (b) side profile showing the cross section of the absorbing pad. Inset: top view of the entire device showing the absorber, isolation arms, and the gold contact pads. Holes were included as a means to imporve the lateral etchability of the device.

etch mask for the silicon nitride etching which was done by RIE with a chemistry of 25 sccm CHF_3, 40 sccm CF_4, 4 sccm O_2, 200 W RF power, 30 mTorr flow rate, and 10 °C platen temperature for 3 minutes. After this step the photoresist was removed and the sacrificial oxide layer was removed via VHF etching. MoS_2 was deposited onto the finished device by PLD under the same condition used previously. The reason the diaphragm contains holes was to assist the oxide etch undercut the diaphragm properly.

The mid-IR response of the nanostring device was tested under the same conditions as the films, and the response time improved significantly. As seen earlier, the response time for MoS_2 thin films was on the order of 10 seconds, which is too long for practical applications. Figure 7.9 shows that the response time has improved by almost 2 full orders of magnitude, decreasing

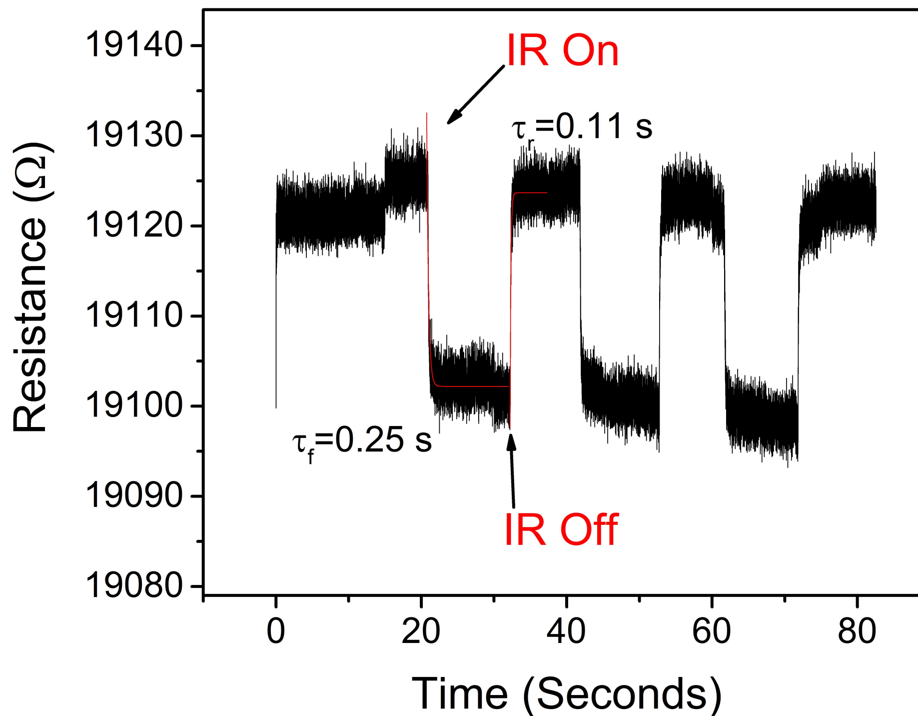

Figure 7.9: Mid-IR photothermal response of the MoS_2 nanostring resonators. Rise and fall times are determined to be 250 and 110 ms, respectively.

to the order of 100's of milliseconds. The response time to the Ir source being turned on was 250 ms, and the response to the IR turned off was 110 ms, marking a hug improvement over the thin film devices. This is a significant improvement that we attribute to the reduced thermal mass achieved by creating a nanosized, suspended structure.

7.5 Conclusions

In this study, MoS_2 thin films were grown on both crystalline and amorphous substrates using the PLD technique. The deposition process was optimized for the substrate temperature, deposition time, and laser energy. The MoS_2 thin films consisting of a few layers were grown uniformly on various substrates and characterized by different techniques, such as XRD, Raman, AFM, SEM, TEM, and XPS. The results showed that the MoS_2 growth was optimized at 800 °C with the growth morphology showing a clear dependence on the substrate type. The TEM results exhibited that the MoS_2 growth on silicon proceeded through twinning because of the incoherent interface formation, whereas that on sapphire formed a layer-by-layer structure through subtle misfit dislocations. The resistance of the MoS_2 film demonstrated a strong mid-IR responsivity because of the broadband mid-IR absorption. The MoS_2 films grown on silicon offered much higher IR sensitivity and responsivity than the other substrates. This result can be explained to be from the high TCR stemming from the twin boundary formation caused by the large lattice mismatch strain between the silicon and MoS_2. Therefore, controlling the interfacial strain of the MoS_2 film by a proper substrate choice offers a method of enhancing its mid-IR responsivity. We also show improved response times for nanostring resonators by controlling the thermal mass, resulting in millisecond response times.

7.6 Electronic Supplementary Material

Table 7.2: Sample codes for MoS_2 on various substrates at different deposition conditions.

Sample Code	Substrates	Deposition temperature (°C)	Laser Energy (mJ)	Time of Deposition (sec)
S7-20	p-type Silicon (100)	700	35	20
S7-300	p-type Silicon (100)	700	35	300
S8-20	p-type Silicon (100)	800	35	20
S8-300	p-type Silicon (100)	800	35	300
S8-5	p-type Silicon (100)	800	50	5
SAP7-20	Sapphire (0001)	700	35	20
SAP7-300	Sapphire (0001)	700	35	300
SAP7-5	Sapphire (0001)	700	50	5
SAP8-20	Sapphire (0001)	800	35	20
SAP8-300	Sapphire (0001)	800	35	300
SAP8-5	Sapphire (0001)	800	50	5
SO7-20	Thermal Oxide (Si/SiO2)	700	35	20
SO7-300	Thermal Oxide (Si/SiO2)	700	35	300
SO8-20	Thermal Oxide (Si/SiO2)	800	35	20
SO8-300	Thermal Oxide (Si/SiO2)	800	35	300
SO8-5	Thermal Oxide (Si/SiO2)	800	50	5
SN7-20	Silicon Nitride (Si/SiN)	700	35	20
SN7-300	Silicon Nitride (Si/SiN)	700	35	300
SN8-20	Silicon Nitride (Si/SiN)	800	35	20
SN8-300	Silicon Nitride (Si/SiN)	800	35	300
SN8-5	Silicon Nitride (Si/SiN)	800	50	5

7.6.1 Structural Characterization of MoS_2 deposited at 700 °C

Figure 7.10 shows the XRD spectra of as-deposited film, grown on various substrates at 700 °C. It is observed that at 35 mJ laser energy and 20 s deposition time none of the substrates show appreciable formation of MoS_2 film with sufficient crystallinity (Figure 7.10(a)), with the exception of SiN. At a relatively longer time of deposition (300 s), SiO_2 (SO7-300) and SiN (SN7-300) substrates show appreciable growth of (0002) and a tiny peak of

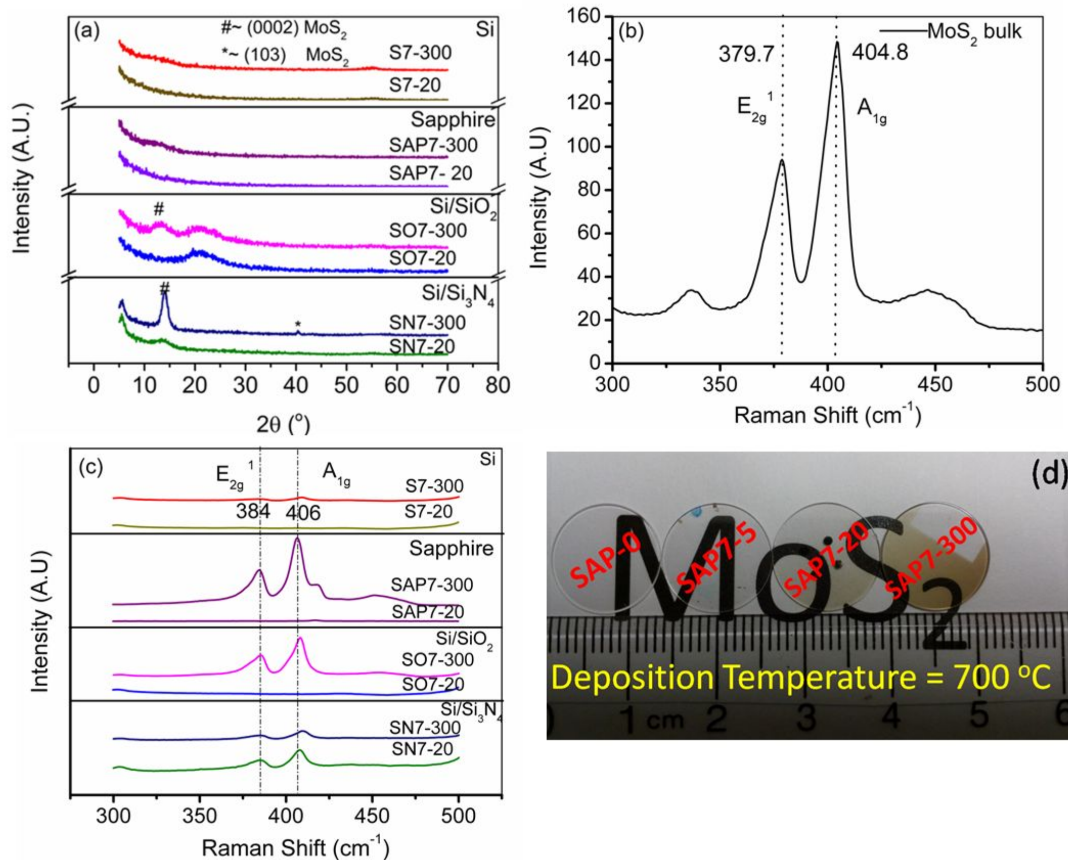

Figure 7.10: (a) XRD of MoS_2 grown on different substrates at 700 °C and at 35 mJ laser energy. Raman spectra of MoS_2 (b) bulk, and (c) grown on different substrates at 700 °C and at 35 mJ laser energy. (d) Photograph of the MoS_2 film grown on sapphire at 700 °C different time and laser energy.

(103) MoS_2 as shown in Figure 7.10(a). However, crystalline substrates (Si and sapphire) do not show considerable crystallinity even at longer deposition (300 s) time. In order to confirm the crystallinity Raman spectroscopy were taken for all the samples. There are two characteristic peaks of bulk MoS_2 (PLD target) normally observed at 379.7 and 404.8 cm^{-1} as shown in Figure 7.10(b) [207]. These correspond to $E^1{}_{2g}$ and A_{1g} vibration of 2H-MoS_2 Raman modes [208]. The former ($E^1{}_{2g}$) is the in-plane vibration of two opposite S atoms corresponding to the Mo atom (in the x-y plane) while the latter (A_{1g}) corresponds to the out of plane vibration of only S atom in the normal plane (z-plane) [209]. Generally, for ultrathin ($\leq$4 layers) MoS_2, there is a

blue shift in the $E^1{}_{2g}$ whereas in the A_{1g} band there is a red shift. From the difference between the Raman peaks frequencies (Δ), the number of stacked layers can be identified and are listed in Table 7.3 [207].

Figure 7.10(c) shows the Raman spectra of as deposited film grown on various substrates at different time and temperature. It is observed from the Raman spectra (Figure 7.10(c)) that SiN is the only substrate to show any appreciable growth of MoS_2 (SN7-20) at 700 °C temperature and 20 s deposition time. However, at 700 °C and 300 s deposition time, the growth is similar for all substrates, and the deposited films show peak broadening.

Atomic force microscopy (AFM) was conducted to observe the evolution of the microstructure of MoS_2 films deposited on different substrates. At 700 °C with a laser energy of 35 mJ, the film grown on the different substrates for 20 s show grainy a morphology as depicted in Figure 7.11. This bear resemblance to Volmer-Weber growth or island growth. The average roughness of all the films at these conditions is 4 to 6 nm which is relatively higher than the film deposited at 800 °C for same time (20 s). But at higher deposition time (300 s) at same temperature (700 °C) the growth morphology turns to be Stransky-Karstinov (SK) growth where both island and layer growth are observed [161]. At 700 °C substrate temperature and 20 s of deposition time the MoS_2 species sit on top of each other due to low atom mobility resulting from high adatom cohesive force. This dominates the surface adhesive force thereby increasing the surface roughness of the films [210]. However, as the temperature increased to 800 °C while keeping deposition time constant (20 s), the roughness of the deposited films is reduced because of the sufficient mobility of the MoS_2 species on the all substrates. This leads to the formation of a smoother film similar to Frank-Van der Merwe (FM) growth where film grows in a layer-by-layer manner.

The oxidation states of all the MoS_2 samples deposited at 800 °C for 20 s at different substrates were confirmed by high resolution XPS. The

Table 7.3: The E^1_{2g} and A_{1g} Raman peaks of as-deposited MoS_2 films on different substrates at various deposition time, temperature and laser energies.

Samples	E^1_{2g} (cm^{-1})	A_{1g} (cm^{-1})	A_{1g}-E^1_{2g} (cm^{-1})($\Delta\omega$)	Estimated Layer numbers
S7-20	-	-	-	-
S7-300	384.3	408.5	25.2	>5 or bulk
S8-20	384	407	23	3 to 4
S8-300	382	408	26	>5 or bulk
S8-5	385 (faint)	407 (faint)	23	3 to 4
SAP7-20	-	-	-	-
SAP7-300	384	406.3	22.3	3 to 4
SAP8-20	383	407.8	24.8	4 to 5
SAP8-300	382	408	26	>5 or bulk
SAP8-5	385	407	22	2 to 3
SO7-20	-	-	-	-
SO7-300	385.6	408.5	23.1	3 to 4
SO8-20	383.5	407.9	24.4	4 to 5
SO8-300	384	409.6	25.6	>5 or bulk
SO8-5	385.4	407.5	22.1	2 to 3
SN7-20	384.8	407.7	22.9	2 to 3
SN7-300	385.5	409.6	24.1	4 to 5
SN8-20	384.7	408.9	24.2	4 to 5
SN8-300	383.5	409.2	25.7	>5 or bulk
SN8-5	385.4	408.3	22.9	2 to 3

survey spectra of XPS for two samples (S8-20 and SAP8-20) are presented in Figure 7.14a. The high resolution XPS data (S8-20, SAP8-20, SO8-20 and SN8-20) are presented in Figure 7.15. Two predominant peaks related to Mo^{4+} are observed in every sample (as shown in Figure 7.15 (a, c, e, g)) at 229

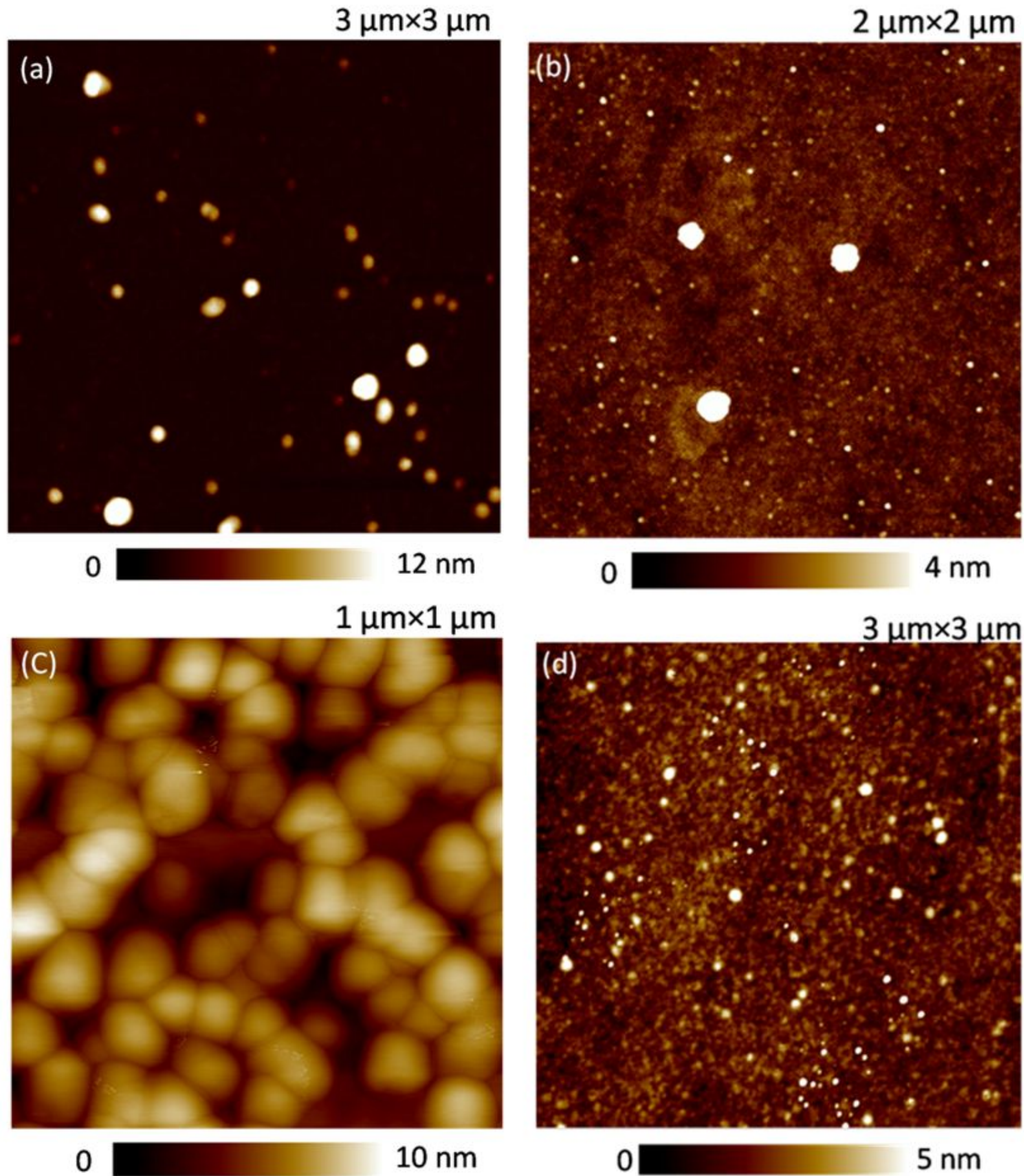

Figure 7.11: AFM images of MoS_2 grown at 700 °C on different substrates and 35 mJ laser energy for 20 s deposition times grown on: (a) silicon (S7-20) (b) sapphire (SAP 7-20) (c) thermally grown oxide SO7-20 (d) LPCVD grown SiN (SN7-20).

and 232.5 eV approximately. These two peaks correspond to Mo^{4+} $3d_{5/2}$ and $3d_{3/2}$ respectively. In addition, all the spectra show S 2s peaks at around 226.3 to 226.7 eV. These peaks correspond to Mo-3d of 2H structure. However, two unwanted peaks also appeared around 233 and 236 eV which corresponds to

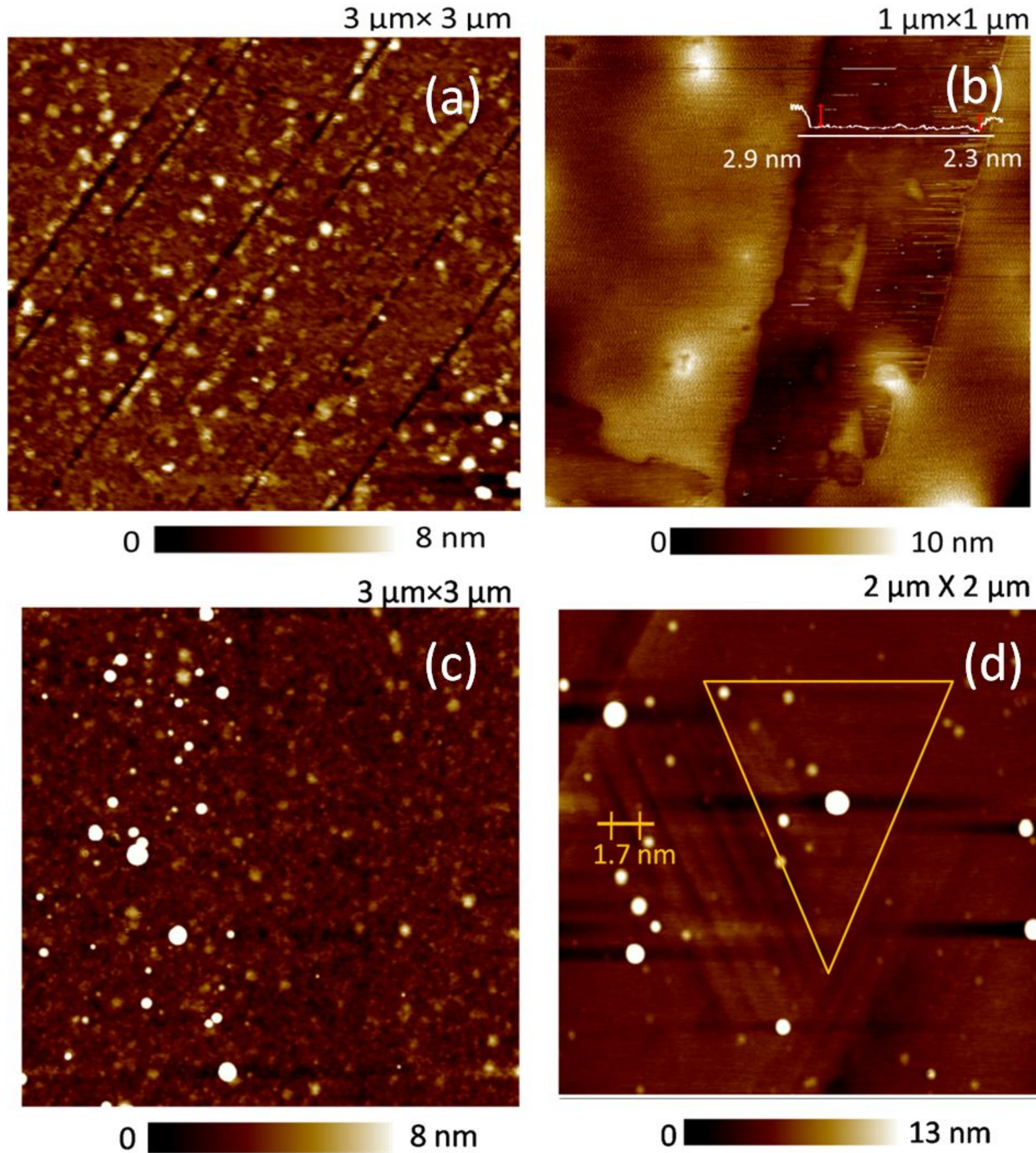

Figure 7.12: AFM images of MoS_2 grown at 800 °C and 35 mJ laser energy for 20 s deposition times on: (a) silicon (S8-20) (b) thermally grown oxide (SO8-20) (c) LPCVD grown SiN (SN8-20) and (d) MoS_2 grown at same temperature and energy for 300 s deposition time on sapphire (SAP8-300). Multiple layers have been grown with increasing the time.

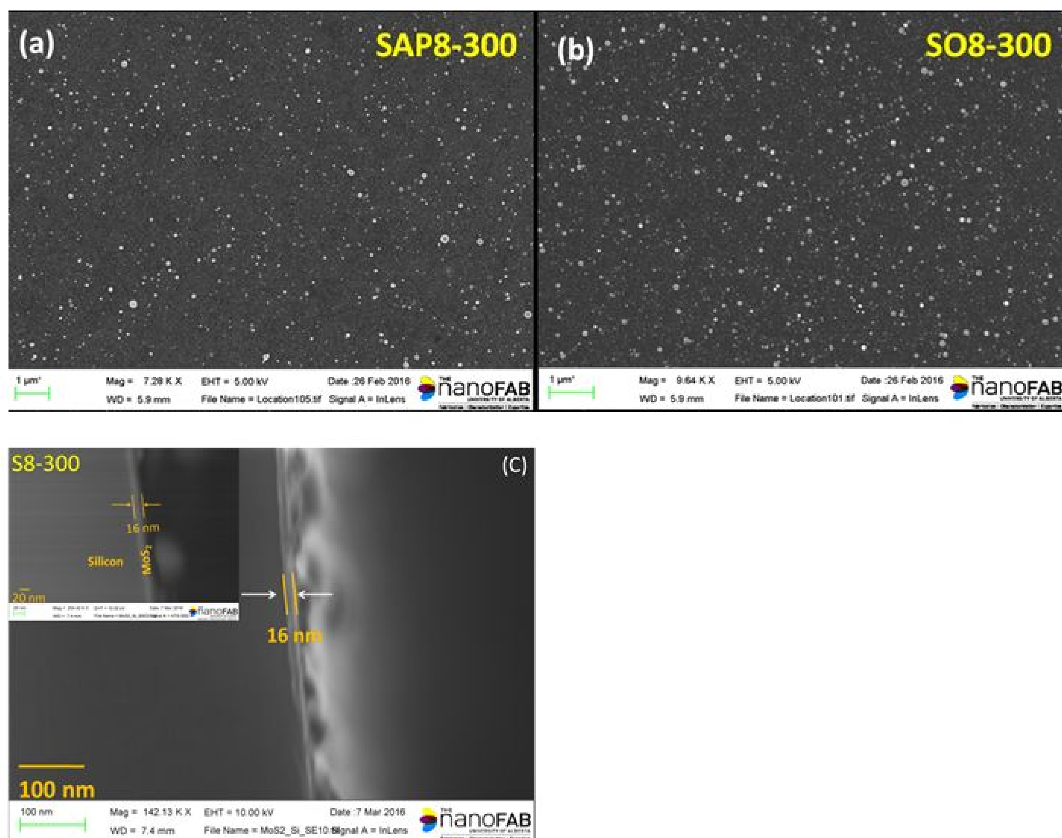

Figure 7.13: SEM topography of MoS_2 deposited at 800 °C for 300 s on (a) sapphire (SAP8-300) and (b) thermal oxide (SO8-300). (c) Cross sectional SEM of MoS_2 on Si for thickness measurement (S8-300). Inset shows the back scattered image to distinguish the compositional contrast between silicon and MoS_2. All the other 300 s deposited films are of same thickness.

$Mo^{6+}3d_{5/2}$ and $Mo^{6+}3d_{3/2}$. These two peaks signify the possible existence of MoO_3 which may be due to contamination or oxidation from exposure of MoS_2 films to the outside atmosphere prior to XPS experiments. All the samples show an S 2p doublet (as shown in Figures 7.15(b), (d), (f), and (h)) around 161.9 to 162.5 eV (S $2p_{3/2}$) and 163.5 eV (S $2p_{1/2}$). There is no other amorphous sulphur observed in any of the samples which confirms all the samples are of crystalline quality. Furthermore, it is also observed from atomic fraction calculation of the XPS data (using Casa-XPS software) that Mo: S ratio was between 1:1.9 to 1:1.95 which confirms MoS_2 films grown by PLD were nearly stoichiometric.

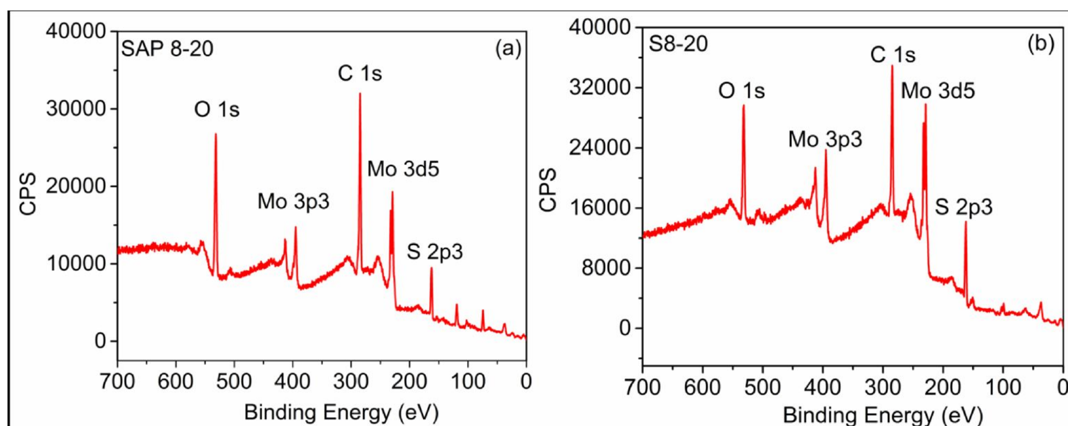

Figure 7.14: XPS survey spectrum of MoS_2 on (a) sapphire (SAP8-20) (b) silicon (S8-20).

MoS_2 grown on sapphire was chosen for UV-Vis study due to excellent optical transparency of sapphire. Fig. 7a shows the optical absorbance spectra of MoS_2 grown on sapphire at 800 °C for three different times (5 s, 20 s and 300 s). It is observed from the spectrum that there are two clearly well-known excitonic absorption bands "A" and "B", which appeared at 671 nm (1.82 eV) and 605 nm (2.04 eV) respectively for SAP8-300 [211]. In the case of SAP8-5 and SAP8-20, the "A" band is weak, but the "B" band is significant (in the inset). However, both the bands ("A" and "B") correspond to the band-edge excitons which happened due to the excitonic transitions at the Brillouin zone K point [42]. Additionally, peak "C" appeared at a lower wavelengths of 431 nm which corresponds to the van Hove singularities in the electronic density of states in layered MoS_2, which is common in 2D layered materials [212].

Photoluminescence (PL) spectra of the same samples are shown in Figure 7.16b. The peak at 653 nm (1.89 eV) of SAP8-5 sample shows the direct excitonic transition from the band gap which contains 2 to 3 layers as confirmed by Raman (Table 7.3) and AFM. As the layer number increases there was both a redshift in the peak position and a decrease in signal intensity. For bulk MoS_2 (SAP8-300) the signal intensity is near negligible as reported in earlier literature [185]. This confirms the band gap of MoS_2 changes with layer

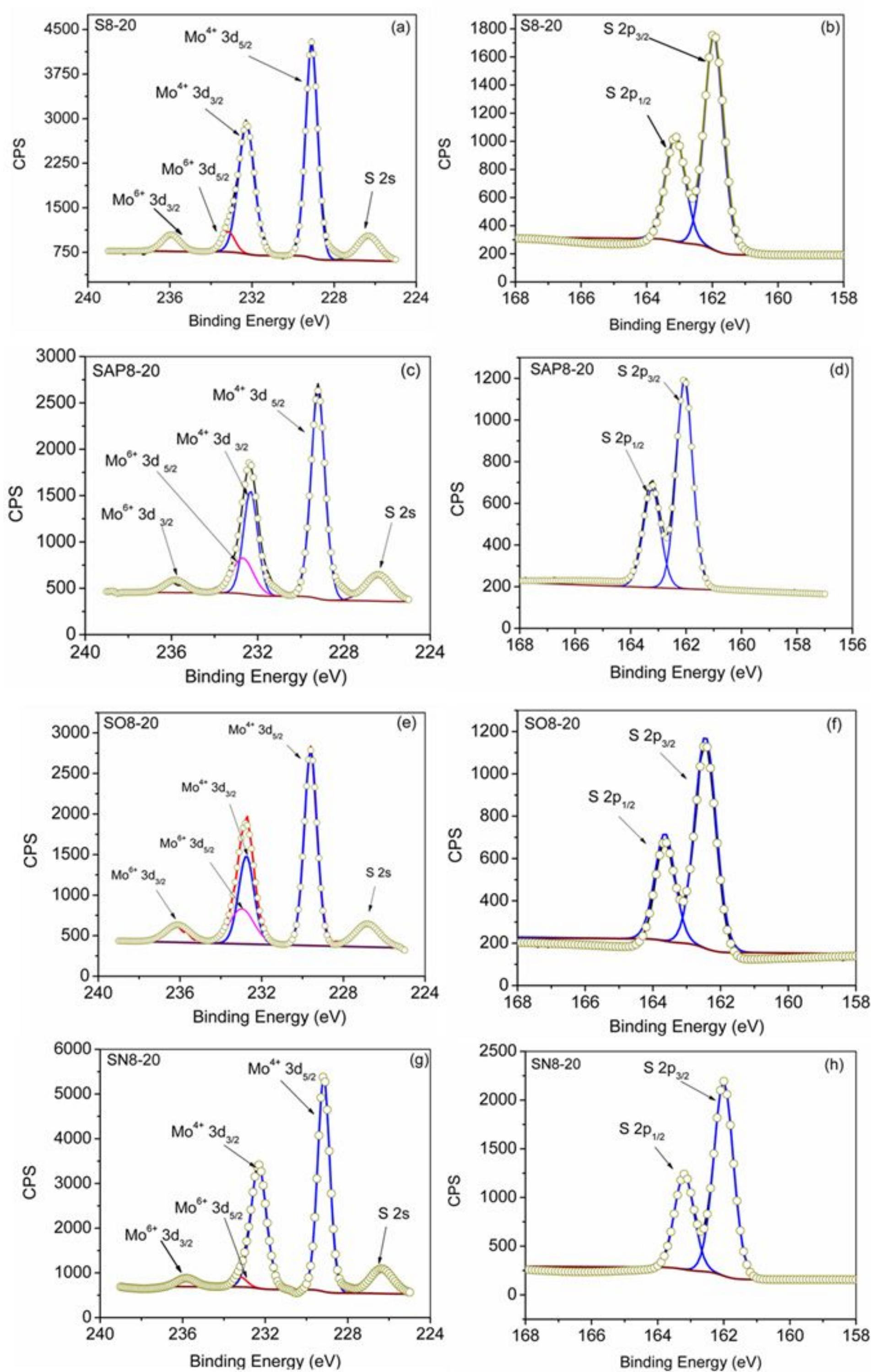

Figure 7.15: XPS spectra of MoS_2 on Si, SiO_2, SiN showing (a), (c), (e) Mo 3d, and (b), (d), (f) S 2s and S 2p core level peak regions respectively.

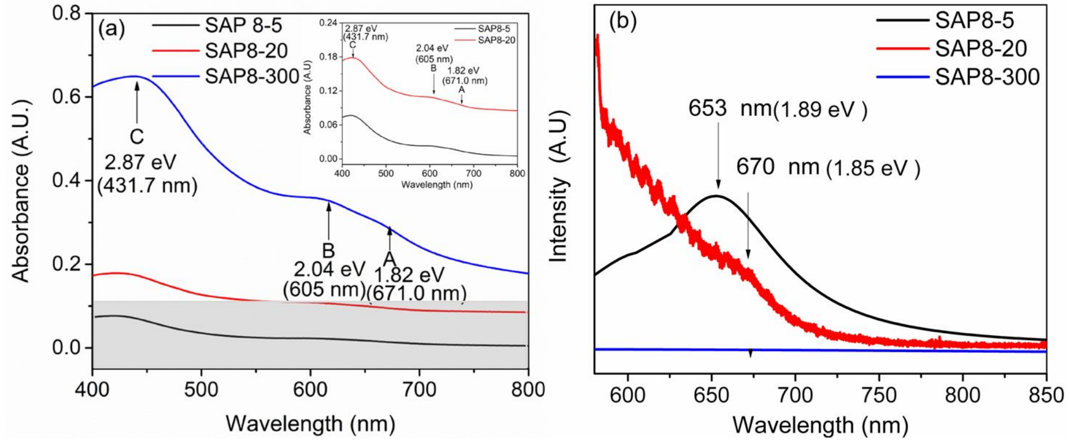

Figure 7.16: Optical and photoluminescence spectra of MoS_2 grown on sapphire at 800 °C at 35 mJ energy for different times.

numbers and we believe the band gap of the multilayer MoS_2 deposited here in all the substrates converges to 1.3 to 1.4 eV as reported in literature [39, 193]

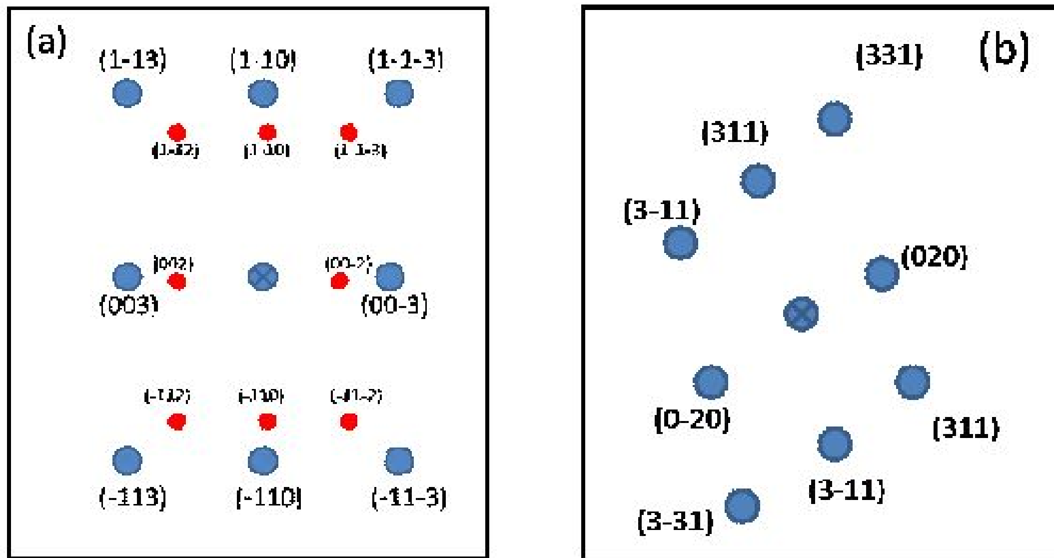

Figure 7.17: (a) and (b) Orientation relationship of MoS_2 on sapphire from the FFT pattern from a TEM cross-sectional image. In Fig 8 (a) blue and red dots represent the FFT of the sapphire substrate and MoS_2 respectively. In Fig 8(b) no MoS_2 spots are seen since the film was not in edge-on condition.

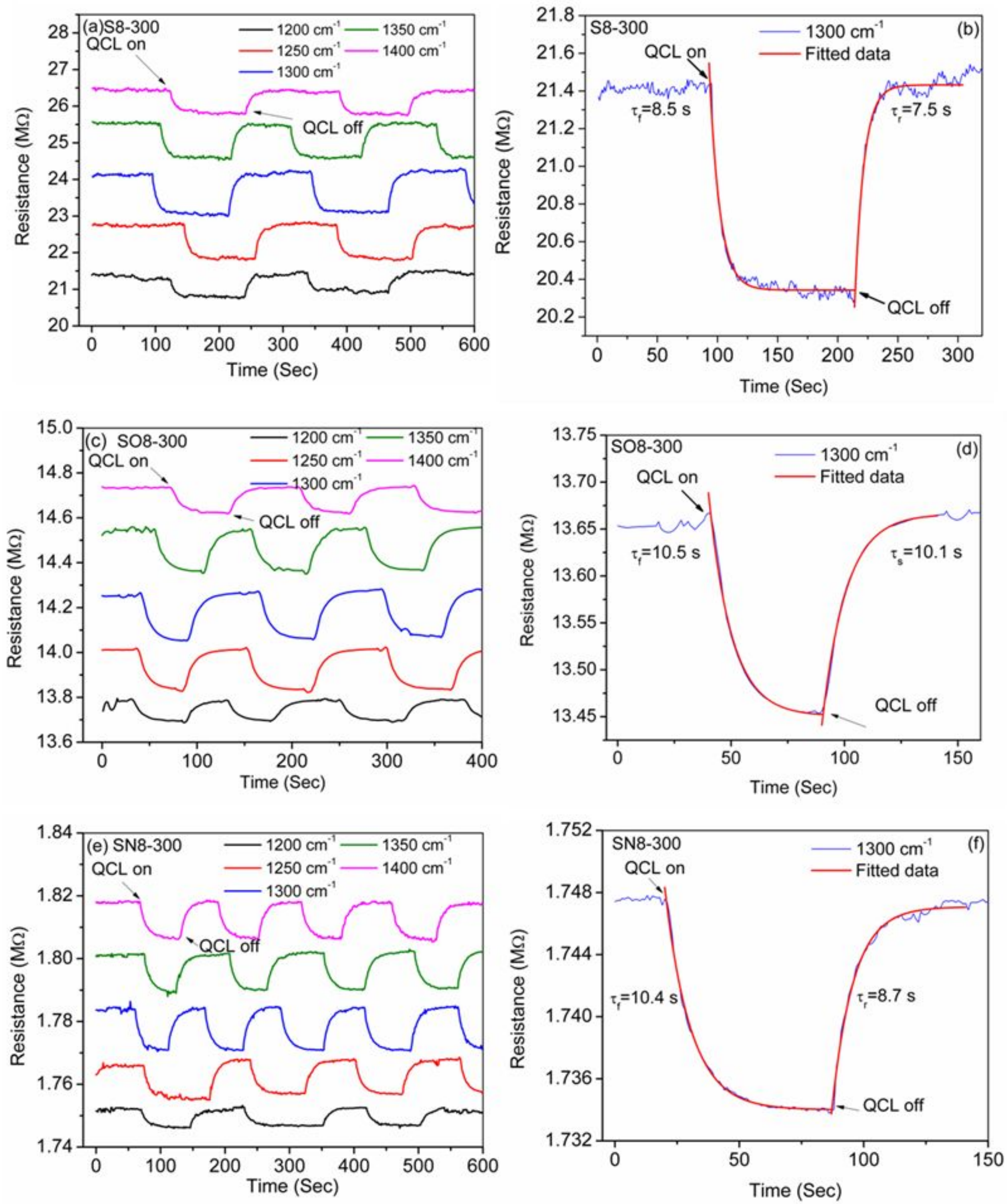

Figure 7.18: Variation of resistance and the response time of MoS_2 on different substrates under IR illumination.

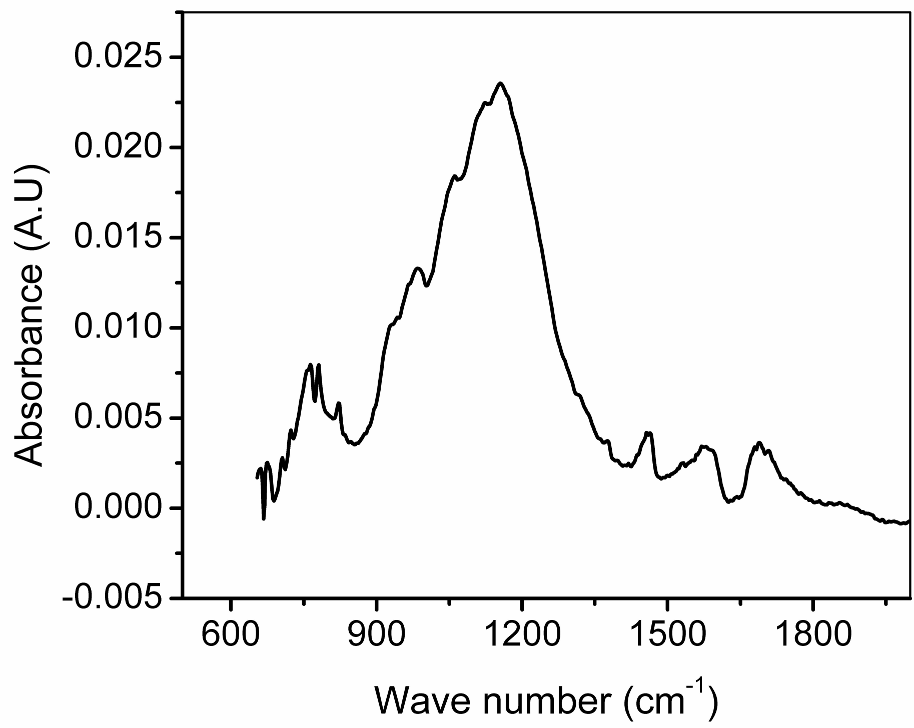

Figure 7.19: FTIR spectra of bulk MoS_2 in order to show the broadband IR absorption from 600 to 2000 cm^{-1} wave number.

7.6.2 Calculation of Reflective Power

Reflectivity (R) of a single thin film deposited on a substrate depends on the following Eq. 7.1 [213]

$$R = |r|^2 = rr^* \tag{7.1}$$

where r is the reflectivity ratio of the film-substrate interface and r^* is the complex conjugate of the same. r and r^* depends on the following Eq. 7.2 and 7.3.

$$r = \frac{\tilde{n}_m - \tilde{n}_s}{\tilde{n}_m + \tilde{n}_s} \tag{7.2}$$

$$r = \frac{\tilde{n}_m^* - \tilde{n}_s^*}{\tilde{n}_m^* + \tilde{n}_s^*} \tag{7.3}$$

where $\tilde{n}_m$ and $\tilde{n}_s$ re the complex refractive indices of MoS_2 and the substrates respectively and $\tilde{n}_m^*$ and $\tilde{n}_s^*$ are their complex conjugate, and they are expressed by the following Eq. 7.4- 7.7:

$$\tilde{n}_m = n_m + ik_m \tag{7.4}$$

$$\tilde{n}_m^* = n_m - ik_m \tag{7.5}$$

$$\tilde{n}_s = n_s + ik_s \tag{7.6}$$

$$\tilde{n}_m^* = n_s - ik_s \tag{7.7}$$

where n_m and n_s are the refractive indices and k_m and k_s are the extinction co-efficient of film and the substrates respectively.

By substituting r and r^* in Eq. 7.1 the expression for reflectivity of film-

Table 7.4

Substrates and films	Optical Constants at 1300 cm^{-1} wave number [214]			
	n	k	α (cm^{-1})	R (reflectivity at interface of MoS_2-substrate and MoS_2-air)
Si	3.4191	3.0×10^{-5}	0.492	0.43 (MoS_2-Si)
SiO_2	0.8114	0.0339	553.5	42.98 (MoS_2-SiO_2)
Sapphire	1.323	0.02746	448.89	24.34 (MoS_2-Sapphire)
SiN	2.04	0.206	3.36×10^{-5}	9.90 (MoS_2-SiN)
MoS_2	3.9	0.004	65.3	0.35 (MoS_2-air)

substrate interface is obtained as shown in following Eq. 7.8.

$$R = \frac{{n_m}^2 + {k_m}^2 + {n_s}^2 + {k_s}^2 - 2n_m n_s - 2k_m k_s}{{n_m}^2 + {k_m}^2 + {n_s}^2 + {k_s}^2 + 2n_m n_s + 2k_m k_s} \tag{7.8}$$

However, in the case of film-air interface n_s=1 and k_s=0 and the reflectivity expression becomes the following

$$R = \frac{(n_m - 1)^2 + {k_m}^2}{(n_m + 1)^2 + {k_m}^2}. \tag{7.9}$$

On the hand, absorption co-efficient (α) of any material can be expressed by the following Eq. 7.10,

$$\alpha = \frac{4\pi f k}{c} \tag{7.10}$$

where f is the frequency of the incident light, k is the extinction co-efficient of material of choice, c is the velocity of light. Using Eq. 7.8 and Eq. 7.9 the optical constant of the MoS_2 and the substrates are determined and tabulated in Table 7.4.

7.6.3 MoS_2 flakes transfer by scotch tape exfoliation and metal contact

Flakes of MoS_2 were mechanically exfoliated from molybdenite single crystal (SPI supplies, West Chester, PA, USA) using the well-known scotch tape cleavage method and transferred onto piranha cleaned silicon and thermal oxide (Si/SiO_2) substrates. Subsequently, electron beam lithography (EBL, RAITH 150^{TWO}) was done on the flakes using PMMA 950k A2 as an electron beam resist. Metal contacts were formed using conventional lift off technique after Ti (10 nm) and Au (50 nm) were deposited by sputtering. Figure 7.20 shows the SEM and AFM images of the same.

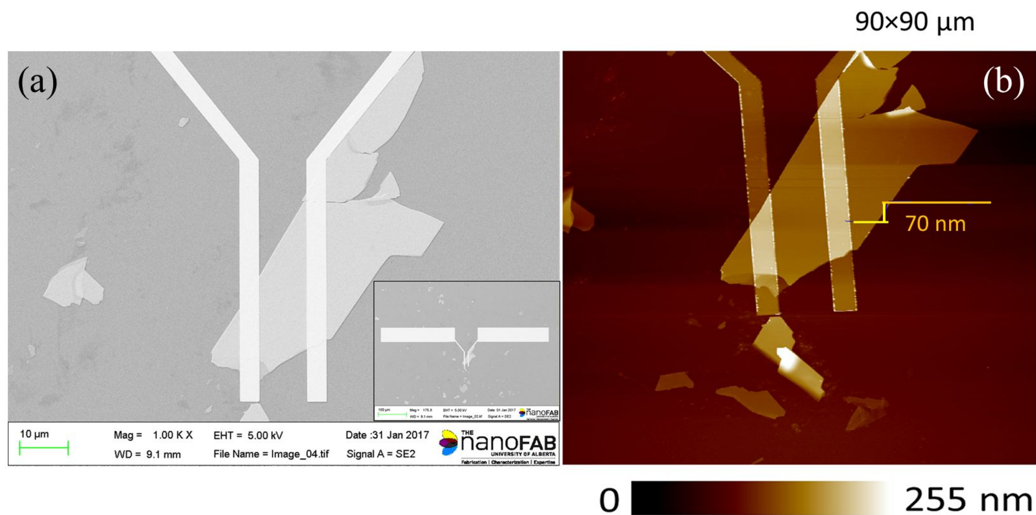

Figure 7.20: (a) SEM image of MoS_2 flakes on silicon with metal contact pad (Ti/Au ∼5/50 nm) separated by 10 µm made by EBL and sputtering. Inset shows the image of the whole contact pad. (b) AFM image of the same flake showing the layer thickness.

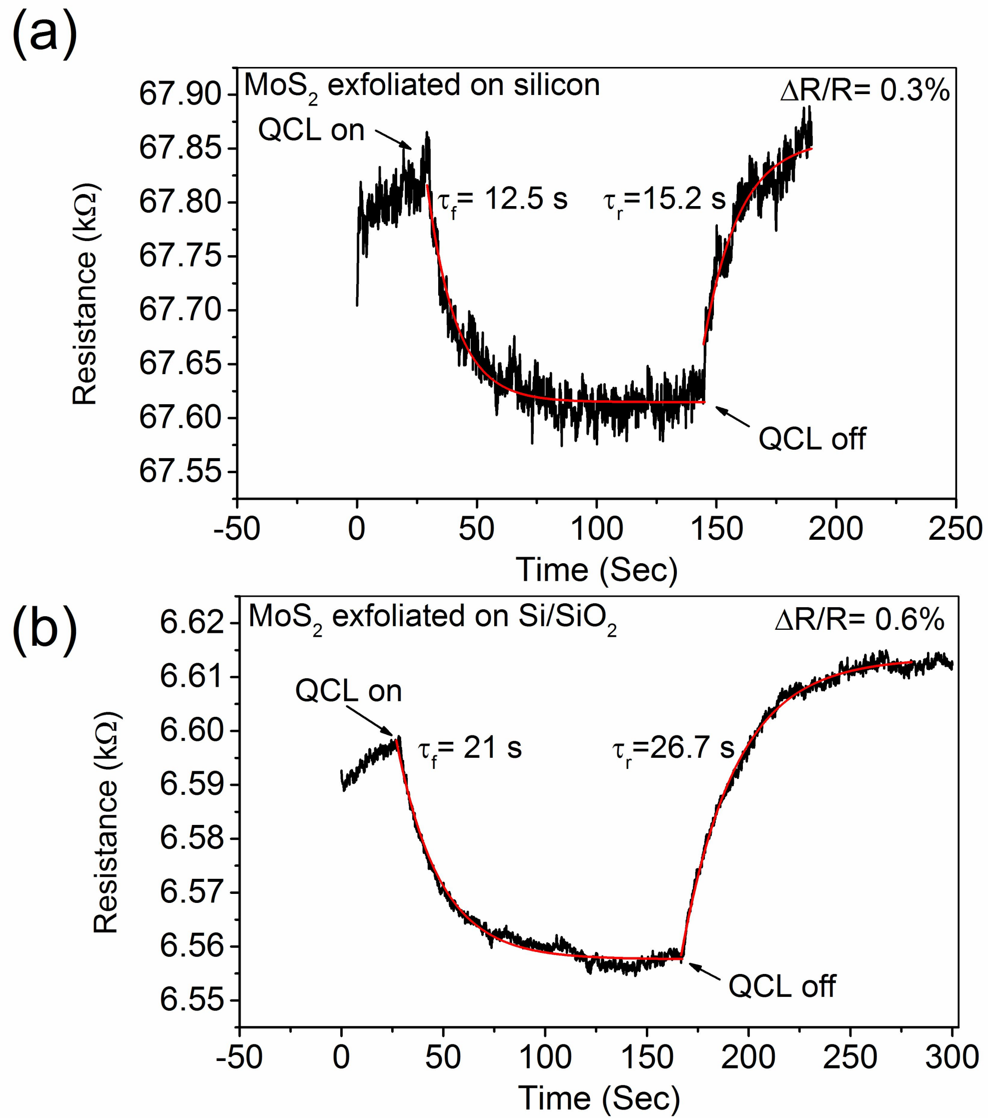

Figure 7.21: Sensitivity of the photothermal response of mechanically peeled MoS_2 on two different substrates (a) silicon and (b) thermal oxide (Si/SiO_2) using mid IR QCL.

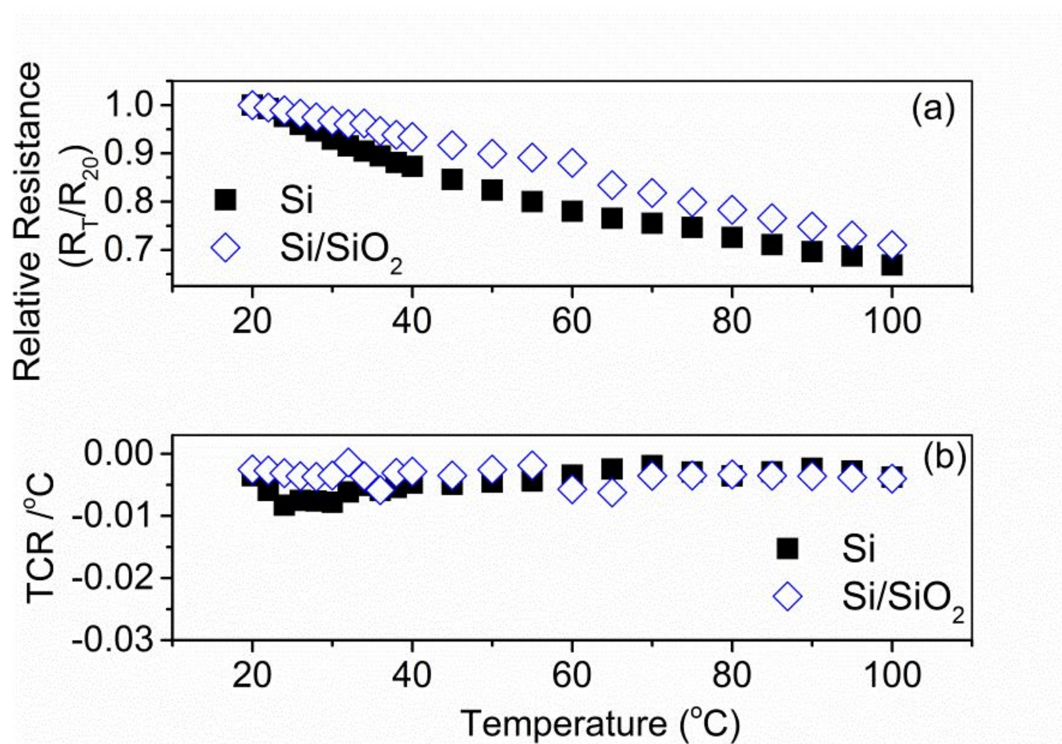

Figure 7.22: (a) Relative resistance with temperature and (b) TCR of mechanically peeled MoS_2 flakes transferred on two different substrates i.e. silicon and thermal oxide (Si/SiO_2).

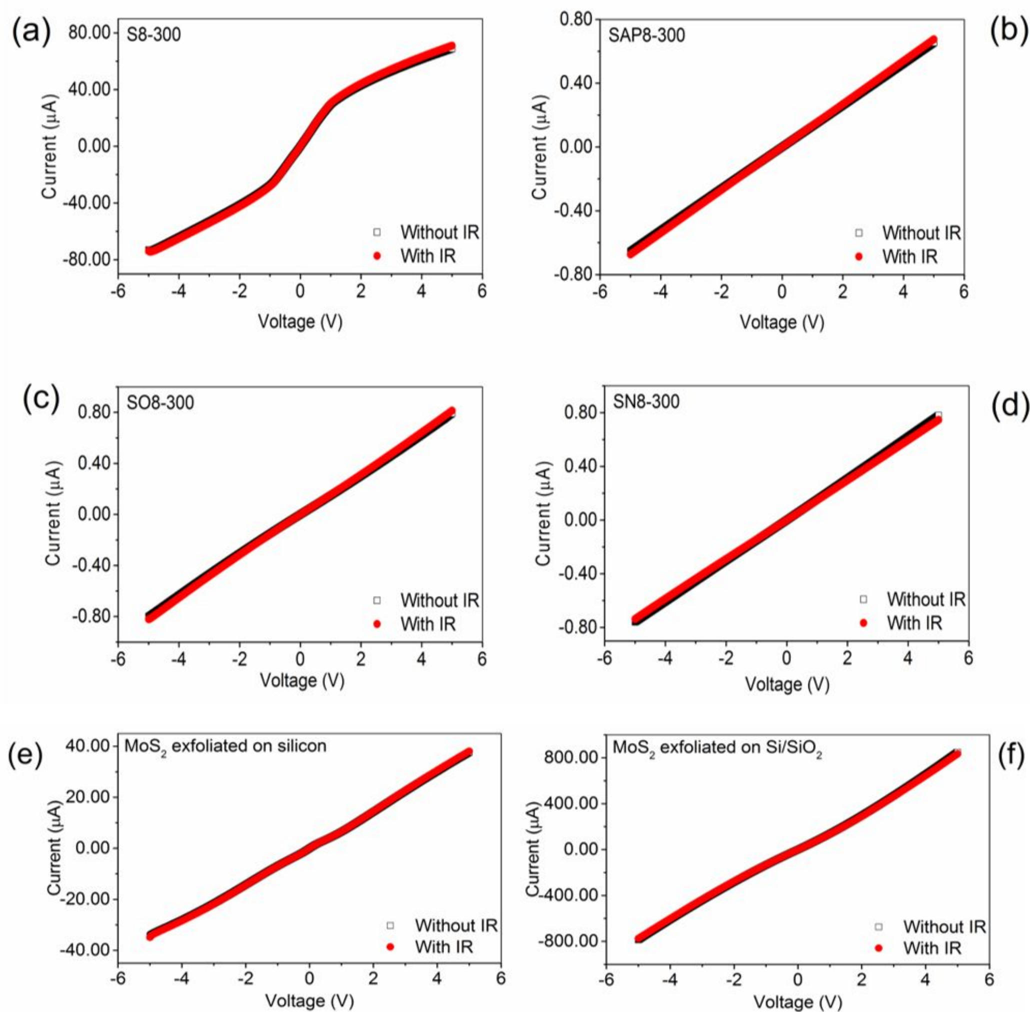

Figure 7.23: I-V Characteristics of PLD grown MoS_2 different substrates on (a) silicon, (b) sapphire, (c) thermal oxide (Si/SiO_2) and (d) silicon nitride (Si/SiN) and exfoliated MoS_2 transferred on (e) silicon and (f) thermal oxide (Si/SiO_2).

7.6.4 Responsivity calculation

Responsivity of any detector is measured by the voltage or current generation with respect to the incident radiant power which falls on the detector [206]. Here, the MoS_2 film acts as a detector which changes its resistance upon incident IR without any external bias. The equivalent circuit of the detector with the multimeter unit is shown in Figure 7.24. The multimeter feeds constant voltage (V_n= 4.3 V) to the circuit which goes through an internal circuit resistance. The internal resistance varies from 1 MΩ to 10 MΩ depending on the range of resistance to measure. Hence, the whole circuit works as a voltage divider. Therefore, the voltage drop due to the resistance change in response to the IR radiation can be calculated from the following formula

$$\Delta V = \frac{\Delta R_{IR(\mathrm{MoS_2})}}{R_M + R_{0(\mathrm{MoS_2})}} V_{in}. \tag{7.11}$$

ΔV is the voltage drop across the MoS_2 resistor as a result of IR modulated resistance. R_M is the multimeter's internal resistance varying from 1 MΩ to 10 MΩ. $R_{0(\mathrm{MoS_2})}$ is the initial resistance of the MoS_2 film prior to the IR radiation and $\Delta R_{IR(\mathrm{MoS_2})}$ is the change of resistance after IR irradiation. Hence, the responsivity is $\Delta V/W$, where W is the power of incident radiation. Here, we measured the responsivity at highest average power of QCL, which was 25mW, found at 1300 cm^{-1} (7.69 µm) corresponding to 25 mW.

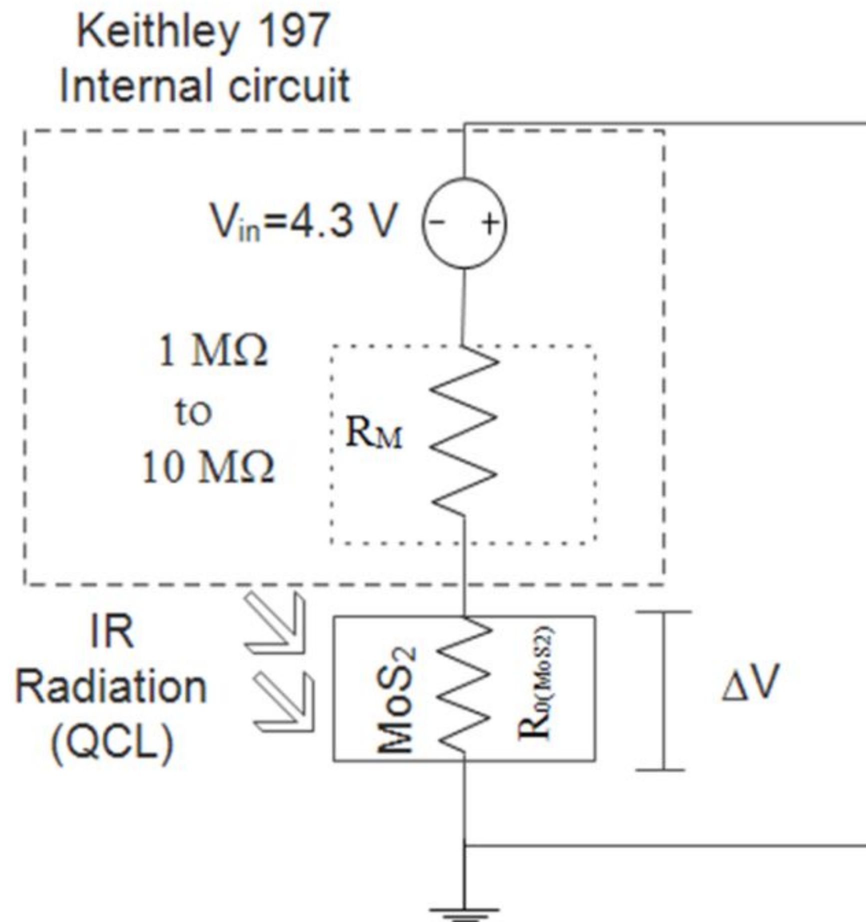

Figure 7.24: Equivalent circuit to calculate responsivity of MoS_2 thin film.

Chapter 8

Conclusions

8.1 Summary of completed work

The work presented in this thesis was concentrated on thin films produced by pulsed laser deposition, and furthering the scientific understanding of the synthesis, characterization, optimization, and applications of such films. The first two chapters of this thesis introduced the background and motivation of thin films, and the emergence of PLD as a viable deposition technique. These two chapters introduce the materials studied, VO_2 and MoS_2, and briefly explained the characterization techniques used within.

The experimental chapters in this thesis (Chapters 3-7) vary in content, with some chapters devoted to furthering the understanding regarding VO_2 film synthesis, including the influence of process parameters and substrate choice on both the phase stability and characteristics of the MIT (Chapters 3 and 4). Later chapters explore the application of VO_2 into mechanical resonators, and investigated the phase change induced resonance frequency shift in VO_2 cantilevers (Chapter 5). The success of Chapter 5 initiated the work in Chapter 6 which presented the synthesis of VO_2 microstring resonators as a means to improve upon the device in Chapter 5. Chapter 7 shifts the focus to PLD deposited MoS_2, where the synthesis, characterization, and mid-IR

photothermal response of such films were investigated. The work presented within this thesis is currently ongoing as well, and the future works, both in progress and recommendations for, will be presented in the following section.

8.2 Recommendation for future work

Given the success of the work presented previously, there are several projects that are currently being investigated for potential applications of both VO_2 and MoS_2 thin films, synthesized by PLD. As has been made clear throughout this thesis is that both of these materials possess unique properties that make them attractive in numerous applications. Currently, there are two areas that are being pursued in our current work, revolving around both of these materials. Additionally, I will discuss potential work that is being considered for future applications.

8.2.1 E-MIT of VO_2 thin films

While the work presented in this thesis on VO_2 has focused on thermally induced phase transitions, there are other ways that the transition can be induced, including the application of electric field [215, 216]. We are currently investigating the synthesis and qualification of such a device to be used in electric switching, memristive, and transistor type applications. By enabling the modulation between metal and insulator by the application of electric field we are able to control the signal transmitted. There is also potential to control the channel width in a field-effect transistor type orientation. We have already begun early work towards these applications with some initial successes and the future in this area looks promising.

8.2.2 Reduced thermal mass mid-IR detectors based on MoS_2 MEMS devices

As presented in Chapter 7, MoS_2 is capable as behaving as a mid-IR detector in addition to the well establish near-IR and visible detectors. What we found, however, was long transient times when the IR was turned on or off. Since the films tested in Chapter 7 were tested as deposited, there remains a large heat sink attached to the underside of the films, which may be one reason for such long times. We are working towards developing a suspended structure that isolates the sensitive layer from the underlying substrate by microfabrication. We have synthesized sub 250 nm wide silicon nitride strings, coated with MoS_2 via electron beam lithography (EBL) that have shown to reduce the response time by an order of magnitude. We are currently working towards the production of a suspended membrane isolated by thin support arms in an effort to increase the active absorbing area while minimizing heat loss through the support structure. We hope this design will further reduce the time to steady state by significantly reducing heat losses.

8.2.3 Future work considerations

In addition to the current work underway there are several ideas that are in the initial stage of work, where we are brainstorming potential applications for both VO_2 and MoS_2. Since MoS_2 was shown to perform admirably as a transistor material [46, 217], the potential application in computing devices has been explored as a way to continue the trend of decreasing transistor size. We are considering an application that utilizes the FET geometry to enhance photodetection of the mid-IR spectrum. Illumination of the MoS_2 channel will result in modulation of the electronic properties of the channel material which should be reflected in the I-V curve.

The final application under consideration for these two materials is to

combine them in vertical and horizontal heterostructure configuration. These types of devices have been explored for various materials, including /ceVO2 and MoS_2 [218], for applications in lasers, energy generation [219], and FETs. Both MoS_2 and VO_2 are n-type semiconductors, and form a type II heterojunction when in contact [218]. We would like to investigate the photoresponse of such a device under various wavelength illumination, as we have shown mid-IR detection with MoS_2, and the band gaps of multilayer MoS_2 and VO_2 of 1.29 and 0.6, respectively, stretches the range of detection well into the UV. We plan to explore multiple geometries and configurations of the heterojunction and investigate the responses of each.

Chapter 9

Bibliography

[1] T. Harper, "Global funding of nanotechnology & its impact," 2011.

[2] C. Palmberg, H. Dernis, and C. Miguet, "Nanotechnology: an overview based on indicators and statistics," *OECD Science, Technology and Industry Working Papers*, p. 112, 2009.

[3] A. K. Maini, "Optoelectronic Devices and Circuits," in *Lasers and Optoelectronics*, pp. 315–377, Chichester, United Kingdom: John Wiley and Sons Ltd, 2013.

[4] R. K. Roy, *Primer on the Taguchi Method (2nd Edition) - Knovel*. Society of Manufacturing Engineers, 1990.

[5] J. H. Park, J. M. Coy, T. S. Kasirga, C. Huang, Z. Fei, S. Hunter, and D. H. Cobden, "Measurement of a solid-state triple point at the metal-insulator transition in VO_2," *Nature*, vol. 500, no. 7463, 2013.

[6] M. Bayati, R. Molaei, F. Wu, J. Budai, Y. Liu, R. Narayan, and J. Narayan, "Correlation between structure and semiconductor-to-metal transition characteristics of VO_2/TiO_2/sapphire thin film heterostructures," *Acta Mater.*, vol. 61, no. 20, pp. 7805–7815, 2013.

[7] O. Lopez-Sanchez, D. Lembke, M. Kayci, A. Radenovic, and A. Kis, "Ultrasensitive photodetectors based on monolayer MoS_2," *Nat. Nanotechnol.*, vol. 8, no. 7, pp. 497–501, 2013.

[8] L. Ye, H. Li, Z. Chen, and J. Xu, "Near-Infrared Photodetector Based on MoS_2/Black Phosphorus Heterojunction," *ACS Photonics*, 2016.

[9] D. Dijkkamp, T. Venkatesan, X. D. Wu, S. A. Shaheen, N. Jisrawi, Y. H. Min-Lee, W. L. McLean, and M. Croft, "Preparation of Y-Ba-Cu oxide superconductor thin films using pulsed laser evaporation from high T_c bulk material," *Appl. Phys. Lett.*, vol. 51, no. 8, pp. 619–621, 1987.

[10] D. P. Norton, "Pulsed laser deposition of complex materials: Progress toward applications," in *Wiley* (R. Eason, ed.), ch. 1, pp. 3–28, John Wiley & Sons, 2007.

[11] J. A. Venables, T. Spiller, and M. Hanbucken, "Reports on Progress in Physics Nucleation and growth of thin films," *Rep. Prog. Phys.*, vol. 47, no. 47, pp. 399–399, 1984.

[12] N. Hansen, "HallâĂŞPetch relation and boundary strengthening," *Scr. Mater.*, vol. 51, no. 8, pp. 801–806, 2004.

[13] A. F. MAYADAS and M. SHATZKES, "Electrical-Resistivity Model for Polycrystalline Films: the Case of Arbitrary Reflection at External Surfaces," *J. Appl. Phys*, vol. 1, no. 39, pp. 315–4241, 1952.

[14] O. Hunderi, "Influence of Grain Boundaries and Lattice Defects on the Optical Properties of Some Metals," *Phys. Rev. B*, vol. 7, no. 8, pp. 3419–3429, 1973.

[15] J. R. Smith and J. Ferrante, "Grain-boundary energies in metals from local-electron-density distributions," *Phys. Rev. B*, vol. 34, no. 4, pp. 2238–2245, 1986.

[16] K. Vanheusden, W. L. Warren, C. H. Seager, D. R. Tallant, J. A. Voigt, and B. E. Gnade, "Mechanisms behind green photoluminescence in ZnO phosphor powders," *J. Appl. Phys.*, vol. 791, no. 10, pp. 41301–122102, 1996.

[17] M. Hillert, "On the theory of normal and abnormal grain growth," *Acta Metall.*, vol. 13, no. 3, pp. 227–238, 1965.

[18] C. V. Thompson, "Grain Growth in Thin Films," *Annu. Rev. Mater. Sci.*, vol. 20, no. 1, pp. 245–268, 1990.

[19] P. Feltham, "Grain growth in metals," *Acta Metall.*, vol. 5, no. February, pp. 97–105, 1957.

[20] F. J. Morin, "Oxides which show a metal-to-insulator transition at the neel temperature," *Phys. Rev. Lett.*, vol. 3, no. 1, pp. 34–36, 1959.

[21] D. B. McWhan, M. Marezio, J. P. Remeika, and P. D. Dernier, "X-ray diffraction study of metallic VO_2," *Phys. Rev. B*, 1974.

[22] J. M. Longo and P. Kierkegaard, "A refinement of the structure of VO_2," *Acta Chem. Scand.*, vol. 24, pp. 420–426, 1970.

[23] Y. Wu, L. Fan, W. Huang, S. Chen, S. Chen, F. Chen, C. Zou, and Z. Wu, "Depressed transition temperature of $W_xV_{1-x}O_2$: mechanistic insights from the X-ray absorption fine structure (XAFS) spectroscopy," *Phys. Chem. Chem. Phys.*, vol. 16, no. 33, p. 17705, 2014.

[24] N. F. Mott, "The Basis of the Electron Theory of Metals, with Special Reference to the Transition Metals," *Proc. Phys. Soc. A*, vol. 62, pp. 416–422, 1949.

[25] N. F. Mott, "Metal-insulator transition," *Rev. Mod. Phys.*, vol. 40, no. 4, pp. 677–683, 1968.

[26] K. A. Penson, A. Holz, and K. H. Bennemann, “Theory of the peierls transition in coupled electron and classical spin systems,” *Phys. Rev. B*, vol. 13, no. 1, pp. 433–440, 1976.

[27] H. W. Verleur, A. S. Barker, and C. N. Berglund, “Optical properties of VO_2 between 0.25 and 5 eV,” *Rev. Mod. Phys.*, vol. 40, no. 4, p. 737, 1968.

[28] K. Okabe, T. Mitsuishi, Y. Sasaki, H. Takei, H. Miyazaki, I. Yasui, S. Ishibashi, A. Yamaguchi, and Y. Suzuki, “Effects of Various Doping Elements on the Transition Temperature of Vanadium Oxide Semiconductors,” *Jpn. J. Appl. Phys*, vol. 8, 1969.

[29] Y. Ke, I. Balin, N. Wang, Q. Lu, A. Iing, Y. Tok, T. J. White, S. Magdassi, I. Abdulhalim, and Y. Long, “Two-Dimensional SiO_2/VO_2 Photonic Crystals with Statically Visible and Dynamically Infrared Modulated for Smart Window Deployment,” *ACS Appl. Mater. Interfaces*, 2016.

[30] J. Zhou, Y. Gao, Z. Zhang, H. Luo, C. Cao, Z. Chen, L. Dai, and X. Liu, “VO_2 thermochromic smart window for energy savings and generation.,” *Sci. Rep.*, vol. 3, p. 3029, 2013.

[31] F. Béteille and J. Livage, “Optical Switching in VO_2 Thin Films,” *J. Sol-Gel Sci. Technol.*, vol. 921, pp. 915–921, 1998.

[32] H. Jerominek and D. Vincent, “Vanadium oxide films for optical switching and detection,” *Opt. Eng.*, vol. 32, no. 9, 1993.

[33] M. Rini, Z. Hao, R. W. Schoenlein, C. Giannetti, F. Parmigiani, S. Fourmaux, J. C. Kieffer, A. Fujimori, M. Onoda, S. Wall, and A. Cavalleri, “Optical switching in VO_2 films by below-gap excitation,” *Appl. Phys. Lett.*, vol. 92, no. 18, pp. 1–4, 2008.

[34] S.-H. Bae, S. Lee, H. Koo, L. Lin, B. Hyun Jo, C. Park, Z. Lin Wang, S.-h. Bae, H. Koo, B. H. Jo C Park, S. Lee, L. Lin, Z. L. Wang, and C. Park,

"The Memristive Properties of a Single VO_2 Nanowire with Switching Controlled by Self-Heating," *Adv. Mater.*, 2013.

[35] B. Wang, J. Lai, H. Li, H. Hu, and S. Chen, "Nanostructured vanadium oxide thin film with high TCR at room temperature for microbolometer," *Infrared Phys. Technol.*, vol. 57, pp. 8–13, 2013.

[36] K. Kosuge, "The phase diagram and phase transition of the V,O,-V,O, system," *J. Phys. Chem. Solids Pergamon Press*, vol. 28, pp. 1613–1621, 1967.

[37] X. Li and H. Zhu, "Two-dimensional MoS_2: Properties, preparation, and applications," *J. Materiomics*, vol. 1, no. 1, pp. 33 – 44, 2015.

[38] B. Schönfeld, J. J. Huang, and S. C. Moss, "Anisotropic mean-square displacements (MSD) in single-crystals of 2*H*- and 3*R*-MoS_2," *Acta Crystallogr. B*, vol. 39, no. 4, pp. 404–407, 1983.

[39] K. F. Mak, C. Lee, J. Hone, J. Shan, and T. F. Heinz, "Atomically Thin MoS_2: A New Direct-Gap Semiconductor," *Phys. Rev. Lett.*, vol. 136805, no. September, pp. 2–5, 2010.

[40] S. Mukherjee, R. Maiti, A. Midya, S. Das, and S. K. Ray, "Tunable Direct Bandgap Optical Transitions in MoS_2 Nanocrystals for Photonic Devices," *ACS Photonics*, vol. 2, no. 6, pp. 760–768, 2015.

[41] H. Zeng, J. Dai, W. Yao, D. Xiao, and X. Cui, "Valley polarization in MoS_2 monolayers by optical pumping," *Nat. Nanotechnol.*, vol. 7, no. 8, pp. 490–493, 2012.

[42] A. Splendiani, L. Sun, Y. Zhang, T. Li, J. Kim, C.-Y. Chim, G. Galli, and F. Wang, "Emerging Photoluminescence in Monolayer MoS_2," *Nano Lett.*, vol. 10, no. 4, pp. 1271–1275, 2010.

[43] D. Akinwande, N. Petrone, and J. Hone, "Two-dimensional flexible nanoelectronics," *Nat. Commun.*, vol. 5, p. 5678, 2014.

[44] Q. H. Wang, K. Kalantar-Zadeh, A. Kis, J. N. Coleman, and M. S. Strano, "Electronics and optoelectronics of two-dimensional transition metal dichalcogenides," *Nat. Nanotechnol.*, vol. 7, no. 11, pp. 699–712, 2012.

[45] F. Xia, H. Wang, D. Xiao, M. Dubey, and A. Ramasubramaniam, "Two-dimensional material nanophotonics," *Nat. Photonics*, vol. 8, p. 899, 2014.

[46] B. Radisavljevic, A. Radenovic, J. Brivio, V. Giacometti, and A. Kis, "Single-layer MoS_2 transistors," *Nat. Nanotechnol.*, vol. 6, no. 3, pp. 147–150, 2011.

[47] B. Radisavljevic and A. Kis, "Mobility engineering and a metal-insulator transition in monolayer MoS_2," *Nat. Mater.*, vol. 12, no. 9, pp. 815–820, 2013.

[48] J. Klinovaja and D. Loss, "Spintronics in MoS_2 monolayer quantum wires," *Phys. Rev. B*, vol. 88, no. 7, p. 075404, 2013.

[49] R. Fivaz and E. Mooser, "Mobility of Charge Carriers in Semiconducting Layer Structures," *Phys. Rev.*, vol. 163, no. 3, pp. 743–755, 1967.

[50] L. Hao, Y. Liu, W. Gao, Z. Han, Q. Xue, H. Zeng, Z. Wu, J. Zhu, and W. Zhang, "Electrical and photovoltaic characteristics of MoS_2/Si *p-n* junctions," *J. Appl. Phys.*, vol. 117, no. 11, p. 114502, 2015.

[51] N. Ashcroft and N. Mermin, *Solid State Physics*. Saunders College, 1976.

[52] J. Goldstein, D. Newbury, D. Joy, C. Lyman, P. Echlin, E. Lifshin, L. Sawyer, and J. Michael, *Scanning Electron Microscopy and X-Ray Microanalysis*. Springer US, 2003.

[53] K. KANAYA and S. OKAYAMA, "Penetration and energy-loss theory of electrons in solid targets," *J. Phys. D*, vol. 5, no. 1, pp. 43–&, 1972.

[54] C. Rao, "Transition metal oxides1," *Annu. Rev. Phys. Chern.*, vol. 40, no. 40, pp. 291–326, 1989.

[55] D. B. McWhan and J. P. Remeika, "Metal-Insulator Transition in $(V_{1-x}Cr_x)_2O_3$," *Phys. Rev. B*, vol. 2, no. 9, pp. 3734–3750, 1970.

[56] Z. Yang, C. Ko, and S. Ramanathan, "Metal-insulator transition characteristics of VO_2 thin films grown on Ge(100) single crystals," *J. Appl. Phys.*, vol. 108, no. 7, 2010.

[57] J. Jeong, N. Aetukuri, T. Graf, T. D. Schladt, M. G. Samant, and S. S. P. Parkin, "Suppression of metal-insulator transition in VO_2 by electric field-induced oxygen vacancy formation.," *Science*, vol. 339, no. 6126, pp. 1402–1405, 2013.

[58] H. Kuwahara, Y. Tomioka, A. Asamitsu, Y. Moritomo, and Y. Tokura, "A First-Order Phase Transition Induced by a Magnetic Field," *Science*, vol. 270, no. 5238, pp. 961–963, 1995.

[59] Y. Tomioka, A. Asamitsu, H. Kuwahara, Y. Moritomo, and Y. Tokura, "Magnetic-field-induced metal-insulator phenomena in $Pr_{1-x}Ca_xMnO_3$ with controlled charge-ordering instability," *Phys. Rev. B*, vol. 53, no. 4, pp. R1689–R1692, 1996.

[60] R. E. Marvel, R. R. Harl, V. Craciun, B. R. Rogers, and R. F. Haglund, "Influence of deposition process and substrate on the phase transition of vanadium dioxide thin films," *Acta Mater.*, vol. 91, pp. 217–226, 2015.

[61] G. Andersson, C. Parck, U. Ulfvarson, E. Stenhagen, and B. Thorell, "Studies on Vanadium Oxides. II. The Crystal Structure of Vanadium Dioxide.," *Acta Chem. Scand.*, vol. 10, pp. 623–628, 1956.

[62] L. Pellegrino, N. Manca, T. Kanki, H. Tanaka, M. Biasotti, E. Bellingeri, A. S. Siri, and D. Marré, "Multistate memory devices based on free-standing VO_2/TiO_2 microstructures driven by Joule self-heating," *Adv. Mater.*, 2012.

[63] A. Rogalski, "Recent progress in infrared detector technologies," in *Infrared Physics and Technology*, 2011.

[64] Q. Cheng, S. Paradis, T. Bui, and M. Almasri, "Design of Dual-Band Uncooled Infrared Microbolometer," *IEEE Sens. J.*, vol. 11, no. 1, 2011.

[65] H. Jerominek, T. D. Pope, M. Renaud, N. R. Swart, F. Picard, M. Lehoux, S. Savard, G. Bilodeau, D. Audet, P. Linh Ngo, and Q. Chu Nong, "6464, 128128, 240320 pixel uncooled IR bolometric detector arrays," in *Infrared Technology and Applications XXIII, 20-25 April 1997*, 1997.

[66] E. Strelcov, Y. Lilach, and A. Kolmakov, "Gas Sensor Based on Metal-Insulator Transition in VO_2 Nanowire Thermistor," *Nano Lett.*, vol. 9, no. 6, pp. 2322–2326, 2009.

[67] B. Hu, Y. Ding, W. Chen, D. Kulkarni, Y. Shen, V. V. Tsukruk, and Z. L. Wang, "External-strain induced insulating phase transition in VO_2 nanobeam and its application as flexible strain sensor," *Adv. Mater.*, vol. 22, no. 45, pp. 5134–5139, 2010.

[68] S. Sengupta, K. Wang, K. Liu, A. K. Bhat, S. Dhara, J. Wu, and M. M. Deshmukh, "Field-effect modulation of conductance in VO_2 nanobeam transistors with HfO_2 as the gate dielectric," *Appl. Phys. Lett.*, vol. 99, no. 6, pp. 2–5, 2011.

[69] M. J. Powell, R. Quesada-Cabrera, A. Taylor, D. Teixeira, I. Papakonstantinou, R. G. Palgrave, G. Sankar, and I. P. Parkin, "Intelligent Multi-

functional $VO_2/SiO_2/TiO_2$ Coatings for Self-Cleaning, Energy-Saving Window Panels," *Chem. Mater.*, vol. 28, no. 5, pp. 1369–1376, 2016.

[70] M. Soltani, M. Chaker, E. Haddad, R. V. Kruzelecky, and J. Margot, "Effects of Ti-W codoping on the optical and electrical switching of vanadium dioxide thin films grown by a reactive pulsed laser deposition," *Appl. Phys. Lett.*, 2004.

[71] H. Lim, N. Stavrias, B. C. Johnson, R. E. Marvel, R. F. Haglund, and J. C. McCallum, "Optical switching and photoluminescence in erbium-implanted vanadium dioxide thin films," *J. Appl. Phys.*, vol. 115, no. 9, 2014.

[72] R. Naorem, G. Dayal, S. A. Ramakrishna, B. Rajeswaran, and A. Umarji, "Thermally switchable metamaterial absorber with a VO_2 ground plane," *Opt. Commun.*, vol. 346, pp. 154 – 157, 2015.

[73] T. Driscoll, H. T. Kim, B. G. Chae, M. Di Ventra, and D. N. Basov, "Phase-transition driven memristive system," *Appl. Phys. Lett.*, vol. 95, no. 4, 2009.

[74] C. V. Ramana, R. J. Smith, O. M. Hussain, and C. M. Julien, "On the growth mechanism of pulsed-laser deposited vanadium oxide thin films," *Mater. Sci. Eng., B*, 2004.

[75] U. Schwingenschlögl, V. Eyert, and U. Eckern, "From VO_2 to V_2O_3: The metal-insulator transition of the Magnéli phase V_6O_{11}," *Europhys. Lett.*, vol. 61, no. 3, pp. 361–367, 2003.

[76] U. Schwingenschlögl and V. Eyert, "The vanadium Magnéli phases V_nO_{2n-1}," *Annalen der Physik (Leipzig)*, vol. 13, no. 9, pp. 475–510, 2004.

[77] S. Lee, I. N. Ivanov, J. K. Keum, and H. N. Lee, "Epitaxial stabilization and phase instability of VO_2 polymorphs," *Scientific Reports*, 2016.

[78] C. Leroux, G. Nihoul, and G. Van Tendeloo, "From VO_2(B) to VO_2(R): Theoretical structures of VO_2 polymorphs and in situ electron microscopy," *Phys. Rev. B*, vol. 57, no. 9, pp. 5111–5121, 1998.

[79] E. Baudrin, G. Sudant, D. Larcher, B. Dunn, and J.-M. Tarascon, "Preparation of Nanotextured VO_2[B] from Vanadium Oxide Aerogels," *Chem. Mater.*, 2006.

[80] D. Fu, K. Liu, T. Tao, K. Lo, C. Cheng, B. Liu, R. Zhang, H. A. Bechtel, and J. Wu, "Comprehensive study of the metal-insulator transition in pulsed laser deposited epitaxial VO_2 thin films," *J. Appl. Phys.*, vol. 113, no. 4, pp. 1–7, 2013.

[81] C. I. Li, J. C. Lin, H. J. Liu, M. W. Chu, H. W. Chen, C. H. Ma, C. Y. Tsai, H. W. Huang, H. J. Lin, H. L. Liu, P. W. Chiu, and Y. H. Chu, "Van der Waal Epitaxy of Flexible and Transparent VO_2 Film on Muscovite," *Chem. Mater.*, 2016.

[82] H. Tabata, H. Tanaka, and T. Kawai, "Formation of artificial $BaTiO_3/SrTiO_3$ superlattices using pulsed laser deposition and their dielectric properties," *Appl. Phys. Lett.*, vol. 6, no. 15, pp. 1970–1972, 1994.

[83] O. Nakagawara, T. Shimuta, T. Makino, S. Arai, H. Tabata, and T. Kawai, "Epitaxial growth and dielectric properties of (111) oriented BaTiO[sub 3]/SrTiO[sub 3] superlattices by pulsed-laser deposition," *Appl. Phys. Lett.*, vol. 77, no. 20, p. 3257, 2000.

[84] H.-U. Krebs, *Pulsed Laser Deposition of Metals*, pp. 363–382. John Wiley & Sons, Inc., 2006.

[85] R. Teghil, L. D'Alessio, A. De Bonis, A. Galasso, N. Ibris, A. M. Salvi, A. Santagata, and P. Villani, "Nanoparticles and thin film formation in

ultrashort pulsed laser deposition of vanadium oxide," *J. Phys. Chem. A*, 2009.

[86] B. Masina, S. Lafane, L. Wu, S. Abdelli-Messaci, T. Kerdja, and A. Forbes, "Optimisation study of the synthesis of vanadium oxide nano- structures using pulsed laser deposition," in *Quantum Dots and Nanostructures: Synthesis, Characterization, and Modeling XI*, 2014.

[87] D. Wegkamp, M. Herzog, L. Xian, M. Gatti, P. Cudazzo, C. L. McGahan, R. E. Marvel, R. F. Haglund, A. Rubio, M. Wolf, and J. Stähler, "Instantaneous band gap collapse in photoexcited monoclinic VO_2 due to photocarrier doping," *Phys. Rev. Lett.*, 2014.

[88] B. S. Allimi, S. P. Alpay, C. K. Xie, B. O. Wells, J. I. Budnick, and D. M. Pease, "Resistivity of V_2O_3 thin films deposited on a-plane (110) and c-plane (001) sapphire by pulsed laser deposition," *Appl. Phys. Lett.*, vol. 92, no. 20, pp. 202103–202105, 2008.

[89] J. Nag, E. A. Payzant, K. L. More, and R. F. Haglund, "Enhanced performance of room-temperature-grown epitaxial thin films of vanadium dioxide," *Appl. Phys. Lett.*, vol. 98, no. 25, pp. 1–4, 2011.

[90] B. N. Masina, S. Lafane, L. Wu, A. A. Akande, B. Mwakikunga, S. Abdelli-Messaci, T. Kerdja, and A. Forbes, "Phase-selective vanadium dioxide (VO_2) nanostructured thin films by pulsed laser deposition," *J. Appl. Phys.*, 2015.

[91] H. Kim, N. Charipar, M. Osofsky, S. B. Qadri, and A. Piqu, "Optimization of the semiconductor-metal transition in VO_2 epitaxial thin films as a function of oxygen growth pressure," *Appl. Phys. Lett.*, vol. 081913, 2014.

[92] A. Srivastava, H. Rotella, S. Saha, B. Pal, G. Kalon, S. Mathew, M. Dykas,

P. Yang, E. Okunishi, D. D. Sarma, T. Venkatesan, A. Srivastava, H. Rotella, S. Saha, and B. Pal, “Selective growth of single phase VO_2 (A, B, and M) polymorph thin films,” *APL Mater.*, vol. 2, 2015.

[93] C. V. Thompson, “Structure evolution during processing of polycrystalline films,” *Mater. Sci.*, no. 12, 2000.

[94] J. BÃijhler, F.-P. Steiner, and H. Baltes, “Silicon dioxide sacrificial layer etching in surface micromachining,” *J. Micromech. Microeng.*, vol. 7, no. 1, p. R1, 1997.

[95] “Minitab 17 statistical software,” 2017.

[96] B. G. Shin, G. H. Han, S. J. Yun, H. M. Oh, J. J. Bae, Y. J. Song, C. Y. Park, and Y. H. Lee, “Indirect Bandgap Puddles in Monolayer MoS_2 by Substrate-Induced Local Strain,” *Adv. Mater.*, vol. 28, no. 42, pp. 9378–9384, 2016.

[97] J. Gonzalo, C. Afonso, and J. Ballesteros, “Ablation of $BaTiO_3$ in a gas pressure: plasma and film optical properties,” *Appl. Surf. Sci.*, vol. 109-110, pp. 606–610, 1997.

[98] P. E. Dyer, A. Isa, and P. H. Key, “An investigation of laser ablation in an oxygen environment and deposition of Y-Ba-Cu-O in an oxygen environment,” *Appl. Surf. Sci.*, vol. 46, pp. 89–95, 1990.

[99] J. L. Bobin, Y. A. Durand, P. P. Langer, and G. Tonon, “Shock-wave generation in rarefied gases by laser impact on beryllium targets,” *J. Appl. Phys.*, vol. 39, no. 9, pp. 4184–4189, 1968.

[100] B. Doggett and J. G. Lunney, “Expansion dynamics of laser produced plasma,” *J. Appl. Phys.*, vol. 1091, no. 10, 2011.

[101] B. Khorshidi, T. Thundat, B. A. Fleck, and M. Sadrzadeh, "Thin film composite polyamide membranes: parametric study on the influence of synthesis conditions," *RSC Adv.*, vol. 5, no. 68, pp. 54985–54997, 2015.

[102] D. L. Mills and A. A. Maradudin, "Surface roughness and the optical properties of a semi-infinite material; the effect of a dielectric overlayer," *Phys. Rev. B*, 1975.

[103] V. Timoshevskii, Y. Ke, H. Guo, and D. Gall, "The influence of surface roughness on electrical conductance of thin Cu films: An ab initio study," *J. Appl. Phys.*, 2008.

[104] B. D. Ngom, M. Chaker, A. Diallo, I. G. Madiba, S. Khamlich, N. Manyala, O. Nemraoui, R. Madjoe, A. C. Beye, and M. Maaza, "Competitive growth texture of pulsed laser deposited vanadium dioxide nanostructures on a glass substrate," *Acta Mater.*, 2014.

[105] J. H. de Boer, E. J. W. Verwey, S. A. H, Bethe, B. L, M. N. F. H, Jones, W. A. H, W. A. H, F. R. H, F. R. H, B. R. F. S, Goudsmit, G. C. J, L. B. M. H, Sachse, G. B, W. C, W. C, V. E. J. W. H, de Boer J, W. C. E, Koch, S. W, J. E. R. F, Foote, K. W. K, Hass, D. H. C, Wagner, S. W. F, Waibel, S. M, D. H. v Baumbach H H, W. C, H. F, d. B. J. H. Ch, van Geel W, J. W. P. W, K. B, B. K, d. B. J. H, d. B. J. H, H. G, V. E. J. W, and d. B. J. H, "Semi-conductors with partially and with completely filled 3 d-lattice bands," *Proc. Phys. Soc. London*, vol. 49, no. 4S, pp. 59–71, 1937.

[106] N. F. Mott and R. Peierls, "Discussion of the paper by de Boer and Verwey," *Proc. Phys. Soc. London*, vol. 49, no. 4S, pp. 72–73, 1937.

[107] J. Hubbard, "Electron Correlations in Narrow Energy Bands," *Proc. R. Soc. London, Ser. A*, vol. 276, no. 1365, pp. 238–257, 1963.

[108] H. Tasaki, "The Hubbard model - an introduction and selected rigorous results," *J. Phys.: Condens. Matter*, vol. 10, no. 20, p. 4353, 1998.

[109] N. F. Mott and L. Friedman, "Metal-insulator transitions in VO_2, Ti_2O_3 and $Ti_{2-x}V_xO_3$," *Philos. Mag.*, vol. 30, no. 2, pp. 389–402, 1974.

[110] R. T. Rajendra, B. Karunagaran, and D. Mangalaraj, "Study of a pulsed laser deposited vanadium oxide based microbolometer," *Smart Mater. Struct.*, vol. 188, pp. 187–192, 2003.

[111] L. Fan, Y. Chen, Q. Liu, S. Chen, L. Zhu, Q. Meng, B. Wang, Q. Zhang, H. Ren, and C. Zou, "Infrared Response and Optoelectronic Memory Device Fabrication Based on Epitaxial VO_2 Film," *ACS Appl. Mater. Interfaces*, 2016.

[112] G. Stefanovich, a. Pergament, and D. Stefanovich, "Electrical switching and Mott transition in VO_2," *J. Phys.: Condens. Matter*, vol. 12, no. 41, pp. 8837–8845, 2000.

[113] A. Gupta, R. Aggarwal, and J. Narayan, "Integration of VO_2 Thin Films on Si (100) for Thermal Switching Devices Applications," *Mater. Res. Soc. Symp. Proc.*, vol. 1174, 2009.

[114] J. Zhu, Y. Zhou, B. Wang, J. Zheng, S. Ji, H. Yao, H. Luo, and P. Jin, "Vanadium Dioxide Nanoparticle-based Thermochromic Smart Coating: High Luminous Transmittance, Excellent Solar Regulation Efficiency, and Near Room Temperature Phase Transition," *ACS Appl. Mater. Interfaces*, 2015.

[115] M. J. Miller and J. Wang, "Influence of grain size on transition temperature of thermochromic VO_2," *J. Appl. Phys.*, vol. 117, no. 96, 2015.

[116] Y. Zhao, J. H. Lee, Y. Zhu, M. Nazari, C. Chen, H. Wang, A. Bernussi, M. Holtz, and Z. Fan, "Structural, electrical, and terahertz transmission

properties of VO_2 thin films grown on c-, r-, and m-plane sapphire substrates," *J. Appl. Phys.*, vol. 1111, no. 10, 2012.

[117] R. McGee, A. Goswami, B. Khorshidi, K. McGuire, K. Schofield, and T. Thundat, "Effect of process parameters on phase stability and metal-insulator transition of vanadium dioxide (VO_2) thin films by pulsed laser deposition," *Acta Mater.*, vol. 137, pp. 12–21, 2017.

[118] L. L. Fan, S. Chen, Z. L. Luo, Q. H. Liu, Y. F. Wu, L. Song, D. X. Ji, P. Wang, W. S. Chu, C. Gao, C. W. Zou, and Z. Y. Wu, "Strain Dynamics of Ultrathin VO_2 Film Grown on TiO_2 (001) and the Associated Phase Transition Modulation," *Nano Lett.*, vol. 14, no. 7, pp. 4036–4043, 2014.

[119] L. L. Fan, S. Chen, G. M. Liao, Y. L. Chen, H. Ren, and C. W. Zou, "Comprehensive studies of interfacial strain and oxygen vacancy on metalâĂŞinsulator transition of VO_2 film," *J. Phys.: Condens. Matter*, vol. 28, no. 25, p. 255002, 2016.

[120] T. Yamin, S. Wissberg, H. Cohen, G. Cohen-Taguri, and A. Sharoni, "Ultrathin Films of VO_2 on r-Cut Sapphire Achieved by Postdeposition Etching," *ACS Appl. Mater. Interfaces*, 2016.

[121] Y. Li, S. Ji, Y. Gao, H. Luo, and P. Jin, "Modification of Mott Phase Transition Characteristics in VO_2@TiO_2 Core/Shell Nanostructures by Misfit-Strained Heteroepitaxy," *ACS Appl. Mater. Interfaces*, 2013.

[122] C. V. Thompson, "Solid-State Dewetting of Thin Films," *Annu. Rev. Mater. Res.*, vol. 42, no. 1, pp. 399–434, 2012.

[123] J. Narayan and B. C. Larson, "Domain epitaxy: A unified paradigm for thin film growth," *J. Appl. Phys.*, vol. 93, no. 1, pp. 278–285, 2003.

[124] A. Moatti, R. Sachan, J. Prater, and J. Narayan, "Control of Structural

and Electrical Transitions of VO_2 Thin Films," *ACS Appl. Mater. Interfaces*, 2017.

[125] W. H. Bragg and W. L. Bragg, "The Reflection of X-rays by Crystals," *Proc. R. Soc. London, Ser. A*, vol. 88, no. 605, pp. 428–438, 1913.

[126] H. Brune, "Epitaxial Growth of Thin Films," in *Surface and Interface Science: Solid-Solid Interfaces and Thin Films* (Klaus Wandelt, ed.), ch. 20, Wiley-VCH Verlag GmbH & Co., first edit ed., 2014.

[127] S. Blonksi and S. Garofalini, "Molecular dynamics simulations of α-alumina and γ-alumina surfaces," *Surf. Sci.*, vol. 295, no. 1-2, pp. 263–274, 1993.

[128] R. G. Frieser, "Characterization of Thermally Grown SiO_2 Surfaces by Contact Angle Measurements," *J. Electrochem. Soc.*, pp. 5–8, 1974.

[129] T. A. Mellan and R. Grau-Crespo, "Density functional theory study of rutile VO_2 surfaces," *J. Chem. Phys.*, vol. 1371, no. 137, 2012.

[130] N. B. Aetukuri, A. X. Gray, M. Drouard, M. Cossale, L. Gao, A. H. Reid, R. Kukreja, H. Ohldag, C. A. Jenkins, E. Arenholz, K. P. Roche, H. A. Durr, M. G. Samant, and S. S. P. Parkin, "Control of the metal-insulator transition in vanadium dioxide by modifying orbital occupancy," *Nat. Phys.*, vol. 9, no. 10, pp. 661–666, 2013.

[131] K. Nagashima, T. Yanagida, H. Tanaka, and T. Kawai, "Interface effect on metal-insulator transition of strained vanadium dioxide ultrathin films," *J. Appl. Phys.*, 2007.

[132] K. Nagashima, T. Yanagida, H. Tanaka, and T. Kawai, "Stress relaxation effect on transport properties of strained vanadium dioxide epitaxial thin films," *Phys. Rev. B*, vol. 74, no. 17, p. 172106, 2006.

[133] A. Kelly and K. M. Knowles, "Appendix 3: Interplanar Spacings and Interplanar Angles," in *Crystallography and Crystal Defects*, pp. 469–472, Chichester, UK: John Wiley & Sons, Ltd, 2012.

[134] M. Oetzel and G. Heger, "Laboratory X-ray powder diffraction: a comparison of different geometries with special attention to the usage of the Cu Kα doublet," *J. Appl. Cryst*, vol. 32, pp. 799–807, 1999.

[135] M. E. Straumanis, E. Z. Aka, and S. And, "Lattice Parameters, Coefficients of Thermal Expansion, and Atomic Weights of Purest Silicon and Germanium Lattice Parameters, Coefficients of Thermal Expansion, and Atomic Weights of Purest Silicon and Germanium," *J. Appl. Phys.*, vol. 23, no. 23, pp. 1456–2324, 1952.

[136] T. Yao, Y. Oka, and N. Yamamoto, "A Structural Study of the High-Temperature Phase of VO_2(A)," *J. Solid State Chem.*, vol. 112, no. 1, pp. 196–198, 1994.

[137] A. H. Al-Bayati, K. G. Orrman-Rossiter, J. A. Van Den Berg, and D. G. Armour, "Composition and structure of the native Si oxide by high depth resolution medium energy ion scattering," *Surf. Sci.*, vol. 241, pp. 91–102, 1991.

[138] A. Rúa, R. Cabrera, H. Coy, E. Merced, N. Sepúlveda, and F. E. Fernández, "Phase transition behavior in microcantilevers coated with M_1-phase VO_2 and M_2-phase VO_2:Cr thin films," *J. Appl. Phys.*, vol. 111, no. 10, p. 104502, 2012.

[139] S. Timoshenko, D. H. Young, and W. Weaver Jr., *Vibration Problems in Engineering*. John Wiley & Sons, Inc., fourth ed., 1974.

[140] Kai Yang, Zhigang Li, Yupeng Jing, Dapeng Chen, and Tianchun Ye, "Research on the resonant frequency formula of V-shaped cantilevers,"

in *2009 4th IEEE International Conference on Nano/Micro Engineered and Molecular Systems*, pp. 59–62, IEEE, 2009.

[141] E. Caruthers and L. Kleinman, "Energy Bands of Semiconducting VO_2," *Phys. Rev. B*, vol. 7, no. 8, pp. 3760–3766, 1973.

[142] J. M. Wu and W. E. Chang, "Ultrahigh Responsivity and External Quantum Efficiency of an Ultraviolet-Light Photodetector Based on a Single VO_2 Microwire," *ACS Appl. Mater. Interfaces*, 2014.

[143] C. Chen, X. Yi, J. Zhang, and B. Xiong, "Micromachined uncooled IR bolometer linear array using VO_2 thin films," *Int. J. Infrared Millimeter Waves*, vol. 22, no. 1, pp. 53–58, 2001.

[144] X. Chen and S. S. Mao, "Titanium dioxide nanomaterials: synthesis, properties, modifications, and applications.," *Chem. Rev.*, vol. 107, no. 7, pp. 2891–959, 2007.

[145] L. L. Fan, S. Chen, Y. F. Wu, F. H. Chen, W. S. Chu, X. Chen, C. W. Zou, and Z. Y. Wu, "Growth and phase transition characteristics of pure M-phase VO_2 epitaxial film prepared by oxide molecular beam epitaxy," *Appl. Phys. Lett.*, vol. 103, no. 101, 2013.

[146] K. Appavoo, D. Yuan Lei, Y. Sonnefraud, B. Wang, S. T. Pantelides, S. A. Maier, and R. F. Haglund, "Role of Defects in the Phase Transition of VO_2 Nanoparticles Probed by Plasmon Resonance Spectroscopy," *Nano Lett.*, 2012.

[147] T. Sasaki, "Etching gas used for plasma-enhanced etching of vanadium oxide film and method of plasma-enhanced etching of vanadium oxide film," no. US6333270B1, 2001.

[148] H. M. Haendler, S. F. Bartram, R. S. Becker, W. J. Bernard, and S. W. Bukata, "The reaction of fluorine with titanium, zirconium and the

oxides of titanium(iv), zirconium(iv) and vanadium(v)," *J. Am. Chem. Soc.*, vol. 76, no. 8, pp. 2177–2178, 1954.

[149] K. R. Williams, K. Gupta, and M. Wasilik, "Etch Rates for Micromachining Processing-Part II," *J. Microelectromech. Syst.*, vol. 12, no. 6, 2003.

[150] "Dry etching method of anisotropic VO_2," no. CN104332393A, 2015.

[151] D. Ruzmetov, G. Gopalakrishnan, C. Ko, V. Narayanamurti, and S. Ramanathan, "Three-terminal field effect devices utilizing thin film vanadium oxide as the channel layer," *J. Appl. Phys.*, vol. 107, no. 11, 2010.

[152] A. Bagolini, S. Ronchin, P. Bellutti, M. ChistÃÍ, M. Verotti, and N. P. Belfiore, "Fabrication of novel mems microgrippers by deep reactive ion etching with metal hard mask," *J. Microelectromech. Syst.*, vol. 26, no. 4, pp. 926–934, Aug.

[153] Y.-H. Ham, A. Efremov, N.-K. Min, H. W. Lee, S. J. Yun, and K.-H. Kwon, "Etching characteristics of VO_2 thin films using inductively coupled Cl_2 /ar plasma," *Jpn. J. Appl. Phys.*, vol. 48, no. 8S1, p. 08HD04, 2009.

[154] A. Efremov, A. Efremov, Y.-H. Ham, S. J. Yun, N.-K. Min, M. Hong, and K.-H. Kwon, "Etching characteristics and mechanism of vanadium dioxide in inductively coupled Cl_2/Ar plasma," *J. Micro/Nanolithogr. MEMS MOEMS*, vol. 8, no. 2, p. 021110, 2009.

[155] O. V. Yazyev and A. Kis, "MoS_2 and semiconductors in the flatland," *Mater. Today*, vol. 18, no. 1, pp. 20–30, 2015.

[156] V. Sorkin, H. Pan, H. Shi, S. Y. Quek, and Y. W. Zhang, "Nanoscale Transition Metal Dichalcogenides: Structures, Properties, and Applications," *Crit. Rev. Solid State Mater. Sci.*, vol. 39, no. 5, pp. 319–367, 2014.

[157] R. Ganatra and Q. Zhang, "Few-Layer MoS_2: A Promising Layered Semiconductor," *ACS Nano*, vol. 8, no. 5, pp. 4074–4099, 2014.

[158] C. R. Serrao, A. M. Diamond, S.-L. Hsu, L. You, S. Gadgil, J. Clarkson, C. Carraro, R. Maboudian, C. Hu, and S. Salahuddin, "Highly crystalline MoS_2 thin films grown by pulsed laser deposition," *Appl. Phys. Lett.*, vol. 106, no. 5, p. 52101, 2015.

[159] S. H. El-Mahalawy and B. L. Evans, "Temperature dependence of the electrical conductivity and hall coefficient in 2H-MoS_2, $MoSe_2$, WSe_2, and $MoTe_2$," *Phys. Status Solidi B*, vol. 79, no. 2, pp. 713–722, 1977.

[160] S. Kallatt, G. Umesh, N. Bhat, and K. Majumdar, "Photoresponse of atomically thin MoS ₂ layers and their planar heterojunctions," *Nanoscale*, vol. 8, no. 33, pp. 15213–15222, 2016.

[161] D. J. Late, P. A. Shaikh, R. Khare, R. V. Kashid, M. Chaudhary, M. A. More, and S. B. Ogale, "Pulsed Laser-Deposited MoS_2 Thin Films on W and Si: Field Emission and Photoresponse Studies," *ACS Appl. Mater. Interfaces*, vol. 6, no. 18, pp. 15881–15888, 2014.

[162] D. J. Late, Y.-K. Huang, B. Liu, J. Acharya, S. N. Shirodkar, J. Luo, A. Yan, D. Charles, U. V. Waghmare, V. P. Dravid, and C. N. R. Rao, "Sensing Behavior of Atomically Thin-Layered MoS_2 Transistors," *ACS Nano*, vol. 7, no. 6, pp. 4879–4891, 2013.

[163] W. Wu, L. Wang, Y. Li, F. Zhang, L. Lin, S. Niu, D. Chenet, X. Zhang, Y. Hao, T. F. Heinz, J. Hone, and Z. L. Wang, "Piezoelectricity of single-atomic-layer MoS_2 for energy conversion and piezotronics," *Nature*, vol. 514, no. 7523, pp. 470–474, 2014.

[164] Y. Zhou, W. Liu, X. Huang, A. Zhang, Y. Zhang, and Z. L. Wang, "Theoretical study on two-dimensional MoS_2 piezoelectric nanogenerators," *Nano Res.*, vol. 9, no. 3, pp. 800–807, 2016.

[165] L. Zhang, C. Liu, A. B. Wong, J. Resasco, and P. Yang, "MoS_2-wrapped

silicon nanowires for photoelectrochemical water reduction," *Nano Res.*, vol. 8, no. 1, pp. 281–287, 2015.

[166] X. Wang, P. Wang, J. Wang, W. Hu, X. Zhou, N. Guo, H. Huang, S. Sun, H. Shen, T. Lin, M. Tang, L. Liao, A. Jiang, J. Sun, X. Meng, X. Chen, W. Lu, and J. Chu, "Ultrasensitive and Broadband MoS_2 Photodetector Driven by Ferroelectrics," *Adv. Mater.*, vol. 27, no. 42, pp. 6575–6581, 2015.

[167] A. Rogalski, "HgCdTe infrared detector material: history, status and outlook," *Rep. Prog. Phys*, vol. 68, pp. 2267–2336, 2005.

[168] A. Rogalski, "Infrared detectors: status and trends," *Prog. Quantum Electron.*, vol. 27, no. 2âĂŞ3, pp. 59–210, 2003.

[169] C. Eng Png, S. Song, and B. Ping, "State-of-the-art photodetectors for optoelectronic integration at telecommunication wavelength," *Nanophotonics*, vol. 4, no. 1, p. 277, 2015.

[170] R. Kumar, B. Karunagaran, D. Mangalaraj, S. Narayandass, P. Manoravi, M. Joseph, V. Gopal, R. Madaria, and J. Singh, "Room temperature deposited vanadium oxide thin films for uncooled infrared detectors," *Mater. Res. Bull.*, vol. 38, no. 7, pp. 1235–1240, 2003.

[171] K. C. Liddiard, "The active microbolometer: a new concept in infrared detection," in *Microelectronics: Design, Technology, and Packaging* (D. Abbott, K. Eshraghian, C. A. Musca, D. Pavlidis, and N. Weste, eds.), vol. 5274, p. 227, International Society for Optics and Photonics, 2004.

[172] K. Liddiard, "Thin-film resistance bolometer ir detectors-ii," *Infrared Phys.*, vol. 26, no. 1, pp. 43 – 49, 1986.

[173] J. J. Bae, J. H. Yoon, S. Jeong, B. H. Moon, J. T. Han, H. J. Jeong, G.-w. Lee, H. R. Hwang, Y. H. Lee, S. Y. Jeong, and S. C. Lim, "Sensitive

photo-thermal response of graphene oxide for mid-infrared detection," *Nanoscale*, pp. 15695–15700, 2015.

[174] P. Gowda, D. R. Mohapatra, and A. Misra, "Photoresponse of double-stacked graphene to infrared radiation," *Nanoscale*, vol. 7, pp. 15806–15813, 2015.

[175] U. Sassi, R. Parret, S. Nanot, M. Bruna, S. Borini, D. De Fazio, Z. Zhao, E. Lidorikis, F. H. L. Koppens, A. C. Ferrari, and A. Colli, "Graphene-based mid-infrared room-temperature pyroelectric bolometers with ultrahigh temperature coefficient of resistance," *Nat. Commun.*, vol. 8, p. 14311, 2017.

[176] J. B. Leroy, *Infrared spectroscopic studies of adsorption on MoS_2 and WS_2: comparison between nanoparticles and bulk materials*. PhD thesis, Ball State University, 2011.

[177] K. Daoudi, T. Tsuchiya, I. Yamaguchi, T. Manabe, S. Mizuta, and T. Kumagai, "Microstructural and electrical properties of $La_{0.7}Ca_{0.3}MnO_3$ thin films grown on $SrTiO_3$ and $LaAlO_3$ substrates using metal-organic deposition," *J. Appl. Phys.*, vol. 013507, no. 2005, pp. 0–6, 2005.

[178] J. C. O. and L. K. E., "Molybdenum disulfide electrical resistance devices," no. US3465278A, 1969.

[179] I. W. Boyd, "Thin film growth by pulsed laser deposition," *Ceram. Int.*, vol. 22, pp. 429–434, 1996.

[180] D. B. Chrisey and G. K. Hubler, *Pulsed laser deposition of thin films*. J. Wiley, 1994.

[181] Z. Lin, B. R. Carvalho, E. Kahn, R. Lv, R. Rao, H. Terrones, M. A. Pimenta, and M. Terrones, "Defect engineering of two-dimensional

transition metal dichalcogenides," *2D Mater.*, vol. 3, no. 2, p. 022002, 2016.

[182] S. Mignuzzi, A. J. Pollard, N. Bonini, B. Brennan, I. S. Gilmore, M. A. Pimenta, D. Richards, and D. Roy, "Effect of disorder on raman scattering of single-layer MoS_2," *Phys. Rev. B*, vol. 91, no. 19, p. 195411, 2015.

[183] M. Amani, M. L. Chin, A. L. Mazzoni, R. A. Burke, S. Najmaei, P. M. Ajayan, J. Lou, and M. Dubey, "Growth-substrate induced performance degradation in chemically synthesized monolayer MoS_2 field effect transistors," *Appl. Phys. Lett.*, vol. 104, no. 20, p. 203506, 2014.

[184] M. Buscema, G. A. Steele, H. S. J. van der Zant, and A. Castellanos-Gomez, "The effect of the substrate on the Raman and photoluminescence emission of single-layer MoS_2," *Nano Res.*, vol. 7, no. 4, pp. 1–11, 2014.

[185] V. Kranthi Kumar, S. Dhar, T. H. Choudhury, S. A. Shivashankar, and S. Raghavan, "A predictive approach to CVD of crystalline layers of TMDs: the case of MoS_2," *Nanoscale*, vol. 7, no. 17, pp. 7802–7810, 2015.

[186] Y. L. Huang, Y. Chen, W. Zhang, S. Y. Quek, C.-H. Chen, L.-J. Li, W.-T. Hsu, W.-H. Chang, Y. J. Zheng, W. Chen, and A. T. S. Wee, "Bandgap tunability at single-layer molybdenum disulphide grain boundaries," *Nat. Commun.*, vol. 6, p. 6298, 2015.

[187] I. J. Beyerlein, X. Zhang, and A. Misra, "Growth twins and deformation twins in metals," *Annu. Rev. Mater. Res.*, vol. 44, no. 1, pp. 329–363, 2014.

[188] N. Takahashi and M. Shiojiri, "Stacking faults in hexagonal and rhombohedral MoS_2 crystals produced by mechanical operation in relation to lubrication," *Wear*, vol. 167, no. 2, pp. 163–171, 1993.

[189] T. P. Inc., "PelcoÂő sapphire substrate discs, technical information." [Online], 2014.

[190] J. K. Srivastava, M. Prasad, and J. B. Wagner, "Electrical Conductivity of Silicon Dioxide Thermally Grown on Silicon," *J. Electrochem. Soc.*, vol. 132, no. 4, p. 955, 1985.

[191] A. Piccirillo and A. L. Gobbi, "Physical-Electrical Properties of Silicon Nitride Deposited by PECVD on III-V Semiconductors," *J. Electrochem. Soc.*, vol. 137, no. 12, p. 3910, 1990.

[192] T. J. Wieting and J. L. Verble, "Infrared and Raman studies of long-wavelength optical phonons in hexagonal MoS_2," *Phys. Rev. B*, vol. 3, no. 12, pp. 4286–4292, 1971.

[193] W. Li, A. G. Birdwell, M. Amani, R. A. Burke, X. Ling, Y.-H. Lee, X. Liang, L. Peng, C. A. Richter, J. Kong, D. J. Gundlach, and N. V. Nguyen, "Broadband optical properties of large-area monolayer CVD molybdenum disulfide," *Phys. Rev. B*, vol. 90, no. 19, p. 195434, 2014.

[194] H. Liang, "Mid-infrared response of reduced graphene oxide and its high-temperature coefficient of resistance," *AIP Adv.*, vol. 4, no. 10, p. 107131, 2014.

[195] K. Prashanthi, A. Phani, and T. Thundat, "Photothermal Electrical Resonance Spectroscopy of Physisorbed Molecules on a Nanowire Resonator," *Nano Lett.*, vol. 15, no. 8, pp. 5658–5663, 2015.

[196] K. Shimamura, Z. Yuan, F. Shimojo, and A. Nakano, "Effects of twins on the electronic properties of GaAs," *Appl. Phys. Lett.*, vol. 103, no. 2, p. 022105, 2013.

[197] H. Dong, J. Xiao, R. Melnik, and B. Wen, "Weak phonon scattering

effect of twin boundaries on thermal transmission," *Sci. Rep.*, vol. 6, p. 19575, 2015.

[198] A. M. van der Zande, P. Y. Huang, D. A. Chenet, T. C. Berkelbach, Y. You, G.-H. Lee, T. F. Heinz, D. R. Reichman, D. A. Muller, and J. C. Hone, "Grains and grain boundaries in highly crystalline monolayer molybdenum disulphide," *Nat. Mater.*, vol. 12, no. 6, pp. 554–561, 2013.

[199] W. Zhu, T. Low, Y.-H. Lee, H. Wang, D. B. Farmer, J. Kong, F. Xia, and P. Avouris, "Electronic transport and device prospects of monolayer molybdenum disulphide grown by chemical vapour deposition," *Nat. Commun.*, vol. 5, p. 3087, 2014.

[200] Z. G. Yu, Y.-W. Zhang, and B. I. Yakobson, "An Anomalous Formation Pathway for Dislocation-Sulfur Vacancy Complexes in Polycrystalline Monolayer MoS_2," *Nano Lett.*, vol. 15, no. 10, pp. 6855–6861, 2015.

[201] D. Jena, A. C. Gossard, and U. K. Mishra, "Dislocation scattering in a two-dimensional electron gas," *Appl. Phys. Lett.*, vol. 76, no. 13, pp. 1707–1709, 2000.

[202] M. R. Esmaeili-Rad and S. Salahuddin, "High Performance Molybdenum Disulfide Amorphous Silicon Heterojunction Photodetector," *Sci. Rep.*, vol. 3, pp. 2–7, 2013.

[203] M. K. L. Man, S. Deckoff-Jones, A. Winchester, G. Shi, G. Gupta, A. D. Mohite, S. Kar, E. Kioupakis, S. Talapatra, and K. M. Dani, "Protecting the properties of monolayer MoS_2 on silicon based substrates with an atomically thin buffer," *Sci. Rep.*, vol. 6, no. January, p. 20890, 2016.

[204] R. Schlaf, O. Lang, C. Pettenkofer, and W. Jaegermann, "Band lineup of layered semiconductor heterointerfaces prepared by van der Waals

epitaxy: Charge transfer correction term for the electron affinity rule," *J. Appl. Phys.*, 1999.

[205] S. Tongay, J. Suh, C. Ataca, W. Fan, A. Luce, J. S. Kang, J. Liu, C. Ko, R. Raghunathanan, J. Zhou, F. Ogletree, J. Li, J. C. Grossman, and J. Wu, "Defects activated photoluminescence in two-dimensional semiconductors: interplay between bound, charged, and free excitons," *Sci. Rep.*, vol. 3, p. 2657, 2013.

[206] P. G. Datskos and N. V. Lavrik, "Detectors: Figures of Merit," in *Encyclopedia of Optical Engineering*, pp. 349–357, Marcel Dekker, 2004.

[207] T. A. J. Loh and D. H. C. Chua, "Pulsed laser fabricated few-layer MoS_2 on silver," *Chem. Phys. Lett.*, vol. 610âĂŞ611, pp. 284–287, 2014.

[208] D. J. Late, B. Liu, H. S. S. R. Matte, C. N. R. Rao, and V. P. Dravid, "Rapid Characterization of Ultrathin Layers of Chalcogenides on SiO_2/Si Substrates," *Adv. Funct. Mater.*, vol. 22, no. 9, pp. 1894–1905, 2012.

[209] T. A. J. Loh and D. H. C. Chua, "Growth Mechanism of Pulsed Laser Fabricated Few-Layer MoS_2 on Metal Substrates," *ACS Appl. Mater. Interfaces*, vol. 6, no. 18, pp. 15966–15971, 2014.

[210] I. V. Markov, *Crystal Growth for Beginners: Fundamentals of Nucleation, Crystal Growth and Epitaxy*. World Scientific Publishing Company, 1998.

[211] J.-W. Jiang and J.-W. Jiang, "Graphene versus MoS_2: A short review," *Front. Phys.*, vol. 10, no. 3, pp. 287–302, 2015.

[212] G. Siegel, Y. P. Venkata Subbaiah, M. C. Prestgard, and A. Tiwari, "Growth of centimeter-scale atomically thin MoS_2 films by pulsed laser deposition," *APL Mater.*, vol. 3, no. 5, p. 56103, 2015.

[213] R. J. D. Tilley and Wiley InterScience (Online service), *Colour and the optical properties of materials : an exploration of the relationship between light, the optical properties of materials and colour*. Wiley, 2011.

[214] J. Kischkat, S. Peters, B. Gruska, M. Semtsiv, M. Chashnikova, M. Klinkmüller, O. Fedosenko, S. Machulik, A. Aleksandrova, G. Monastyrskyi, Y. Flores, and W. Ted Masselink, "Mid-infrared optical properties of thin films of aluminum oxide, titanium dioxide, silicon dioxide, aluminum nitride, and silicon nitride," *Appl. Opt.*, vol. 51, no. 28, p. 6789, 2012.

[215] H. A. Bafrani, M. Ebrahimi, S. B. Shouraki, and A. Z. Moshfegh, "A facile approach for reducing the working voltage of Au /TiO_2/ Au nanostructured memristors by enhancing the local electric field," *Nanothechnology*, pp. 1–9, 2017.

[216] S. Won, S. Y. Lee, J. Hwang, J. Park, and H. Seo, "Electric field-triggered metal-insulator transition resistive switching of bilayered multiphasic VO_x," *Electron. Mater. Lett.*, vol. 14, no. 1, pp. 14–22, 2018.

[217] B. Radisavljevic, M. B. Whitwick, and A. Kis, "Integrated Circuits and Logic Operations Based on Single-Layer MoS_2," *ACS Nano*, vol. 5, no. 12, pp. 9934–9938, 2011.

[218] N. Oliva, E. A. Casu, C. Yan, A. Krammer, T. Rosca, A. Magrez, I. Stolichnov, A. Schueler, O. J. F. Martin, and A. M. Ionescu, "Van der Waals MoS_2/VO_2 heterostructure junction with tunable rectifier behavior and efficient photoresponse," *Sci. Rep.*, 2017.

[219] J. Liu, A. Goswami, K. Jiang, F. Khan, S. Kim, R. McGee, Z. Li, Z. Hu, J. Lee, and T. Thundat, "Direct-current triboelectricity generation by a sliding schottky nanocontact on MoS_2 multilayers," *Nat. Nanotechnol.*, vol. 13, no. 2, pp. 112–116, 2018.